Composition-dependent precipitation in Mg/Si graded 6xxx aluminium alloys : From powder metallurgy to hardening kinetics simulation

Justine Taurines

To cite this version:

Justine Taurines. Composition-dependent precipitation in Mg/Si graded 6xxx aluminium alloys : From powder metallurgy to hardening kinetics simulation. Materials. INSA de Lyon, 2023. English. NNT : 2023ISAL0023 . tel-04233511

HAL Id: tel-04233511
https://theses.hal.science/tel-04233511v1
Submitted on 9 Oct 2023

N°d’ordre NNT : 2023ISAL0023

THESE de DOCTORAT DE L’UNIVERSITE DE LYON
opérée au sein de
L’Institut National des Sciences Appliquées de Lyon

Ecole Doctorale N° ED 34
Matériaux de Lyon

Spécialité de doctorat : Matériaux

Soutenue publiquement le 27/03/2023, par :
Justine Taurines

Composition-dependent precipitation in Mg/Si graded 6xxx aluminium alloys: from powder metallurgy to hardening kinetics simulation

---

Devant le jury composé de :

Myriam DUMONT	Professeure	ENSAM	Rapporteure
Aude SIMAR	Professeure	UCLouvain	Rapporteure
Williams LEFEBVRE	Professeur	Université de Rouen	Examinateur
Véronique MASSARDIER	Maitre de conférences	INSA Lyon	Examinatrice
Michel PEREZ	Professeur	INSA Lyon	Directeur de thèse
Olivier DEZELLUS	Maitre de conférences	UCBL	Directeur de thèse
Xavier BOULNAT	Maitre de conférences	INSA Lyon	Co-encadrant
Alexis DESCHAMPS	Professeur	INP Grenoble	Co-encadrant
Fanny MAS	Docteure	Constellium	Invitée

INSTITUT NATIONAL
DES SCIENCES
APPLIQUÉES
LYON

Département de la Formation par la Recherche et des Études Doctorales (**FEDORA**)

Bâtiment INSA direction, 1er étage
37, av. J. Capelle
69621 Villeurbanne Cédex
fedora@insa-lyon.fr

Référence : TH0956_TAURINES

L'INSA Lyon a mis en place une procédure de contrôle systématique via un outil de détection de similitudes (logiciel Compilatio). Après le dépôt du manuscrit de thèse, celui-ci est analysé par l'outil. Pour tout taux de similarité supérieur à 10%, le manuscrit est vérifié par l'équipe de FEDORA. Il s'agit notamment d'exclure les auto-citations, à condition qu'elles soient correctement référencées avec citation expresse dans le manuscrit.

Par ce document, il est attesté que ce manuscrit, dans la forme communiquée par la personne doctorante à l'INSA Lyon, satisfait aux exigences de l'Etablissement concernant le taux maximal de similitude admissible.

Département FEDORA – INSA Lyon - Ecoles Doctorales

SIGLE	ECOLE DOCTORALE	NOM ET COORDONNEES DU RESPONSABLE
CHIMIE	**CHIMIE DE LYON** **https://www.edchimie-lyon.fr** Sec. : Renée EL MELHEM Bât. Blaise PASCAL, 3e étage secretariat@edchimie-lyon.fr	**M. Stéphane DANIELE** C2P2-CPE LYON-UMR 5265 Bâtiment F308, BP 2077 43 Boulevard du 11 novembre 1918 69616 Villeurbanne **directeur@edchimie-lyon.fr**
E.E.A.	**ÉLECTRONIQUE, ÉLECTROTECHNIQUE, AUTOMATIQUE** **https://edeea.universite-lyon.fr** Sec. : Stéphanie CAUVIN Bâtiment Direction INSA Lyon Tél : 04.72.43.71.70 secretariat.edeea@insa-lyon.fr	**M. Philippe DELACHARTRE** INSA LYON Laboratoire CREATIS Bâtiment Blaise Pascal, 7 avenue Jean Capelle 69621 Villeurbanne CEDEX Tél : 04.72.43.88.63 **philippe.delachartre@insa-lyon.fr**
E2M2	**ÉVOLUTION, ÉCOSYSTÈME, MICROBIOLOGIE, MODÉLISATION** **http://e2m2.universite-lyon.fr** Sec. : Bénédicte LANZA Bât. Atrium, UCB Lyon 1 Tél : 04.72.44.83.62 secretariat.e2m2@univ-lyon1.fr	**Mme Sandrine CHARLES** Université Claude Bernard Lyon 1 UFR Biosciences Bâtiment Mendel 43, boulevard du 11 Novembre 1918 69622 Villeurbanne CEDEX **sandrine.charles@univ-lyon1.fr**
EDISS	**INTERDISCIPLINAIRE SCIENCES-SANTÉ** **http://ediss.universite-lyon.fr** Sec. : Bénédicte LANZA Bât. Atrium, UCB Lyon 1 Tél : 04.72.44.83.62 secretariat.ediss@univ-lyon1.fr	**Mme Sylvie RICARD-BLUM** Institut de Chimie et Biochimie Moléculaires et Supramoléculaires (ICBMS) - UMR 5246 CNRS - Université Lyon 1 Bâtiment Raulin - 2ème étage Nord 43 Boulevard du 11 novembre 1918 69622 Villeurbanne Cedex Tél : +33(0)4 72 44 82 32 **sylvie.ricard-blum@univ-lyon1.fr**
INFOMATHS	**INFORMATIQUE ET MATHÉMATIQUES** **http://edinfomaths.universite-lyon.fr** Sec. : Renée EL MELHEM Bât. Blaise PASCAL, 3e étage Tél : 04.72.43.80.46 infomaths@univ-lyon1.fr	**M. Hamamache KHEDDOUCI** Université Claude Bernard Lyon 1 Bât. Nautibus 43, Boulevard du 11 novembre 1918 69 622 Villeurbanne Cedex France Tél : 04.72.44.83.69 **hamamache.kheddouci@univ-lyon1.fr**
Matériaux	**MATÉRIAUX DE LYON** **http://ed34.universite-lyon.fr** Sec. : Yann DE ORDENANA Tél : 04.72.18.62.44 yann.de-ordenana@ec-lyon.fr	**M. Stéphane BENAYOUN** Ecole Centrale de Lyon Laboratoire LTDS 36 avenue Guy de Collongue 69134 Ecully CEDEX Tél : 04.72.18.64.37 **stephane.benayoun@ec-lyon.fr**
MEGA	**MÉCANIQUE, ÉNERGÉTIQUE, GÉNIE CIVIL, ACOUSTIQUE** **http://edmega.universite-lyon.fr** Sec. : Stéphanie CAUVIN Tél : 04.72.43.71.70 Bâtiment Direction INSA Lyon mega@insa-lyon.fr	**M. Jocelyn BONJOUR** INSA Lyon Laboratoire CETHIL Bâtiment Sadi-Carnot 9, rue de la Physique 69621 Villeurbanne CEDEX **jocelyn.bonjour@insa-lyon.fr**
ScSo	**ScSo*** **https://edsciencessociales.universite-lyon.fr** Sec. : Mélina FAVETON INSA : J.Y. TOUSSAINT Tél : 04.78.69.77.79 melina.faveton@univ-lyon2.fr	**M. Bruno MILLY** Université Lumière Lyon 2 86 Rue Pasteur 69365 Lyon CEDEX 07 **bruno.milly@univ-lyon2.fr**

*ScSo : Histoire, Géographie, Aménagement, Urbanisme, Archéologie, Science politique, Sociologie, Anthropologie

Acknowledgements

On imagine souvent le ou la thésarde comme une créature solitaire penchée sur un semblant de trouvaille. En réalité, de nombreuses personnes contribuent aux travaux du ou de la doctorante de manières très variées. C'est grâce à ces personnes que ces quatre dernières années ont été, pour moi, si passionnantes professionnellement et épanouissantes personnellement, avec comme aboutissement un manuscrit et une défense qui me procurent une certaine fierté.

Dans un premier temps, j'aimerais remercier les membres du jury qui ont pris le temps d'examiner et de discuter ce travail. J'aimerai tout particulièrement remercier les rapporteures Aude Simar et Myriam Dumont pour leur rapport complet et éclairant sur les points d'amélioration de ce travail. J'aimerais ensuite remercier Fanny Mas pour avoir amené un regard industriel à ces travaux de recherche lors de la soutenance. J'aimerai ensuite remercier Williams Lefebvre pour son rôle d'examinateur lors de la défense, mais également pour son aide sur les analyses SAT et le temps qu'il a consacré à mes échantillons capricieux malgré son emploi du temps tendu. Enfin, un très très grand merci à Véronique Massardier pour nous avoir partagé son expertise sur les alliages d'Aluminium, pour nous avoir donné sa vision globale sur ce projet pendant la soutenance et puis surtout, pour tout son temps accordé avec générosité à nos analyses MET inscrites dans un contexte des plus compliqués.

Ensuite, j'aimerais remercier mes directeurs de thèse à qui je dois tout.

Merci Olivier, d'abord, d'avoir été le porteur du projet. Puis merci surtout pour ta pédagogie indiscutable sur un sujet aussi complexe que la thermodynamique. Dès que je sortais de ton bureau, j'avais l'impression que le monde était limpide. Merci pour le calme que tu inspires, ta gentillesse et ta rigueur scientifique.

Alexis, merci pour ta connaissance sur la caractérisation de la précipitation et pour ton audace pour faire avancer la science. Finalement, je ne t'ai pas vu souvent, mais tu as toujours été présent et réactif. Merci aussi pour ta franchise et attention à bien fermer les vannes au synchrotron !

Michel, merci ! Tu as la physique dans le sang, c'est impressionnant. Tu y mets toute ta bonne volonté lorsque tu veux comprendre certains phénomènes, et tout en bonne humeur. Je suis très heureuse d'avoir été initiée aux codes et à la modélisation par toi. Je n'aurai pas pu tomber mieux. Je tiens aussi à te remercier pour ton accueil et pour tout ce que tu donnes à la vie du laboratoire. Continue de proposer des sorties sportives et de faire découvrir cette très belle région (que tu connais si bien) aux nouveaux et nouvelles arrivantes.

Enfin Xavier, merci. Merci pour ton suivi régulier, pour tes encouragements et pour toutes nos discussions. Même lorsque l'on s'est écarté de ton domaine, tu n'as pas arrêté de prendre des nouvelles et tu m'as toujours conseillée avec sagesse et modestie. J'ai appris ce que proactif signifie en te voyant fonctionner, même si, les trois-quarts de nos plans ne sont pas sortis du papier (DIC, HIP, élaboration de nuances commerciales…). Et puis bien sûr, merci pour ta bonne humeur et ton humour à toute épreuve. C'était un immense plaisir de travailler avec toi.

Quelle belle brochette vous faites ! Je tiens aussi à vous dire que tout au long de ma thèse, je me suis sentie très bien accompagnée. Merci à chacun de m'avoir transmis connaissances et conseils avec bienveillance et merci d'avoir répondu présent quand j'en avais besoin.

Maintenant, j'aimerais remercier ceux et celles qui m'ont aidée de plus ou moins près dans ce projet. Bien entendu, je tiens à remercier, Frédéric De Geuser, pour son implication à différents niveaux. Merci pour sa disponibilité, pour ses conseils, pour sa pédagogie (!) et finalement merci pour sa gentillesse. Ensuite, je remercie chaleureusement Janna Attari, pour sa persévérance, sa rigueur et sa curiosité. La quasi-totalité des points de dureté présentés dans ce manuscrit provient de ses mesures. Merci également à Florian Mercier pour son aide précieuse sur le SPS et puis, plus généralement, pour sa prise en main des différents déménagements qui ont ponctué mes années à MATEIS. Merci à François et Rodica pour leur accompagnement sur la plateforme thermique du LMI. Merci pour leur accueil, leur disponibilité et leur gentillesse. Je tiens ensuite à remercier Sophie Cazottes pour ses précieux conseils et son aide de microscopiste, Jérôme Adrien entre autres pour les analyses tomo RX et Florence Robaut pour les longues analyses WDS au SIMAP. J'aimerai ensuite remercier plus généralement Bérangère, Kader, Carole, Delphine, Justine et Joël pour leurs aides sur les thématiques aussi variées que le polissage et l'informatique. Enfin, une bonne partie des formations ou des conseils proviennent directement des doctorant.es. Merci aux ancien.nes, dont Marion C., Quentin S., Arnaud A., Manon et Gwen. Merci à ceux et celles qui ont galéré juste avant ou avec moi, dont Laurabelle, Lucas, Julien G., Romain F. et Marion B. Merci à un post-doc en particulier (aussi cobureau et pro de la DRX à ses heures perdues) : Maël.

J'en viens donc à la vie de labo. J'aimerai d'abord remercier le LMI pour son accueil. J'étais clairement une touriste chez vous, mais je me suis toujours sentie bien accueillie. Je pense notamment à Jérôme, Bruno, Nicolas et Yamina.

J'aimerais maintenant me pencher sur l'imposante tâche qui est de remercier les différents acteurs de MATEIS. Je vais commencer par remercier toute l'équipe Corris qui a gentiment accepté la salle chimie Métal ainsi que deux métalleuses pendant la période des algecos. Merci à toustes ! Puis, je vais continuer avec la grande partie de mes interactions : doctorant.es MATEIS merci !

- Merci à la team sportive
- Merci à la team sportive moins sportive
- Merci à la team fêtarde/flémarde/fléchettes (merci de m'avoir laissé faire des trous sur un certain mur)
- Merci à la team originelle de Blaise Pascal (et aux parties Among us pendant les confinements)
- Merci aux petits nouveaux
- Merci aux grands nouveaux
- Merci à la team manif

- Merci à chaque cobureau de l'Aquarium (dont les poissons)
- Merci aux stagiaires, PFE et PFE qui sont devenus doctorant.es
- Merci à ceux et celles qui ne se retrouvent pas dans ces cases. C'est nul les cases.

Je tiens à remercier plus particulièrement ici plusieurs personnes.

Dans la famille du deuxième de Saint-Ex, je demande Laurabelle et Quentin. Laurabelle, merci pour tes nombreux conseils et tous nos échanges. Tu es pleine d'énergie et tu la partages naturellement. Ça stimule bien un tempérament comme le mien. J'ai adoré faire de multiples sports avec toi malgré la disparition progressive de la team sportive. Quentin S., merci pour toutes nos discussions ensemble, souvent entre deux manips, et pour ton humour. Tu as toujours répondu présent quand j'en avais besoin. Merci à vous deux d'avoir rallongé votre séjour ici, pour mon bien-être bien entendu. Ça m'a fait très bizarre de vous voir partir. Je ne me fais pas de soucis pour vos parcours pros. J'espère juste qu'on arrivera à se revoir même dans le cas où je ne me retrouverais pas dans la bonne région.

Maël, j'ai beaucoup aimé t'avoir dans le bureau pendant tout ton postdoc. Quel parcours ! Je suis trop contente pour toi. Super sympa et drôle, il n'y a pas de doute que tu te feras ta place dans ton nouveau labo. J'ai toujours adoré nos conversations sur tout et n'importe quoi : monnaie de collection, Formule 1, politique, sciences... Et en plus, j'étais heureuse de voir que tu devenais de plus en plus écolo ! Sache que, comme nous, les poissons ont eu du mal à accepter ton départ. J'espère que je passerai sur Bordeaux dans pas trop longtemps !

Un méga remerciement spécial pour Louis H. the cobureau de la vie. Merci de m'avoir supportée tout ce temps et merci d'avoir instauré un super tournoi de baby-foot au moment où je partais ;). J'ai adoré tous nos moments de lâché prise, absolument nécessaire à notre survie en milieu ultra productif : basé sur une vidéo plus ou moins nulle, ou grâce à un peu de musique dans le bureau à 18 h ou encore avec l'ultime, le magnifique, encartonnage professionnel en 6 min (on pense à toi Seb <3). Mais j'ai adoré aussi, tous nos moments de déblocage scientifique, où juste en écoutant les galères de l'autre et en ouvrant un nouveau point de vue : pouf une solution se dessinait. Merci pour les raccourcis mac ou python à la volée. Merci pour les passages devant chez moi pour me rendre les trucs que j'avais oublié. Merci pour la découverte du basket villeurbannais. Tellement de merci. Un grand merci pour la soutenance aussi ! Pour l'installation, pour m'avoir fait passer le temps avec Jyves pendant la longue attente du jury, pour ta gamelle inoubliable à vélo ce soir-là. Je crois que je me souviendrai de ton étalement de crêpe toute ma vie. En vrai, bravo pour ta résilience avec ton vélo de galère, à côté de ça la fin de thèse, ce sera les doigts dans le nez. Bon et toi, on se tient au jus, obligé.

Merci à Théophile pour ta façon d'être, ta sympathie naturelle et pour la teuf ! J'aurais bien aimé en faire plus (de la teuf) mais d'un autre coté ; pour le bien de cette thèse, je me dis qu'il ne valait mieux pas ;).

Merci à Florian S., quelle personnalité ! Tu es tellement gentil, accommodant et droit dans tes bottes, tu nous amènes à nous introspecter. Je ne me fais pas de doutes sur ton pouvoir d'aller au bout, malgré toutes les complications que tu as pu avoir. Ne prends pas trop ton temps quand même. À voir la vitesse à laquelle tu manges, si on fait un produit en croix, tu en as encore pour deux ans de thèse.

Un grand merci également à Akkiz, à Lucas, à Alex et à Julien G. pour toutes nos conversations. J'espère de tout cœur vous revoir et je vous souhaite plein de réussite (certaine).

Maintenant que j'en ai fini avec les CDD, je m'adresse aux permanent.es Métal : un énorme merci ! Je mets quelques noms ici : Patrice, Laura, Hélène, Stéphanie, Eric, Pierre-Antoine, Frida et toustes ceux et celles que j'ai déjà évoqué précédemment. C'était top, restez comme ça. J'ai une petite pensée spéciale pour JYB : merci pour l'ambiance que tu mets dans cette équipe. Mes derniers mois de rédaction ont été beaucoup plus doux avec tes passages réguliers dans notre bureau, pour officiellement discuter avec tes doctorants, officieusement pour nous soutirer de la tisane. C'est drôle, je me souviens de toi lors de mon premier jour, tu étais installé dans la salle café jaune de Saint-Ex accompagné de Stéphanie. Tu m'as dit que j'allais m'éclater avec Michel et Xavier tandis qu'Alexis G. passait par là en chaussettes car soi-disant en rédaction. Michel, tu m'avais prévenu : « tu verras, dans 3 ans, ce sera toi ». Je ne suis pas allée jusqu'aux balades en chaussettes, mais qu'est-ce que je me suis sentie à ma place parmi vous toustes. En résumé Métal, je tiens à vous dire que je suis triste de vous quitter et que je ferai tout pour retrouver un environnement de travail proche de celui-là.

C'est le moment des proches. Famille et ami.es merci d'être là. Merci de nous avoir accueilli.es pour des week-ends divers et variés (Sion, Fribourg, Strasbourg, Chambéry, Marseille, Toulouse, Paris, Nantes, Corrèze, Serre Chevalier. . .) au cours de ces dernières années. Merci à ceux et celles qui sont venu.es nous voir et/ou avec qui on a partagé de superbes vacances (dans le ter-ter, en Dordogne, au bord de la mer méditerranée, à l'île de Ré, à Ikaria ou en Roumanie). Comme disait ma grand-mère : « le boulot, c'est bien, mais le chill aussi ».

J'aimerais remercier plus particulièrement, ceux et celles qui sont venu.es jusqu'à Lyon pour ma soutenance de thèse. J'ai été extrêmement touchée de vous avoir auprès de moi durant ce week-end et de me sentir si bien entourée. J'espère qu'à défaut d'avoir compris, vous avez pu un peu visualiser l'atmosphère dans laquelle s'est inscrit mon travail. C'est une occasion rare de pouvoir ainsi rassembler milieux professionnel et personnel.

Une dédicace à ma tribu : Lucie, Manon, Lisa, Margaux et Paul. Ce qui est génial avec notre nombre, c'est quand général, il y en a toujours un de dispo quand on a besoin de parler. Merci, entre autres, pour nos appels du dimanche matin et puis, si je remonte au confinement, pour la bonne ambiance virtuelle ou réelle (Mrraou). On a une immense chance de s'avoir et de se faire avancer au détriment de nos différences. J'espère de tout cœur qu'on continuera à rester aussi soudé. Naturellement, j'en viens aux parents. Papa, Maman, merci d'être ce que vous êtes. Merci d'avoir rallongé le terme de votre clause de parentalité en vous occupant de nouveau de moi pendant les périodes de rédaction à la maison. Maman, tu m'as tellement donnée. Merci pour tout et en particulier pour tes bons conseils. J'espère que je pourrai te rendre la pareille à ma manière et te souffler un peu de ma sérénité apparente.

Le meilleur pour la fin : Cristian, merci. Je pense que tu ne t'en es pas vraiment rendu compte, mais tu as été mon roc pendant ces dernières années. Je suis plutôt de nature détendue, mais je prends les choses à cœur et je peux donc être stressée par les enjeux d'un tel projet. Tu as toujours su trouver les mots simples, coulant de source pour toi, pour remettre les choses à leur place et me faire prendre de la distance. Merci aussi de t'occuper si bien de moi, en particulier quand je suis impactée par la fatigue au travers de maladies ou de migraines. Désolée de ne pas avoir pris à cœur les tâches ménagères quelque temps (surtout notre amie la vaisselle) mais quand même va falloir arrêter avec cette anecdote de l'assiette ! Je me rends de plus en plus compte de nos différences, mais je suis toujours aussi bien avec toi. Que la route continue, j'ai hâte de voir où elle nous mènera.

Merci à toustes pour ces quatre dernières années. Sans vous, cette expérience n'aurait pas été ce qu'elle a été : riche et tendre.

French summary

Le recyclage des alliages d'aluminium peut conduire à des gammes non contrôlées de compositions d'éléments d'alliage. La conception des alliages basée sur le recyclage doit donc tenir compte de ces variations de composition sur les propriétés de l'alliage. Pour fournir de nombreuses données expérimentales dans l'espace de composition du système Al-Mg-Si, des gradients de Mg-Si ont été fabriqués par métallurgie des poudres. Ces échantillons à gradient ont été étudiés de différentes manières tout au long du processus de fabrication. Ensuite, des caractérisations microstructurales, principalement au cours d'un vieillissement isotherme à 170 °C, ont été réalisées le long du gradient. Enfin, des modèles de précipitation et de durcissement basés sur la physique ont simulé la précipitation et la compétition de cinq types de précipités (β", β', U2, B' et Si) dans des gradients numériques afin de tenter d'expliquer ce qui a été observé expérimentalement.

Fabrication d'alliages Al-Mg-Si à gradient de composition

Un procédé de fabrication par frittage flash (SPS) sur deux mélanges de poudres, suivi d'un traitement d'interdiffusion de 10 jours à 550 °C a permis d'obtenir le gradient de Mg-Si visé sur une longueur de 3 mm. Le gradient en question contient une variation des teneurs en Mg_2Si possible et une variation de l'excès de Mg ou de Si par rapport à l'alliage pseudo-binaire ($x_{Mg}/x_{Si} = 2$). Le gradient peut être allongé par laminage à 6 mm. Une voie similaire pourrait être appliquée à d'autres systèmes métalliques pour des études combinatoires.

En raison de la métallurgie des poudres, les caractéristiques microstructurales suivantes ont été observées dans les gradients :

- La distribution de la taille des grains dans les échantillons massifs est fortement liée à la taille initiale des poudres, même après un long traitement de mise en solution.
- La poudre riche en Mg fournit un réseau important d'oxydes.
- La petite taille des grains semble être responsable de la dualité de diffusion (volume et joints de grains) de l'élément Si. Cet effet a été modélisé pour prédire avec plus de précision l'étendue du gradient.

Dans le gradient de composition entre Al-1.2.%Si et Al-2.6.%Mg, l'effet du durcissement par la solution solide a été évalué et les coefficients de durcissement de Mg et Si ont été déterminés.

Etude expérimentale de la precipitation dans les gradients

Des études sur la précipitation ont été menées à différentes échelles et pour différents objectifs. Des investigations globales utilisant microdureté et diverses expériences de calorimétrie différentielle à balayage (DSC) ont permis d'obtenir, entre autres, les cinétiques de précipitation.

À l'échelle nanométrique, des états de précipitation spécifiques ont été observés et caractérisés (précipités et solution solide) en utilisant diffusion anomale des rayons X aux petits angles (ASAXS), microcopie electronique en transmission (MET) et sonde atomique tomographique (SAT).

D'après les mesures de microdureté, après un traitement de vieillissement interrompu à 170 °C, la résistance la plus élevée est obtenue pour deux compositions spécifiques : l'une pour laquelle la teneur en Mg+Si est maximale ($x_{\mathrm{Mg}}+x_{\mathrm{Si}}$ = 1,7 at.%) et l'autre pour laquelle la composition était la plus proche de Mg_5Si_6 (avec Mg/Si = 1,2). Ces caractéristiques ont été confirmées par DSC isotherme et expliquées, en partie, grâce à la DSC sous chauffage continu. Le premier maximum semble être obtenu en raison d'une cinétique de précipitation rapide tandis que le second en raison d'une fraction volumique élevée de clusters et de phases cohérentes.

En combinant les résultats de la microdureté, de la DSC et de l'ASAXS, différents régimes de cinétique de précipitation ont été mis en évidence:

- Mg/Si $\leq$ 0,3 : excès extrême de Si, précipitation principale de Si pur, pas d'amélioration majeure de la dureté, précipitation très lente, diamètres des précipités très petits (env. 2.6 nm)
- 0.4 $\leq$ Mg/Si $\leq$ 1 : fort excès de Si (domaine Si), précipitation de Si pur, amélioration de la dureté, précipitation lente mais durcissement rapide, précipités de petits diamètres en début de vieillissement (env. 2.8 nm)
- 1 $\leq$ Mg/Si $\leq$ 3 : compositions quasi pseudo-binaires (domaine PB), pouvant présenter des restes de précipitation de Si pur, amélioration maximale de la dureté, durcissement plus rapide, variation importante du diamètre des précipités (env. 8 nm sur 1 mois de vieillisement) et diamètre moyen initial assez important (env. 3.2 nm)
- Mg/Si > 3 : fort excès de Mg (domaine Mg), amélioration de la dureté, durcissement lent mais précipitation semi-cohérente rapide, diamètre moyen initial assez important (env. 3.3 nm)

Ensuite, les caractérisations MET sur deux états spécifiques de vieillissement (T6 et survieilli) et pour différents domaines de compositions (Si, PB et Mg) ont confirmé l'observation faite avec ASAXS : après 1 mois, les diamètres des précipités ont augmenté de manière plus significative pour les compositions proches de Mg/Si = 2. Des observations similaires ont été faites sur la longueur moyenne des précipités. La spécificité de croissance finale peut être résumée pour les trois domaines observés comme suit :

- domaine Si : les précipités sont plutôt courts au départ et s'étendent principalement en longueur.
- domaine PB : les précipités s'épaississent beaucoup et s'allongent également.
- domaine Mg : les précipités s'épaississent et ne semblent pas s'étendre beaucoup en longueur

Les charactérisations MET ont également montré qu'à l'état T6 (16 h à 170 °C), le site du domaine Mg présente une séquence de précipitation en avance par rapport au site PB qui était également en avance par rapport au site Si. En effet, des précipités β' ont été observés pour le site Mg alors que des précipités β_0' semblaient présents pour le site PB et seulement β" pour le site Si.

Enfin, des informations complémentaires ont été accumulées dans une perspective de simulation : identification des précipités pour le site Si après sur-vieillissement (MET-HR) et évolution des teneurs en solutés pour 2 gradients de composition (SAT).

Simulation de la précipitation à travers les gradients

Un modèle couplé précipitation/durcissement adapté à cette étude a été développé et confronté avec succès aux données expérimentales (notamment pour un traitement de vieillissement à 170 °C). Ce modèle a la particularité de prendre en considération cinq types de précipités et de fournir des résultats pour une large gamme de compositions initiales simultanément.

Pour un traitement de vieillissement à 170 °C, comme prévu, le modèle a montré que les propriétés mécaniques maximales (limite d'élasticité ou dureté) sont principalement influencées par la précipitation β". Les différences de vitesse de précipitation β" (et semi-cohérente) sont observées en fonction de la composition :

- pour le ratio atomique Mg/Si $\leq$ 0,3 : précipitation principale de Si pur
- pour 0,3 $\leq$ Mg/Si $\leq$ 1,2 : augmentation de la vitesse de précipitation de β" avec l'augmentation de la teneur en Mg
- pour 1,2 $\leq$ Mg/Si $\leq$ 2.5 : légère diminution moyenne de la vitesse de précipitation de β" avec l'augmentation de la teneur en Mg
- pour Mg/Si $\geq$ 2,5 : diminution de la vitesse de précipitation β" et augmentation de la vitesse de précipitation semi-cohérente avec l'augmentation de la teneur en Mg

Les régimes sont similaires à ceux observés expérimentalement avec les différentes caractérisations de précipitation.

Ce modèle est également capable de fournir le domaine de précipitation de chaque phase et les pics de durcissement pour différentes températures de vieillissement (entre 150 et 350 °C) et compositions initiales de solutions solides. Pour diverses compositions, le modèle montre une fenêtre étroite de température, autour de 175 °C pour laquelle le durcissement est maximal.

Conclusion

D'un point de vue général, les **principaux objectifs ont été atteints** à savoir l'obtention de gradient de Mg/Si dans le système Al-Mg-Si, la caractérisation de la précipitation associée et le développement d'un modèle prédictif de cette précipitation et du durcissement mécanique qu'elle entraine. Cependant, il est important de préciser que les échantillons ont compliqué l'étude. En effet, ces matériaux ont accumulé diverses faiblesses :

- la voie par la métallurgie des poudres a engendré des **pores** au sein des matériaux : compliquant l'analyse WDS et les différentes préparations d'échantillons (TEM, ASAXS, éprouvettes de traction).
- les **gradients** de Mg-Si étaient intéressants pour les aspects introduits dans ce document mais ils ont aussi : compliqué la préparation des échantillons (DSC, TEM, APT) et conduit à une importante incertitude sur la composition.
- le **système Al-Mg-Si** était lui-même un défi considérable pour les expériences ASAXS.

Ces problèmes ont entraîné soit des incertitudes, soit un manque de données expérimentales. Le modèle présenté aurait pu être plus précis et plus complet, tout comme les interprétations de cette étude. Les résultats permettent donc d'envisager également des améliorations dans les protocoles de préparation et d'analyses.

Contents

Introduction

Context

Aluminium (Al) is the most widespread non-ferrous metal in the industry. This is explained by several facts. Aluminium is the third most abundant element in the earth crust and therefore many bauxite deposits sprinkle the world surface. Aluminium has also very useful properties. It has an important ductility at moderate temperature and can then be easily manufactured and transformed. It is relatively light compared to most of the other alloys which is highly sought for transport applications. And its passivation layer brings very good resistance to oxidation. Aluminium has many qualities except mechanical strength. Fortunately, many chemical elements in small quantities can improve the properties of pure Al. The main ones used to bring mechanical strength are copper (Cu), manganese (Mn), magnesium (Mg), silicon (Si) and zinc (Zn). In two hundred years, these Al alloys spread out in all domains. Mirrors, cables, electronic devices, windows, boats, planes is an non exhaustive list of everyday objects using these alloys.

Al is not found pure in its ore, the sedimentary rock named bauxite. It is its Al hydroxide: hydrated alumina (Al_2O_3) that is present. In the bauxite, there are also other oxides of Silicon (Si), Iron (Fe), Titanium (Ti) and Calcium (Ca). To obtain pure Al from bauxite, two refining steps are required. The Bayer process is separating alumina from the other oxides and dehydrating it. Then, the Hall-Héroult process, also named the alumina electrolysis, forms the metallic Al. These two processes are greedy in energy, and they create undesired products such as red mud and carbon dioxide (CO_2). In addition, mining promotes the biodiversity destruction [LAD 15]. Here, the focus will be put on the global greenhouse gas (GG) emissions (in kg of equivalent of CO_2 per kg of produced Al). These emissions are summarised per unit process in the histogram Figure 1 depending on the emission type. These datas of the year 2010 were gathered by Nunez *et al.* [NUN 16].

The worldwide Al production is responsible in 2010 for 17 kg of CO_2 per kg of Al produced. The electrolysis consumption of energy is so important that it is causing 50% of the GG emissions. As expected, depending on the energy used, that emission post and consecutively the total GG emissions can be very different.

The Table 1 gives the equivalent CO_2 emitted in kg/MWh for electricity production of each energy source in 2008 [TUR 13].

Countries using natural gas and coal for electricity production will have an Al production which emits more GG.

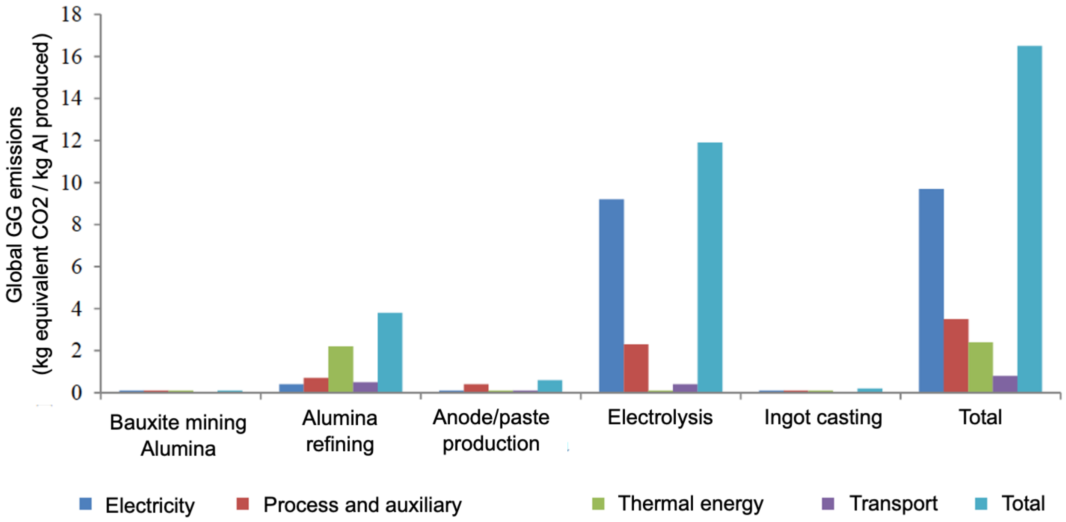

Figure 1: Global greenhouse gas emissions (in kg of equivalent of CO_2 per kg of produced Al) per unit process depending on the emission type. The electrolysis is the main responsible process of greenhouse gas emissions in the world production of Al [NUN 16].

Energy sources	Hydro	Coal	Natural gas	Oil	Nuclear
Equivalent CO2 (kg/MWh)	2 - 20	660 - 1050	380 - 1000	530 - 900	3 - 35

Table 1: Equivalent CO_2 emitted in kg/MWh for electricity production of each energy source in 2008 [TUR 13]

Table 2 gives, for the year 2010, the distribution of energy sources used in Al production for the main countries or regions producers of Al [NUN 16].

Al produced from Asian countries or from the Gulf states emits more GG than Canadian or Russian Al. Even though some countries are emitting less (9 tonnes CO_2 / tonnes of Al produced for Canada in 2010), the electricity of the world Al production stands mostly on coal (59%).

Some Al producer countries, like Canada, continue to reduce their carbon footprint in this industry. They succeed to reduce of 2 equivalent CO_2 tonnes (out of 9) per tonne of produced Al by using less fossil energy and by upgrading the electrolysis. Since 2008, a cleaner process named Orbite could replace the Bayer one but, for now, no profit encourages the industry to change their industrial lines.

Al alloys can also be easily and infinitely recycled [GRA 11, DAH 07] with small amount of supplementary energy: only 5% of the energy required to produce Al from ore [GUT 13]. Therefore, against 12 kg CO_2/kg emitted in average for new Al, recycled Al is producing only 0.6 kg CO_2/kg [DAS 10]. Today 75% of all the Al produced in history (near a billion metric tons) is still in use [SCH 13]. And in average, one third of Al produced today is from recycled scrap [GRA 11]. The proportion of available Al from recycling should increase in the next

Production region	Hydro	Coal	Natural gas	Oil	Nuclear
Africa	57	43	0	0	0
North America	74	24	1	0	1
South America	72	0	27	0	0
Asia (except China)	14	86	0	0	0
Canada	100	0	0	0	0
China	10	90	0	0	0
Gulf states	0	0	100	0	0
Europe	68	10	5	1	16
Oceania	27	73	0	0	0
Russia and Eastern Europe	98	2	0	0	0
World	30	59	9	0	2

Table 2: Distribution of energy sources (in %) used in Al production for the main countries or regions producers of Al in 2010 [NUN 16]

years until becoming predominant [SVE 15]. The losses are unavoidable though and the storage of Al in the products tends to prove that production have to go on to pursue the rhythm of global consumption. Figure 2 shows the evolution of Al world production over the years and its distribution between the different regions [JÉG 21].

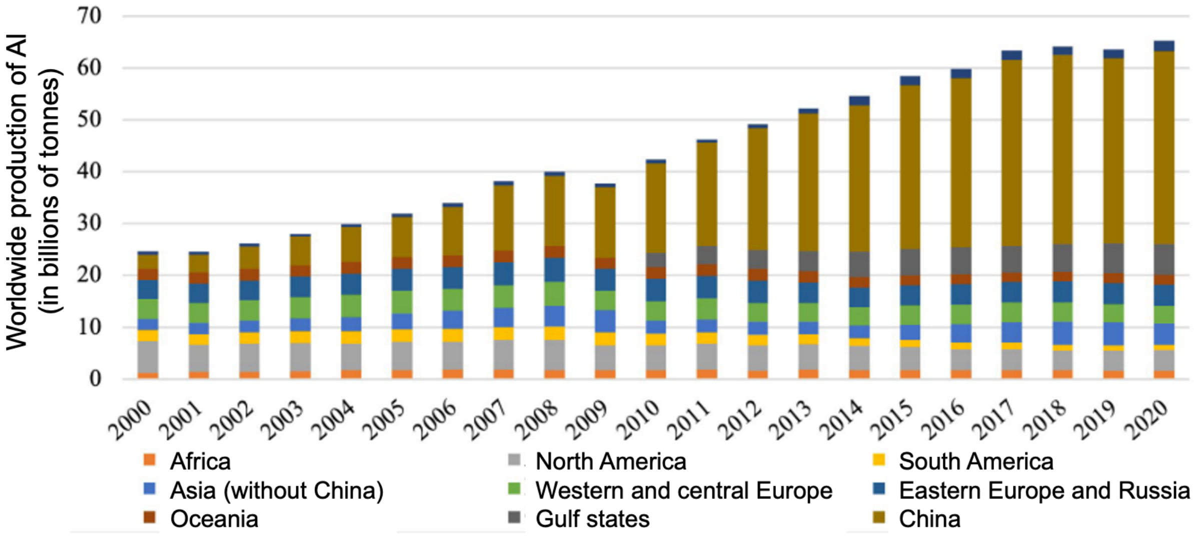

Figure 2: Evolution of Al world production over the years and its distribution between the different regions [JÉG 21]

On this graph, the evolution of Al production over the years is outstanding. It has doubled in 15 years until 65 billions of tonnes produced in 2020 despite recycling. China succeeds to acquire most of that growth.

Today, France is no longer a producer of Al and buys most of this resource to Russia (80%) and China [JUL 21]. In China, 90% of the energy used in the Al production is produced from coal [PAR 16], the dirtiest energy for the environment. Efforts for climate consideration in North-American, Russian and European production could make China react [JÉG 21]. But this year, geopolitical tensions with Russia are ongoing, the Al sector is not spared [POR 22] and China producers could easily impose their vision.

In these changing times, sobriety, durability and environmental impact should be in the centre of the decision process to choose any material. The best compromise must be found between its targeted properties and its equivalent CO_2 weight produced during all its life cycle, including recycling.

While Al is helping to save fuel thanks to its low density, producing it requires a lot of energy. Recycling it could help this metallurgical sector to get closer to circular economy. In order to achieve this goal, wide investigations must take place: first, on the impact of the high levels of impurities on Al alloys and then, on the design of scrap-compatible and composition-tolerant future alloys [RAA 22]. The impurities related to scrap impact the microstructure of the alloys through thermodynamics and kinetics of precipitation reactions and therefore on mechanical and electrochemical macro-properties. The new Al alloys should then be chosen using these informations to contain the highest possible scrap fractions.

These problems have many dimensions because there are various manufacturing parameters. The main Al alloys used are multi-component alloys of typically 4 or 5 elements. In addition, the processing parameters range is even larger: heating and quenching rates, duration of heat treatment, plastic deformation amount etc. All those parameters directly influence the microstructure at different levels: size, morphology and texture of grains, nature, shape, size and distribution of both intermetallics and nanosized precipitates, and dislocation density. Recycled alloys have an even greater variety of parameters because of the additional chemical species present in scraps. The alloy design space is therefore brought to regions which are currently essentially unexplored. The prediction models commonly used are here insufficient or maladjusted. Extensive experimental data are mandatory to improve the material knowledge and to identify the optimal solutions.

Extensive microstructure and properties data-sets should privilege high-throughput methodologies, also related to combinatorial (randomly combining many parameters) methods [POT 11, GRE 13]. In metallurgy, the objective is preferably to make quasi-continuously varying some of the alloy design parameters and to measure quasi-continuously the relevant microstructure parameters and properties of interest along that specific variation [MIR 17]. This method has been considerably used these recent years in order to cover the influences of composition, temperature or strain on microstructures and mechanical properties [SPR 12].

Methodology for combinatorial metallurgy

Combinatorial metallurgy can be used for various studies. The challenge is to manufacture the adapted sample to the parameter of interest. For instance, it is possible to create samples with variation of strain or with variation of thermal history [NIN 13, WEI 18]. In the literature, compositionally graded samples are the most common in this approach. They are mainly fabricated via diffusion bonding Figure 3a [GHO 03] and multiples 3b [ZHA 04]. The idea is to place different metal blocks in contact under high temperature in order to link them via thermal interdiffusion. Deposits followed by annealing [SPE 03] or imperfect arc melting [MIY 12] are other interesting manufacturing routes. And finally, additive manufacturing and powder metallurgy can also result in the variation of composition sought within the samples. For example Figure 3c, additive manufacturing by laser-powder directed energy deposition provided graded steel alloys with strong interface and controlled gradient of chromium content [VIL 21].

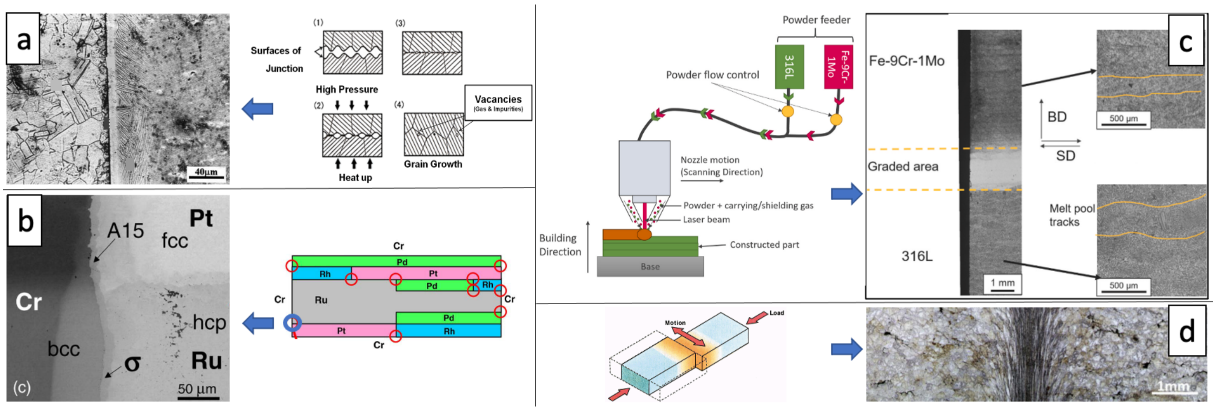

Figure 3: Optical microscopy images of gradded materials with different techniques. a: diffusion bonding [GHO 03], b: multiples [ZHA 04], c: additive manufacturing [VIL 21], d: linear friction welding [GUM 16]

Compositionally graded samples permit phase diagram [SPE 03, ZHA 04] and interfacial energy [MIY 12] determinations that contribute to thermodynamics data bases. They are also used for kinetics and microstructure understanding of phase transformation [CAO 15] and more precisely of precipitation studies [DEG 15]. Finally, macro-properties such as thermal conductivity [ZHA 12], heat capacity [WEI 13] and thermal expansion [ZHE 08] can be investigated through these specific samples.

Regarding Al alloys, Gumbmann *et al.* [GUM 16] and then Ivanov *et al.* [IVA 18] manufactured compositionally graded samples using linear friction welding, Figure 3d, to study precipitation composition dependence in Al-Cu-Li-Mg systems. After micro-hardness profiles Figure 4a, differential scanning calorimetry (DSC) Figure 4b and small angle x-ray scattering (SAXS) measurements, they were able to prove the triggering effect of Mg on both : kinetics of copper clustering and precipitate formation, by a continuous evaluation of the influence of its composition.

On microhardness measurements, the influence of Mg on hardness values are clearly visible for various ageing states. On DSC results, the two peaks of clustering and metastable precipitation are directly influenced by Mg content (amplitude and position).

From elemental powders, only the laser engineered net shaping (LENS^{TM}) additive manufacturing process was used to produce a gradient of Al in a complex concentrated alloy $Al_xCrCuFeNi_2$ $(0 \leq x \leq 1.5)$ [BOR 16]. The aim is to understand the influence of compo-

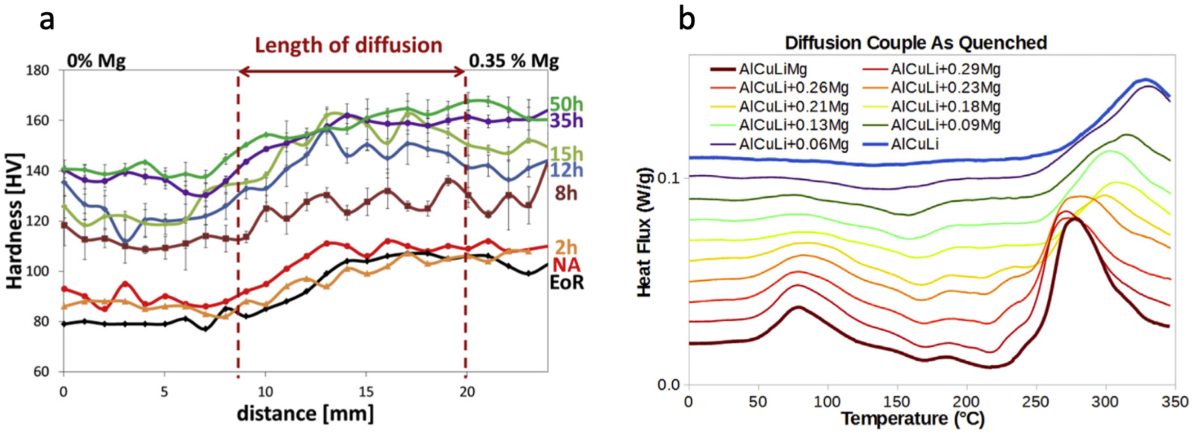

Figure 4: Precipitation composition dependence in Al-Cu-Li-Mg alloys. a: hardness measurements along an Al-Cu-Li-Mg gradient at different thermal state [GUM 16]. b: DSC thermograms across the diffusion couple [IVA 18]. Mg content hardens the sample at different stages of the ageing. It has also direct influence on clustering.

sition on both microstructure and macro-properties (mechanical and magnetic) in high entropy alloys (HEA).

Some graded samples have also been manufactured not for combinatorial study but in order to obtain graded functionality. For the Al-Mg-Si system, a cable with a radial gradient between pure Al and 6201 Al-Mg-Si alloy has been recently manufactured by Yang *et al.* using co-drawing and interdiffusion treatment. This graded cable has been developed for industrial applications in order to optimise the combination of electrical conductivity and torsion strength. Figure 5, the core, close to pure Al, is highly conductive and the protective sleeve in Al6201 is less conductive but has better mechanical strength to avoid the deterioration of the cable [YAN 20].

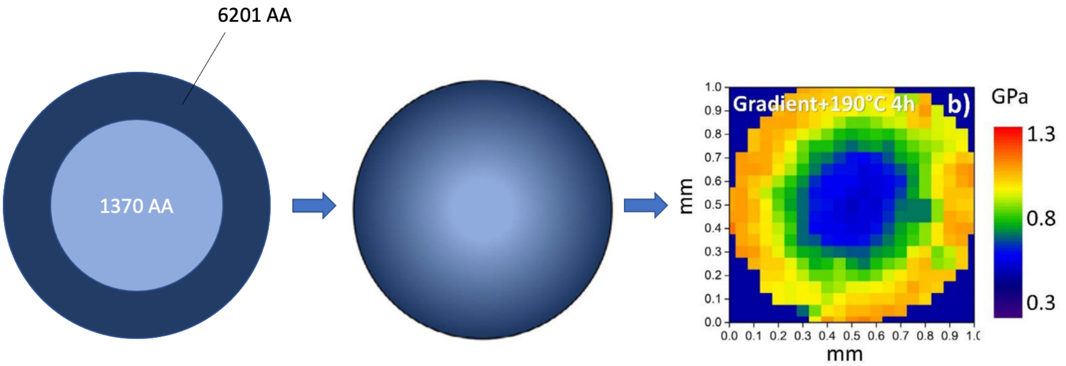

Figure 5: Cross section of the 1 mm Al graded wire before and after 2 h annealing at 550 °C to achieve a composition gradient and nanohardness map after 4 h ageing at 190 °C to achieve precipitation hardening.

The cable is stronger in the protective sleeve with nanohardness measurements going near to

1 GPa. The center has low mechanical strength as expected for 1370 Al alloys.

In Al-Mg-Si alloys, no gradient of Mg or Si and no combinatorial studies are made yet to fully understand their composition effects. Multiple classic precipitation analysis on homogeneous samples were made thought to verify the microstructural changes.

Precipitation in 6xxx Al alloys

The Aluminium 6xxx series

Improving lightweight alloys requires contradictory constraints of high strength, reached through nano-precipitation, and high formability, which requires high levels of plasticity. Among all alloys, Al structure-hardenable alloys offer a very good compromise between these properties thanks to precipitation hardening. During thermal treatment, nano-particles formed in the sample bring mechanical strength. 2000 and 7000 series show the highest level of hardening with the formation of precipitates whose stable form is mainly Al_2Cu and $MgZn_2$, respectively. In 6xxx series, the main stable precipitate is Mg_2Si. Since Mg and Si are the main alloying elements, 6xxx series are suited to many applications through their compromise between strength, formability and corrosion resistance.

Magnesium (Mg) is important for Al alloys. Indeed, it has a high solubility in Al and Mg hardens also directly the solid solution because of its difference in atomic size with Al. In addition, Mg improves the oxidation resistance when its composition stays under 4 at.% [MON 76].

Silicon (Si) is always present in small quantity in Al alloys because bauxite contains silicon oxides. A significant presence of Si is positive for formability because it rises castability and resistance to hot tearing during molding. Solubility of Si in Al at low temperature (under 227°C) is less than 10^{-2} wt.% but it still rises slightly the yield stress when in supersaturated solid solution [MON 76].

The alloys of this 6xxx series are defined with their contents in Mg (between 0.3 and 1.5 at.%) and in Si (between 0.3 and 1.4 at.%). They contain secondary alloying elements such as chromium (Cr), manganese (Mn), copper (Cu) and others. Among them, the 6061 aluminium alloy is one of the most widespread alloys of this series. Its composition is summarised in Table 3.

Mass %	Si	Fe	Cu	Mn	Mg	Cr	Zn	Ti	Others (each)	Others (total)
Min	0.40	-	0.15	-	0.80	0.04	-	-	-	-
Max	0.80	0.70	0.40	0.15	1.20	0.35	0.25	0.15	0.05	0.15

Table 3: Range of composition of the 6061 alloy after ASTM B209 standard

This alloy is particularly used thanks to its good mechanical strength (see Table 4), its good resistance to oxidation and its good weldability. Numerous car structures, carpentry, materials handling and finally most of the welded structures are made from Al 6061.

A simplifying approach to study 6xxx Al alloys is to deal with model alloys containing only Al, Mg and Si as alloying elements. Indeed, the stable precipitate phase β is described as Mg_2Si.

Yield stress $\sigma_{0.2}$ (MPa)	Tensile strength σ_{UTS} (MPa)	Elongation at break ϵ (%)	Young's modulus E (GPa)	Poisson's ratio ν
280	310	15	70	0.33

Table 4: Admitted mechanical properties for 6061 Al alloys [DEV 92, SHA 00]

The pseudo-binary section of the phase diagram between Al and β is presented further in the Figure 7. For the 6061 alloy, the content in Mg_2Si is between 1.2 and 1.8 wt.%.

All ternary alloys with twice more at.% Mg than at.% Si, or with the Mg/Si ratio in mass equal to 1.73, are named pseudo-binary alloys and are presented on this particular section. Other alloys, with more Mg or more Si, will be named alloys with Mg excess or Si excess. At room temperature, Mg_5Al_8 is thermodynamically stable in alloys with excess of Mg < 4 at.% and pure Si is for alloys with Si excess.

It is important to note here two aspects. First, Mg increases the solubility of Mg_2Si in Al. This means that the solid solution α domain is larger for Mg excess alloys. Higher content of Mg_2Si can then be reached for precipitation and therefore the volume fraction of precipitates could be higher. Then, the microstructure can be relatively different from strong Mg excess to strong Si excess because of the precipitation of different intermetallics.

In parallel, direct correlation between strengthening of Al-Mg-Si alloys and amount of Mg and Si has been found. Figure 6 represents strengthening evolution during ageing depending on the amount of available Mg_2Si in the alloys.

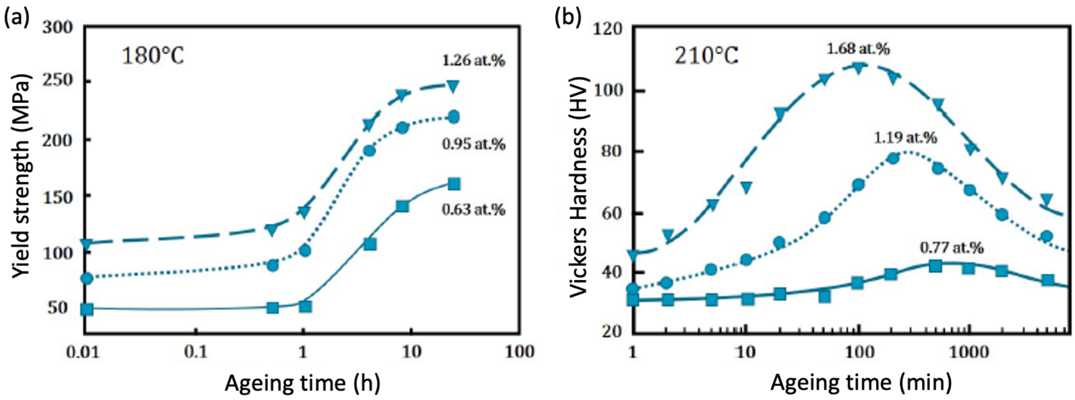

Figure 6: Evolution of the mechanical properties of Al-Mg-Si alloys with the amount of Mg_2Si in the alloy during isothermal treatments. a: Yield strength [GUP 01] and b: Vickers hardness [TAK 96]

During isothermal treatments at the origin of hardening precipitation, the maximum yield stress and hardness rise with at.% of Mg_2Si and at the same time, the time to get to those peaks are shorter. This is an important feature but the precipitation hardening phenomenon is more complex then uniquely this dependence in Mg_2Si. Indeed for Gupta *et al.* [GUP 01] and for Takeda *et al.* [TAK 96], precautions were taken for the three alloys presented to be near pseudo-binary alloys. Small excesses of Si and/or Mg are reported though.

Precipitation sequence

At room temperature, the microstructure of a 6xxx Al alloy should be composed of two phases: the solid solution α in face centred cubic (FCC) crystallography and β - Mg_2Si the hardening phase (Figure 7). In this condition, the strength is not optimised. To do so, the sample has to be homogenised during a solution treatment at high temperature (around 550 °C) and then rapidly cooled down: quenched. Its structure will not have the time to stabilise during this fast cooling process. It will be in a metastable state where all the atoms are in one phase: a supersaturated solid solution (SSSS). Quickly after, the alloy has to be aged at lower temperature (between 100 and 250 °C). By bringing small amount of energy to the system, the precipitation sequence toward β can be controlled.

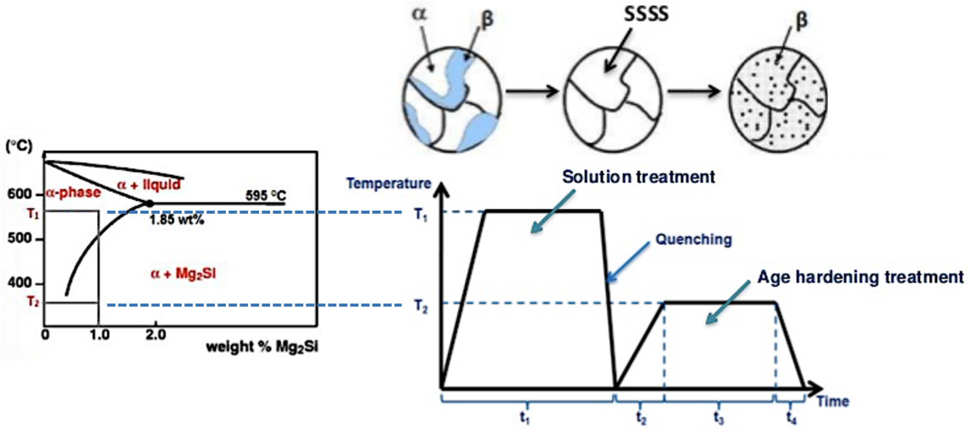

Figure 7: Pseudo-binary phase diagram, thermal cycle and microstructure evolution during precipitation hardening

The stable phase β does not precipitate directly. During the early stage of the isotherm treatment, atoms diffuse through vacancies in the solid solution (Figure 8a) to form clusters of solutes (Figure 8b) called Guinier-Preston zones (GPZ) when large enough. These clusters are perfectly continuous with the Al matrix, they are coherent, but elastic distortions occur around them because of the misfit between atoms of different sizes. These clusters have a preferential orientation along the [100] directions of the matrix. First, these atoms are unorganised. Then, when Mg solutes alternate with Si atoms, these zones can also correspond to β''. β'' is the hardening phase (this important feature will be discussed further).

β' thin precipitates arrives after longer ageing treatment These precipitates have another crystallography. They are semi-coherent with the matrix. On Figure 8c, only the direction [010] is coherent with the matrix. Elastic deformations are mainly present on that direction. They have first a needle morphology and then, with time, a rod shape.

If the treatment is maintained (at higher temperature than 160 °C), over-ageing and softening occurs while β equilibrium precipitates with a chemistry of Mg_2Si are formed (Figure 8d). They

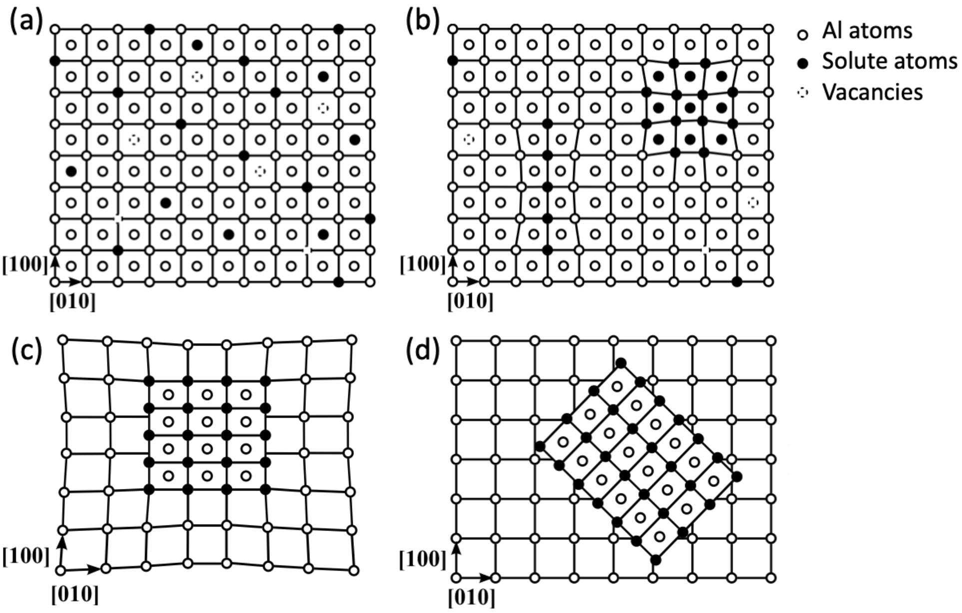

Figure 8: Representation of the different stages of precipitation in Al matrix [MAI 10]. a: Supersaturated solid solution, b: Guinier-Preston zones and β'' phase, c: β' and d: β

have a plate shape. This phase is non-coherent with the Al matrix.

This metastable precipitates cascade is called the precipitation sequence. As described, the simplified version of the precipitation sequence in pseudo-binary alloys is

$$SSSS \rightarrow GPZ \rightarrow \beta'' \rightarrow \beta' \rightarrow \beta$$

Each precipitate of this sequence will be properly introduced following three main characteristics roughly introduced here. Crystallographic structure will be detailed in Chapter 2. Surface energy will provide information on the nature of the interface between matrix and precipitate. Finally the energy barrier concept will be developed to perceive the volume energy gain obtained from precipitation. Those last two characteristics will be detailed in Chapter 3.

Influence of composition on precipitation hardening phenomenon

Composition has major influences on precipitation in 6xxx Al series. For pseudo-binary alloys, it has been shown that variation of secondary alloying elements has a direct effect on the crystallography of the precipitates. For those with a high content in Cu, all the precipitates are enriched in Cu [MAS 00]. With more Cu in the alloy, new precipitates participate: the metastable precipitate Q' giving the stable precipitate Q. In some conditions, Q' can completely replace β'' [GAB 07].

Al-Mg-Si alloys with an excess of Mg are often associated with pseudo-binary alloys as they remain within the FCC+Mg_2Si pseudo-binary section. The precipitation sequence is usually the same and their precipitates have also chemistrys which tend to Mg_2Si. Some interesting features have been raised though. Starting an ageing temperature above 245 °C, the precipitation sequence can be altered with a higher tendency to form the cuboid-β phase [DOA 02].

An other important feature for Mg excess alloys should be pointed out. Their precipitation is more influenced by incomplete solutionising condition. Indeed Doan *et al.* [DOA 02] show that hardness is improved with Mg excess when the composition permits complete solutionising. In the other hand, the excess of Mg can result in a reduction of hardness for composition with incomplete solutionising. With undissolved β-Mg_2Si particles, Mg and Si atoms of solid solution migrate near them in order to magnify them (like for coarsening in Chapter 3). This growth consumes the free Mg and Si available for β'', reducing their density and thus hardness. For Si excess alloys, the metastable precipitates are very rich in Si and continue to precipitate before any possibility of enlarging coherent phases.

Silicon excess in pseudo-binary Al alloys has the most important composition influence on precipitation. First the mechanical strength rises with the content of Si while the time for peak hardness decreases (Figure 9).

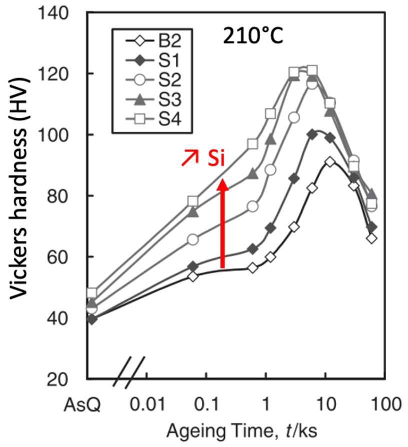

(at.%)

Alloy	Mg	Si	Mg_2Si	Excess Si
B2	0.83	0.40	1.19	0.04
S1	0.83	0.58	1.24	0.17
S2	0.83	0.71	1.25	0.29
S3	0.83	0.95	1.25	0.54
S4	0.82	1.03	1.23	0.62

Figure 9: Evolution of hardness with variation of Si excess during ageing treatment at 210°C after solutionising and quenching [FUK 06]

The rise of mechanical strength with Si content is mainly explained by a better distribution (more and homogeneously disseminated) of smaller β'' precipitates in the matrix. Indeed, microstructural modifications cause macro-properties changes.

For example, Si excess decreases the lattice distortion in the matrix which improves electrical conductivity to Al6101 [XU 16] and to Al-Mg-Si alloys [HAN 17]. Si excess can also be negative: intergranular corrosion is enhanced by the larger number of precipitates present on the grain boundaries [ZHE 17].

During natural ageing, there are also more clusters in Si excess alloys and these ones are richer in Si [TAK 96, ARU 15]. During pre-ageing at 70°C, there are more clusters as well, and these ones are nucleation sites for β" formation, accelerating hardening [MUR 98a].

With an excess of Si, the precipitation sequence changes significantly. Over the years, DSC measurements coupled with characterisation techniques, such as TEM, clarified the succession of the new phases involved [MAR 97, DON 98, MAT 05, AFI 08]. Three new semi-coherent phases U1, U2 and B' (or type A, type B and type C) can precipitate. And the proportion of these phases are dependent of the excess of Si and of the thermal state (see Figure 10).

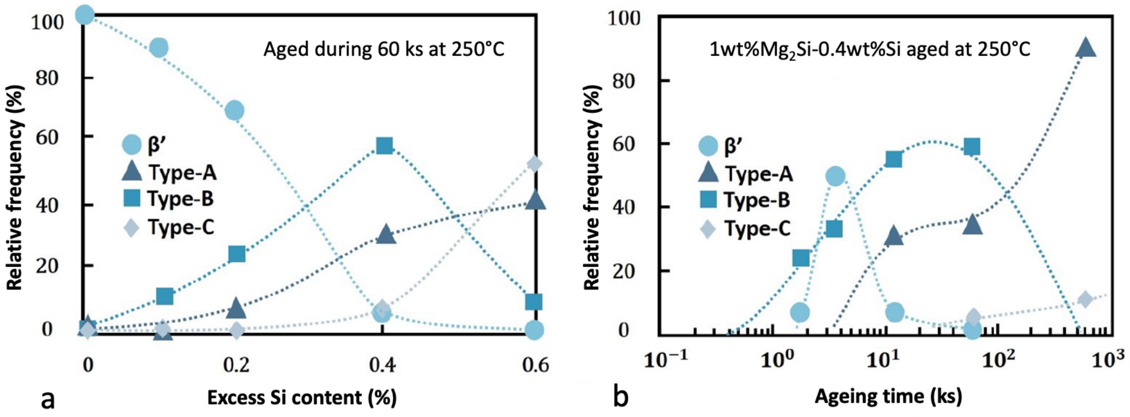

Figure 10: Frequency of each semi-coherent phase a: depending on the Si content for samples aged at 250°C [MAT 05] and b: depending on ageing time for a sample with 0.4 Si excess [MAT 00]

Other differences have been observed compared to pseudo binary alloys. Most of the precipitates are richer in Si. These changes of chemistry even bring β'' to have a significant variation of crystallography (see Tables 2.1 and 2.1 Chapter 2). This new β'' precipitate seems less stable: in Figure 9, hardness values drop after hardness peak more significantly when Si content is high.

Pure Si can precipitate as well with sufficient Si excess. In some cases, these particles are formed concurrently with β'' [AFI 08], in other cases, they appear after the formation of β [MAT 05].

The effect of Si excess in Al-Mg-Si alloys on precipitation has been significantly studied and properly documented (Chapter 2). But the range of compositions is not that clear. For example, an Al6351 alloy with an Si excess of 0.3 at.% remains with a precipitation sequence typical of pseudo-binary alloy excepted for pure Si precipitation and a particularly quick depletion of Si in the solid solution [MEY 18a]. On the Figure 10, many cases are not presented and studied and variation of Mg_2Si content could also have a major influence on the apparition of new semi-coherent phases. 2 major composition parameters seem to be important for precipitation in Al-Mg-Si alloys : the Si excess and the Mg_2Si content. The Si excess can also be quantified with the Mg/Si ratio to represent as well Mg excess. Marioara *et Al.* showed that this ratio can be a good indicator to highlight the complex semi-coherent phases succession [MAR 06].

PhD objectives

Al-Mg-Si alloys are precipitation hardening alloys. During thermal treatment, nano-particles are formed in the sample and increase the mechanical strength. These precipitates are composed of Mg and Si and thus, Mg and Si compositions are highly important for the control of this strengthening phenomenon. This dependence has been well investigated in the last years. However, there are still key questions regarding the effect of alloy composition in this system on the characteristics of the nano-precipitation. Several crystallographic phases of different composition may form in competition, with different morphologies and volume fractions. The precipitation kinetics, the sequence and the resulting size and morphology show a complex dependence on the alloy composition and especially the Mg/Si ratio [FUK 06, MAT 05, MEY 18a].

The goal of this PhD is to provide many points in the composition space of the Al-Mg-Si system in order to identify the changes in precipitation sequence. In order to achieve this goal, three objectives were fixed. The first one is to manufacture gradients of Mg and Si composition in samples of Al-Mg-Si alloy. The second objective is to perform high-throughput characterisations on their microstructure along the gradient. Finally, the last aim is to simulate and understand what has been observed with physically based models.

A powder metallurgy route has been chosen to manufacture gradients of Mg/Si ratio to pilot this combinatorial study. Powder metallurgy has been chosen for two reasons. It is versatile enough to produce various chemical gradients through the compaction of different powder blends. The high-pressure compaction enables to break the aluminium oxide layer that is hard to avoid during bonding of bulk materials [SHI 01].

Organisation of the manuscript

As previously presented, three major themes organised this PhD and will structure this manuscript:

- Gradients manufacturing
- Precipitation characterisations through the gradients
- Simulation of precipitation and hardening through the gradients

The first part of the manuscript will describe the manufacturing of Mg-Si composition gradients adequate for this combinatorial metallurgy study. After materials and methods presentation, microstructure, diffusion regime and initial mechanical properties will be discussed. Real and simulated composition profiles will be compared.

The second part of the manuscript is dedicated to precipitation characterisations in Mg-Si gradients. First a bibliographic study will gather the knowledge on the various precipitation sequences observed in Al-Mg-Si alloys. Then ageing kinetics and precipitation states of the compositionally graded samples will be studied in order to emphasise the major composition influences on precipitation and to highlight transitions in precipitation sequences.

The last part will be focused on simulations of precipitation in Mg-Si gradients. A bibliography of the existing models will be followed by the explanation of the strategy for simulations through a gradient. Then the definition of the model will be described with the chosen parameters. Finally, the model and the previous experimental data will be confronted.

Chapter 1

Manufacturing compositionnally graded Al-Mg-Si alloys by spark plasma sintering

A compositionally-graded alloy was obtained by Spark Plasma Sintering (SPS) of Al-Si and Al-Mg model alloys atomised powders. The fabrication process includes a sequence of (i) SPS of two powder beds (ii) interdiffusion heat treatment (iii) homogenisation and quenching. Small pores, identified by X-ray micro-tomography, are formed during the interdiffusion treatment with a volume fraction of the order of 1%. Energy dispersive X-ray spectroscopy (EDX) and wavelength dispersive X-ray spectroscopy (WDS) confirm a well-controlled gradient of Mg and Si in a single direction. The description of the experimental composition profiles after interdiffusion requires a two mode diffusion model, linked to bulk diffusion and grain-boundary diffusion. Microhardness measurements along the composition gradients on an as-quenched state permits to evaluate the contribution of the solid solution to the mechanical strength. Please note that this chapter has been submitted as an article to Met. Trans. A.

Contents

1.1 Introduction

Developing new lightweight alloys with improved properties is urgently needed in the transport industry in order to drastically decrease its greenhouse gas emissions. In this context, Aluminium alloys are increasingly used in cars, especially with the development of electric vehicles to compensate for the battery weight. Increasing the vehicle light-weighting requires developing alloys that answer contradictory constraints of high strength, reached through nano-precipitation, and high formability, which requires high levels of plasticity. Among all Aluminium alloys, Al-Mg-Si based alloys offer a very good compromise between these properties [MON 76]. However, key questions are still pending on the effect of alloy composition in this system on the characteristics of the nano-precipitation which controls the strength. Several metastable phases of various compositions may form in competition, with different morphologies and volume fractions. The precipitation kinetics, the sequence and the resulting size and morphology show a complex dependence on the alloy composition and especially the Mg/Si ratio [FUK 06] [MAT 05] [MEY 18a].

Combinatorial studies are efficient fundamental approaches to cover the influence of composition, temperature or strain on microstructures and mechanical properties [SPR 12]. Regarding Al alloys, Gumbmann *et al.* [GUM 16] and then Ivanov *et al.* [IVA 18] manufactured compositionally graded samples using linear friction welding to study precipitation composition dependence in Al-Cu-Li-Mg systems. After micro-hardness profiles, differential scanning calorimetry (DSC) and small angle x-ray scattering (SAXS) measurements, they were able to prove the triggering effect of Mg and his range of composition on both kinetics of copper clustering and precipitate formation.

Powder metallurgy and additive manufacturing are also attractive ways to produce graded specimens. For example, additive manufacturing by laser-powder direct energy deposition provided graded steel alloys with strong interface and controlled gradient of chromium content [VIL 21]. An equivalent process was used to produce an Al graded complex concentrated alloy $\mathrm{Al}_x\mathrm{CrCuFeNi}_2$ ($0 \leq x \leq 1.5$) from elemental powders [BOR 16].

In the Al-Mg-Si system, a graded cable between pure Al and 6201 AlMgSi alloy has been recently manufactured by Yang *et al.* [YAN 20] using co-drawing for application in electrical power transmission. The core in pure Al is highly conductive and the protective sleeve in Al6201 is less conductive but has better mechanical strength to avoid the plastification of the cable.

In this study, a compositionally-graded alloy was obtained with high-temperature compaction using Spark Plasma Sintering of Al-Si and Al-Mg model alloys atomised powders. Consolidation of powders instead of diffusion bonding of bulk metal sheets may have advantages, mainly because the oxide barrier can be broken by local shearing on the powder particles but also because powder metallurgy allows for flexible composition through powder blends [LE 13].

Compositionally graded samples were produced by the compaction of two powder beds. To author knowledge, these graded samples are rather new for the system Al-Mg-Si, with a controlled variation of Si and Mg contents. Those samples are designed for combinatorial metallurgy and therefore, extensive characterisation will be carried out to provide full knowledge of the sample before any ageing treatment. In terms of resulting microstructure and properties, the scope of the present chapter will thus be limited to the study of the solution strengthening in the graded alloys produced, while the evaluation of the precipitation kinetics during ageing and its link to the mechanical properties will be the subject of the next chapter.

1.2 Materials and methods

1.2.1 Raw powders

In order to obtain Mg-Si graded aluminium samples, the diffusion couple is formed by contact between an Al-Mg layer with 2.6 wt.%Mg (2.9 at.%Mg) powder and an Al-Si layer with 1.22 wt.%Si (1.18 at.%Si) powder.

The target compositions were obtained from blends of three initial model powders provided by Goodfellow: Pure Al, Al-2Si and Al-8Mg in mass percent. The Al-Mg layer was made from a blend between pure Al with Al-8Mg powders with a mass ratio of Al-8Mg/Al = 0.56 and the Al-Si layer from a blend between pure Al with Al-2Si with a mass ratio of Al-2Si/Al = 1.53. The initial powders were weighed and then blended correctly in a Turbula mixer during 10 min just before the next manufacturing steps to come.

Figure 1.1 shows scanning electron microscope (SEM) images of the initial powders.

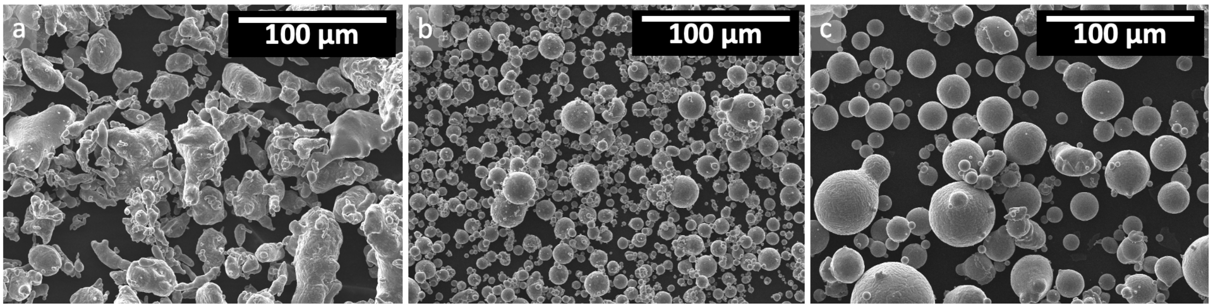

Figure 1.1: SEM images of the initial powders. a: pure Al, b: Al-8Mg and c: Al-2Si. Pure aluminium is non spherical. Size differences are visible.

Unlike the two other powders, pure aluminium was air atomised, implying important oxide shells around the particles and the non spherical morphology observed. Those pictures show also the size differences. These dimensional information can be crossed with distributions of size of the powders obtained by laser diffraction, shown in Table 1.1.

The Al-8Mg median diameter (D50 value) is the smallest at 16 µm. It is also the most uniform powder with a narrow range of sizes. Pure Al powder distribution is quite uniform as well but the non sphericity enlarges the range of sizes. 80% of its particles are between 14 and 63 µm. In comparison, Al-2Si powder has a wide distribution with 80% of its diameters range between 27 and 163 µm.

X-Ray diffraction (XRD) analyses on each initial powder are summarised Figure 1.2.

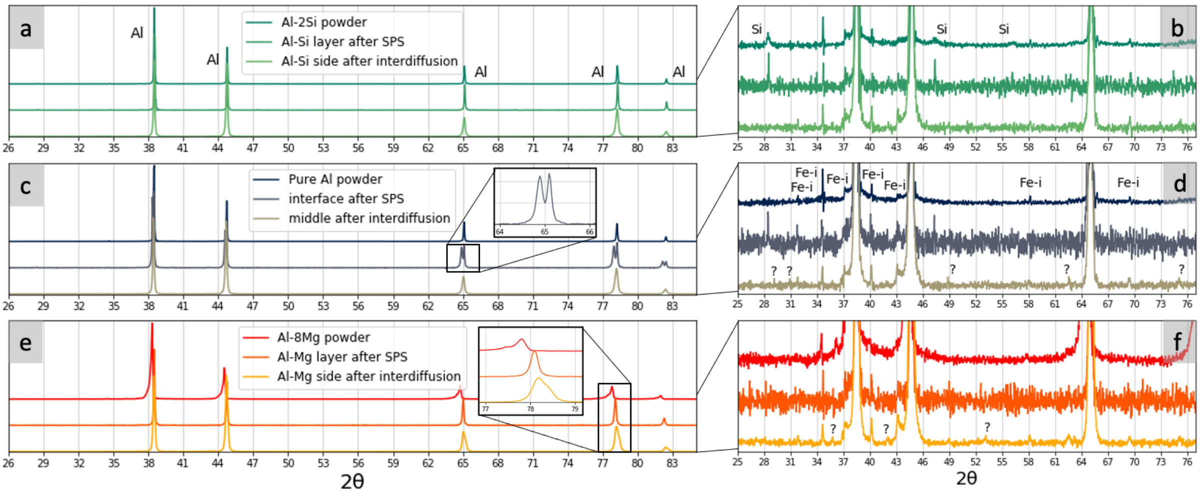

Figure 1.2: X-ray diffractograms of Al alloys. In a and b: with high content of Si, in c and d: with medium or no content of Si and Mg and in e and f: with high content of Mg. The five main peaks are from the FCC aluminium phase. Al-8Mg has a shift of its Al peaks explained by the dilation of the lattice due to Mg insertions.

The five major peaks are related to the Al phase FCC. The peaks are slightly shifted toward low angle values for the Al-8Mg powder and they are splitted in two peaks that may overlap: one from nearly pure Al grains and the other from those supersaturated in Mg. Indeed, with 7.6 wt.% of Mg, the Mg inserted in the matrix increases the lattice parameter. For Al-2Si, small characteristic peaks of Si were spotted, see Figure 1.2b, for 2θ at 28°, 47° and 56° [YAM 11]. As expected from the equilibrium phase diagram, all the Si of the powder is not in solid solution [MUR 84].

All the important features of the powders are summarised in Table 1.1, including compositions from our own ICP analyses after dissolution in acid mixture, containing a few amount of HF to ensure dissolution of free Si. In all of them, small quantities of Fe are present.

	Pure Al	Al-2Si	Al-8Mg
Atomisation atmosphere	Air	Gas	Gas
Small diameter D10 (μm)	14	27	6
Medium diameter D50 (μm)	31	71	16
Large diameter D90 (μm)	63	163	30
Morphology	Non spherical	Spherical	Spherical
Internal porosity (%)	0.2	0.3	0.4
Composition of Fe, Si and Mg measured by ICP (wt.%)	Al-0.13Fe-0.04Si-0.01Mg	Al-2.06Si-0.09Fe-0.03Mg	Al-7.29Mg-0.17Fe-0.06Si

Table 1.1: Microstructural features of the initial powders used for the diffusion couple

1.2.2 Manufacturing route of the graded samples

Figure 1.3 describes the manufacturing steps of the graded samples.

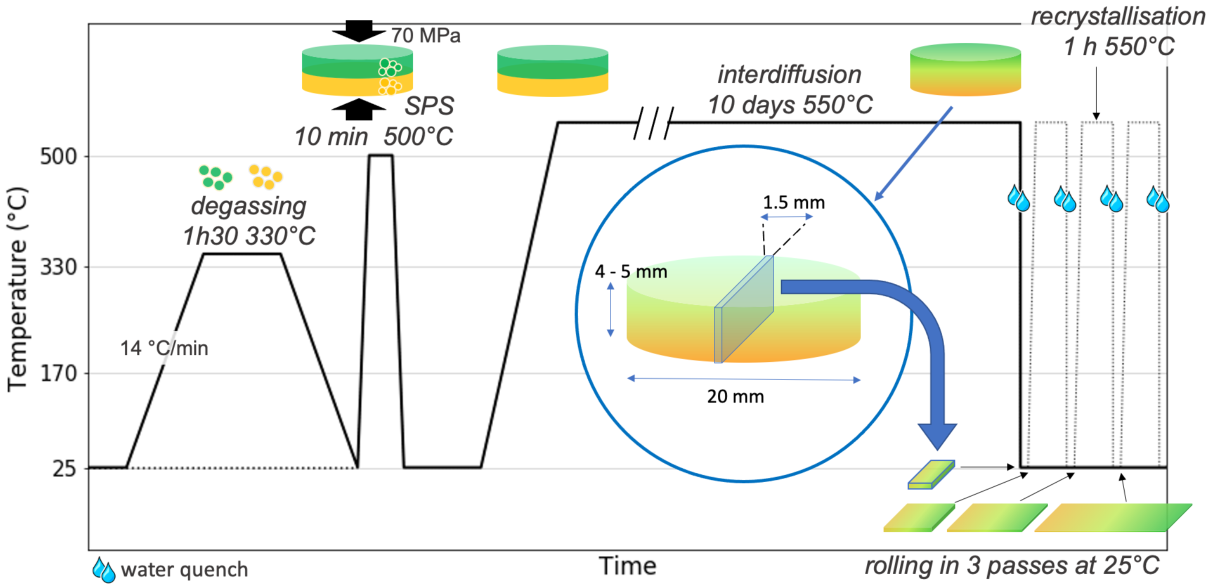

Figure 1.3: Detailed manufacturing steps to obtain the graded samples. In full line, the route the most used. Degassing and rolling with recrystallisation steps can be added, depending on further characterisations.

First, the powders in alumina crucibles were inserted in a tubular oven to degas under high vacuum (10^{-4} mbar) in order to suppress the humidity retained in the powder. The vacuum was vented with Argon gas. Then the powders were carefully poured in layers in a cylindrical graphite die. The consolidation using a Spark Plasma Sintering (SPS) apparatus type HP D25 from FCT was performed under 70 MPa with a heating rate of 91 °C/min followed by a soaking step at 500 °C for 10 min and a cooling rate at about 85 °C/min, which produced a fully dense bi-composition cylindrical compacts with 20 mm diameter and 5 mm thickness. These parameters are in agreement with the optimal ones found in the literature in order to obtain a relative density near 100% [ZAD 07, SWE 14, CHU 15].

In order to create the gradient, slices were extracted from the compacts, heated at 550 °C in a conventional air oven and water quenched. Several treatment durations were tested and compared with diffusion simulations using the Dictra software. Dictra was used with the thermodynamic database TCAL4 and the mobility database MOBAL3. The simulation of the heat treatment was performed in a one-phase configuration, with a step concentration in Mg and Si within the FCC solid solution. For a 4 mm total length diffusion couple, the initial Mg and Si contents on each side of the initial interface (in the center) were assigned using the values obtained from EDX analysis.

Experimentally, after 10 days, Mg and Si diffuse towards opposite directions on a distance of 3 mm. This gradient length can then be elongated by rolling from 3 mm to 6 mm on an extracted slice with a thickness of 1.5 mm. The rolling procedure consisted of 3 rolling steps using a rolling mill of 6 cm diameter at room temperature. Each rolling step was followed by 1 h recrystallision at 550 °C.

1.2.3 Characterisation methods

All the X-Ray Diffraction (XRD) analyses presented in this article were performed on a Bruker AXS D8 (Billerica, Massachusetts, USA) device equipped with a copper tube. The X-Ray tube was set at 40 kV voltage and 40 mA current with a Cu K_α of 1.54 Å irradiation wavelength. The detector used was a Lynxeye, which was used over a range 2θ from 10 to 90° with an 0.0167° increment, with a slit of 0.4 mm and a scan speed of 1s/step during spinning at 20 rpm. Bulk samples were polished before the experiments.

Energy-dispersive X-ray spectroscopy (EDX) analyses were performed with an Oxford Instruments apparatus in a Scanning Electron Microscope (SEM) Zeiss Supra 55 VP at 10 keV at a working distance of 8.5 mm and with an aperture of 60 µm. The obtained profiles were fitted with an erf function after aberrant values withdrawal.

Electron probe microanalysis (EPMA) was carried out with a Cameca SX100 instrument in wavelength dispersive spectroscopy (WDS) mode with operating voltage at 15 keV and probe current at 1 µA. Mg, Si, Fe and O elements were measured using the cristals TAP (for Mg and Si K_α), LiF for Fe K_α, and the pseudo-cristal in multilayer W/Si for O K_α. The standards used were MgO, Si-wafer and Fe. Al was determined by difference at 100 wt.%. The PAP (Pouchou And Pichoir) quantitative analysis program was used [POU 84].

Powder and compacts were imaged by micro-tomography (μCT) at high resolution using an EasyTom Nano tomograph (RX Solutions, Chavanod, France). This tomograph is equipped with a LaB6 cathode for the X-ray source. The detector is a Varex 2520DX flat panel with a pixel size of 127 µm. The parameters used were the following: X-Ray tube voltage ranging from 80 to 100 kV, 4000 projections over a 360 rotation, exposure time ranging from 0.35 to 0.4 s, 0.7 µm voxel size. In both cases 3D volumes were reconstructed from the collected radiographs using a filtered back projection Feldkamp-algorithm. Images analysis was then performed using the free and open-source Fiji software.

Hardness values were measured with a micro-hardness tester Buehler Micromet 5104 with a load of 0.5 kg. 2 measurements were made for each mean value presented. The uncertainties were calculated from standard deviations.

1.3 Results and discussion

1.3.1 Microstructure evolution upon processing

After SPS, the μCT scan exhibits a fully dense microstructure for degassed as well as for non-degassed samples (not shown here). On a degassed sample presented in the images of Figure 1.4, the microstructure is different on each side of the interface, showing the inheritance of the initial two powder beds and the moderate interdiffusion upon SPS.

The Mg-rich part stands out with a partial cellular microstructure made of Mg oxides around the former powder (image b and c) and with small crystallographic grains (image d and e). Small

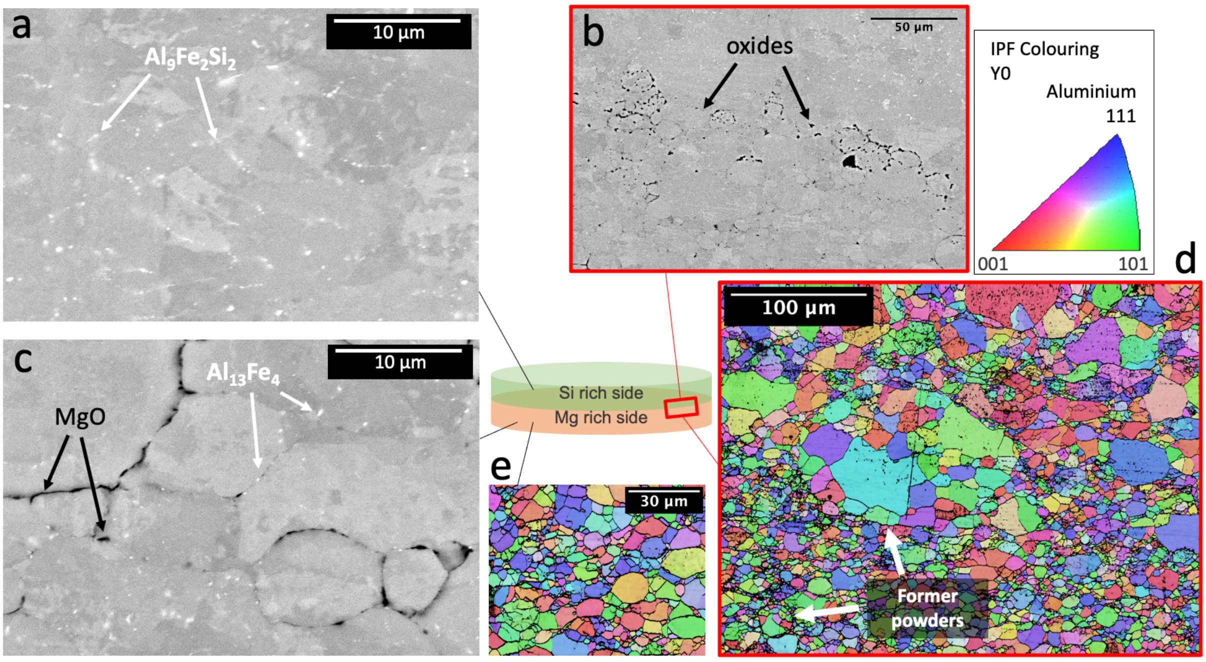

Figure 1.4: Microstructure of a sample after sintering from an Al-1.2.wt.%Si Al-2.6wt.%Mg diffusion couple. image a, b and c: BSE images of Si side, of the interface and of Mg side respectively. image d and e: EBSD images at the interface and of Mg side.

grains of few microns are mixed with larger grains up to 20 µm in diameter. Submicronic spherical intermetallic particles are present. They were identified as iron-rich intermetallic particles that could be $Al_{13}Fe_4$ based on the TCAL4 database.

The Si-rich part has more Fe-rich intermetallic particles (image a and b). They are also spherical and submicronic but aligned along grain or subgrain boundaries. Considering actual alloy composition and temperature, these are expected to be $Al_9Fe_2Si_2$ from TCAL4. The same mixture of grain sizes is present but the main grains are larger; up to 50 µm in diameter (image d).

At the initial interface, large oxide particles are present in cellular shapes and some small β-Mg_2Si particles are formed near them (image b).

A wide grain size distribution can be seen on both sides of the diffusion couple and is accentuated on Si-rich side (figure 1.5). These features can be explained by size distribution of the initial powder particles. As shown in figure 1.4, former powder particles somehow guide the final grain size since the metallurgical grain size is limited by the powder particle, especially when oxides at particles surfaces inhibit the grain growth. The larger grains are contained in pure Al powders that can be recognised by their non spherical shape whereas the smaller grains are contained in Al-Mg powders. At this stage, the microstructure of the compact is clearly inherited from the respective initial powder microstructures due to fast sintering.

X-ray diffractograms after SPS, from one side to the other, are presented in Figure 1.2. Al-Si

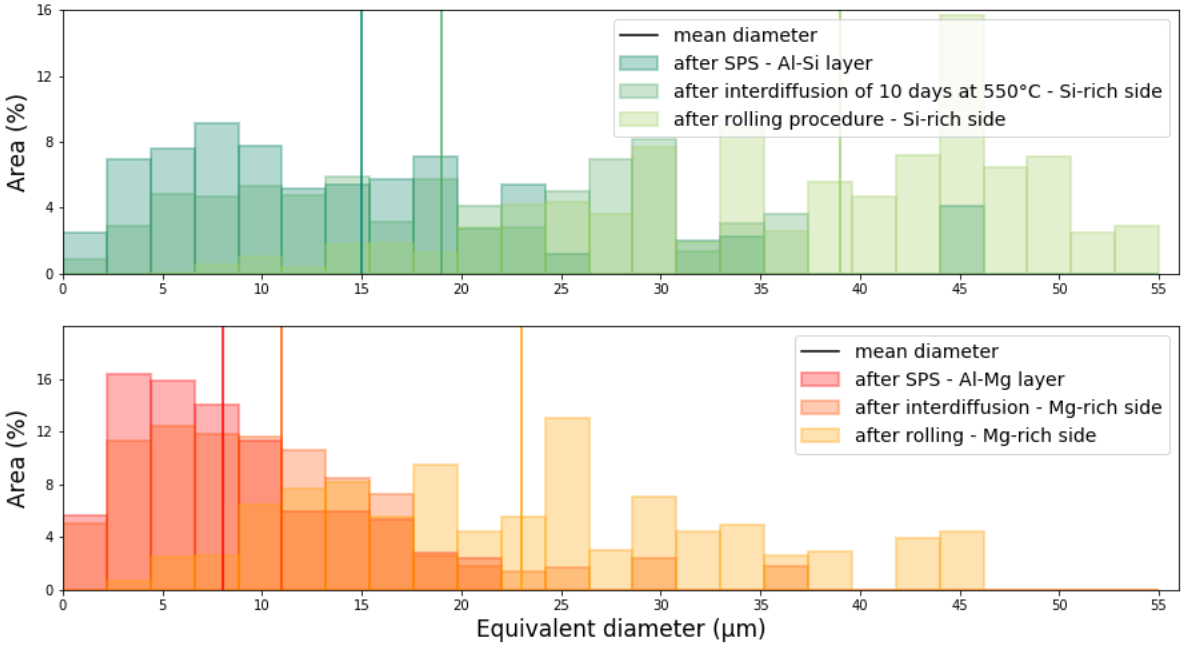

Figure 1.5: EBSD grain size distribution from samples out of Al-1.2wt.%Si and Al-2.6wt.%Mg diffusion couple. Grains slowly grew during interdiffusion treatment at 550 °C on both sides. Medium diameter is a weighted average with the areas.

and Al-Mg XRD were performed on two different homogeneous bulk with the same compositions as the extremities of the diffusion couple. The interface diffractogram was obtained from a typical bi-layer slice after SPS which has followed the manufacturing route described previously.

As for the initial powders, only the FCC aluminium peaks are clearly visible. On Al-Si side the three peaks of Si are still present at 28, 47 and 56 degrees. Even if Si is expected to be fully dissolved in the FCC solid solution at 550 °C, the cooling rate after SPS is too low to avoid desaturation and formation of Si diamond precipitates. On the diffractogram acquired nearby the initial interface, the duality of each aluminium peak proves the coexistence of two near composition FCC phases thanks to the small peaks shifting of Al-Mg side. Indeed, the right peaks refers to Al-Si side and the left ones to Al-Mg side.

After an interdiffusion treatment of 10 days at 550 °C on a non-degassed sample, the μCT scan (not shown) reveals pores that represent a volume fraction of 1%. On the images of a degassed sample shown in Figure 1.6, the microstructure has evolved.

Fe-rich intermetallic particles along the gradient have gathered and grown bigger. On the Mg side (image 1.6g), they remain spherical but have now a diameter of few microns. On Si side, the aligned particles become large needle shape particle of length between 2 to 10 µm (image 1.6a). The dark oxides of Mg side grow while small pores are created next to them. On the Al-Si side, larger pores are created more randomly. Nanometric spherical oxides aligned around the grain boundaries have formed as well and are now visible on the Al-Si side (image 1.6b).

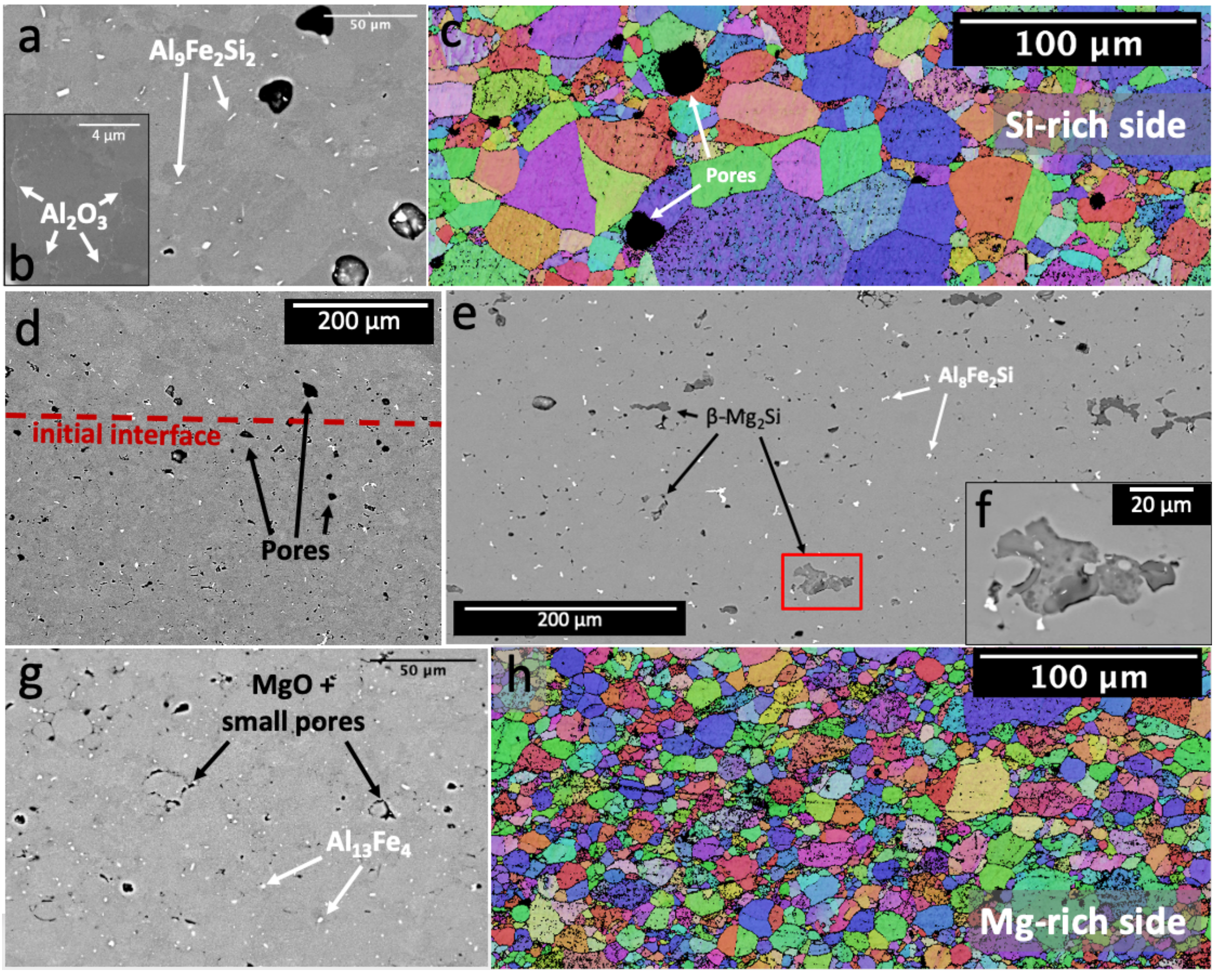

Figure 1.6: Microstructure of a sample from an Al-1.2wt.%Si Al-2.6wt.%Mg diffusion couple after interdiffusion and water quench. a, b and c : Al-Si side BSE, SE and EBSD images respectively. d, e and f : BSE images of the middle of the sample. g and h : BSE and EBSD images of Al-Mg side. The microstructure is different along the gradient. Pores are larger on Si side. Fe-intermetallic particles are varying in their chemistry, sizes and morphologies. Mg_2Si phase is present near the interface on the Mg side.

In Figure 1.6 d and e, the BSE images focus on the interface between the two initial powder beds. Bigger aligned pores and oxides (along the reference line) delimit the two different microstructures (image 1.6d). Near that interface, between the grains, large white Fe-rich intermetallic particles are visible. Those were attributed as Al_8Fe_2Si based on TCAL4 database. They can have a length up to 50 µm.

On the Mg side of the interface (image 1.6e), large grey particles of β-Mg_2Si have also formed between and around the grains (image 1.6f). They have similar shapes as the large Fe-rich intermetallic particles of the area and are bigger; up to 80 µm.

On both sides, grain growth occurred (1.6c and h) and the medium diameter of grains increased from 15 µm to 19 µm on Al-Si side and from 8 to 11 µm on Al-Mg side (Figure 1.5). This increase in grain size during this treatment was moderate since heterogeneities at grain boundaries such as pores, oxides and precipites can inhibit grain growth. But globally, the grains tend to have similar morphology to that after SPS.

The lengths of compositional gradient of interdiffused samples are too small to be correctly analysed by spatially resolved techniques. Rolling is then a good solution to elongate the gradient. It is also a way to close the pores.

In Figure 1.5, grain size distribution after rolling procedure and water quench are also extracted from EBSD analysis on each side of the sample.

The grains have significantly grown this time on both sides. The average weighted diameter for Si-rich side is 39 µm and for Mg-rich side it is 23 µm.

XRD analyses on a rolled sample - not finally recrystallised - which underwent an interdiffusion of 10 days at 550 °C are presented in the Figure 1.2. Three sites were analysed along the gradient.

As previously, the FCC aluminium peaks are visible. On Al-Si side (Figure 1.2b) and in the middle of the gradient (Figure 1.2d), the three peaks of Si are no longer evidenced. On the three diffractograms, small peaks appeared. No certain identification could be made, but SEM and EDS analysis evidenced the growth of Fe-rich intermetallic specific particles along the gradient and β phase in the middle of the sample.

Working with Aluminium powders requires precautions. Indeed, those particles have an oxide shell highly sensitive to humidity. The degassing procedure would require a thermal treatment until 550 °C to remove all the water from the sample. Unfortunately, oxidation of aluminium occurs above 310 °C [YAM 06] :

$$2\mathrm{Al} + 3\mathrm{H_2O} \rightarrow \mathrm{Al_2O_3} + 3\mathrm{H_2} \quad [310 - 500]^\circ\mathrm{C} \tag{1.1}$$

Mg-rich powders cause additional creation of oxides from 400 °C [DAV 95] :

$$\mathrm{Mg_{(s)}} + \mathrm{H_2O_{(l)}} \rightarrow \mathrm{MgO_{(s)}} + \mathrm{H_{2(g)}} \quad \text{from} \quad 400^\circ\mathrm{C} \tag{1.2}$$

During interdiffusion treatment at 550 °C, the hydrogen of the water remaining on humid oxides reacts with bulk Al or Mg. These reactions form more oxides such as alumina (Al_2O_3) or magnesia (MgO) and dihydrogen (H_2). Because the sample is dense after SPS treatment, the H_2 is trapped within the material and creates porosity. The formation of Mg or Si oxides from the residual water present in the powder leads to a decrease in the concentration of these elements in the solid solution and therefore their available amount for future precipitation.

Indeed, on the SEM-BSE images, despite the degassing step, the initial oxide shells of the Mg side are getting more dense with interdiffusion while in the Si part, small oxide particles have formed on the grain boundaries.

A typical alloy for good mechanical properties is 6061, where composition lies around 1.2at.% of Mg and 0.6at.% of Si [BAR 14]. In order to have significant Mg and Si element in solid solution despite the formation of oxides and intermetallic particles rich in Si, the end compositions of the diffusion couples have been heightened regarding to the Al6061 compositions. As presented in Figure 1.6d, this conducted to the formation of the β-Mg_2Si phase in the middle/Mg-side of the sample. It is therefore important for the upcoming ageing experiments to quantify properly along the gradient the solid solution composition.

1.3.2 Gradients for different interdiffusion times

Interdiffusion treatments at 550 °C for 20 h, 66 h and 10 days were performed on different sample slices. These samples did not experience degassing step. On Figure 1.7, EDX solid solution compositions along their gradients are presented and compared with calculated diffusion profiles from the MOBAL3 database. Coloured bands, representing the uncertainties, are surrounding the experimental fits.

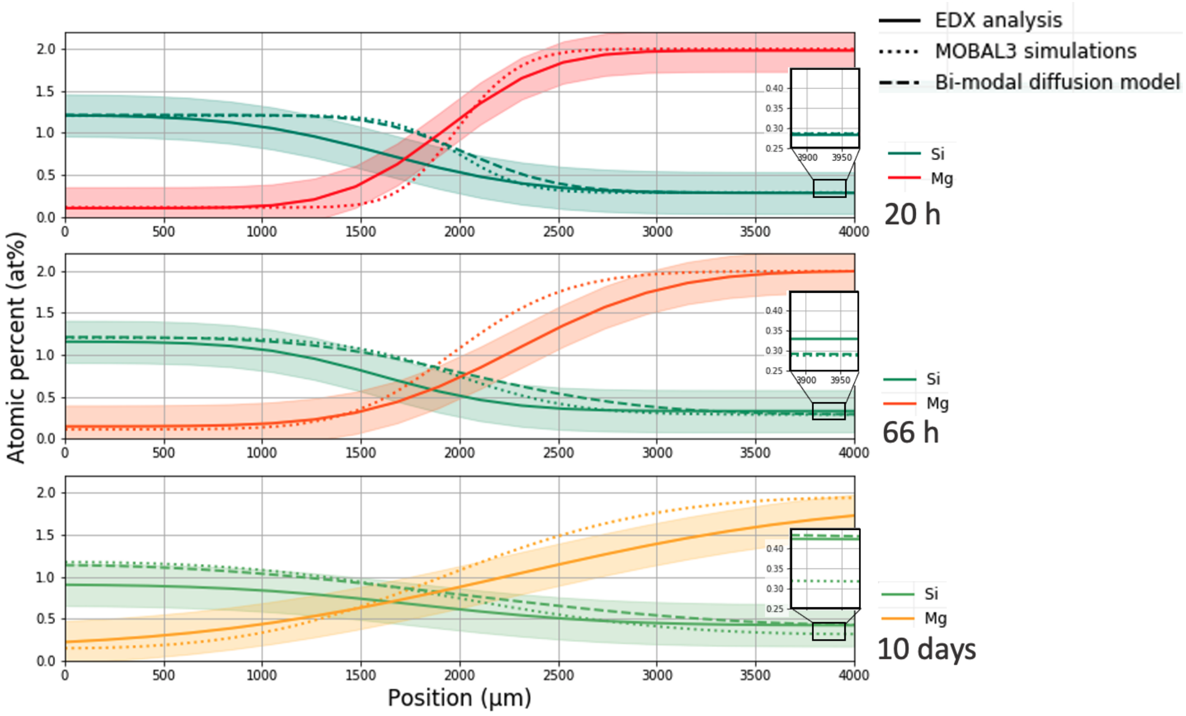

Figure 1.7: Mg and Si EDX fits of solid solution compositions along the gradient on an Al-1.2.wt.%Si Al-2.6wt.%Mg diffusion couple after homogenisation at 550 °C for 3 different times (20 h, 66 h and 10 days). The results show differences with MOBAL3 simulations and better correlation on the Mg edge of the gradient with the bi-modal diffusion model. The thermal treatment of 10 days at 550 °C is optimal to obtain a 3 mm gradient of both Mg and Si elements.

Thanks to diffusion, the sharp interface between the two initial layers becomes a larger interdiffusion zone as interdiffusion time at 550 °C increases. For Si, the difference of composition between the extremities of the couple is 1.0 at.%. Whereas for Mg, that difference is 1.9 at.%.

It is important to note at first, that after 20 h at 550 °C, only 2.0 at.% of the initial 2.9 at.% of Mg is actually present in solid solution. The rest is mainly trapped in oxides. Then, what is striking is the loss of Mg and Si in solid solution after 10 days at 550 °C. Thanks to the previous microstructural analyses, the formation of oxides and intermetallic particles explains this tendency. This loss prevents the good comparison with MOBAL3 expectations after 10 days. A comparison at 20 h and 66 h of the lengths with a decrease in concentration compared to the initial values shows that diffusion occurs faster than expected with MOBAL3 calculation for both Mg and Si elements.

A slight difference between Mg and Si diffusion regime is notable though. For Mg, the interdiffusion zone seems to grow with time until the edge of the sample before any change of composition at the extremity of the diffusion couple. Whereas for the diffusion of Si in the Mg part, the extremity composition seems to slightly rise before the arrival of the diffusion front. WDS precise analysis on the edge of Si-parts confirms this tendency. For 20 hours, $w_{\mathrm{Si}} = 0.07$ wt.%, for 66 hours, $w_{\mathrm{Si}} = 0.12$ wt.% and for 10 days $w_{\mathrm{Si}} = 0.31$ wt.%. Those very low values are at the limit of WDS detection. Therefore, they should not be considered quantitatively but only comparatively.

Table 1.2 summarises the interdiffusion coefficients at 550 °C extracted from the two previous EDX profiles (at 20h and 66h) analysed using an erf function, and from MOBAL3 database.

	EDX	MOBAL3	Literature
$D_{\mathrm{Al-Mg}}$ (10^{-13} m^2/s)	9.9	4.5	5.3 [MIN 83]
$D_{\mathrm{Al-Si}}$ (10^{-13} m^2/s)	15.2	4.6	4.7 [FUJ 78]

Table 1.2: Extracted interdiffusion coefficients

At 550 °C, the interdiffusion coefficient of Mg in Al is estimated at $5.3 \times 10^{-13}\,\mathrm{m}^2/\mathrm{s}$ for Al-2at.%Mg by Minamino *et al.* [MIN 83] and the Si one at $4.6 \times 10^{-13}\,\mathrm{m}^2/\mathrm{s}$ for Al-Si alloys containing 0.58 to 1.15 at.% Si by Fujikawa *et al.* [FUJ 78]. MOBAL3 Mg interdiffusion coefficients are slightly lower than these litterature coefficients. It has to be noted that Si and Mg interdiffusion coefficients determined by fitting of our experimental EDX profiles are higher than the ones calculated from the MOBAL3 database. This is certainly due to the contribution of grain boundary diffusion.

Grain boundaries (GB) have been identified as high diffusivity paths in metals since the 1950s [BAR 50]. Their structure (width and distance between each other) and their chemical composition (segregation factor) are influencing their capacity for fast diffusion path. It is assumed here that their diffusion coefficient D_{GB} is much greater that D, the bulk diffusion coefficient. To evaluate the total diffusion kinetics in a system, several elementary processes are taken in consideration: direct volume diffusion, diffusion along GB, partial leakage from GB to the bulk and subsequent volume diffusion near GB. In general, 1 or 2 elementary processes control the overall kinetics [MIS 99].

Recently, segregation of Mg in Al-Mg alloys GB has been studied by Koju *et al.* [KOJ 20]. Mg tends to segregate in high-angle GB. Its segregation increases with decreasing temperature. Mg segregation slows down GB diffusion of Al and Mg. In our case, Mg oxides are present on grain boundaries. Their effect on Si diffusion have not been studied yet. Despite this uncertainty, segregation is often directly taken in consideration in the effective diffusion coefficient [MIS 99].

We propose a new diffusion model attempting to reproduce the faster diffusion behaviour for Si. The model is based on an interconnected two regimes diffusion with one regular bulk diffusion and one accelerated grain-boundary diffusion. Figure 1.8 is representing the different atoms fluxes. The details of the model are presented in Appendix A.

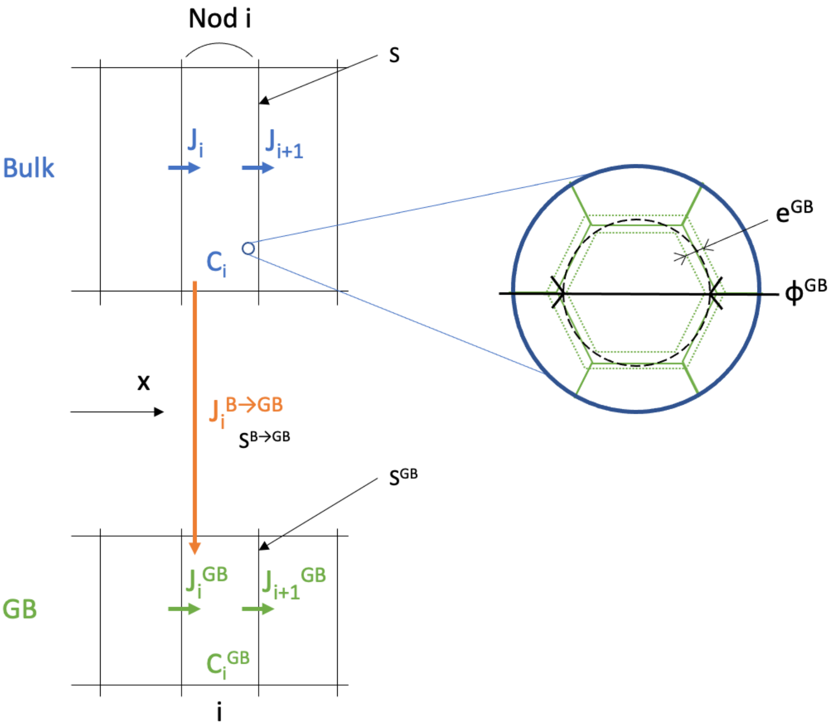

Figure 1.8: Schematic of the Si bi-diffusional regime model. Si solutes can diffuse through the bulk or faster through the grain boundaries (GB). A flux between the two systems is also present for each node i.

The results presented Figure 1.7 correspond to the total content of Si: $X^{tot} = C^{tot} v_{at}$. The parameters used are summarised in Table 1.3. The mean diameter of the grains is considered on each side of the initial interface according to the experimental values obtained after SPS (Figure 1.5).

Compared to MOBAL3 calculations, these simulations better represent the variations of Si characterised by WDS on the Mg side of diffusion couple, even if they are not fitting perfectly to the data on the whole profile. Oxidation should be taken in consideration in order to improve the model.

The specific diffusion of Si through the Mg part of the sample can be explained by grain boundaries diffusion enhanced by small grains sizes under long and high annealing treatment

Table 1.3: Parameters used in the Si bi-modal diffusion model

Fixed parameters	**Value**	**Unit**	
I	30	-	
L	4.15	mm	
ϕ_{Mg}^{GB}	8	μm	This study
ϕ_{Si}^{GB}	15	μm	This study
D_{Si}	4.7×10^{-13}	m^2/s	[FUJ 78]
v_{at}	1.66×10^{-29}	m^3	[VIS 07]
Optimised parameters	**Value**	**Unit**	
γ	1500	-	
$\mathrm{D}_{\mathrm{Si}}^{GB}$	7.8×10^{-10}	m^2/s	
e^{GB}	4	nm	
X_{max}^{GB}	50	at.%	

[MIS 99]. On the other side (Si-rich side), Mg solute either does not have the proper grains (too large) network, either its segregation slows its diffusion through grain boundaries. Both systems diffuse faster than MOBAL3 expectations, though, thanks to grain boundary diffusion.

Figure 1.9 presents the EDX solid solution compositions of a rolled gradient after an inter-diffusion of 10 days at 550 °C. This sample has been manufactured from degassed powders.

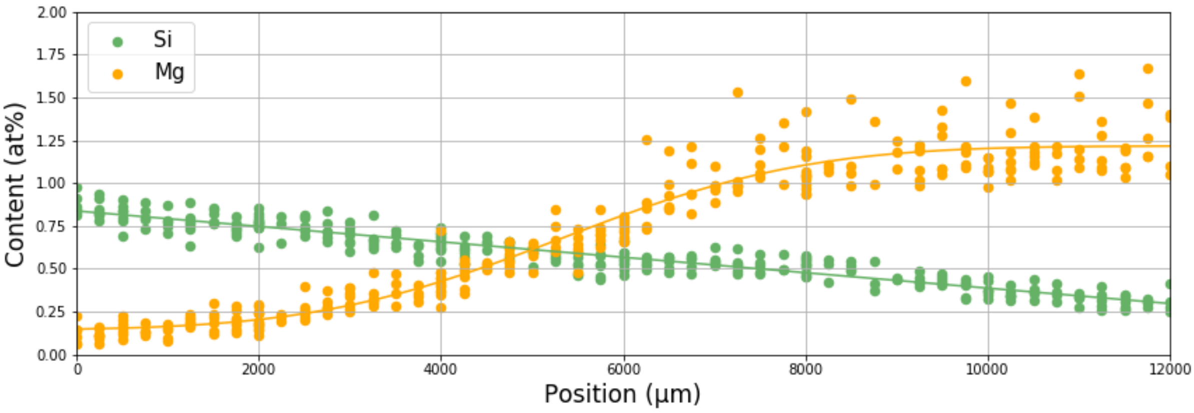

Figure 1.9: Mg and Si EDX solid solution compositions along the gradient on an Al-1.2.wt.%Si Al-2.6wt.%Mg diffusion couple after homogenisation at 550 °C of 10 days and rolling procedure. The Si gradient could be elongated on 12 mm whereas Mg could be elongated on 6 mm.

Homogeneity has been checked for the presented rolling procedure through multiple EDX measurements in the three directions. The Si gradient could be elongated on 12 mm whereas the length of the variation in Mg occurs within 6 mm.

1.3.3 Mechanical results

Right after water quenching of the most appropriate interdiffusion treatment (10 days at 550 °C) with degassing step, Vickers hardness was measured along the gradient. The gradient composition is described Figure 1.10a. WDS Mg content measurements on the Mg-part were noisy due to the oxidation of the sample. This uncertainty is represented with a shaded band around the fitted Mg content. From WDS measurements of the solid solution, available content of $\mathrm{Mg_2Si}$ in mole of atoms and excess of Si or Mg regarding that content are calculated along the gradient.

If Mg is limiting, $X_{\mathrm{Mg_2Si}} = \frac{3}{2}X_{\mathrm{Mg}}$ and $X_{\mathrm{Si}}^{excess} = X_{\mathrm{Si}} - \frac{1}{3}X_{\mathrm{Mg_2Si}}$.
If Si is limiting, $X_{\mathrm{Mg_2Si}} = 3X_{\mathrm{Si}}$ and $X_{\mathrm{Mg}}^{excess} = X_{\mathrm{Mg}} - \frac{2}{3}X_{\mathrm{Mg_2Si}}$.

The hardness measurements (HV0.5) of this sample are presented Figure 1.10b.

From left to right, Mg solid solution composition rises whereas Si decreases. The variation of hardness along the gradient presents a maximum in the middle of the Mg side.

The hardness data were converted to yield stress thanks to Myhr *et al.* equation [MYH 01] :

$$HV = a\sigma_y + b \tag{1.3}$$

With

- HV the Vickers hardness and σ_y the yield stress in MPa
- a = 0.33 HV/MPa [MYH 01]
- b = 16.0 HV [MYH 01]

From the yield stress, one can extract the solid solution contribution σ_{SS} following this equation of a classical law of mixture considering the various obstacles strengths [DES 98] :

$$\sigma_y = \sigma_{Al} + \sigma_{SS} + \sigma_p \tag{1.4}$$

With

- $\sigma_{Al} = \sigma_0 + \frac{k}{\sqrt{d}}$ from Hall-Petch law [COR 16]
  - $\sigma_0 = 10$ MPa the chemistry-dependent constant for pure aluminium [DES 98, COR 16]
  - $k = 90$ MPa.$\mu m^{1/2}$ the microstructure-dependent constant [COR 16]
  - $d = 11$ μm for Mg-side or 19 μm for Si-side the medium grain diameters from EBSD results Figure 1.5
- $\sigma_p = 0$ MPa the precipitation contribution after water quench

Finally σ_{SS} can also be expressed as :

$$\sigma_{SS} = \sum k_j x_j^{2/3} \tag{1.5}$$

with k_j the solid solution mechanical parameter of the element j and x_j the concentration of the element j in solid solution (wt.%)

In Figure 1.10c, equation 1.5 is fitted to the experimental solid solution yield stress results (converted from hardness) along the gradient. The gradient is going from the left to the right

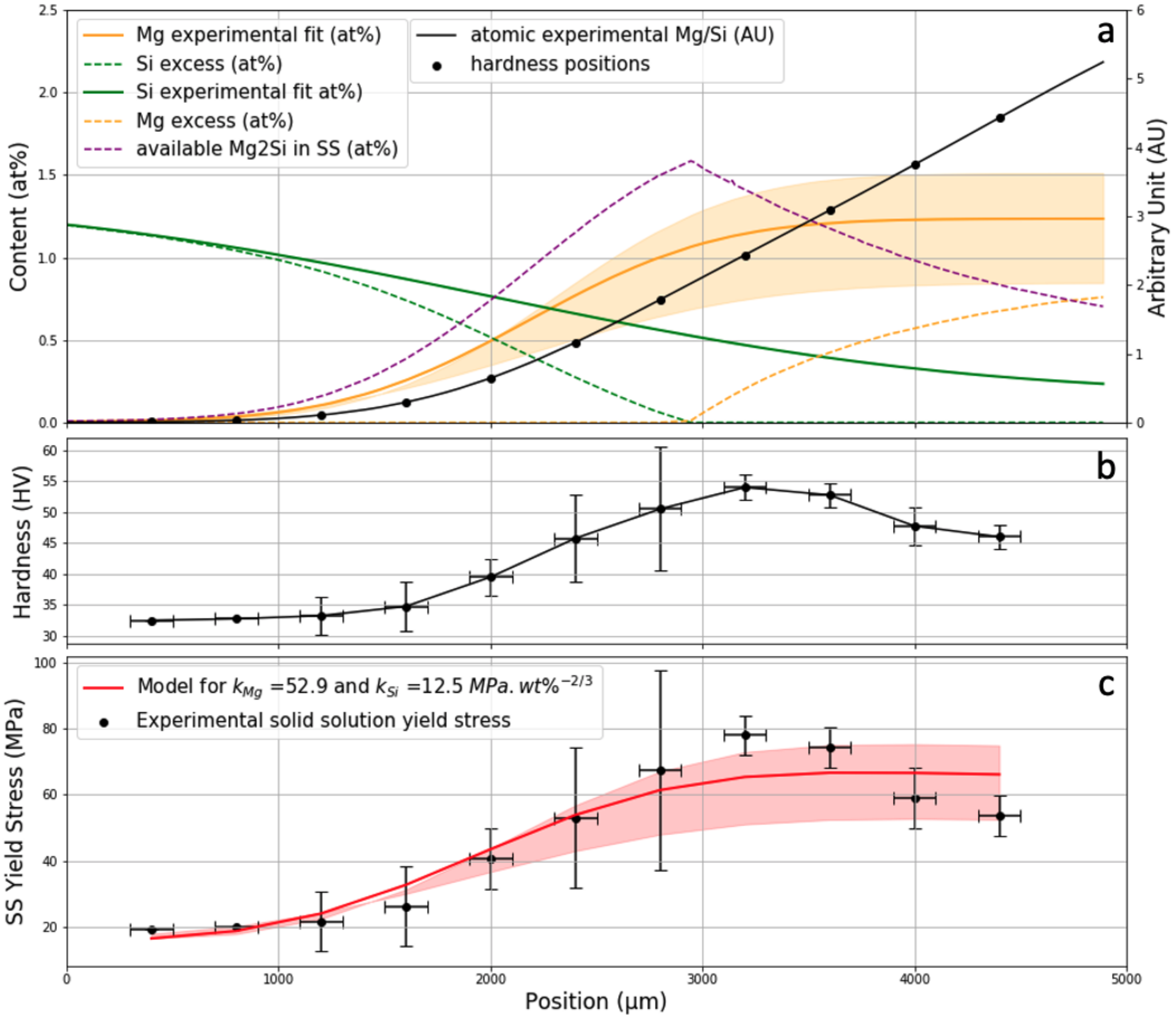

Figure 1.10: Analyses on a gradient of an Al-1.2.wt%Si Al-2.6wt%Mg diffusion couple after 10 days homogenisation at 550 °C and water quench. a: WDS solid solution composition, b: Vickers hardness and c: solid solution yield stress along the gradient.

from high concentration in Si to high concentration in Mg. For this fit, k_{Mg} and k_{Si} have respective values 52.9 and 12.5 MPa.wt$\%^{-2/3}$.

In pure Al, the solid solution strengthening was first observed higher for Mg than for Si with 17.3 MPa/at%Mg against 9.3 MPa/at.%Si [MON 76]. Myhr et al. then obtained 29.0 MPa.wt.$\%^{-2/3}$ for k_{Mg} and 66.3 MPa.wt.$\%^{-2/3}$ for k_{Si} in 6xxx commercial aluminium alloys though, proving the importance of other parameters such as the grain size. According to their parameters, in their samples, Si is a more efficient hardening element for the solid solution than Mg. Sjolander et al. used linear dependence of solid solution strengthening for Al-7Si-Mg castings with content of both Mg and Si [SJÖ 11] and they concluded that, for them, strengthening is more important for Mg than for Si with parameters 17 MPa.wt.$\%^{-1}$ for k_{Mg} and 11

MPa.wt.$\%^{-1}$ for k_{Si}. Therefore, from literature results, the solid solution mechanical parameters seem to be highly dependent on the studied material. Impurities and their particles could also play a non negligible role.

Considering the hardness uncertainties, the model used to calculate solid solution yield stress from Si and Mg content, is representing correctly the experimental values along the gradient with our new coefficients. In our samples, hardness measurement shows similar features than expected by Sjolander *et al.* model for Al-7Si-Mg casting alloys but hardens more especially for Mg side. The presence of cellular Mg oxides (in Al-Mg side) and of Fe-rich intermetallic particles (along the gradient) formed during interdiffusion treatment are certainly explaining the higher strength of our samples than those of Sjolander.

1.4 Conclusions

Manufacturing

This study provides a processing route to manufacture compositionnaly-graded aluminium alloys by powder metallurgy. Using Spark Plasma Sintering (SPS) on two blends of powders and after 10 days at 550 °C, 3 mm Mg-Si composition gradients were created. They have the specificity of containing a variation of possible Mg_2Si fractions and a variation of Mg or Si excess with respect to the pseudo-binary alloy (Mg/Si = 2). These gradients, depending on further characterisation needs, can then easily be elongated by rolling to 6 mm. This route could be applied to other metallic systems for combinatorial studies.

Microstructure and gradients

Due to the powder metallurgy route, the following microstructural features were observed in the gradient:

- Grain size distributions in the compacts are strongly linked to the initial powders sizes, even after a long solution treatment ;
- Mg-rich powder provides an important network of oxides and a finer grain size ;
- The small grain size seems to be responsible for the duality of diffusion (bulk and grain boundaries) of Si element. This effect has been modelled to predict more accurately the extent of the gradient.

Solid solution strengthening

Using a large gradient of composition between Al-1.2.wt.%Si and Al-2.6wt.%Mg, the solid solution strengthening effect was assessed and the Mg and Si strengthening coefficients were determined. The defects from the powder metallurgy route seem to modulate the pure solid solution effect: on one hand, the network of Mg-oxides and/or the Fe-intermetallic particles may increase the hardness, whereas the pores assumed to be H_2 degassing may lower the hardness.

Chapter 2

Precipitation characterisations on Al-Mg-Si graded samples

High-throughput precipitation characterisations have been conducted on compositionnaly graded Al-Mg-Si alloys in order to investigate the influence of Mg and Si on metastability cascades. First, microhardness measurements on interrupted treatment (at 170 ℃*) and Differential Scanning Calorimetry (DSC) experiments provided hardening and precipitation kinetics along Mg-Si gradients. Two compositions parameters seem to import: initial Mg+Si content and excess of Si. Then, Anomalous Small Angle Scattering (ASAXS) for numerous ageing states explored the evolution of precipitates mean diameter. Finally, for some specific ageing states, precipitates were identified using High Resolution Transmission Electron Microscopy (HR-TEM) and their sizes distribution were extracted with conventional TEM. Chemistry of solid solution and precipitates were analysed, for two ageing states, thanks to Atom Probe Tomography (APT). Four main regimes were identified: (i) extreme Si excess compositions with main precipitation of pure Si, (ii) strong Si excess compositions with important growth in length of the precipitates, (iii) near pseudo-binary compositions with important growth in diameter of the precipitates and (iv) strong Mg excess compositions with fast semi-coherent precipitation.*

Contents

2.1 Bibliographic review: precipitation in Al-Mg-Si alloys

In the first part of this literature review, each phase of the metastability cascade of β is detailed (crystallography, chemistry and morphology). Alloys composition changes on these precipitates are also evoked, especially for Si excess composition that have been predominantly investigated. In the second part of this bibliography, hardening mechanisms responsible for the mechanical properties of precipitation hardening alloys are introduced and the common mechanical evolution for Al-Mg-Si alloys are presented, depicting the ageing kinetics. Then, in the last part of this literature review, the influence of temperature on precipitation sequences is discussed either through pre-ageing or through continuous heating.

2.1.1 Precipitating phases involved during isothermal ageing

2.1.1.1 Coherent metastable phases

Clusters

After quenching, the super-saturated solid solution (SSSS) is metastable and will lead to the formation of clusters of atoms thanks to diffusion. The presence of quenched-vacancies improves this diffusion of elements in the matrix [GUI 59]. The concentration of vacancies in the sample is rising with the solutionising temperature and with the quenching rate. Three types of clusters have been identified: mono-species clusters of Si or Mg, co-clusters of Mg and Si and Guinier-Preston zones (GPZ). They can influence the hardness during artificial ageing treatment [ABD 08].

The first clusters to appear are mono-species, unorganised and with a strong concentration in vacancies. For some authors, Mg clusters are directly present after quench [MUR 98b]. Others claim that Si clusters are the ones trapping the quench-vacancies [DUT 91, FAL 16]. Then, with the enrichment of Mg, Si clusters are becoming co-clusters of Mg and Si. Those clusters can be organised as mono atomic layers (for mono-species) or as multi-layers (for co-clusters).

Finally, with sufficient Mg atoms, the clusters with one atom of Si for one atom of Mg are MgSi co-clusters. Vacancies are still present among them [GAB 07, EDW 94]. With further enrichment in solutes and coarsening, the clusters are forming the GPZ. These are observable by transmission electron microscopy (TEM) Figure 2.1a, b and c [MAT 98]. Their chemistry is similar to that of MgSi co-clusters.

With a Si excess, the chemistry of the clusters is richer in Si. Similarly, with a Mg excess the chemistry is richer in Mg. Otherwise the Mg/Si atomic ratio of these GPZ is close to 1 [POV 13]. Povoden [POV 13] proposed the chemistry of Al_2MgSi (see Figure 2.1e) allowing to be coherent with the Matrix, instead of MgSi proposed by Matsuda *et al.* (see Figure 2.1d).

β” precipitate

With ageing, GPZ become nucleation sites for β” precipitates [MUR 99]. This is why β” are sometimes considered as GPZ. The transformation between GPZ and β” is indeed progressive. For example, pre-β” has a chemistry close to β” but its organisation is still rather random.

The chemistry of β” in pseudo-binary alloys is close to a Mg/Si atomic ratio of 2 (Table 2.1).

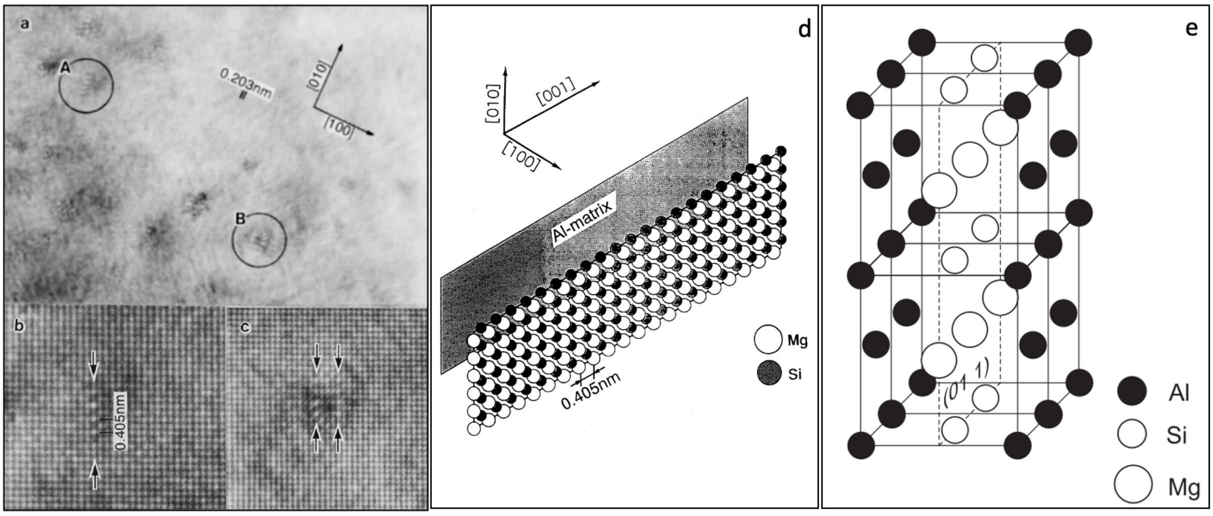

Figure 2.1: a: GPZ aged at 70 °C observed by TEM, b and c: enlarged photographs of regions marked by circles A and B in a, d: structure of the GPZ observed next to Al layer [MAT 98], e: structure of ordered GPZ [POV 13]. Matsuda GPZ are defined as a singular layer whereas Povoden is considering multi-layers GPZ surrounding Al plans.

With a Si excess, this Mg/Si ratio is around 1. Anderson *et al.* [AND 98] defined the β” chemistry as Mg_5Si_6. Thanks to *ab-initio* calculations [NIN 14] and atom probe analysis [HAS 09], a likely more stable chemistry is found: $Mg_5Al_2Si_4$. However, Povoden [POV 13] proved with thermodynamic calculations that this chemistry is only valid at low temperature. At 170 °C, the chemistry is rather around Mg_5Si_6. This chemistry has to be considered carefully though. Indeed, Son *et al.* [SON 11] found, for maximum hardness during ageing at 210 °C, the average of Mg/Si ratio of β” precipitates around 0.87 but with a wide range, between 0.027 and 2.33. Some Si-rich β” rod precipitates were even found without any Mg.

	References	Chemical composition			Crystallographic structure	Lattice parameters (nm)	Orientation relationship	Phase chemistry
		% Mg_2Si/Mg/Si	% Si in excess	Other elements				
Pseudo-binary alloys (without secondary elements)	[LYN 82]	1.6 wt.%			Monoclinic	a = 0.3; b=0.33; c=0.4 ; $\alpha = \beta = 90°$; $\gamma = 71°$	$[001]_{\beta''}//[001]_{\mathrm{Al}}$ $[100]_{\beta''} \wedge [001]_{\mathrm{Al}} = 5°$	
Pseudo-binary alloys (with secondary elements)	[MAR 97]	0.63 wt. % Mg; 0.35 wt.% Si		0.05 wt.% Fe; 0.01 wt.% Ti	Monoclinic	a=0.714; b=0.658; c=0.405; $\gamma = 75°$	$[100]_{\beta''}//[3\bar{1}0]_{\mathrm{Al}}$; $[010]_{\beta''}//[230]_{\mathrm{Al}}$	Mg/Si = 1.74
Alloys with Silicon excess	[ZAN 97]	0.5 wt.% Mg; 0.5 wt.% Si	0.4 wt.%		Centered monoclinic	a=1.516; b=0.405; c=0.674; $\beta = 105.3°$		Mg_5Si_6

	[AND 98]	0.5 at.% Mg; 0.53 wt.% Si		0.01 at.% Mn; 0.2 wt.% Fe	Centered monoclinic (space group C2/m)	a=1.516; b=0.405; c=0.674; $\beta = 105.3°$	$(010)_{\beta''}//(010)_{\mathrm{Al}}$;
							$[001]_{\beta''}//[\bar{3}10]_{\mathrm{Al}}$;
							$[100]_{\beta''}//[230]_{Al}$
								Mg_5Si_6

	[EDW 98]	0.80 wt. % Mg; 0.79 wt.% Si		0.18 wt. % Cu; 0.022 wt.% Fe; 0.01 wt.% Ti	Based-centered monoclinic	a=1.534; b=0.405; c=0.683; $\beta = 106°$	$(010)_{\beta''}//(001)_{\mathrm{Al}}$; $[001]_{\beta''}//[3\bar{1}0]_{\mathrm{Al}}$	Mg/Si = 1.2
	[AFI 08]	1 wt. % Mg; 0-1.6 wt.% Si		1.16 wt.% Ti	Monoclinic	a=1.516; b=0.405; c=0.674; $\beta = 105.3°$	$(010)_{\beta''}//(001)_{\mathrm{Al}}$; $[001]_{\beta''}//[3\bar{1}0]_{\mathrm{Al}}$	Mg_5Si_6
	[SAG 96]	Mg/Si=1.54			Monoclinic	a=0.65; b=0.76; c=0.405; $\gamma = 70°$		
	[MAR 97]	0.64 wt. % Mg; 0.81 wt.% Si		0.01 wt.% Fe	Monoclinic	a=0.714; b=0.658; c=0.405; $\gamma = 75°$	$[100]_{\beta''}//[3\bar{1}0]_{\mathrm{Al}}$; $[010]_{\beta''}//[230]_{\mathrm{Al}}$	Mg/Si = 1
	[MAT 99]	1 wt.%	0.4 wt.%		Monoclinic (space group P_2/m)	a=0.77; b=0.67; c=0.203; $\gamma = 75°$	$[100]_{\beta''}//[310]_{\mathrm{Al}}$; $(001)_{\beta''}//(001)_{\mathrm{Al}}$	Mg_3Si_6Al

Table 2.1: Summary of the properties of the β” phase found in the literature [MEY 18b]

During the first stages of β" formation, the pre-β" chemistry would still have Al in substitution: (Al,Mg)$_5$Si$_6$ [MAT 99] before getting to Mg$_5$Si$_6$. The degree of coherency would decrease as the loss of atoms of Al to the profit of Mg occurs [MAR 01].

All the observed β" precipitates have a monoclinic crystallography, see Figure 2.2b. There are lattice differences though depending on the composition of the alloys. With secondary elements or with Si excess, the crystallography changes from that of Al-Mg-Si model pseudo-binary alloys. Mainly, those changes are grouped in two families. Those with in average : a = b = 0.7 nm, c = 0.4 nm and $\gamma = 73°$ and those with a = 1.5 nm, b = 0.4 nm, c = 0.7 nm and $\beta = 105°$. Those two families are actually linked. Their lattice are only defined differently.

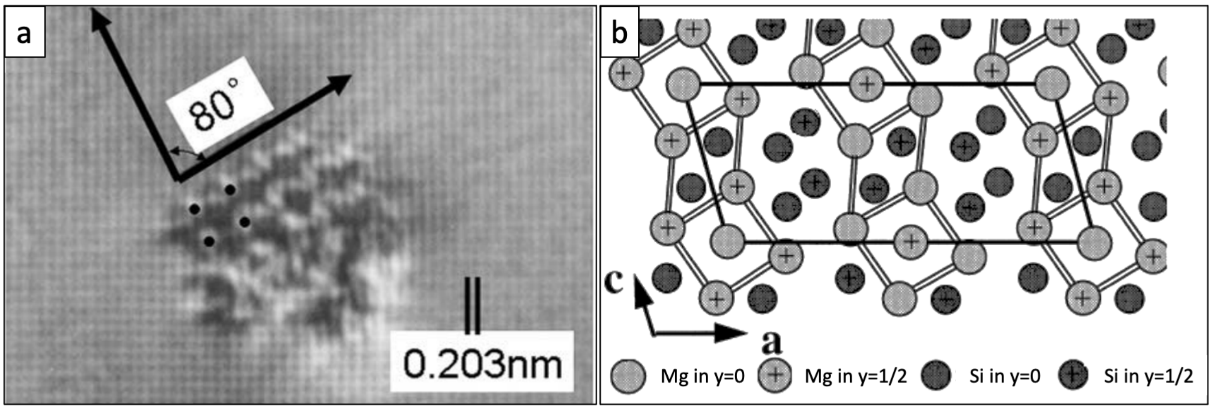

Figure 2.2: a: TEM image of a slice of an erected β" precipitate [MAT 05] and b: structure of the β" lattice [AND 98]

Matsuda showed by high resolution TEM (HR-TEM) that the angle γ (60-90°) depends on the Si excess in Al-Mg-Si alloys, Figure 2.2a. With a Si excess γ is around 75°, with a Mg excess or a pseudo-binary chemistry, γ is around 60° (as for β') [MAT 05]. This means that the shape of the parallelogram-type precipitate is controlled by the Mg (or Si) content.

Due to orientation relationships with the matrix, the β" precipitates are in a rod shape. Their length can have few nm to 50 nm [SON 11]. With Si excess in an Al-0.5Mg-0.53Si-0.2Fe-0.01Mn (wt.%) alloy aged for 8 h at 185 °C, the morphology and the sizes are similar [AND 98]. Anderson *et al.* measured a mean diameter of β"of 4 nm and a mean length of 50 nm. With coupled TEM and small angle neutrons scattering (SANS) experiments on a 6056 Al alloy (Mg-0.81wt.% Si-0.87wt.%), which has a similar Si excess, Donnadieu *et al.* measured a mean diameter of 2.5 nm at maximum strengthening obtained with an ageing treatment of 8 h at 175 °C [DON 98]. Chang *et al.* [CHA 15] followed the evolution of diameter and length during ageing at 180 °C by SANS on Al-Mg-Si alloy with Si excess. The diameter of the precipitates between 1h and 18h is growing from 3.6 to 4.4 nm while the length increased from 14 until 35 nm. SANS is giving an average value of precipitates sizes, but at those temperatures and times, most of them are β".

2.1.1.2 Semi-coherent metastable phases

From β" to β', the process is still unclear. It could be continuous; β" transforms into β', or the dissolution of β" could happen before β' precipitation.

The β' precipitates are large rods. Their diameter have several tens of nm, Figure 2.3a, and their length are between 200 nm and 2 µm. Vissers *et al.* [VIS 07] measured their mean diameter at 10 nm. With a Si excess, the morphology is similar.

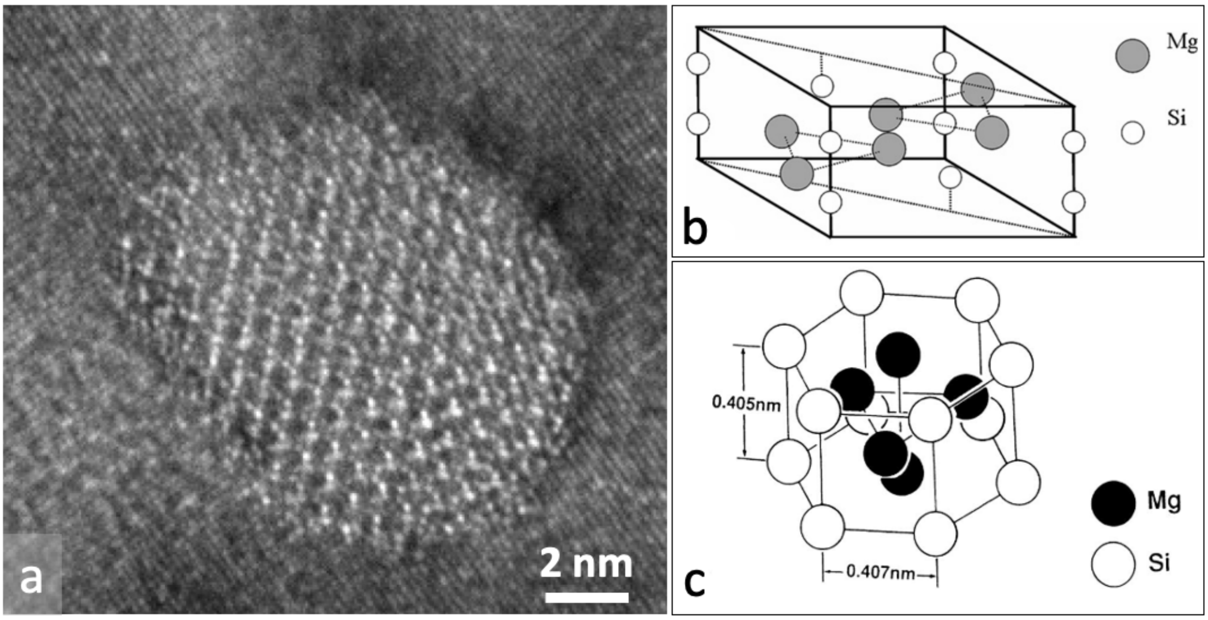

Figure 2.3: a: TEM image of a β' precipitate [MEY18], b: structure of the β' lattice [VIS07] and c: lattice structure of β_0' [MAT00]

Compositions of β' precipitates are summarised in Table 2.2. They tend to be close to Mg_2Si. Mg_9Si_5 is the chemistry generally admitted.

All the information related to the crystallography of β' is summarised in Table 2.2. All lattice structures are hexagonal. For pseudo-binary alloys, there are two families of β' precipitates. Those with a = 0.7 nm and c = 0.4 nm, Figure 2.3b, can have 3 different orientations with the matrix [MAT 93b]. The second family are those with a = c = 0.4 nm, which are actually a less organised form of β', Figure 2.3c. These early β' precipitates are named β_0'.

For Si excess alloys, β' and β_0' lattice structures present almost no changes compared to pseudo-binary alloys. These phases are only richer in Si. However, three new semi-coherent phases can be observed.

	References	Chemical composition			Crystallographic structure	Lattice parameters (nm)	Orientation relationship	Phase chemistry
		% Mg_2Si/Mg/Si	% Si in excess	Other elements				
Pseudo-binary alloys (without secondary elements)	[JAC 72]	1.2 wt.%			Hexagonal	a = 0.705; c=0.405; *c=1.215	$(001)_{\beta'}//(100)_{\mathrm{Al}}$ $[100]_{\beta'}//[01\bar{1}]_{\mathrm{Al}}$	1.73
	[LYN 82]	1.6 wt.%			Hexagonal	a = 0.708; c=0.405 ; $\alpha = \beta = 90°; \gamma = 60°$	$[001]_{\beta'}//[110]_{\mathrm{Al}}$ $[100]_{\beta'}//[110]_{\mathrm{Al}} = 5°$	$Mg_{0.44}Si$
	[MAT 93a]	1 wt.%			Hexagonal	a = 0.407; c=0.405		
Pseudo-binary alloys (with secondary elements)	[WES 79]	1 wt.%		< 0.01 wt.% Fe	Hexagonal	a = 0.708; c=0.405		
	[MAR 97]	0.63 wt. % Mg; 0.35 wt.% Si		0.05 wt.% Fe; 0.01 wt.% Ti	Hexagonal	a=0.407; c=0.405		Mg/Si=1.75
	[CAY 00]	1 wt.% Mg; 0.65 wt.% Si		0.25 wt.% Cu; 0.5 wt.% Cr	Hexagonal (**Space group $P\bar{6}2m$)	a=0.71; c=0.405		Mg/Si=1.36

Silicon excess alloys	[MAR 97]	0.64 wt. % Mg; 0.81 wt.% Si		0.01 wt.% Fe	Hexagonal	a=0.407; c=0.405	$[0001]_{\beta'}//[001]_{\mathrm{Al}}$
							$(\bar{1}100)_{\beta'}//(110)_{\mathrm{Al}}$
							$(\bar{1}2\bar{1}0)_{\beta'}//(100)_{\mathrm{Al}}$
							$(\bar{1}3\bar{2}0)_{\beta'}//(100)_{\mathrm{Al}}$
								Mg/Si=1.21

	[AFI 08]	1 wt. % Mg; 0-1.6 wt.% Si		1.16 wt.% Ti	Hexagonal	a=0.72; c=0.812		
	[VIS 07]	0.6 wt. % Mg; 0.9 wt.% Si		0.5 wt.% Mn; 0.2 wt.% Fe	Hexagonal (Space group $P6_3/m$)	a=0.715; c=1.215		$**Mg_9Si_5$
	[MAT 96]	1 wt.%	0.4 wt.%		Hexagonal	a=0.705; c=0.407	$(\bar{1}2\bar{1}0)_{\beta'}//(001)_{\mathrm{Al}}$ $[\bar{1}2\bar{1}0]_{\beta'}//[001]_{\mathrm{Al}}$	Mg/Si =0.83
	[MAT 00]	1 wt.%	0.4 wt.%		Hexagonal	a=0.71; c=0.405		Mg/Si =1.68

Table 2.2: Summary of the properties of the β' phase [MEY 18b] *(with (*) c value for long ageing times and (**) results obtain from calculations)*

The first one named U1 (or type A) is composed of large rods of average diameter ranging between 50 and 100 nm (Figure 2.4a). They are very rich in Si. They could be formed from dissolved solutes of β' in addition with Si present in the Al matrix. Their chemistry can have a Mg/Si atomic ratio down to 0.3. Based on experiments, Matsuda *et al.* [MAT 00] proposed a composition of Al_4MgSi_5 but Froseth *et al.* [FRØ 03a] ab-initio calculations considered the chemistry of Al_2MgSi_2 more relevant. Their crystal structure is also hexagonal with a = 0.405 nm and c = 0.67 nm (Figure 2.4d).

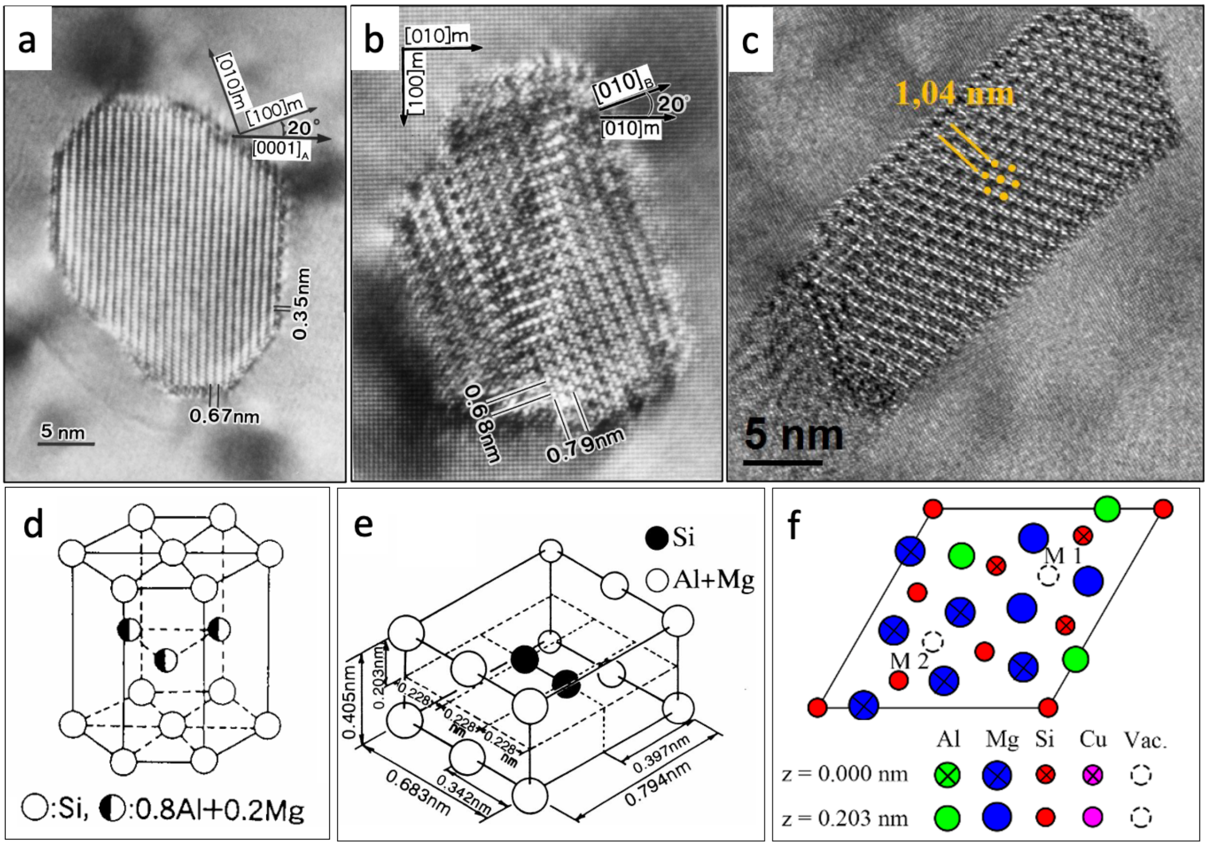

Figure 2.4: TEM images of a: U1 [MAT 00], b: U2 [MAT 00], c: B' [MEY 18a] and their lattice structure respectively d, e and f [CHE 20]

The second one, U2 (type B), precipitates as smaller rods of diameter included between 10 and 30 nm, Figure 2.4b. The Mg/Si ratio can go only down to 0.4. Those precipitates are also very rich in Si. The chemistry is therefore established as $Mg_2Al_4Si_5$ experimentally or as $Mg_4Al_4Si_4$ thanks to ab-intio calculations [FRØ 03b]. Their crystal structure is orthorhombic with a = 0.683 nm, b = 0.79 nm and c = 0.405 nm Figure 2.4e. This U2 lattice has a clear relationship with U1 described by Matsuda *et al.* [MAT 00]. Their hypothesis is that U2 precipitates are formed at the same time as β' and they are transforming into U1 during ageing.

The last new semi-coherent phase is B' (type C). These precipitates are flattened rods with large equivalent diameter between 10 and 100 nm (Figure 2.4c). Their chemistry is still rich in Si but not as the two previous ones. Mg/Si ratio is only going down to 0.84. This phase is only appearing in very overaged states. Their interface and relationship with U2 and the matrix are described by Matsuda *et al.* [MAT 96, MAT 00]. Their nucleation is more frequently heterogeneous than the other metastable phases [MAT 05, TEI 11]. DFT calculations again is giving a stable form for $Mg_9Al_3Si_7$ chemistry [RAV 04, POV 13]. The structure lattice is once again hexagonal with a = 1.04 nm and c = 0.405 nm and is very close from Q' and Q precipitates that are formed in Al-Mg-Si-Cu alloys, Figure 2.4f [CHE 20].

2.1.1.3 Non coherent stable phases

The stable phase β appears finally for long overageing treatments or at high temperature. It is responsible for the apparition of low mechanical properties (hardness and strength) sometimes called the softening sequence of the alloy. β precipitates form as large plates of 0.01 to 20 µm (Figure 2.5b) [JAC 72].

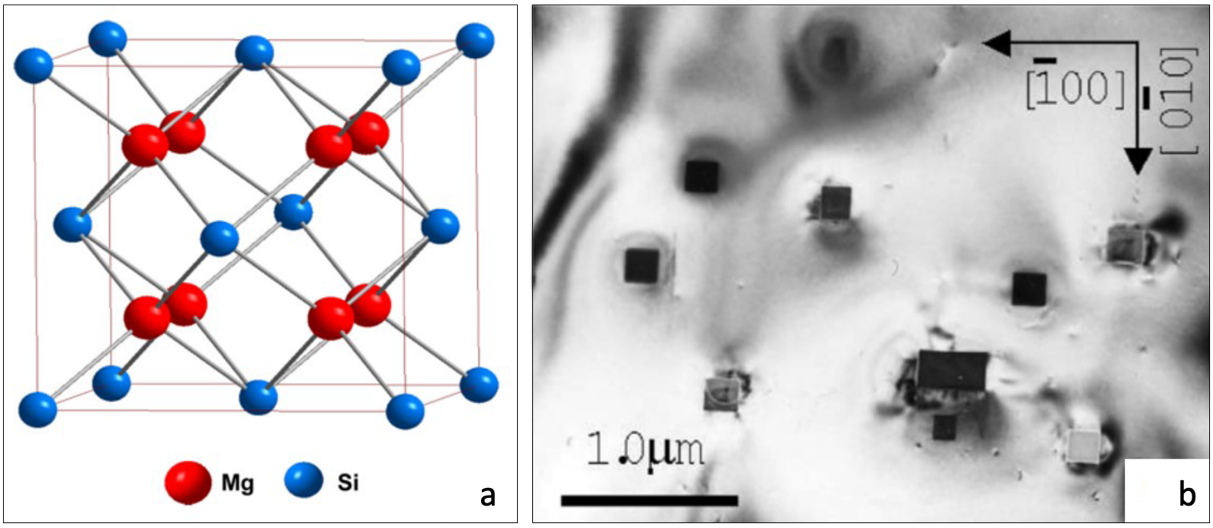

Figure 2.5: a: lattice structure of β [MOR 14] and b: conventional TEM images of β plates [GAB 07]

The structure of β is face-centered cubic (FCC) and the prototype is Fluorite (CaF_2) with a lattice parameter a = 0.639 nm (Figure 2.5a) [VIS 07]. β is incoherent with the matrix. The chemistry of β is Mg_2Si.

The microstructure of semi-coherent phases are very different from that of β. Dissolution of the metastable phases before β precipitation is expected during isothermal ageing. Indeed, during continuous heating this phenomenon was observed [GAB 07, OST 15]. But it was also found that β nucleates on β' precipitates and consume them [THO 61, OHM 02].

In some cases, β is present in the early stage of precipitation. These events are certainly occurring for very fast quenching. Indeed, fast quenching create large vacancies concentration providing propitious defaults for nucleation of more advance phases such as β plates [OHM 02, WES 79].

With Si excess, the β stable phase is unchanged. But, for sufficient Si in SS, another stable phase can precipitate at different ageing states: pure Si. Si has a FCC diamond structure. The morphology of these precipitates are also in rods. Pure Si has been observed along with β" precipitation [DOA 02, OHM 02, AFI 08] or only after β formation [MAT 05].

2.1.1.4 Summary of precipitation trajectories

To summarise, the real precipitation sequences of Al-Mg-Si are more complex than the simplified version of pseudo-binary alloys presented in the introduction of this PhD manuscript. The Table 2.3 recapitulates the general characteristics of the precipitates that participate to them.

	GPZ	β"	β_0'/β'	U1 (typ.A)	U2 (typ.B)	B' (typ.C)	β
Morph.	at. layer	small rod	rod	rod	small rod	flatten rod	plate
Chem.	Al_2MgSi	Mg_5Si_6	Mg_9Si_5	Al_2MgSi_2	AlMgSi	$Al_3Mg_9Si_7$	Mg_2Si
Crys.	FCC	monoclinic	hexagonal	hexagonal	orthorhombic	hexagonal	FCC*

* *fluorite*

Table 2.3: General characteristics of the different precipitates involved in the precipitation sequence of Al-Mg-Si alloys

Finally the precise precipitation sequence of pseudo-binary and Mg excess alloys during isothermal treatment is :

$$\text{SSSS} \rightarrow \text{Mg and Si clusters} \rightarrow \text{MgSi co-clusters} \rightarrow \text{GPZ} \rightarrow \beta'' \rightarrow \beta'(\beta'_0) \rightarrow \beta$$

As discussed, this precipitation sequence can change with fast quenching :

$$\text{SSSS} \rightarrow \text{Mg and Si clusters} + \beta \rightarrow \text{MgSi co-clusters} + \beta \rightarrow \text{GPZ} + \beta \rightarrow \beta'' + \beta \rightarrow \beta'(\beta'_0) + \beta \rightarrow \beta$$

The precipitation sequence of Si excess alloys is also different :

$$\text{SSSS} \rightarrow \text{Mg and Si clusters} \rightarrow \text{MgSi co-clusters } \mathbf{(rich\ in\ Si)} \rightarrow \text{GPZ } \mathbf{(rich\ in\ Si)} \rightarrow \beta'' + \mathbf{Si}$$

$$\rightarrow \beta'(\beta'_0) + \mathbf{U1} + \mathbf{U2} + \mathbf{B'} + \mathbf{Si} \rightarrow \beta + \mathbf{Si}$$

with the changes compared to pseudo-binary sequence highlighted in bold font

Depending on the Si content excess, differences are observed. For example, Meyruey *et al.* [MEY 18a] showed that for 6351 Al with a strong Si excess of 0.7 at.% the precipitation sequence is rather:

$$\text{SSSS} \rightarrow \text{GPZ} \rightarrow \beta'' \rightarrow \beta' + \mathbf{U2} + \text{Si} \rightarrow \mathbf{U1} + \text{B}' + \text{Si} \rightarrow \beta + \mathbf{Si}$$

with the main phases (largest volume fraction) highlighted in bold font

Whereas in that same study for 0.3 at.% Si excess, the precipitation sequence is :

$$\text{SSSS} \rightarrow \text{GPZ} \rightarrow \beta'' + \boldsymbol{\beta'_{\text{disloc}}} + \text{Si} \rightarrow \beta' + \boldsymbol{\beta'_{\text{disloc}}} + \text{B'} + \text{Si} \rightarrow \beta + \text{Si}$$

with the main phases (largest volume fraction) highlighted in bold font
Where the appearance and the proportion of semi-coherent phases are impacted.

On the next Figure 2.6, the evolution of the microstructure with these precipitates are represented with ageing conditions.

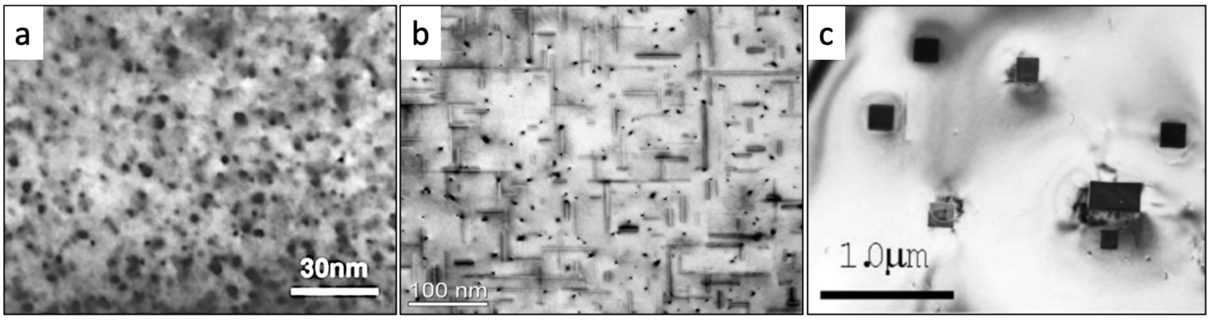

Figure 2.6: Evolution of the microstructure during artificial ageing on TEM conventional images in a: GPZ [MUR 98b], in b: β" hardening precipitates [SON 11] and in c: β stable precipitates [GAB 07]

Phases are growing and precipitates distributions within the matrix are changed. The maximum mechanical strength is measured for microstructural configuration of Figure 2.6b. Explanations are described in the next section.

2.1.2 Hardening mechanisms and mechanical behaviours

2.1.2.1 Hardening mechanisms

Precipitation is a diffusional phase transformation schematically separated in three stages: nucleation, growth and coarsening [POR 09]. In order to induce precipitation hardening, the phase which precipitates has to be homogeneously distributed in the matrix. Optimising the radius and the distribution of the hardening precipitates in the matrix is the key to control the mechanical strength of the alloy. In 6xxx series, the maximum resistance is associated to β'' [BAS 06]. Two explanations are at the origin of this characteristic.

Mechanical strength of precipitation hardening alloys is directly linked to the movement of the dislocations and their interactions with the precipitates. So first, the presence of **elastic distortions in the matrix around precipitates** impedes the movement of dislocations [BAR 08]. As shown in introduction, the coherent β'' precipitate is the phase which induces the most important elastic distortions. Recently, this effect has been measured by considering the decrease of the mechanical properties induced by the formation of β'. Compared to β" precipitates, β' precipitates have smaller lattice strains relative to the matrix of 0.99% versus 2.10% (for β") [YAN 20]. The force required for a dislocation to approach the coherent precipitates will therefore be more important than for others such as semi or non-coherent precipitates. The mechanical strength of the material will thus be higher when this precipitate is present.

Then, an approach with two mechanisms explains the **dislocations interaction within precipitates**. For non-coherent precipitates, the by-pass of Orowan, Figure 2.7a, is dominant in order for the dislocation to stay in its slip plane. For coherent and semi-coherent precipitates, there is also the possibility of shearing the precipitate, Figure 2.7b. The effective mechanism will be the one requiring the smallest obstacle force for the dislocation to pass.

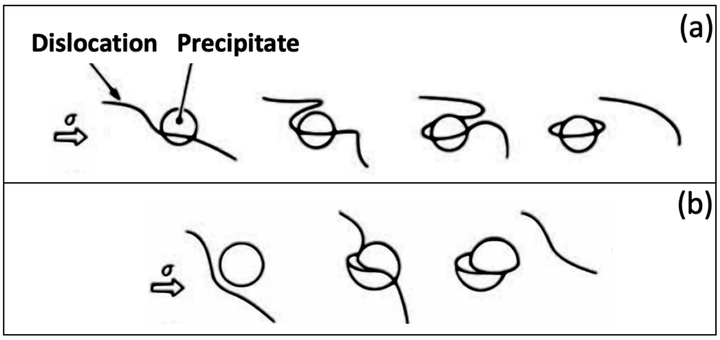

Figure 2.7: Representation of a: the Orowan by pass and b: the shear mechanism [MAI 10]

For one distribution of those precipitates, i.e. at constant volume fraction and for one mean radius, there is a transition radius from which the mechanism will switch, see Figure 2.8.

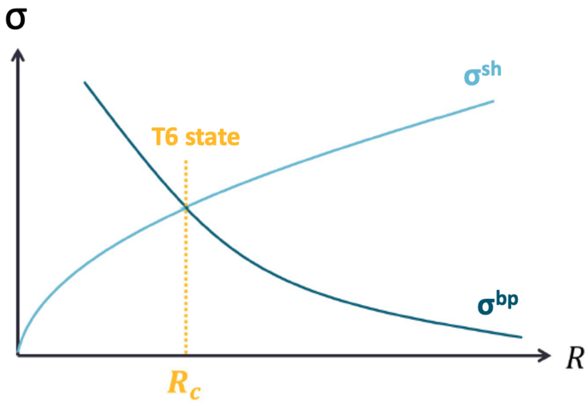

Figure 2.8: For a constant volume fraction, illustration of the stress required to cross the precipitate depending of its radius. σ^{bp} represents the strength to by-pass and σ^{sh} the strength to shear [POL 95, MEY 18b].

The small precipitates are sheared whereas the large ones are by-passed. If the precipitate size distribution is narrow and around an average radius equals to the transition radius R_c, the force required for the dislocation to pass through the precipitate is usually maximum. The thermal treatment which provides this optimal sizes distribution, leading to maximum strength, is called T6.

These two precipitate effects presented (elastic distortions and dislocation interactions with the precipitates) slow down the dislocation movements and therefore increase the strength. Logically, strength increases with the increase of precipitates number, volume fraction and content useful to precipitation. These dependencies explain the increase of mechanical strength with Mg_2Si content (seen in **Introduction**).

To summarise, maximum strength is obtained with precipitation of the largest number of β'' with the right size distribution (T6 state). This state is usually observed around 8 h at 170 °C for 6xxx series. But these ageing conditions are influenced by the prior microstructure of the sample, which depends on composition and thermo-mechanical history. For example, all previous thermal treatments to ageing (solution treatment, natural ageing at 25 °C during storage or pre-ageing at lower temperature like 70 °C) can influence the mechanical properties.

2.1.2.2 Mechanical evolution during isothermal ageing

As presented in **Introduction**, the solid solution (SS) Mg_2Si content has major influences on precipitation hardening phenomenon and therefore on the mechanical properties such as hardness. Takeda *et al.* [TAK 96] showed that, for a pseudo-binary alloy of 0.77 Mg_2Si at.% (B3) under ageing at 180 °C, the hardness peak is initially at 67 h, presented in Figure 2.9a and composition in Table 2.4.

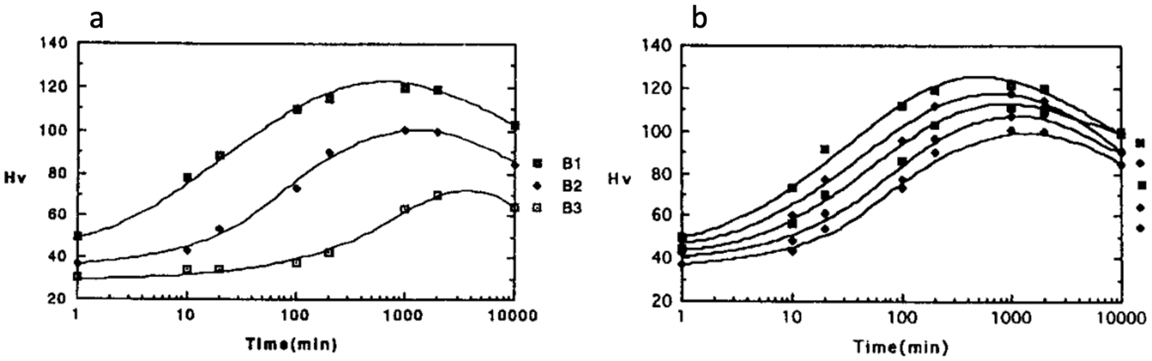

Figure 2.9: Hardness evolution with ageing time at 180 °C depending on a: Mg_2Si content and b: solute content [TAK 96], Table 2.4 for detailed compositions

	Mg	Si	Mg_2Si	Mg+Si	Mg/Si
B1	1.28	0.56	1.68	1.84	2.29
B2	0.83	0.4	1.19	1.23	2.08
B3	0.54	0.26	0.77	0.8	2.08
S1	0.83	0.58	1.24	1.41	1.43
S2	0.83	0.71	1.25	1.54	1.17
M1	1.01	0.4	1.21	1.41	2.53
M2	1.18	0.37	1.12	1.55	3.19

Table 2.4: Compositions in at.% of the different alloys studied by Takeda *et al.* [TAK 96]

These samples compositions are also represented on the 200 °C isothermal section of the ternary phase diagram of the Figure 2.10. S1 and S2 belong to a ternary domain (Al, Mg_2Si and pure Si) whereas all the others are in the bi-phased domain (Al and Mg_2Si).

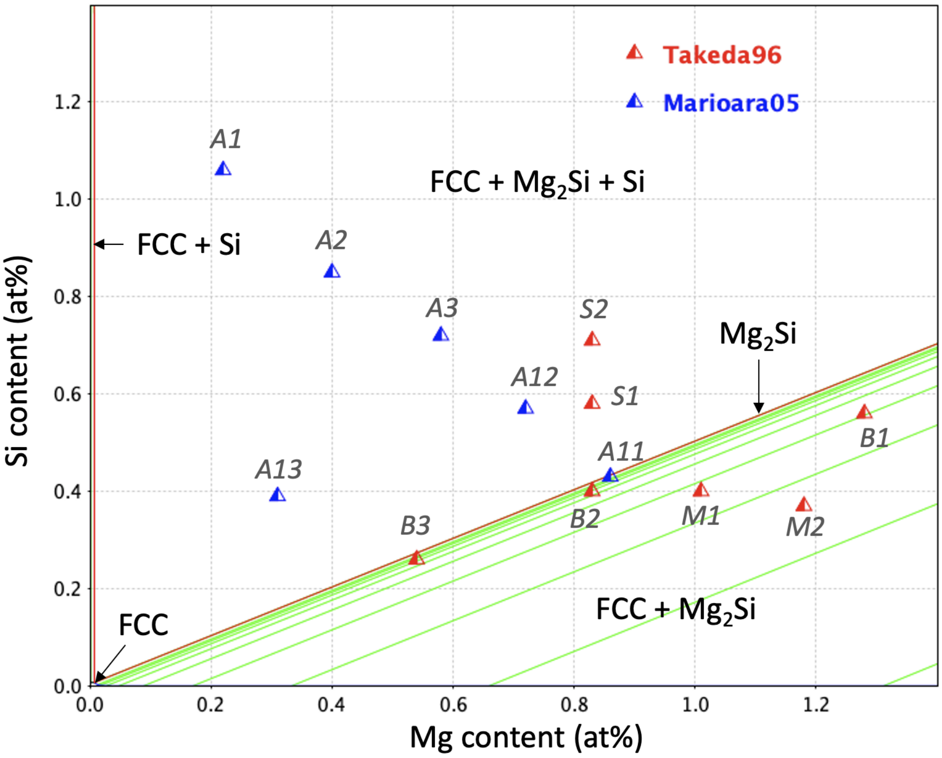

Figure 2.10: Takeda and Marioara samples compositions on an isothermal section at 200 °C

In an alloy with 1.68 Mg_2Si at.% (B1), the hardness peak is appearing after only 13 h. Hardness values are also increasing with Mg_2Si content. For those same samples, their hardness peak rises with Mg_2Si content from 70 HV to 120 HV.

In that same study, the effects of solutes on hardness are also investigated for ageing at 180 °C in Figure 2.9b. Alloys with relatively close Mg_2Si content (near 1.2 at.%) but with different Si or Mg excess are compared, Table 2.4. Once more the maximum hardness peaks are obtained for the shortest ageing times. The best precipitation hardening is obtained with Si excesses.

More recently, Marioara *et al.* studied as well the effect of alloy composition on hardness evolution (Figure 2.11) and precipitates formation. For them, the SS content in Mg_2Si is not exactly the important parameter to refer, one should rather use the sum of SS solutes content Mg+Si. All the alloys studied contain 1.3 at.% of Mg+Si except for A13 which contains half of it see Table 2.5.

These samples compositions are also represented in the Figure 2.10 on the 200 °C isothermal section. A11 belongs to the two-phases domain (Al and Mg_2Si) whereas all the others are in the ternary domain (Al, Mg_2Si and pure Si).

For high Si excesses ($Mg/Si < 1$), Figure 2.11a, the hardness rises with decreasing Si until $Mg/Si = 5/6$ (A3). Caution must be taken though because in those 3 samples, as Si is decreasing, Mg_2Si is also increasing. A hardness peak due to GP zones is also visible at 3h of

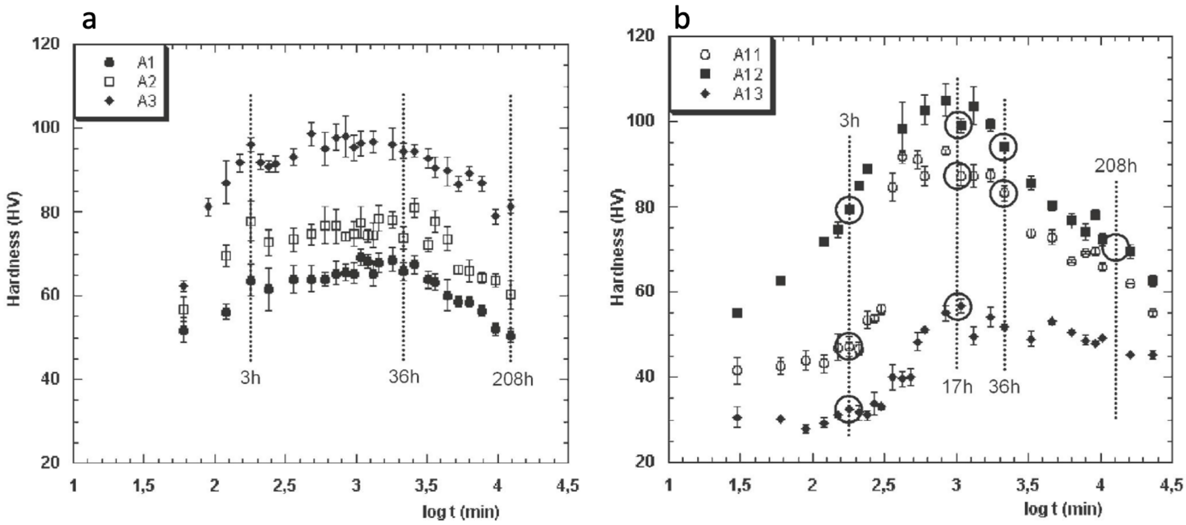

Figure 2.11: Hardness evolution with ageing time at 175 °C depending on the solute content a: for Si excess alloys and b: for Mg excess alloys and Si excess with low Mg + Si content [MAR 05]

	Mg	Si	Mg_2Si	Mg+Si	Mg/Si
A1	0.22	1.06	0.33	1.28	0.21
A2	0.40	0.85	0.60	1.24	0.47
A3	0.58	0.72	0.87	1.3	0.81
A13	0.31	0.39	0.47	0.7	0.79
A12	0.72	0.57	1.08	1.29	1.26
A11	0.86	0.43	1.29	1.29	2.00

Table 2.5: Compositions in at.% of the different alloys studied by Marioara *et al.* [MAR 05]

175 °C ageing. By performing TEM characterisations on specific ageing states, Marioara *et al.* noticed that in Si-rich alloys, a very fine precipitate microstructure produces the high hardness state despite the low volume fraction of precipitates. After 17 h at 175 °C, β" precipitates are largely dominant. For longer ageing times, U2 precipitates seem to have a higher stability than β'. Therefore, combinations of β", β' and U2 are observed while over-ageing is slowed down.

For low Si excesses ($1 < Mg/Si < 2$), Figure 2.11b, the hardness rises with decreasing Mg until $Mg/Si = 5/6$ (A12). GP zone peaks are not visible at 3 h. The Si rich alloy with low Mg+Si content (A13) behaves like low Si excess alloys. The hardness peak is narrower and is coinciding with the centre of the hardness plateau of high excess Si alloys. β" and β' precipitates are both present at that T6 state but β" is the one responsible of strength. The precipitates are coarser and therefore, they overage faster than the high Si excess alloys. The precipitates of the Si-rich alloy with a lower total content of solutes (A13) are among the coarsest. During longer ageing, β' is majoritarian even if few U phases precipitate.

To conclude, with the rise of Si excess in 6xxx Al alloys, the hardness peak rises and arrives faster certainly thanks to thinner precipitates. But, if Mg+Si (or Mg_2Si decreases, the Si excess alloys can be found with similar, or even worse, hardening than alloys will less Si. This can be explained partially because of coarser precipitates.

Finally, precipitation is impacted by the ageing temperature and therefore hardening as well. Takeda *et al.* [TAK 96] showed that, above 180 °C hardness is decreasing with the increase of ageing temperature and that the solute influences are impacted. More recently, Doan *et al.* [DOA 02] provided overall experiments on that two aspects. For their samples, the highest hardness values were obtained between 150 and 200 °C. Other thermal influence on precipitation are presented in the next section.

2.1.3 Influence of temperature on the precipitation sequences

2.1.3.1 Influence of samples thermal history on isothermal precipitation

During natural ageing, Mg-Si clusters are formed. With a Si excess the formation of those clusters are promoted but they are richer in Si [TAK 96, ARU 15]. Afterwards, during classical ageing treatment at higher temperature, the GPZ formed after these clusters do not seem to be nucleation sites for β''. Dissolution has to occur first, delaying the precipitation process and therefore the T6 state. This provides also a decrease in the number density of the hardening precipitates [MUR 98a, TSA 05].

In contrast, after pre-ageing at 70 °C, the GPZ formed seem to be efficient nucleation sites for the metastable precipitates and thus accelerate the precipitation [MUR 99]. With Si excess, there are again more clusters [MUR 98a].

Doan *et al.* [DOA 02] showed that a solution treatment of 30 min at 590 °C on various Al-Mg-Si alloys brings higher hardness values during ageing than with a solution treatment of 560 °C. The clusters or GPZ, which consist of Mg, Si and vacancies (Mg-Si-V), are the beginning of precipitation, and vacancies play also an important role in nucleation. It has been proven that the vacancy concentration is more important when the solutionising temperature is higher [MAT 06].

Quenched-in vacancies can also influence the precipitation of a special phase: the cuboid phase. This cube phase is an intermediate phase between the β'-phase and β-Mg_2Si with a Mg/Si ratio of 3 [MAT 06].

2.1.3.2 Precipitation sequence during continuous heating

Differential Scanning Calorimetry (DSC) measures the heat exchange of the sample during thermal treatment in comparison with a reference. The common DSC experiment is performed under continuous heating. During that experiment on precipitation hardening alloys, the sample is generating thermal energy when precipitation (exothermic reaction) occurs and is requiring heat when dissolution (endothermic reaction) happens. The phases with lowest interfacial energies, generally metastables, will form first at low temperatures, whereas nucleation of stable phases will require higher temperatures. DSC peak identification based on TEM showed that a precipitation sequence close to the one of isothermal treatment is therefore observable during a continuous increase of temperature [GAB 07].

In Figure 2.12, Son *et al.* [SON 11] performed DSC on a pseudo-binary alloy with a composition of Al-0.83at.%Mg-0.4at.%Si. DSC curves are presented depending on their pre-ageing time under 210 °C before DSC.

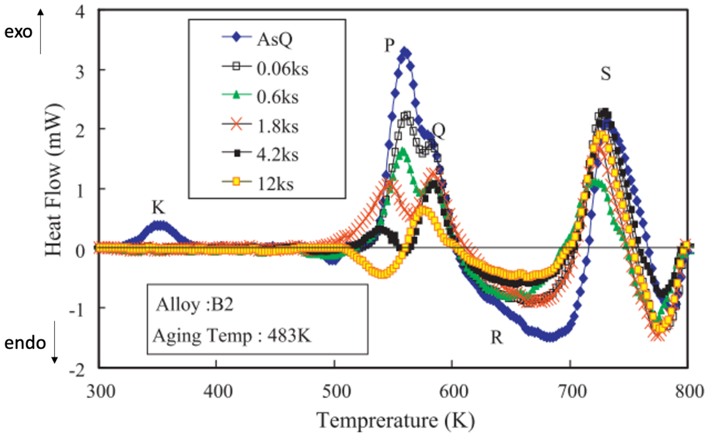

Figure 2.12: DSC thermograms on Al-0.83at.%Mg-0.4at.%Si alloys at different 210 °C ageing states [SON 11]

In the as-quenched sample, clusters (peak K), coherent (P), semi-coherent (Q) and non coherent (S) phases are formed and dissolved (R) during the temperature increase. These peaks are diminishing with the increase of ageing time and some (K and P) have completely vanished after 4 min and 3 h, respectively, at 210 °C. Indeed, after 3 h at 210 °C, clusters and coherent precipitates have already formed during the previous ageing treatment. During the DSC, dissolution occurs before the pursuit of the precipitation sequence.

On the next Figure 2.13A, Gupta *et al.* [GUP 01] performed DSC measurements (10 K/min) on as quenched pseudo-binary samples with various Mg_2Si content. The amplitude of the peaks increases with Mg_2Si content. The quantity of phases transformed is more important. With 1.26 wt.%, the semi-coherent peak (B') is finally detected.

Similar DSC measurements were performed on the three same alloys, after an ageing treatment of 24 h at 180 °C Figure 2.13B. At this ageing state, the semi-coherent peak (B') is, this time, entirely visible (for the two highest content in Mg_2Si) because the coherent transformation already occurred before the continuous heating. Instead a dissolution peak (F') is present. For the lowest content of Mg_2Si (a), semi-coherent peak is not present though because the corresponding precipitates are already formed. Precipitation sequence is faster with the decrease in Mg_2Si content.

Then, Takeda *et al.* [TAK 96] investigated with DSC an other composition influence on precipitation sequences. They performed DSC (10 K/min) on as-quenched samples with fixed composition of Mg_2Si but various contents in Mg and Si (Figure 2.14).

As presented in the part before, clusters formation are enhanced with Mg or Si excess content regarding to the pseudo-binary composition. Here the highest clustering is obtained with Si excess. Coherent precipitation seems also increased by Si and Mg excesses. And finally, with Si excess, coherent and semi coherent peaks no longer overlap mainly because the coherent pre-

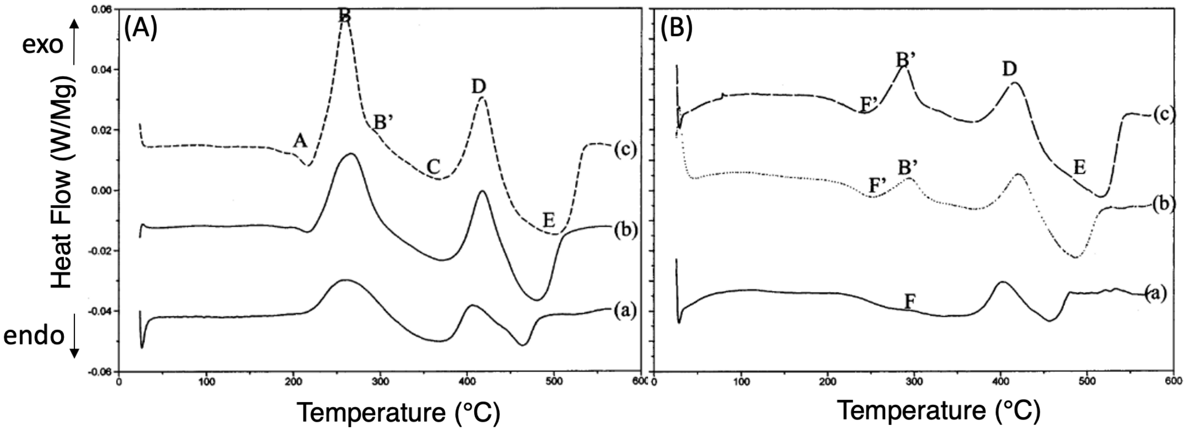

Figure 2.13: DSC measurements (10 K/min) on pseudo-binary as-quenched (A) and on 24 h at 180 °C aged (B) samples with (a): 0.63, (b): 0.95 and (c): 1.26 Mg_2Si wt.% [GUP 01]

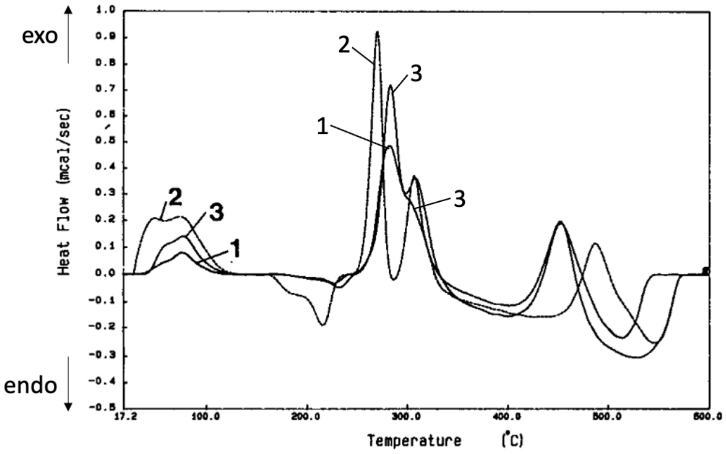

Figure 2.14: Mg and Si content effect on DSC thermograms with heating rates of 10 K/min upon as-quenched samples 1: Pseudo-binary Al-0.83at.%Mg-0.40at.%Si 2: Si excess Al-0.83at.%Mg-0.95at.%Si 3: Mg excess Al-1.41at.%Mg-0.040at.%Si [TAK 96]

cipitation peak is appearing before.

After this bibliography study on precipitation in pseudo-binary and Si excess alloys, the structure and specificity of each precipitate involved in the metastability cascade is clearer. The hardening mechanisms have been described. And finally the influences of Si and Mg on thermal and mechanical behaviours have been enlightened. After this literature review, the results of the vast investigation on precipitation along the manufactured Mg-Si gradients of Chapter 1 will be directly presented. It has been chosen that the traditional Materials and Method section will be incorporated within appendixes and will be present as a support in due course to describe the many materials and methods used.

2.2 Influence of composition on precipitation kinetics at 170 °C

In this section, the influence of composition on the ageing kinetics at 170 °C has been studied on the graded samples from the manufacturing route and the diffusion couple presented in Chapter 1. Micro-hardness measurements on interrupted treatments, continuous heating Differential Scanning Calorimetry (DSC) analyses and isothermal DSC precipitation are performed along the graded samples in order to investigate the microstructural and mechanical variations.

2.2.1 Microhardness measurements upon interrupted treatments

The same graded sample (A) as presented at the end of Chapter 1 is used in this paragraph. The composition of the solid solution (SS) in Mg and Si obtained from WDS analyses along the graded material position is presented again Figure 2.15. From those two experimental fits (procedure detailed in Appendix B), different parameters have been calculated such as: the Mg/Si atomic ratio. The available contents for formations of β - Mg_2Si or β" - Mg_5Si_6 are represented in at.%. The excesses of Si or Mg to the pseudo-binary composition are represented as well in at.%.

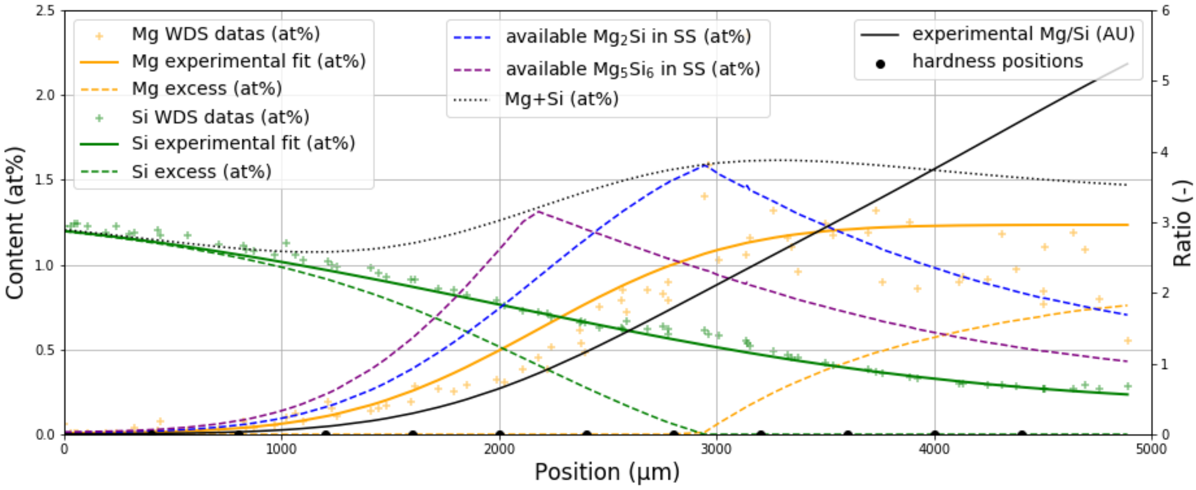

Figure 2.15: WDS solid solution composition of a gradient of an Al-1.2.wt%Si Al-2.6wt%Mg diffusion couple after 10 days homogenisation at 550 °C and water quench.

The A sample is in a super saturated solid solution state after an homogenisation at 550 °C and a water quench. Microhardness measurements were performed at that moment (as presented in Chapter 1). The sample is then aged at 170 °C. The treatment is interrupted to perform similar microhardness measurements at specific time and positions in the gradient. The initial solid solution composition of each hardness position is precisely described in Table 2.6 and presented on an 200 °C isothermal section of the ternary diagram Figure 2.16.

Position (μm)	At. Mg/Si	Available Mg_2Si (at.%)	Mg excess (at.%)	Si excess (at.%)
400	0.01	0.02	-	1.13
800	0.03	0.05	-	1.04
1200	0.11	0.16	-	0.92
1600	0.30	0.39	-	0.74
2000	0.65	0.74	-	0.52
2400	1.17	1.15	-	0.27
2800	1.79	1.50	-	0.06
3200	2.44	1.41	0.20	-
3600	3.09	1.18	0.42	-
4000	3.75	0.98	0.57	-
4400	4.43	0.83	0.68	-

Table 2.6: WDS solid solution composition of a gradient of an Al-1.2.wt%Si Al-2.6wt%Mg diffusion couple after 10 days homogenisation at 550 °C and water quench.

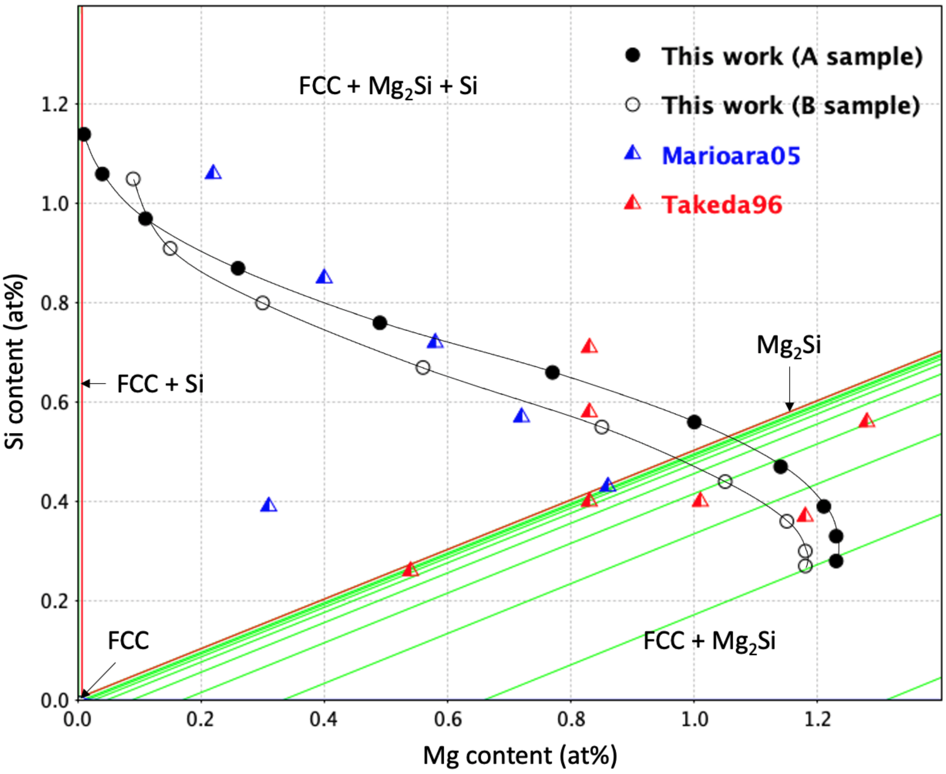

Figure 2.16: Gradients compositions represented on 200 °C isothermal section of ternary phase diagram

The micro-hardness results are first presented in the color map of Figure 2.17a. For each value presented, two measures were made. The standard deviation is situated between 0 and 14 HV. Microhardness values are plotted depending on the ageing time at 170 °C and depending on the position in the gradient. The Mg content increases with the position whereas Si decreases with it.

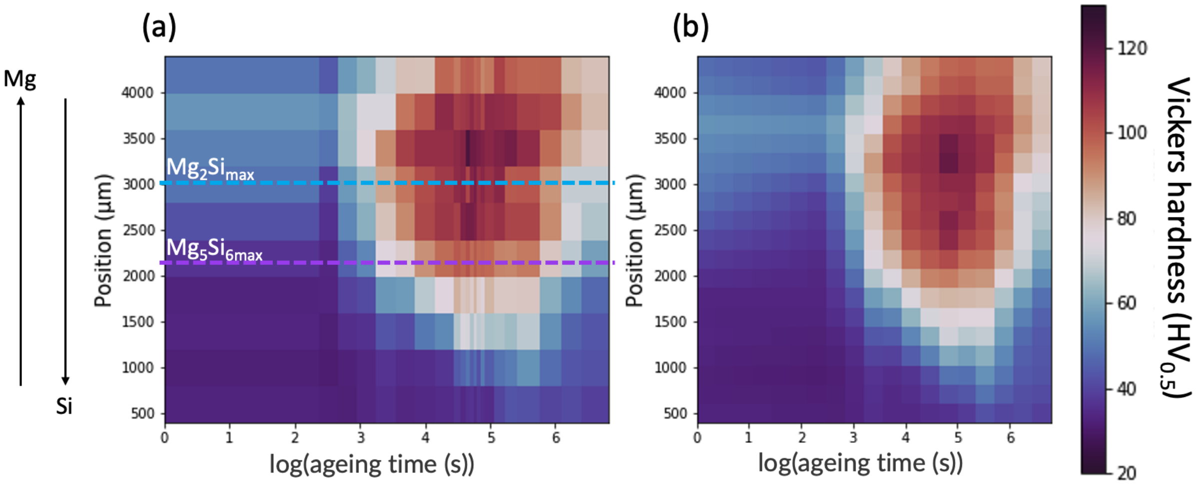

Figure 2.17: Coloured map of the microhardness measurements during interrupted treatment at 170 °C on a gradient of an Al-1.2.wt%Si Al-2.6wt%Mg diffusion couple after 10 days homogenisation at 550 °C and water quench. a: real data b: linear interpolation. The maximum strengthening is obtained almost in the centre of the gradient.

2.2.1.1 Influence of composition on hardness maximum values

During the entire ageing treatment, the highest hardness values, above 110 HV, are positioned between 2400 and 3600 µm. Those positions correspond to the part of gradient with high content of possible Mg_2Si, between 1.1 and 1.5 at.% from Table 2.6. Underneath 0.4 at.% (for position $\leq$ 1600 µm), the hardness values do not exceed 85 HV during all the ageing treatment. The maximum value 122 HV is obtained for the position of 3200 µm for which the composition has a small excess of Mg with Mg/Si = 2.4 and is near the maximum available SS content in Mg_2Si with 1.4 at.%. As presented in **Introduction** (Fig. 6), hardness rises consequently with Mg_2Si available content in SS.

Two maxima seem to be present especially on the interpolated values of Figure 2.17b. These maxima are localised on two particular positions. The first one is at 3200 µm, which is where the Mg+Si content is maximum and near the maximum content of Mg_2Si, Figure 2.15. The second one is at 2400 µm near where the content of Mg_5Si_6 is maximum in SS. Still in the Figure 2.15, at their maxima, the SS content in Mg_2Si is superior to the content in Mg_5Si_6. This can lead to a difference in the amount of β" precipitates and explain why $HV_{Mg_2Si_{max}} > HV_{Mg_5Si_{6max}}$. In any case, these 2 contributions are influencing the hardness results, they will be evaluated with Mg_2Si content in SS (with the maximum at 1.6%) and with Mg/Si atomic ratio for Mg_5Si_6 content (with the maximum at Mg/Si = 1.3).

These experimental values of hardening are situated between 30 and 130 HV. They belong to a similar range values as those presented in the literature review.

2.2.1.2 Influence of composition on the hardness peak times

Mg_2Si available content in SS has also an influence on kinetics. To define properly the hardness peak for each position/composition, kinetics curves are interpolated with 3 degree polynomial fits in Figure 2.18a.

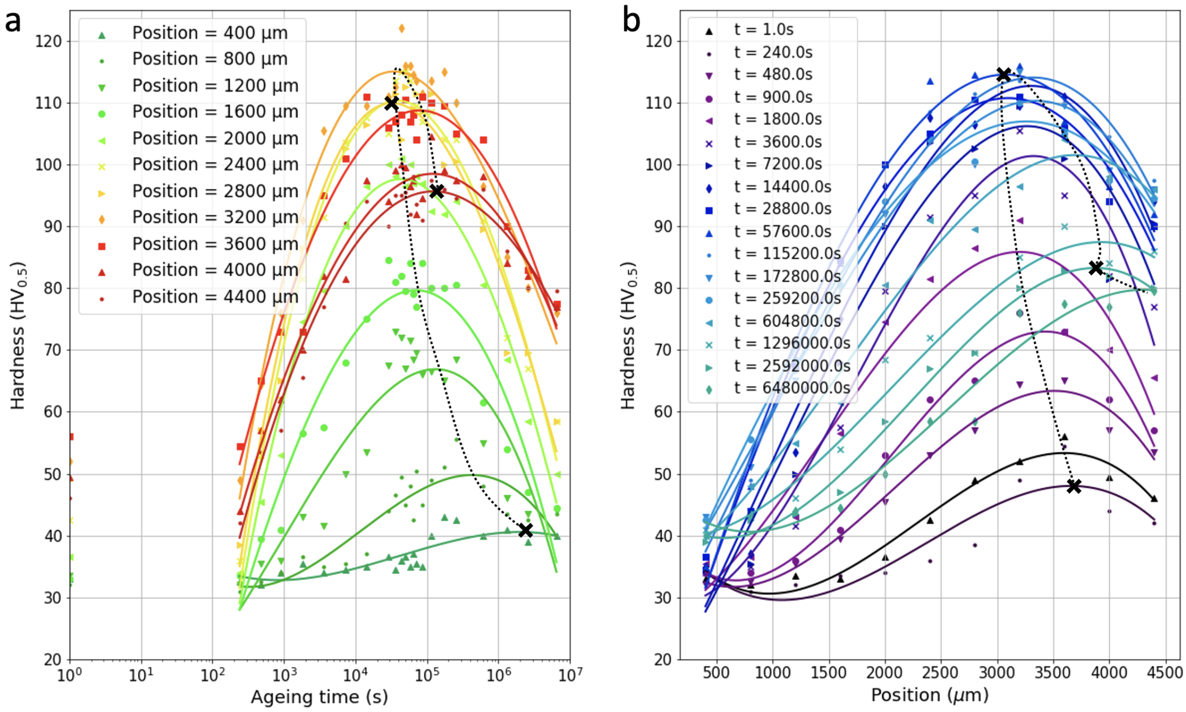

Figure 2.18: Microhardness measurements during interrupted treatments at 170 °C on a gradient of an Al-1.2.wt%Si Al-2.6wt%Mg diffusion couple after 10 days homogenisation at 550 °C and water quench. 3 degrees polynomial fit depending on a: time b: position. Precipitation kinetics are different depending on the composition.

Three categories of kinetics are visible. First from 400 to 1600 µm, i.e. with an important Si excess ($Mg/Si \leq 0.3$) and a low Mg_2Si content (≤ 0.4 at.%) in green, hardness peaks are measured near 17 h. Then from 2000 to 3200 µm ($0.7 \leq Mg/Si \leq 2.4$ and $0.7 \leq Mg_2Si \leq 1.4$ at.%), the hardness peaks occur between 8 and 14 h (yellow lines). Finally for positions between 3600 and 4400 µm ($Mg/Si \geq 3.1$ and $Mg_2Si \leq 1.2$ at.%), the hardness peaks are delayed after 25 h (red lines).

The hardening values at hardening peaks are situated between 40 and 120 HV. Their hardening peak times are measured between 8 h and 25 days. They have a similar characteristics as those presented in the literature review (**section 2.1.2.2**).

Two specific positions are worth mentioning. The position of 2800 µm, with 1.5 at.% Mg_2Si and an atomic Mg/Si of 1.8 typical for very low excess of Si (0.1 at.%), which presents the shortest time until its hardness peak. And the position of 2400 µm with 1.2 at.% Mg_2Si and Mg/Si = 1.2 (excess of Si of 0.3 at.%) which has the steepest hardening rate.

2.2.1.3 Influence of composition on hardness peak shapes

These differences of kinetics are also visible in Figure 2.18b. First, until 15 min (900 s) of ageing treatment at 170 °C, the highest hardness value is measured at 3600 µm. Then until 14 h (50 400 s), the hardest position is shifted on the Si side of the gradient until the position of 3000 µm which corresponds to the pseudo-binary composition. Then with over-ageing, the peak position is again shifted towards higher Mg contents until the edge of the sample for 2.5 months of treatment.

On this last figure, the hardness decrease with ageing time of Mg-rich positions is clearly less abrupt and less important than the one on the Si-rich side. Indeed on Figure 2.18a, the peaks are narrower for Si positions except for the two extreme positions.

To visualise differently the precipitation kinetics, Figure 2.19 gives a 3D representation of the microhardness values plotted depending on the ageing time at 170 °C and on the position in the gradient. The Mg content increases with the position whereas Si decreases with it.

At the beginning of ageing, Mg-side is harder than Si-side. Then, between 2000 and 4400 µm, precipitation occurs for both sides and reach similar hardening. Mg-side ($>$ 3000 µm) precipitation is slower and its variation of hardness is less important than Si excess precipitation ($<$ 3000 µm).

The faster rise is reported for the composition positioned at 2400 µm with a Mg/Si = 1.2 with a rise of 61 HV in 2 h. At 4000 µm, the content of Mg_2Si is similar but the precipitation kinetic is the slowest with Mg/Si = 3.8. In 2 h, the variation of its hardness is only of ΔHV = 32 HV.

2.2.1.4 Summary of the microhardness results

This microhardness analysis on interrupted ageing treatments proved that the mechanical properties of the sample A are improved with the amount of Mg_2Si like typical Al-Mg-Si alloys. The hardness is maximal for a content almost maximum of Mg_2Si (1.4 at.%) and, surprisingly, with an excess of Mg of 0.2 at.% (Mg/Si = 2.4). According to literature, if more Mg_2Si content would have been present, hardness could have been even higher [TAK 96].

The Si strengthening effect is also evidenced. First, with the second local maximum hardness present for Mg/Si = 1.2. This value is in line with the literature and the maximum hardness obtained for Mg/Si = 1.3 by Marioara *et al.* [MAR 05] and for Mg/Si = 1.2 by Takeda *et al.* [TAK 96]. This second local maximum could even be the main one if Mg_2Si content was the same as for Mg/Si = 2.3 and would maybe be shifted towards composition with lower Mg/Si values. The Si strengthening effect plays also an important role concerning precipitation kinetics. The faster hardness peak is reached for only 0.1 at.%Si (Mg/Si = 1.8) but the stiffest hardening peak's slope is obtained with 0.3 at.%Si excess (Mg/Si = 1.2). And it explains the movement

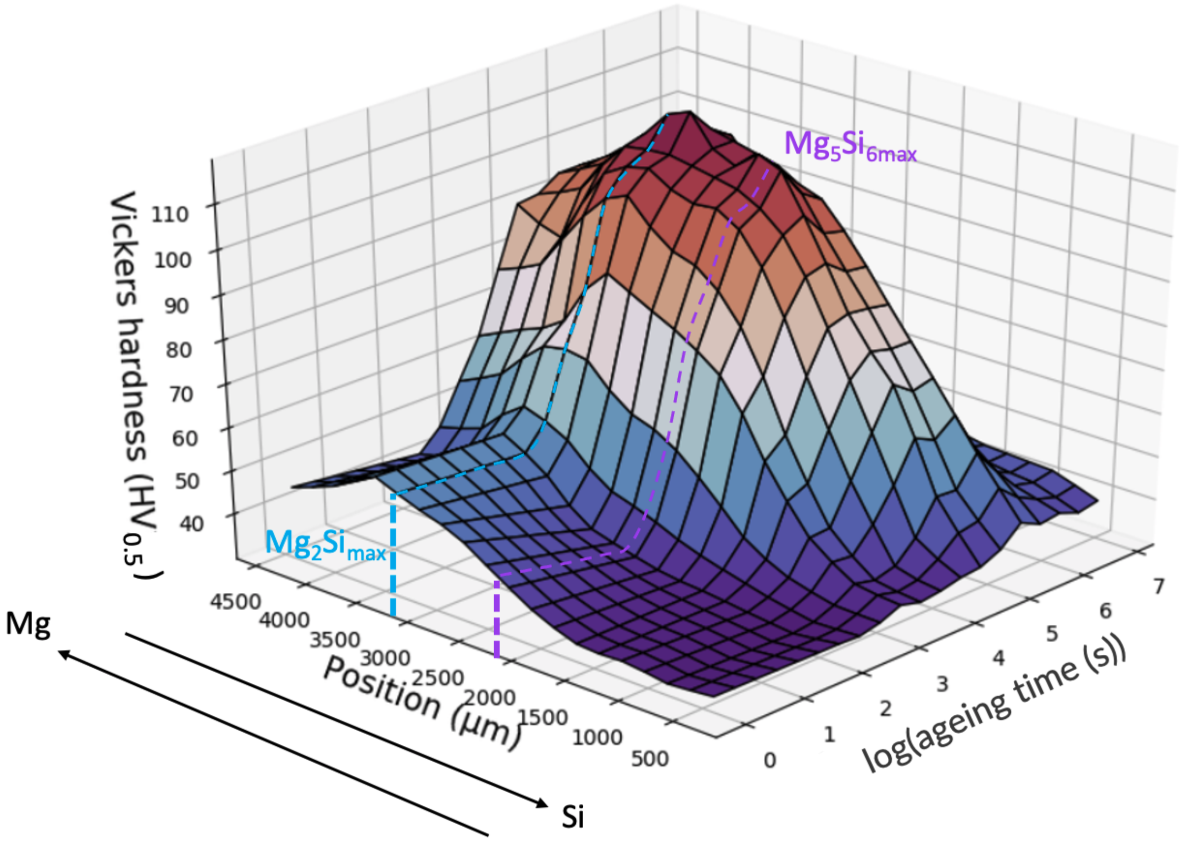

Figure 2.19: 3D representations of the microhardness measurements linearly interpolated during interrupted treatment at 170 °C on a gradient of an Al-1.2.wt%Si Al-2.6wt%Mg diffusion couple after 10 days homogenisation at 550 °C and water quench. Precipitation kinetics are different depending on the composition.

of peak position in the gradient until the same Si excess content of 0.3 at.%.

For the continuation of this chapter, the indicative T6 state of the overall graded sample will be situated at 16 h under 170 °C. It is important to note that some compositions in the gradient will be actually at 16 h in an overageing state, whereas others will be in a pre-T6 state.

A simplification, by only using the Mg/Si atomic ratio, splits the different hardness evolution behaviours in three regimes :

- First, when Mg/Si ≤ 0.1: the strengthening is very low and very slow. The hardness peak is very large.
- Then, with $0.7 \leq$ Mg/Si ≤ 3.1: the strengthening is important and fast. The hardness peak is narrow.
- And finally, with Mg/Si ≥ 3.8: the strengthening is less important and slower. The hardness peak is large.

This precipitation hardening interpretation are complicated because the graded materials have at the same time a variation of Si and a variation of Mg_2Si. Si and Mg_2Si are known to be both involved in the rise of mechanical strength. There is here certainly an interference between these two aspects. Some compositions, not represented on this gradient, would have brought complementary information for a proper overview and interpretation of the hardness results.

2.2.2 Continuous heating DSC analyses

To analyse the precipitation sequence along these graded materials, differential scanning calorimetry (DSC) is used. The standard analysis are following a heating rate of 5 °C/min from −25 °C to 550 °C. Further information concerning this method is detailed in Appendix B. For this technique, the interpretation of the peaks (nature of precipitation/dissolution) is based on the characterisations during interrupted treatments from literature presented in **section 2.1.3.2**.

A new compositional gradient sample (B) is used for DSC analysis. On the next Figure 2.20, the WDS fitted SS compositions of Mg and Si are presented along the sample position.

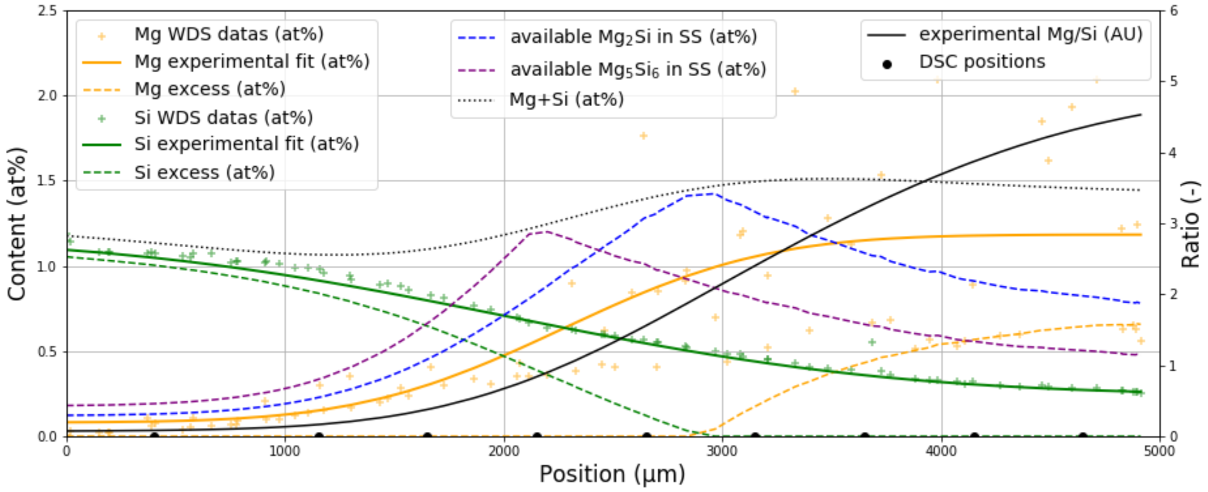

Figure 2.20: WDS solid solution composition of a gradient of an Al-1.2.wt%Si Al-2.6wt%Mg diffusion couple after 10 days homogenisation at 550 °C and water quench.

Sample B is different from sample A of the previous paragraph. The Mg data have a wider deviation around the mathematical fit. By still considering that fit, there is a bit less Mg content on the Mg edge (1.2 at.% against 1.3 Figure 2.15). The maximum content in Mg_2Si and in Mg_5Si_6 are therefore slightly lower but still approximately positioned in the same way: Mg_2Si at 2200 µm and Mg_5Si_6 at 2900 µm.

Table 2.7 is recapitulating those compositions for the 9 studied slices. The slices are assumed to be homogeneous. The compositions are also presented on the 200 °C isothermal section of the ternary diagram Figure 2.16.

The DSC thermograms are gathered in the Figure 2.21. On each curve, between 2 and 4 exothermic pics are present until 450 °C.

Position (μm)	At. Mg/Si	Available β (at.%)	Mg excess (at.%)	Si excess (at.%)
400	0.08	0.13	-	1.00
1150	0.17	0.23	-	0.84
1650	0.38	0.45	-	0.65
2150	0.84	0.84	-	0.39
2650	1.56	1.28	-	0.12
3150	2.40	1.32	0.18	-
3650	3.20	1.08	0.43	-
4150	3.87	0.91	0.57	-
4650	4.35	0.82	0.64	-

Table 2.7: WDS solid solution composition of a gradient of an Al-1.2.wt%Si Al-2.6wt%Mg diffusion couple after 10 days homogenisation at 550 °C and water quench.

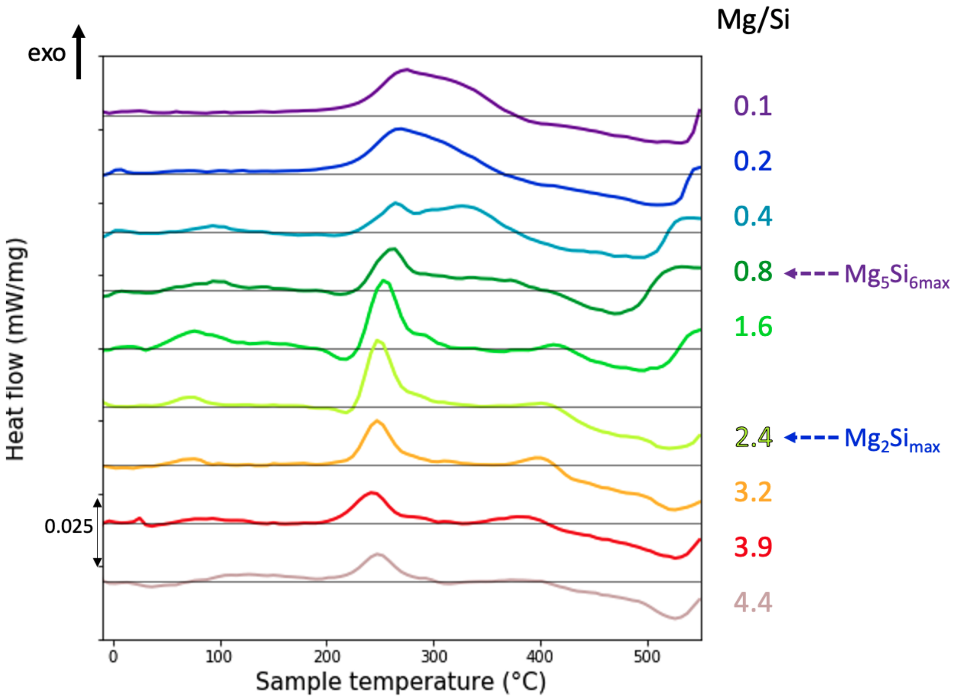

Figure 2.21: DSC thermograms on 9 homogeneous slices along a gradient of an Al-1.2.wt%Si Al-2.6wt%Mg diffusion couple after 10 days homogenisation at 550 °C and water quench.

2.2.2.1 Pure Si precipitation

For the four first DSC curves (Mg/Si $\leq$ 0.8), precipitation of pure Si is predicted by the thermodynamic database TCAL4 with a maximum content near 0.12 wt.%. For 1.6 $\leq$ Mg/Si $\leq$ 3.2, maximum precipitation of Si is not significant ($\leq$ 0.03 wt.%). Finally, for Mg/Si $\geq$ 3.9, no Si precipitation is expected.

On the DSC curves of slices with Mg/Si = 0.1 and 0.2, the large exothermic peak near 300 °C is certainly an overlapping of two precipitation peaks. The first one, at the lowest temperature, should correspond to a metastable precipitate of the β family and the second one to pure Si. For $0.4 \leq$ Mg/Si ≤ 0.8, the two peaks are now separated and the one corresponding to Si is fading away.

The precipitation peak of the stable phase Si lies between 290 and 310 °C for the very strong excess of Si. It is shifting until 350 °C with Mg/Si = 0.8 and is disappearing with the rise of Mg in the sample.

Si precipitation is appearing earlier with the increase of Si in the sample and the decrease of available Mg_2Si in SS. Indeed, with less Mg and Si in the sample, less metastable phases are formed and the thermal energy provided by the DSC heating is available for the formation of these stable Si precipitates. In the same way, dissolution (endothermic peak) is also appearing earlier with the decrease of Mg/Si ratio.

2.2.2.2 Clustering

The small peak, that appears for Mg/Si > 0.2 between 75 and 100 °C, could be related to the first stage of precipitation: clustering. With the rise of Mg/Si, this exothermic transformation appears before and its integral is greater (the volume fraction of phase transformation is higher).

The highest integral is measured for Mg/Si = 1.6 (with a Si excess of 0.1 at.%). Indeed, coherent phases (clusters, GPZ and β") have, in general, a composition with a Mg/Si ratio near 1 (literature review **section 2.1.1.1**). Their greater volume fraction will be thus measured for this composition.

The earliest peak is measured for Mg/Si = 2.4 which corresponds to an excess of Mg of 0.2 at.%.

There is a more consequent and a faster clustering until some limiting Mg/Si values (1.6 and 2.4 respectively).

2.2.2.3 Coherent precipitation

The second exothermic reaction seems to be present for all the slices but overlapping with a third close exothermic peak can bring confusions. This peak represents more advanced coherent phases (GPZ and β").

This second peak starts at 280 °C for Mg/Si = 0.1. Then, with the rise of Mg/Si until 3.9, it is shifting down to 240 °C.

The maximum amplitude of that peak is observed for Mg/Si = 1.6. The observed peak integral is actually underestimated. Indeed, dissolution of clusters (endothermic) towards formation of β" (exothermic) can inhibit the emission of heat due to the cancellation of those thermal behaviours. Therefore some β" formations are not represented on the thermograms. Given the amplitude of clustering peak for Mg/Si = 1.6, the maximum volume fraction of β" is still reported for that composition. This composition is not actually the nearest ratio to β" chemistry but Si precipitation (at Mg/Si = 0.8 for example) could actually decrease the truly precipitating Mg_5Si_6 amount which changes the predicted curve from Figure 2.20 and shifts the maximum value to higher Mg content (Mg/Si > 1).

There is a more consequent precipitation of coherent phases (GPZ or β") with the rise of Si excess until a value of Mg/Si which should be around 1.6. There is also a faster precipitation of these metastable phases with the decrease of Si until a strong Mg excess threshold of Mg/Si = 3.9. Additional values for highest Mg excess (Mg/Si > 4.4) would have permitted to conclude more surely on that tendency and value. It is striking though that Mg+Si content in SS is actually almost maximum at this composition (Figure 2.20).

2.2.2.4 Semi-coherent precipitations

The coherent precipitation peaks often present a shoulder on the right (slightly before 300 °C), which is actually a second smaller peak hidden by the overlap. This shoulder represents semi-coherent phases precipitations. It is clearly visible for Mg/Si = 1.6. An asymmetry of the peak is certainly also that same kind of shoulder: Mg/Si = 2.4 to 4.6. The compositions with Mg/Si ratio inferior to 1.6 certainly still present that shoulder but the Si precipitation peak is unfortunately hiding that information.

After this shoulder (above 300 °C), thermal variations are very small. It is therefore hard to interpret the data. Indeed, for Mg/Si $\geq$ 1.6, a plateau is present until the main dissolution peak. This plateau could be either an absence of events or, more likely, the endothermic and exothermic events succession identified as the continuation of the precipitation sequence (semi-coherent and non coherent phases) until full dissolution.

2.2.2.5 Summary of the continuous heating DSC results

Clustering kinetic is accelerated with the increase of Si from strong Mg excess compositions and with the increase of Mg from Si excess compositions until the composition of Mg/Si = 2.4 (near maximum content of Mg_2Si).

Mechanical strength is related to β" precipitation. As presented the faster coherent precipitation is occurring for Mg/Si = 3.9. Generally speaking, precipitation of coherent (and semi-coherent) phases is delayed with the increase of Si. The greatest formation of coherent phase is achieved for Mg/Si = 1.6 (near maximum content of Mg_5Si_6).

These results are consistent with the hardness results. Indeed, the highest hardness peak was obtained with maximum Mg+Si content in SS and here Mg/Si = 3.9 is as well near that maximum Mg+Si content. Then, the second hardness maximum presented a ratio similar to 1.6 (Mg/Si = 1.2 not represented here).

As expected from literature [TAK 96], semi-coherent peaks were not properly separated from coherent peaks even for Si excess. Indeed, as presented in the literature review (**section 2.1.3.2**) with Gupta *et al.* [GUP 01] Figure 2.13, Mg_2Si contents were too low.

2.2.3 Precipitation during isothermal DSC

An isothermal treatment at 170 °C was conducted within the DSC, as it is close from the reality of ageing in Al-Mg-Si alloys. Further information concerning this method is detailed in Appendix B. The interpretation of the thermal events is here only based on the previous standard DSC analysis.

Figure 2.22 gathers the isothermal DSC measurements on the same sample B used in the previous part. Composition profiles are presented in Figure 2.20 and the specific composition data of each homogeneous slice is recapitulated Table 2.7.

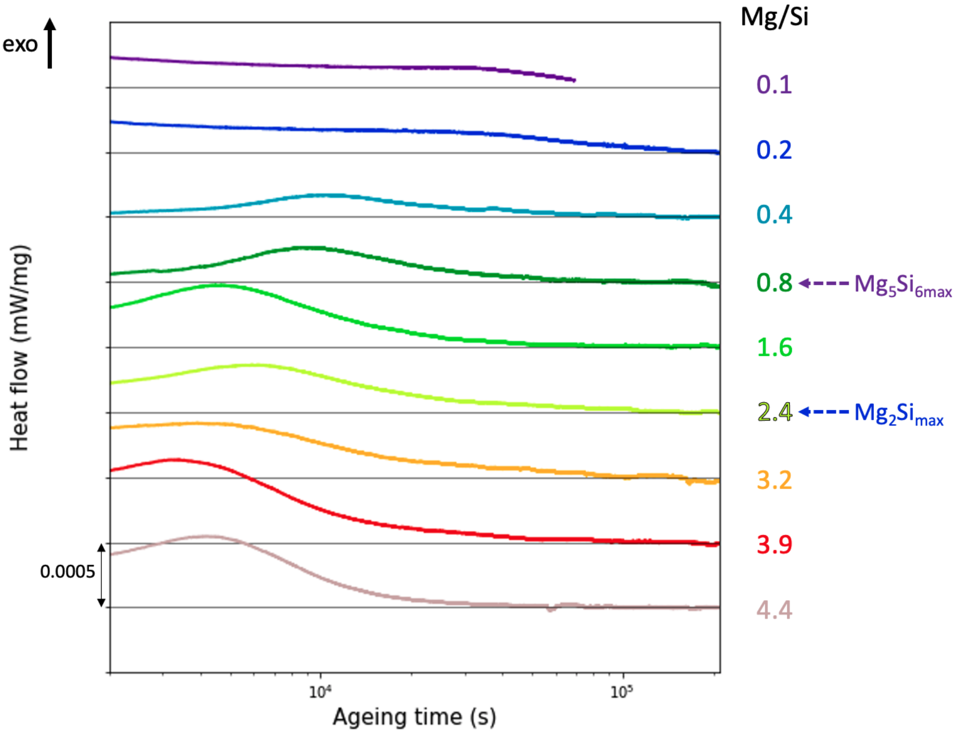

Figure 2.22: DSC thermograms during isothermal treatment at 170 °C on 9 homogeneous slices along a gradient of an Al-1.2.wt%Si Al-2.6wt%Mg diffusion couple after 10 days homogenisation at 550 °C and water quench.

The isothermal DSC thermograms are separated in three types depending on the composition of the sample. The nature of the precipitating phase is deducted from the previous non-isothermal DSC analysis.

- Mg/Si $\leq$ 0.2: slow and main precipitation of pure Si
- Mg/Si $\geq$ 1.6: maximum precipitation formation of metastable phases of the β family is before 2 h
- 0.4 $\leq$ Mg/Si $\leq$ 0.8: maximum precipitation formation of metastable phases of β is delayed after 2 h

Two compositions show faster kinetics and have the maximum amplitude recorded regarding to their composition neighbours. The faster and highest peak is the one having a composition of Mg/Si = 3.9. Its time to the maximum amplitude is 50 min. The other one has a composition with Mg/Si = 1.6 and its peak is maximum at 70 min.

These two distinctive compositions are joining the noteworthy ones obtained from continuous heating DSC experiments. These results are in the same way as presented before in good agreement with those found with maximum hardness values during interrupted treatments (on a different graded sample). The wide deviation of Mg content data for high content of Mg (Figure 2.20) around the proposed fit must be kept in mind. The uncertainty on the initial SS composition on Mg-side is quite important. Mg_2Si content (or Mg+Si) in SS and Si excess are, for DSC and hardness experiments, important parameters that enhance precipitation (faster and stronger).

This first attempt of isothermal DSC experiment is relevant. It is important to note here also that repeatability measurements were not perfectly conclusive and should be re-conducted on new samples. It would be also preferable to have more compositions between those 9 compositions, especially around the important composition of Mg/Si = 1.6.

2.3 Influence of composition on precipitation states

In this section, the composition influence on different precipitation states is studied. First, Anomalous Small Angle X-ray Scattering (ASAXS) analyses on rolled samples, aged at 170 °C at 5 different ageing times, give an overview of the precipitates mean diameter variation. Then, a focus is made on 2 ageing times with Transmission Electron Microscopy (TEM) techniques. In total 7 positions at different compositions were investigated in order to identify the precipitates and deepen the knowledge on their size and shape. In addition, two states have been investigated using Atom Probe Tomography (APT). This investigation procedure is represented in Figure 2.23.

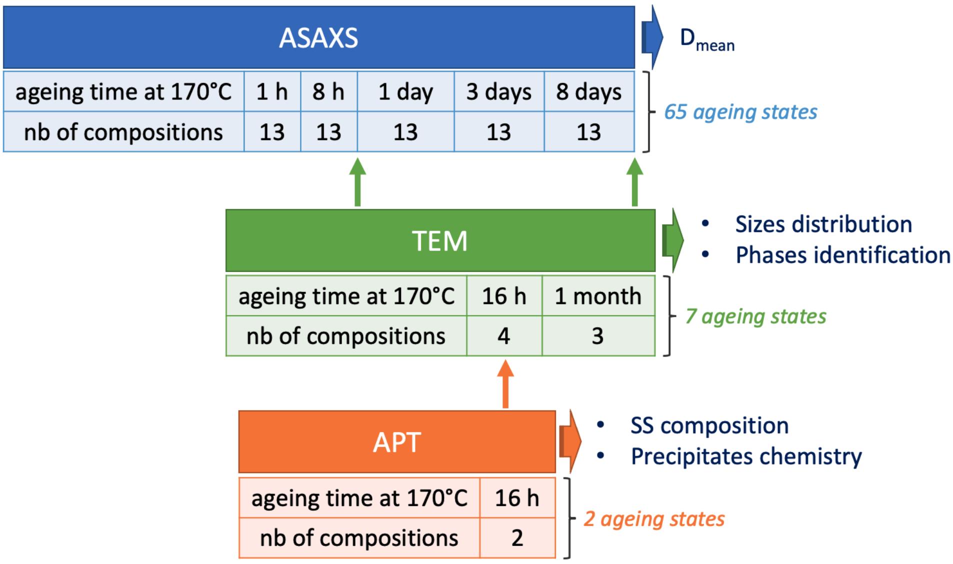

ageing time at 170°C	1 h	8 h	1 day	3 days	8 days
nb of compositions	13	13	13	13	13

ageing time at 170°C	16 h	1 month
nb of compositions	4	3

ageing time at 170°C	16 h
nb of compositions	2

Figure 2.23: Precipitation states investigation and results obtained from each characterisation techniques

The compositions of the ageing states studied by TEM and APT are reported on a 200 °C isothermal section of the ternary diagram in Figure 2.24.

2.3.1 Overview of the mean diameter variation during ageing using ASAXS

Thanks to ASAXS, mean equivalent diameter of the rod type precipitates could be extracted along the gradients. Further information concerning this method and sample preparation is detailed in Appendix B. It must be emphasised that these low-energy ASAXS measurements were exploratory, actually the first ones of the kind.

2.3.1.1 Accuracy of the measured diameters and protocol for data treatments

In order to verify the accuracy of extracted (rod type precipitate) diameters from ASAXS, Al 6xxx homogeneous samples from two previous PhD thesis [MEY 18a, BAR 08] were characterised as well. In their studies, precipitates mean diameters were measured using TEM for a

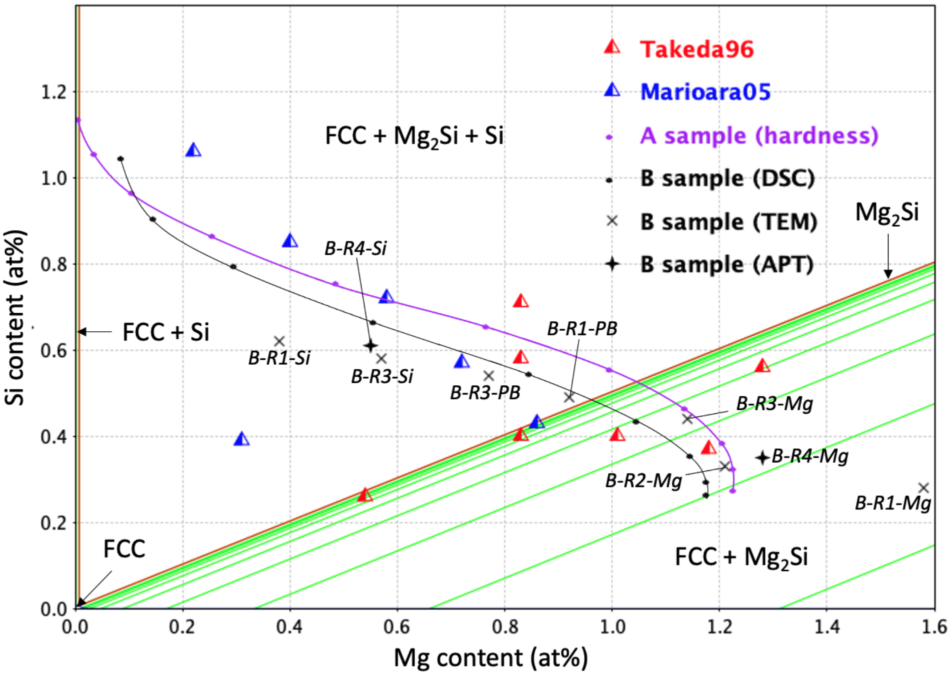

Figure 2.24: Representation of the studied compositions on 200 °C isothermal section of ternary phase diagram depending on the characterisation techniques used

specific state.

In Figure 2.25, mean ASAXS diameter are plotted for 4 ageing states at 170 °C for an Al6351 with a Si excess. For each state, scattering images were acquired at 5 different X-ray energies (E1 - E5) detailed in Appendix B.

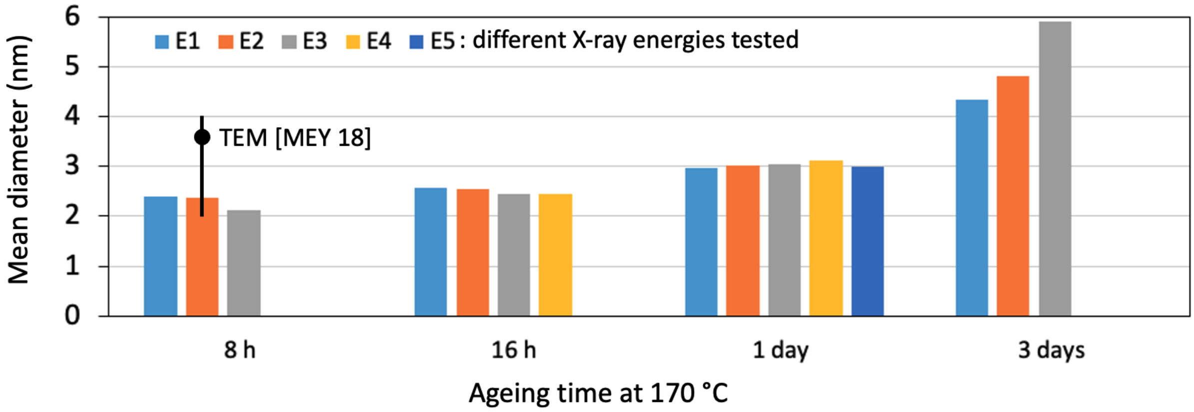

Figure 2.25: Precipitates mean diameter evolution measured by SAXS at different ageing treatments at 170 °C for an Al-1.0Si-0.6Mg-0.1Fe-0.2Mn homogeneous sample in at.%. 5 different X-ray energies are tested.

As ageing occurs, the mean diameter of precipitates is increasing, from 2 to 5nm. The value is stable for the different energies used except for the sample at 3 days. The TEM diameter measured by Meyruey on a sample aged at 8 h is at 3.6 nm with a distribution between 2 and 4 nm. There can be two reasons for over-estimation during statistic conventional TEM measurements: the 2D stereographic projection of a 3D object and measurement bias because small precipitates are harder to see and measure.

On the next Figure 2.26, precipitates diameter extracted by ASAXS are plotted in the same way. The results of the 6061 Al alloy are presented for 3 ageing states at two different temperatures: 170 and 250 °C.

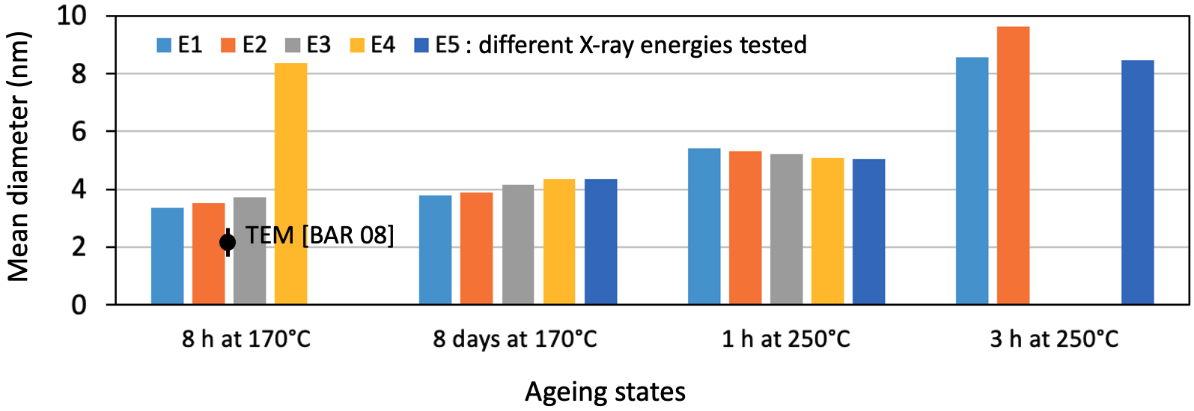

Figure 2.26: Precipitates mean diameter evolution measured by SAXS at different ageing states for an Al-0.6Si-1.0Mg-0.12Cu-0.13Fe-0.1Cr-0.06Mn homogeneous sample in at.%. 5 different X-ray energies are tested.

After 8 days at 170 °C, that sample has precipitates with an average diameter of 4 nm. For a shorter ageing of 8 h at 170 °C, the values found by ASAXS are not that stable for all the energies used. If the E4 value is excluded, the mean diameter perceived is of 3.5 nm. For 8 h at 175 °C, Bardel found mean diameters around (2.0 ± 0.3) nm with TEM and of (1.7 ± 0.3) nm with SANS. The values proposed by ASAXS for the same state are above these values but they still seem plausible. After 1 h at 250 °C, the values are stable but no longer for 3 h.

All the X-ray energies on each sample did not provide proper scattering images to extract precipitates mean diameter. From all the energies, E1 and E2 have the most stable and coherent diameter values. The measurable diameters by this ASAXS experimentation are situated between [2;5] nm. The next mean diameters presented will be a mean value of the two values obtained from both energies E1 and E2. The variation of precipitates mean diameter in the different samples are quite small (some nm). Hopefully the uncertainties, from square deviation, calculated between the two values is even smaller due to the stability of the results between 2 and 5 nm.

2.3.1.2 Measured diameters for the graded samples

ASAXS measurements were then successfully performed on five Mg-Si graded rolled slices extracted from the same bulk sample (C). Each slice gradient was aged at different states: 1 h, 8 h, 1 day, 3 days and 8 days at 170 °C. The EDX composition profiles of these samples are presented in Appendix C. Unfortunately, profiles of Mg_2Si and of excesses content in SS show some differences from one sample to another. And, more important, those values count a non negligible uncertainty which is due to the sample preparation. Especially on Mg-rich side for Mg content. Relative uncertainty of the Mg/Si ratio is therefore calculated with $\Delta x_{\mathrm{Si}} = 0.05\%$ and $\Delta x_{\mathrm{Mg}} = 0.2\%$.

The SAXS results are presented regarding to Mg/Si atomic ratio Figure 2.27.

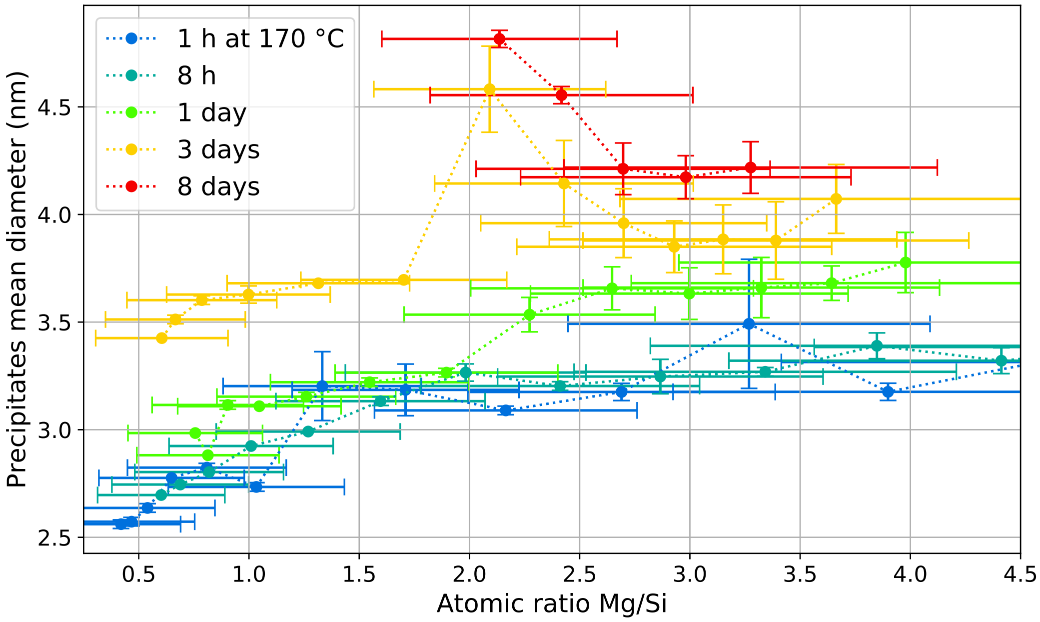

Figure 2.27: Precipitates mean diameter evolution measured by SAXS for the first two energies (E1 and E2) at different ageing treatments at 170 °C for different compositions (Mg/Si ratio) along gradients of an Al-1.2.wt%Si Al-2.6wt%Mg diffusion couple.

After 1h at 170 °C, two families of precipitates are present along the gradient. For compositions with Mg/Si ≤ 1.1, the mean diameter of the precipitates are between 2.5 and 3 nm. For compositions with Mg/Si above 1.1, the precipitate diameters are higher, between 3 and 3.5 nm.

While ageing continues, precipitates are growing slowly. After 3 days, on Mg-rich side, precipitates have now a mean diameter around 4 nm and on Si-rich side, it is near 3.5 nm. Diameter growth has occurred faster in the middle of the sample. Indeed for Mg/Si between 1.7 and 2.7, the mean diameter rises up to 4.5 nm.

For compositions with Si excess (Mg/Si < 2), at any ageing state, the precipitates mean diameter is increased with Si decrease. As described by Marioara *et al.* [MAR 05], precipitates are smaller with strong Si excess. All the precipitates present are taken in consideration though, even pure Si precipitates. If those precipitates are present and are really small they could lower the mean diameter even if the metastable precipitates of β are not smaller.

In the literature, to the author's knowledge, only Chang *et al.* [CHA 15] measured precisely the diameter of precipitates in a model Al-Mg-Si alloy with Si excess (0.43wt.%Mg-0.47wt.%Si). *In-situ* SANS experiments, during ageing at 180 °C, described an evolution from 3.6 to 4.4 nm of the mean diameter between 1 and 18 h. Those results can be compared with ours of compositions with Mg/Si near 1. The mean diameter evolved here from 2.7 to 3.1 nm. The results are not perfectly correlated. From previous state of the art, Mg_2Si content seems to be also playing an important role in the precipitates diameters. Indeed alloys with similar Mg/Si ratio had diameter differences [DON 98, AND 98]. One of the reasons could be the difference of content in Mg_2Si available in SS. Precipitates diameter should be smaller when there is more Mg_2Si content in the alloy. It seems coherent that more precipitates nucleate with large amount of Mg_2Si and that for fewer amount, the ones present use the remaining solute to grow. Now, in our samples, for Mg/Si near 1 aged during 1 h, 8 h or 1 day, Mg_2Si content was measured around 1.1 at.%. Whereas, in Chang's samples only 0.7 at.% of Mg_2Si is available, confirming this theory.

This last feature highlights the importance of Mg_2Si content on the evolution of precipitates diameters even if that varying parameter is not represented here. Caution must be taken though where those contents are the most changing in our gradients: in the centre and on the edges (Appendix C). Especially on the edges, the Mg_2Si content is decreasing. Therefore, precipitates diameters should increase. This is maybe what we are observing on Mg-rich side for some samples. On Si-rich side, the opposite strong Si influence is certainly hiding the Mg_2Si influence.

Now, let's focus on the general composition influence on precipitates diameters depending on the ageing situation. The ASAXS study along the graded samples shows two regimes. One is linear after 8 h of ageing at 170 °C; precipitates diameters rise with Mg content. The other one presents in addition a bump for pseudo-binary and near pseudo-binary compositions after 3 days at 170 °C; larger precipitates are observed for Mg/Si near 2.

By combining (rounded) values from microhardness, DSC and ASAXS: different precipitation kinetics regimes were enlightened during ageing at 170 °C:

- under Mg/Si $= 0.3$: extreme Si excess, main precipitation of pure Si, no major improvement of properties, delay of precipitation, very small mean diameters
- $0.4 \leq$ Mg/Si ≤ 1: strong Si excess (Si), still pure Si precipitation, improvement of hardness, small delay of precipitation but not of hardening, small mean diameters at the beginning of ageing
- $1 \leq$ Mg/Si ≤ 3: near pseudo-binary compositions (PB), could present remains of pure Si precipitation, maximum improvement of hardness, faster hardening, important variation of mean diameters and initial mean diameter quite large
- Mg/Si > 3: strong Mg excess (Mg), improvement of hardness, slow hardening but fast

semi-coherent precipitation, initial mean diameter quite large

To deepen this investigation, specific precipitation states will be characterised (precipitates and solid solution) in three of these domains (Si, PB, Mg). First, for two ageing times at 170 °C (16 h and 1 month) with TEM and then, by APT for the T6 state (16 h).

2.3.2 Focus on two ageing times using TEM

Precipitates at different ageing states were also analysed using TEM analysis. With conventional TEM, diameter and length of the rod type precipitates are statistically analysed. The uncertainties presented on the extracted mean dimensions are square deviations upon all the measurements provided from the different images. High-Resolution (HR) TEM analyses were also performed in order to identify the present precipitates. Further information concerning this method and sample preparation is detailed in Appendix B.

In this part, three rolled samples were used with the same manufacturing conditions as previously. Their content profiles are recapitulated in Appendix C. The bulk sample from which they are coming from is the same bulk as the non rolled sample B used for DSC characterisations.

Only some specific positions (sites) in the gradient were analysed by TEM. Their compositions and their ageing stages are recapitulated in Table 2.8. These sites positions are presented within their respective gradients in the Appendix C. The name of each site is here specifying: the sample (B), which slice is referring to (1-3), if this slice has been rolled (R) and the position in the gradient: Si for strong Si excess domain, PB for near pseudo-binary domain or Mg for strong Mg excess domain. These domains have been identified according to the relevancy of the different domains observed from the previous precipitation characterisations (hardness, DSC and ASAXS). For example, the site B-R1-PB was situated in the pseudo-binary (PB) area of the rolled slice 1 (R1) extracted from the bulk B (B).

Name	Site composition (at.%)						Ageing at 170 °C	
sample-position	Mg	Si	Mg_2Si	Mg excess	Si excess	Mg/Si	Time	State
B-R1-Mg	1.6	0.3	0.8	1.0	-	5.6	16 h	pre-T6
B-R2-Mg	1.2	0.3	1.0	0.6	-	3.7	16 h	pre-T6
B-R3-Mg	1.1	0.4	1.3	0.3	-	2.6	30 days	over-aged
B-R1-PB	0.9	0.5	1.4	-	0.03	1.9	16 h	slightly over-aged
B-R3-PB	0.8	0.5	1.2	-	0.15	1.4	30 days	over-aged
B-R3-Si	0.6	0.6	0.9	-	0.3	1.0	30 days	over-aged
B-R1-Si	0.4	0.6	0.6	-	0.4	0.6	16 h	T6

Table 2.8: EDX solid solution composition of the different TEM sites extracted from graded samples of an Al-1.2.wt%Si Al-2.6wt%Mg diffusion couple after 10 days homogenisation at 550 °C, water quench and their specific ageing states.

B-R1 and B-R2 samples were prepared using electro-polishing. These preparations were complicated. Only a few images could be analysed. Therefore, B-R3 over-aged sites were extracted using FIB technique. However, unfortunately, surface amorphization occurred for two specimens: B-R3-Mg and B-R3-PB and prevented the proper HR-TEM analyses of their precipitates.

2.3.2.1 Near T6 states

Size information

In Figure 2.28, conventional TEM images of the different specimens aged at 170 °C during 16 h orientated along (100) Al axes and viewed along a <100>Al zone axis are presented. Three families of precipitates are observable: two lied down and one on top view.

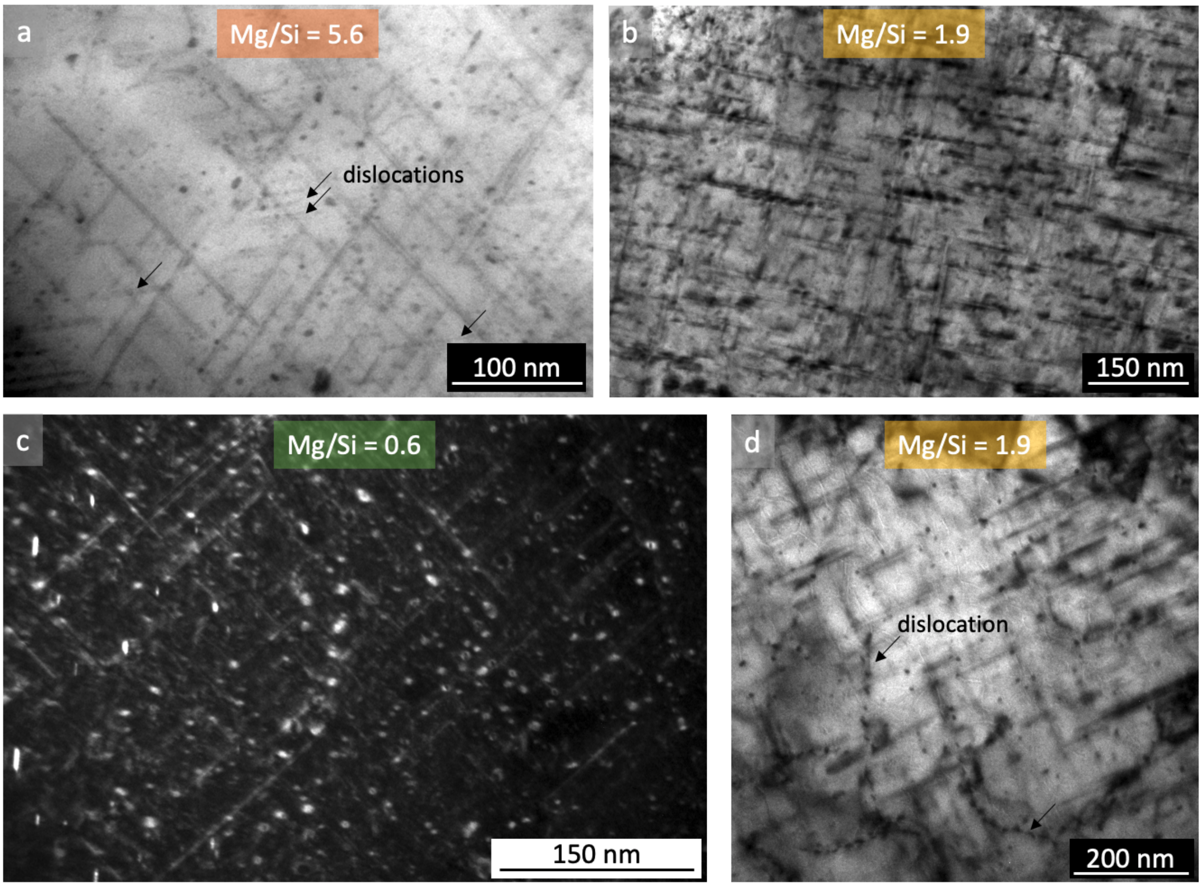

Figure 2.28: Conventional TEM images of precipitates with an ageing treatment of 16h at 170 °C for different sites of the gradients. a: B-R1-Mg (not perfectly orientated), b and d: B-R1-PB in bright field, c: B-R1-Si in dark field

On Figure 2.28a (not perfectly orientated), the analysed site has a composition with an excess of Mg (Mg/Si = 5.6). According to the previous micro-hardness results, after 16 h at 170 °C, this state should be in a pre-T6 stage. The elongated precipitates are quite long and thin. Some standing precipitates seem to be aligned along what should be dislocations on a third orientation in the picture's plane (arrows). Only one type of precipitates appears to be present. Similar TEM images were analysed in order to measure the distribution of sizes of those precipitates.

The results are presented Figure 2.29. 17 precipitates were used for diameter measurements and 19 for the length. The mean diameter is (2 ± 1) nm and the mean length is (150 ± 50) nm.

The sample presented in Figures 2.28b and d has almost a pseudo-binary composition (Mg/Si = 1.9). This state is here slightly over-aged. The elongated precipitates seem long and thicker (only due to the elastic distortion). Only one type of precipitates seems present as well here. In Figure 2.28d, some standing precipitates are clearly aligned on dislocations (arrows). Numerous measurements on various pictures show, on Figure 2.29, that they are not thicker and that they have a wider length range than the previous state. The statistic analysis were here performed on 28 precipitates regarding to the diameter and on 33 precipitates for the length. The mean diameter obtained is (2 ± 1) nm and the mean length is (150 ± 60) nm.

The microstructure presented Figure 2.28c in dark field is a bit different. The composition of this sample has a strong excess of Si (Mg/Si = 0.6). According to microhardness results, after 16 h, it is here a T6 state. The elongated precipitates seem thin but the standing precipitates show a wide range of diameters distribution. These results are represented and compared with the other states in Figure 2.29. They have larger diameters and shorter lengths. The statistical analysis was performed on 46 precipitates for the diameter and on 16 precipitates for the length. The mean diameter is (3 ± 1) nm and the mean length is (80 ± 50) nm.

Figure 2.29a, after 16 h at 170 °C, the diameter results show good agreement in order of magnitude (few nm) with ASAXS measurements but the tendancy observed is opposite. Indeed, from TEM images the diameter slightly increases with the content in Si and not with the Mg content. Several aspects have to be taken in consideration. First, the quality of the conventional images was not high enough to perform more elaborated statistical analyses. Then, the extreme composition of the Mg-rich sample with a very important excess of Mg (Mg/Si = 5.6) has not been analysed by ASAXS and therefore can not be correctly compared. Figure 2.29b, the length is increasing as well with the content in Mg but, the wider distribution is observed for the pseudo-binary alloy.

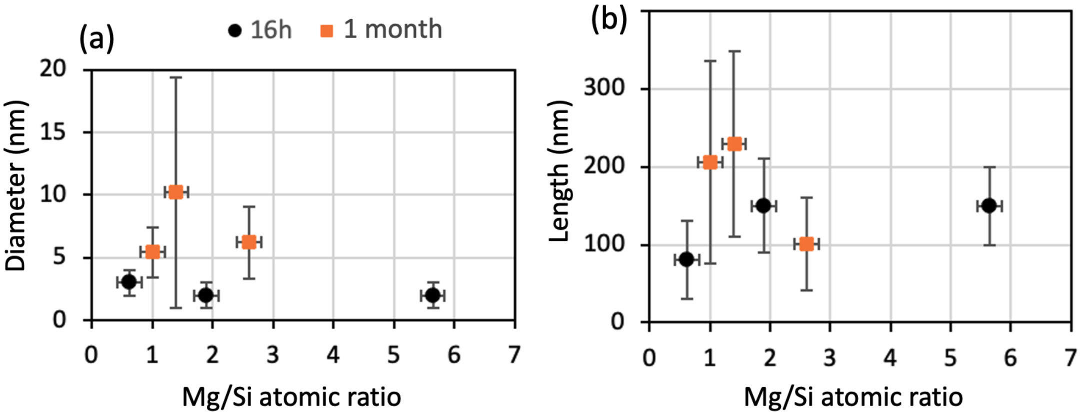

Figure 2.29: Precipitates sizes extracted from TEM conventional images for the different sites aged at 170 °C.

Phases identification

The best observable precipitate from a sample with a mean Mg excess (Mg/Si = 3.7) is presented Figure 2.30a with its diffraction patterns extracted from Fast Fourrier Transform (FFT).

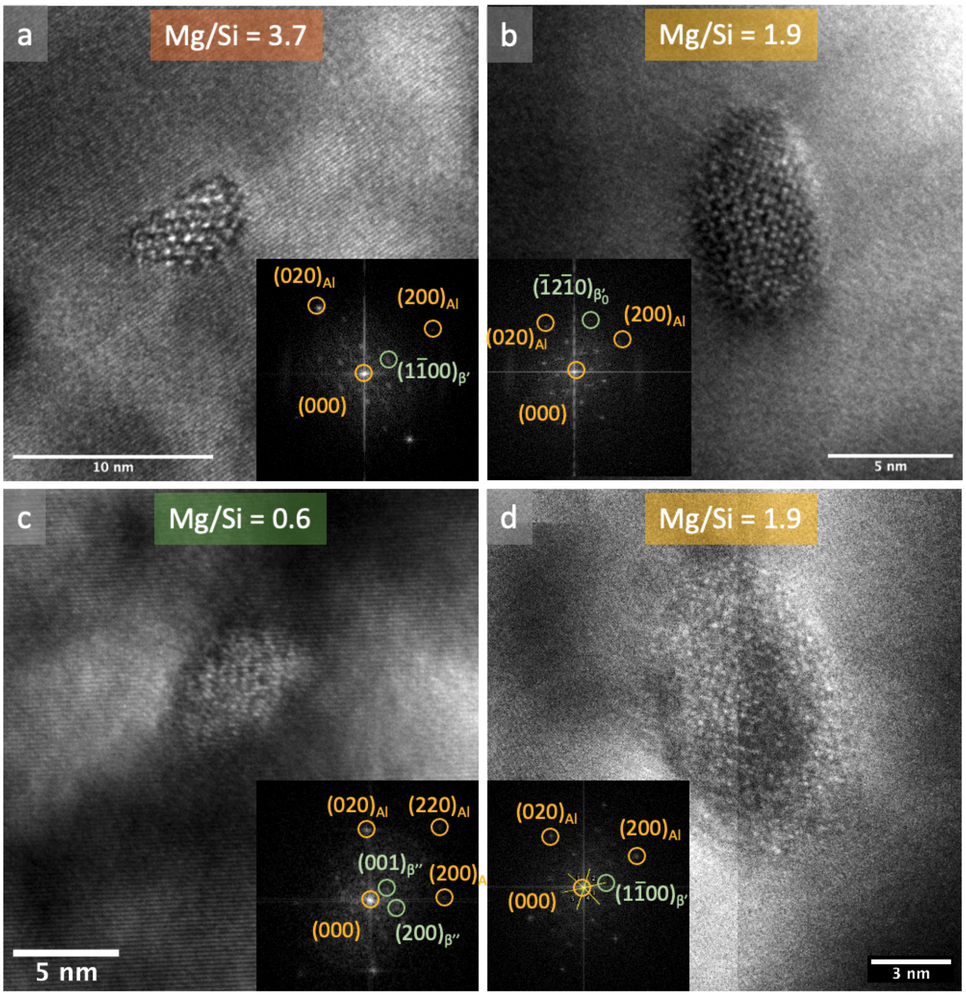

Figure 2.30: HR TEM images and their FFT of precipitates present for an ageing treatment of 16 h at 170 °C for different sites of the gradients. a: B-R2-Mg, b and d: B-R1-PB and c: B-R1-Si

The FFT image permits to identify the metastable precipitate as β'. Indeed, the precipitate hexagonal lattice in FFT presents 6 spots, around the $(000)_{Al}$ stain, regularly positioned with an angle of 60°.

In the near pseudo-binary sample (Mg/Si = 1.9), two kind of precipitates are presented Figure 2.30b and d. The FFT images show a β'_0 precipitate and a β'. The β'_0 has clear distinctions from β' precipitates. First the HR image shows a more unorganised structure and the FFT image present partial extinctions of the first stains in (100).

For the strong Si excess sample (Mg/Si = 0.62), a β” precipitate is clearly identified on the Figure 2.30c. Indeed, the monoclinic lattice presents 6 first stains around $(000)_{Al}$ with specific angles.

The hardness peak (or the T6 state) is related to β” precipitations. For the presented samples, the Si excess site is the only real T6 state (Table 2.8). On that state, β” are indeed observed. The pseudo-binary site is slightly overaged. It is therefore logical to observe β’ precipitates and more especially its early form: β'_0. The β’ precipitates are more surprising when observed on the Mg excess sample. Indeed that sample is, according to the hardness study, in a pre-T6 state. It is not yet to its maximum strength and yet has already β’ precipitates. The high lengths advanced for Mg excess and pseudo-binary states are compatible with the identification of β’. There is certainly though a mix of this semi-coherent phase β’ and β”. Indeed, at the hardness peak, few semi-coherent phases are expected. β” is also smaller and therefore more complicated to identify with HR-TEM.

The Table 2.9 is recapitulating the precipitates information extracted from TEM regarding these studied T6 and near T6 states.

Domain	Mg/Si	diameter (nm)	length (nm)	possible phases
Strong Mg excess (Mg)	5.6	(2 ± 1)	(150 ± 50)	-
	3.7	-	-	β’ (+β”)
Near pseudo-binary (PB)	1.9	(2 ± 1)	(150 ± 60)	β’ + β_0’ (+ β”)
Strong Si excess (Si)	0.6	(3 ± 1)	(80 ± 50)	(β' +) β”

Table 2.9: Summary table of T6 and near T6 states information extracted from TEM

2.3.2.2 1 month overaged states

Size information

In Figure 2.31, conventional TEM images of different sites aged at 170 °C during 1 month orientated along (100) Al axes and viewed along a <100>Al direction are presented.

On Figure 2.31a, the analysed specimen has a composition with a small Mg excess (Mg/Si = 2.6). The elongated precipitates seem to have large diameters and mean lengths. The top viewed precipitates are not that circular. Distribution of diameter and length were extracted from several similar images and are presented in the Figures 2.32a and 2.33a. The mean dimensions were then plotted on the summary Figure 2.29.

In this Mg-rich site, the majority of precipitates have a diameter included between 3 and 8 nm. Some precipitates have large diameters in general up to 15 nm. The mean diameter equals (6.2 ± 2.9) nm.

This Mg-rich specimen has precipitates with lengths distributed properly around a mean value. The mean length is (101 ± 59) nm. Most of the precipitate lengths are situated between 17 and 150 nm.

The sample presented in the Figure 2.31b has a near pseudo-binary composition (PB domain)

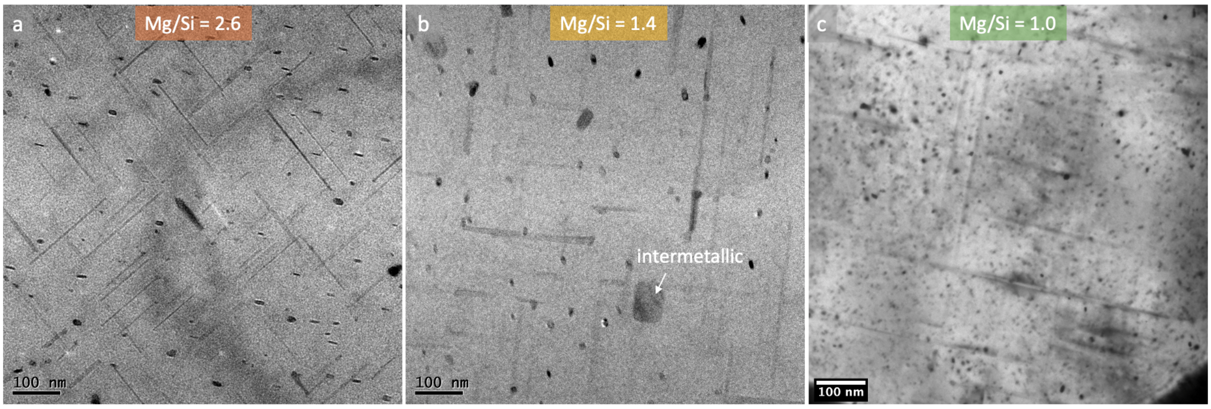

Figure 2.31: Conventional TEM images in bright field of precipitates with an ageing treatment of 1 month at 170 °C for different sites of the gradients. a: B-R3-Mg, b: B-R3-PB and c: B-R3-Si

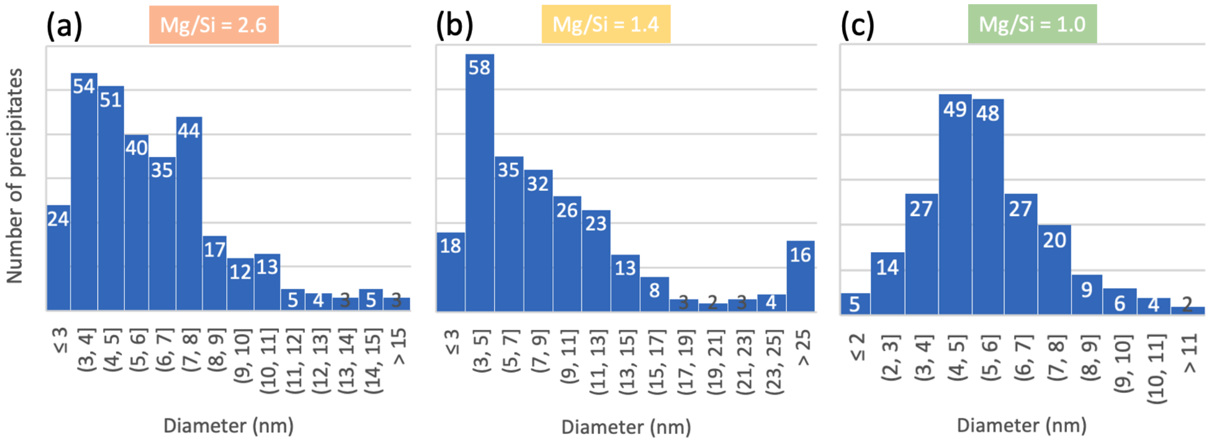

Figure 2.32: Distribution of diameter extracted from conventional TEM images on samples aged during 1 month at 170 °C. a: B-R3-Mg, b: B-R3-PB and c: B-R3-Si

with a small excess of Si (Mg/Si = 1.43). The conventional TEM image show large precipitates in diameter and length. The size distributions are represented Figure 2.32b for diameter and 2.33b for length. The mean dimensions are reported in the Figure 2.29.

The diameter distribution shows two types of precipitates of different diameter sizes. The first one around 4 nm and the second one with large diameter above 25 nm. The small precipitate population is more numerous. By considering both populations, the mean diameter is (10.2 ± 9.2) nm.

By watching the length distribution, this near pseudo-binary sample seems also to have two types of precipitate population: one with a mean length between 100 and 150 nm and the other one with the average length situated between 200 and 250 nm. The major part of the precipitates are between 46 and 300 nm. The mean length is calculated as (229 ± 119) nm.

The third sample, presented in the Figure 2.31c, has an important Si excess (Mg/Si = 1.0). This composition is at the limit between Si (strong Si excess) and PB (near pseudo-binary)

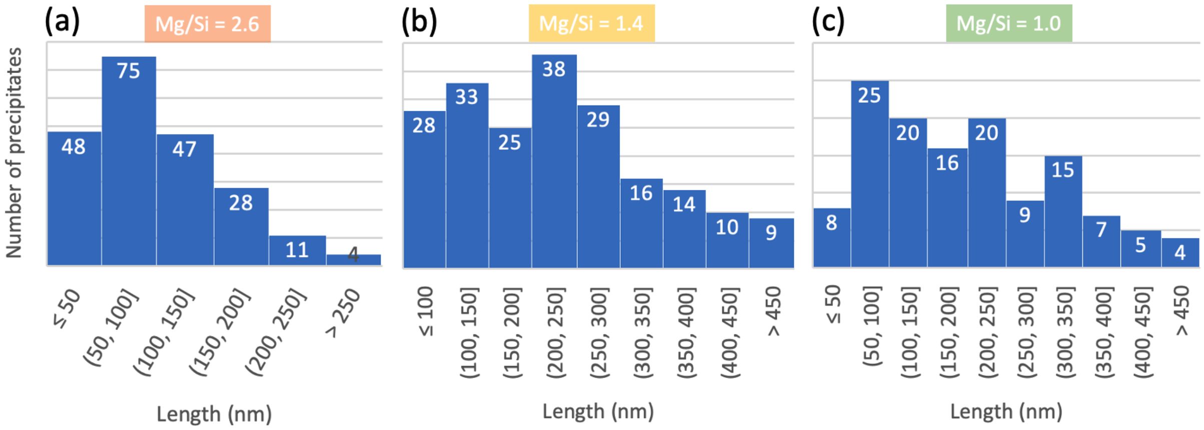

Figure 2.33: Distribution of length extracted from conventional TEM images on samples aged during 1 month at 170 °C. a: B-R3-Mg, b: B-R3-PB and c: B-R3-Si

domains. The main elongated precipitates seem thin and long. Large top viewed precipitates are observable though in specific locations. The size distributions are presented Figure 2.32c for diameters and 2.33c for lengths. The mean dimensions are also reported in the summary Figure 2.29.

That Si-rich sample has, after 1 month, the smallest diameters range of the three samples. The distribution follows a clear Gaussian function. The mean diameter measures (5.5 ± 2.0) nm. The majority of the precipitate diameters do not exceed 11 nm.

The length distribution is a bit more chaotic with 3 specific lengths which stand out: between 50 and 100 nm, between 200 and 250 nm and between 300 and 350 nm. The mean length is calculated at (206 ± 130) nm.

To conclude on that overageing time of 1 month, Figure 2.29a recapitulates the mean diameters of the precipitate. There, a maximum diameter is obtained for the near pseudo-binary composition with a small Si excess (Mg/Si = 1.4). Then, the Mg excess site has larger precipitates than the strong Si excess site. These tendencies are in good correlation with ASAXS observed regime after 3 days of ageing treatment at 170 °C. The values of those diameters, between 5 and 10 nm, are also in good correlation with ASAXS measurements. Indeed, the ASAXS diameters after 3 days are between 3.4 and 4.6 nm. On figure 2.29b, the precipitate lengths are longer for small and strong Si excess compositions than for Mg excess composition.

On this same summary Figure 2.29, the conventional TEM results show that during ageing, Mg-rich precipitates are growing in diameter but less in length. Pseudo-binary precipitates are growing the most in diameter and importantly in length whereas the Si-rich precipitates have grown the most in length and the less in diameter.

Phases identification on Si excess site

After 1 month the large precipitates are now easily identified. Unfortunately, surface amorphization of B-R3-Mg and B-R3-PB prevented their HR TEM analysis. On the next Figure

2.34, three precipitates from the same strong Si excess site (Mg/Si = 1.0) are presented.

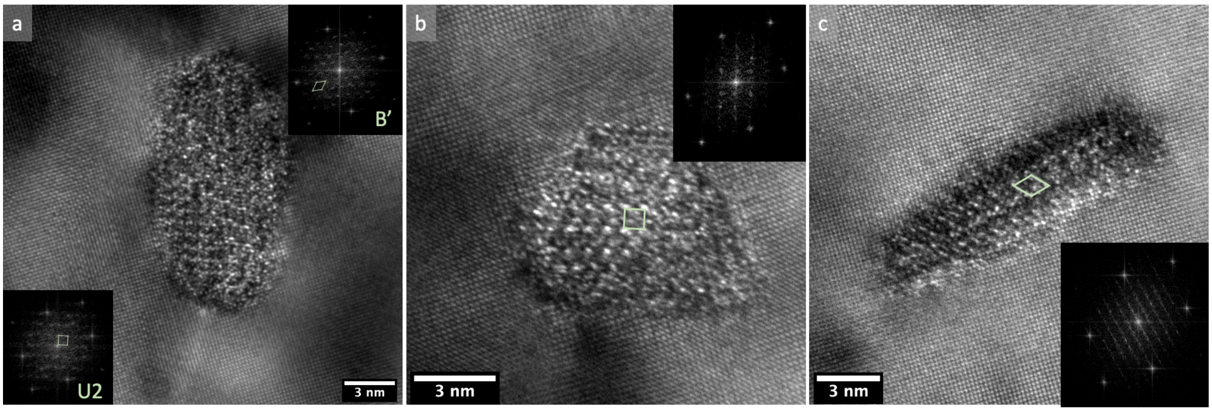

Figure 2.34: HR TEM images and their FFT of three typical precipitates present for an ageing treatment of 1 month at 170 °C for Si excess site (B-R3-Si). a: precipitate presenting two lattice types U2 on the left and B' on the right, b: U2 precipitate and c: B' precipitate

Three types of precipitates are observed : U2, B' and U2-B' precipitates. U2 has an orthorhombic structure oriented on $[100]_{Al}$. This makes it observable as a square. B' is hexagonal as for β' and its morphology is flatten. U2-B' precipitates were already observed by Meyruey *et al.* [MEY 18b] for long ageing times. It is admitted in the literature that B' have a tendency to nucleate on U2 precipitates [MAT 00] (**section 2.1.1.2**), which could be the case here.

Table 2.10 is recapitulating the information extracted from TEM from the 1 month overaged states.

Domain	Mg/Si	diameter (nm)	length (nm)	possible phases
Mg excess (PB)	2.6	(6.2 ± 2.9)	(101 ± 59)	(β')
Near pseudo-binary (PB)	1.4	(10.2 ± 9.2)	(229 ± 119)	(? + ?)
Strong Si excess (Si)	1.0	(5.5 ± 2.0)	(206 ± 130)	U2 + B'

Table 2.10: Summary table of 1 month overaged states information extracted from TEM

2.3.3 Focus on two near T6 states using APT

In order to obtain chemistry informations related to precipitation, atome probe analyses are conducted for 2 specimens on belonging to Mg and the other to Si domains. The observed precipitates chemistry can be precisely measured as well as the solid solution composition surrounding them. Further information concerning this method and sample preparation is detailed in Appendix B.

In this part, one other rolled sample aged 16 h at 170 °C from the same bulk B as previously. This slice name is thus B-R4. Its content profile is recapitulated in Appendix C. Then, two specimen were collected from that gradient, by procedures detailed in Appendix B, and analysed by APT. Their supposed homogeneous composition has an Mg/Si atomic ratio of 3.7 for

B-R4-Mg (Strong Mg excess domain) and 0.9 for B-R4-Si (Strong Si excess domain).

Mg excess specimen

The 130 × 140 × 60 nm^3 probed volume of the Mg excess specimen is presented in Figure 2.35. Two precipitates are visible and their erosion profiles were extracted. The profile of the larger precipitate is presented in the Figure 2.36.

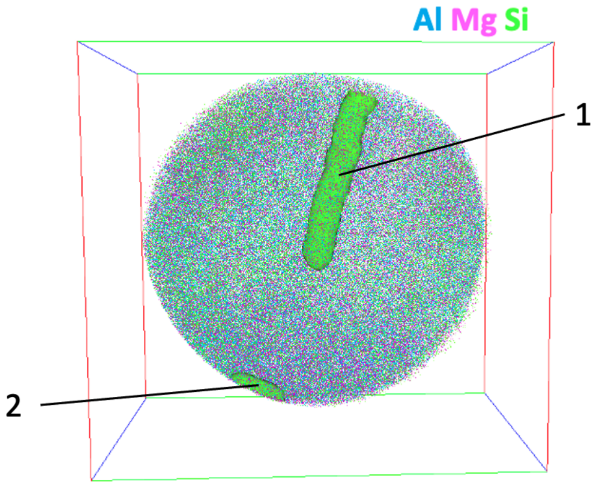

Figure 2.35: APT reconstructed volume of Mg/Si = 3.7 specimen extracted from B-R4-Mg rolled sample. Two precipitates are highlighted with the isosurfaces of 12% Mg+Si.

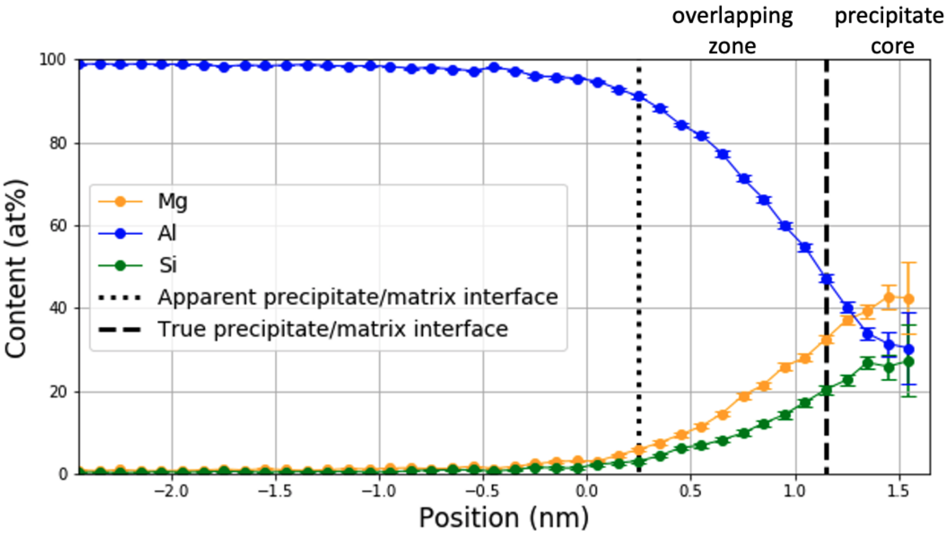

Figure 2.36: APT content profile from the solid solution to the centre of the large precipitate 1 of Mg/Si = 3.7 specimen extracted from B-R4-Mg rolled sample

The compositions of the two precipitates are recapitulated in Table 2.11 with two SS compositions: one before ageing (obtained with EDX) and one after ageing (obtained from APT).

		Al (at%)	Mg (at%)	Si (at%)
As-quenched	SS	98.3 ± 0.2	1.3 ± 0.2	0.4 ± 0.1
Aged 16h at 170 °C	SS	98.84 ± 0.04	0.76 ± 0.02	0.40 ± 0.05
	Precipitate 1	17.3 ± 0.3	52.0 ± 0.5	30.7 ± 0.4
	Precipitate 2	25.7 ± 1.1	42.3 ± 1.3	32.0 ± 1.2

Table 2.11: Compositions of the Mg/Si = 3.7 specimen extracted from B-R4-Mg rolled sample

The atomic ratio of the precipitates are Mg/Si = 1.7 for precipitate 1 and Mg/Si = 1.3 for precipitate 2. More precipitates needed to be observed to have a correct idea of the mean atomic ratio of the precipitates in this Mg excess specimen. In the **literature review (section 2.1.1)**, β" showed a wide range of chemistry between each alloy of different composition but also within a homogeneous material [SON 11]. The Mg/Si ratio is generally observed around 1.6 for β" precipitate in pseudo-binary alloys [MAR 97]. This ratio should also be near to the composition of β' for pseudo-binary or Mg excess alloys according to Matsuda *et al.* [MAT 05] which is set around 1.8. Even if the composition of this specimen is not exactly pseudo-binary, the few observed precipitates in this study could follow these trends. It is complicated to know exactly though if precipitate 1 is a β' or β" precipitate. But, because at this pre-T6 state, β' precipitates were observed on TEM. It can be assume that precipitate 1 is a β' precipitate and the precipitate 2: β".

As expected, the Mg content in SS dropped during the 16 h of ageing at 170 °C. The variation of Si is less obvious due to the uncertainty. This lower variation is in line though with the richer content in Mg in the precipitates. It can be also observed that at this point of the ageing process (pre-T6), Mg and Si are still present in SS and available for precipitation. There is more Mg than Si as expected from the initial composition.

Si excess specimen

In the analysed volume of the strong Si excess specimen, no precipitate was found. The solid solution (SS) was analysed though and is presented in the Table 2.12 with the initial SS measured by EDX.

		Al (at%)	Mg (at%)	Si (at%)
As-quenched	SS	98.9 ± 0.2	0.5 ± 0.1	0.6 ± 0.1
Aged 16h at 170 °C	SS	99.05 ± 0.08	0.21 ± 0.04	0.74 ± 0.08

Table 2.12: Compositions of the Mg/Si = 0.9 specimen extracted from B-R4-Si rolled sample

As for the Mg excess specimen, the Mg content has significantly decreases whereas the Si does not seem to have move much. At this near T6 state, some Mg is remaining in SS but not as much as the Si.

2.4 Summary

During that precipitation study at 170 °C, the Mg-Si composition influences the ageing kinetics and the precipitation states.

Two local maxima of precipitation

As expected from the literature, two specific influences of composition are clearly standing out through microhardness measurements. They are related to the initial solid solution (SS) composition through its maximum available contents in Mg_2Si and Mg_5Si_6. The maximum hardness were obtained near those compositions. To represent those influences of composition: Mg_2Si content and Mg/Si ratio are used but Mg+Si showed its importance. The compositions specificity of these two maxima is gathered in Figure 2.37 and confronted to the isothermal DSC maxima. In this figure, the information obtained for clustering and coherent phase precipitation from continuous heating DSC are also presented in parallel in order to explain these observed maxima.

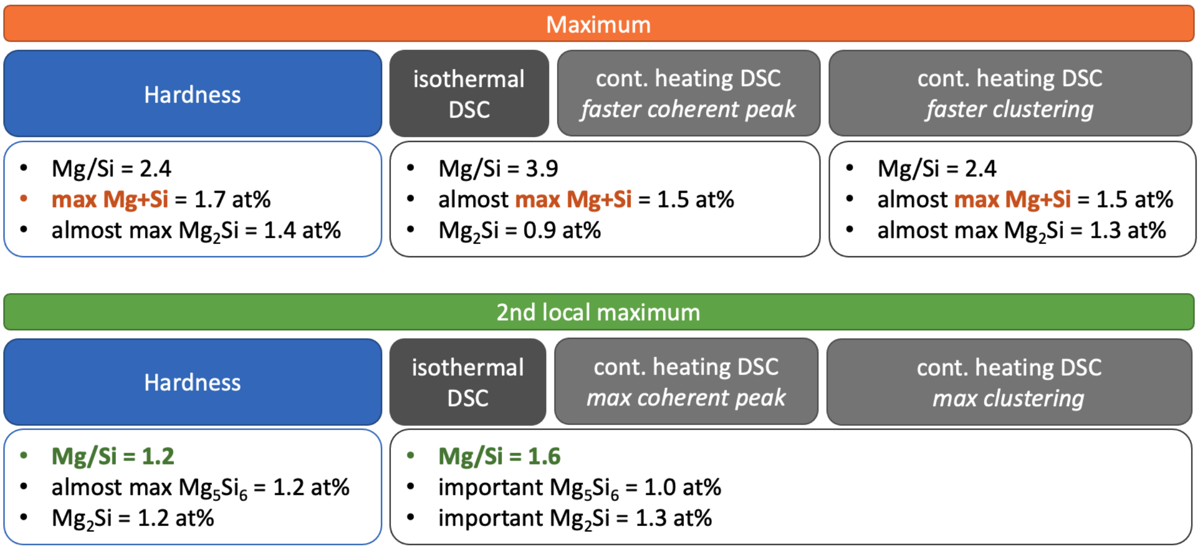

Maximum

Hardness
- Mg/Si = 2.4
- **max Mg+Si** = 1.7 at%
- almost max Mg_2Si = 1.4 at%

isothermal DSC / cont. heating DSC *faster coherent peak*
- Mg/Si = 3.9
- almost **max Mg+Si** = 1.5 at%
- Mg_2Si = 0.9 at%

cont. heating DSC *faster clustering*
- Mg/Si = 2.4
- almost **max Mg+Si** = 1.5 at%
- almost max Mg_2Si = 1.3 at%

2nd local maximum

Hardness
- **Mg/Si = 1.2**
- almost max Mg_5Si_6 = 1.2 at%
- Mg_2Si = 1.2 at%

isothermal DSC / cont. heating DSC *max coherent peak* / cont. heating DSC *max clustering*
- **Mg/Si = 1.6**
- important Mg_5Si_6 = 1.0 at%
- important Mg_2Si = 1.3 at%

Figure 2.37: Confrontation of the two hardness maxima with the two isothermal DSC maxima and continuous heating observations

For hardness and isothermal DSC, the maxima are quite similar. For the highest maximum, the Mg+Si content is maximum or near the maximum in the gradient for both hardness and isothermal DSC. This is where the faster precipitation of coherent phases was actually observed. The faster clustering could also contribute to the hardness maximum. It is not clear though if clustering speed depends more on the atomic ratio (Mg/Si = 2.4), on the Mg_2Si content or on the Mg+Si content.

For the second local maximum, the compositions seems to point out the effect of Si excess via its Mg/Si atomic ratio (near 1) even if they are slightly different: Mg/Si = 1.2 (for hardness measurements) against 1.6 (for isothermal DSC). This difference can be explain by the lack of analysed compositions for each graded samples around those compositions, see Figure 2.16. Here the hardness gain can be attributed to the important clustering and precipitation of coherent phases. Indeed, they are amplified with the rise of Si excess until near the composition of β”.

Different domains within the gradients

From the hardness results, three domains are clearly visible: the extreme Si excesses (Mg/Si ≤ 0.7), the near pseudo-binary compositions ($1.2 \leq$ Mg/Si ≤ 3.1) and the extreme Mg excesses (Mg/Si > 3.1). In continuous heating DSC, these three domains are also observed with small differences: extreme Si excesses (Mg/Si ≤ 0.8), the near pseudo-binary compositions ($1.6 \leq$ Mg/Si ≤ 3.9) and the extreme Mg excesses (Mg/Si > 3.9). For both DSC experiments: sub-domains are observed for the extreme Si excesses depending if pure Si precipitation is majoritarian or not. Therefore the real Si extreme compositions have Mg/Si ≤ 0.2 and the strong Si excesses have $0.4 \leq$ Mg/Si ≤ 0.8.

It is interesting to note that for these Si strong excesses, DSC predicts a slower precipitation of the β metastable cascade. This feature has been confirmed using HR-TEM observation on 16 h at 170 °C ageing state. β” were only observed on a strong Si excess specimen of Mg/Si = 0.6 against β’ for the other compositions: Mg/Si = 1.9 (with β_0’) and 3.7.

ASAXS measurements also evidenced different domains. After 3 days of ageing at 170 °C, the mean diameter (D_{mean}) grows proportionally to the ageing time for Mg/Si ≤ 1.1. For $1.1 <$ Mg/Si ≤ 4, D_{mean} increases more significantly around Mg/Si = 2 (especially between 1.7 and 2.7). Above Mg/Si = 4, not enough information were extracted. Conventional TEM confirms this feature with a higher diameter near Mg/Si = 2 (Mg/Si = 1.4) after 1 month of ageing at 170 °C. Conventional TEM results showed also a similar disposition for the mean length of the precipitates. These large and long precipitates for pseudo-binary compositions seems to be explain by the presence of two populations of thin (d = 4 nm) and very large precipitates (d > 25 nm). Unfortunately these precipitates were not identified by HR-TEM.

Chemistry of precipitates and solid solution composition

More generally, differences of precipitates and of solid solution variations have been observed, by HR-TEM and APT respectively, depending on the initial composition in the gradient for same ageing treatments. Finally, the observed β’ precipitates by HR-TEM in Mg/Si = 3.7 specimen after 16 h at 170 °C were also evidenced by APT with two precipitates of chemistry near β’ and β”. The additional solid solution compositions extracted for two ageing states of 16 h at 170 °C by APT will be further discussed in the precipitation simulation context of the next chapter.

Chapter 3

Simulation of precipitation through Al-Mg-Si graded alloys

In the literature, various precipitation and hardening models were developed for Al-Mg-Si alloys: each with its specific asset (hardening in Al6xxx, multiple precipitates consideration, heterogeneous nucleation etc.). In this chapter, a mean field framework based on classical nucleation and growth theories coupled with a hardening model has been developed to study the effect of composition on precipitation hardening in Al-Mg-Si alloys. In this perspective, the model is considering a composionally graded material and five precipitates types which are defined using TCAL4 database. The simulations obtained on specific gradients were successfully compared to the experiments. From this model, β" is shown as the crucial precipitate for mechanical properties and its precipitation kinetics is highly influenced by the initial composition. With this model, ageings above 200 ℃ *do not show sufficient improvement of mechanical properties for all the gradient of solid solution composition between 1.1 at.%Si and 1.3 at.%Mg with Mg/Si atomic ratios between 0.01 and 4.5.*

Contents

3.1 Bibliographic review: microstructural and mechanical evolution described by precipitation simulations

This literature review will first present the major precipitation models. Then, the Kampmann and Wagner Numerical (KWN) approach will be explained in more detail. Finally, strengthening models will be introduced.

3.1.1 Precipitation kinetics models

Various ways to simulate precipitation exist at different time and space scales. The atomistic methods describe the physics with the best accuracy but they are limited in simulation times and therefore in space through the number of simulated atoms (from 500 to few million atoms). Continuous scale methods regroup all the other methods which describe precipitation at a larger scale. The physics behind the equations is less exact but the simulated time can here incorporate entire complex precipitation phenomena [DES 21]. Among these methods: phase field and mean field methods will be presented. First, a brief recap on the main precipitation stages is conducted.

3.1.1.1 Precipitation stages

To present the four major precipitation stages, Figure 3.1 describes the evolution of precipitates mean radius, precipitates number density and solid solution content during ageing [DES 98].

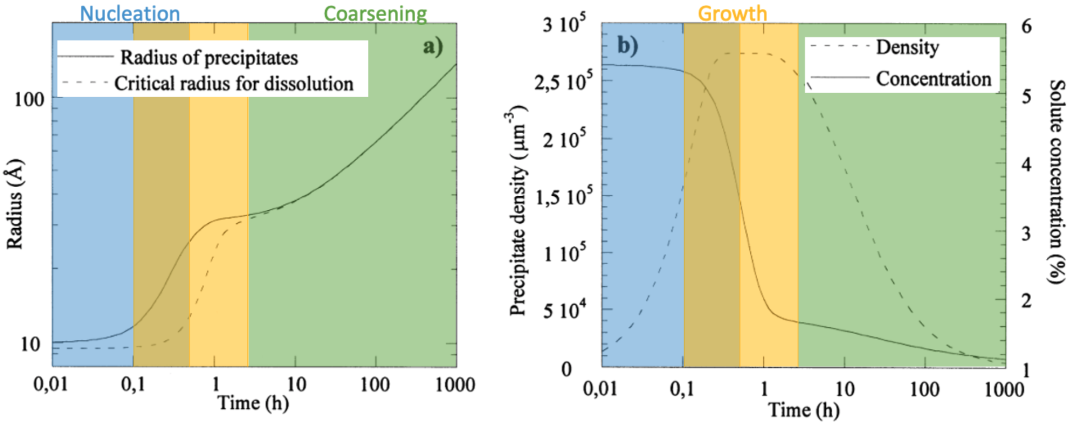

Figure 3.1: Precipitates and solid solution (SS) evolution during ageing, a: precipitates mean radius and critical radius and b: precipitates number density with solute content in SS [DES 98]

During nucleation, nuclei emerge in the matrix at preferential locations (heterogeneous) or homogeneously. The solute concentration in the solid solution decreases slightly. The precipitate density rises whereas the mean radius remains stable. All the nuclei have approximatively the same critical radius.

During the beginning of growth, the radius of the nuclei increases thanks to diffusion. This leads to an important decrease of the solute content in the solid solution. This decrease changes the value of the driving force Δg (detailed further) and, consequently, increases the critical radius r* above which, a nucleus is stable. Newly formed nuclei are larger. The density continues its rise while the precipitates average radius stalls.

During pure growth, the precipitates with radius below the current critical radius become unstable. They will dissolve to the benefit of larger precipitates. During this local equilibrium, the average radius and the number of precipitates are stable. The solute concentration continues to decrease but slower.

Around each precipitate, the solid solution has been subjected to a depletion of its solute content. This depletion is all the more important as the precipitate is large. To overcome this gradient of concentration, the small precipitates will gradually dissolve to diffuse solute in the poorest regions, close to the large precipitates. Therefore, during coarsening, the small precipitates disappear to the benefit of the largest ones. The local diffusion of solute has almost no impact on the concentration of solute. However, there are fewer and fewer precipitates; the density of precipitates decreases. And they are getting larger and larger; the average radius increases.

3.1.1.2 Atomistic approaches

Density-functional theory (DFT) is a computational method which describes quantum mechanics interactions between the atoms. By solving the Schrödinger equation within the DFT, enthalpies can be extracted and relaxation/binding studies are possible. This is especially interesting for metastable nano-particles embedded in a matrix. Unfortunately, the simulation box can only have at maximum about 500 atoms, which is very small. It is also only suited for very short simulation times. Precipitation of the full metastability cascade is not conceivable for Al-Mg-Si system but DFT can study the formation of the first precipitates structures that form from solid solution [SAN 07]. DFT can also evaluate the energetic stability of any chemistry structures independently. In this end, Ravi *et al.* [RAV 04], supplied convex hull diagrams with the formation enthalpy of each possible cluster see Figure 3.2. Ravi could then also affirm that for Si-rich compositions, pre-β" seems energetically more likely against, for Mg-rich alloys, the $L1_0$-type Mg_1Si_1 (GPZ) structure of Matsuda et al. [MAT 98].

Molecular dynamic is simplifying the interaction between the atoms by using second Newton law with a potential energy (that can sometimes be extracted from DFT). All the movements, induced by thermal activation, of each atom are simulated. Crystallographic structure and strength field generated by the interfaces (points defects and dislocations) are thus taken in consideration. The calculation is less intensive than DFT, permitting to simulate up to several million atoms but still for rather limited simulation times. To the author's knowledge, no molecular dynamic studies were conducted on Al-Mg-Si system.

Finally, **Kinetic Monte Carlo** (KMC) method is using probabilities to predict the phase transformations [CLO 04]. These probabilities can be approximated in different ways (for example using molecular dynamics or only based on the nucleation energy barrier). On 1 million of atoms, some will constitute the new phase. Metastable cascade such as the precipitation sequence of β can be simulated. The calculation cost is lighter than for the previous presented models. In Al-Mg-Si, Lee *et al.* [LEE 22] investigated the atomic-scale mechanism of cluster formation during natural, pre-ageing and artificial ageing using KMC (Figure 3.3). The clusters showed differences of composition and in vacancies content depending on the ageing conditions. Si-rich clusters also presented an important ability to trap the vacancies.

Using the cluster expansion method of DFT, Sandberg *et al.* [SAN 07] found the same more

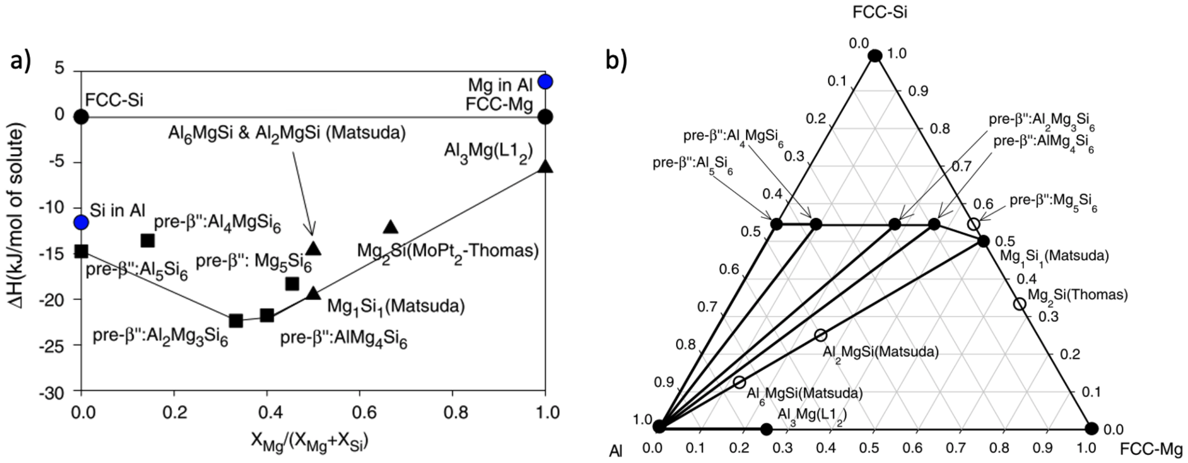

Figure 3.2: [RAV 04] a: First-principles energetics of fcc-based GP zones in Al-Mg-Si alloys. Geometries for each model are fully relaxed. The Al-containing pre-β" and Mg_1Si_1 structures fall on or near the convex hull of fcc-based structures. b: Schematic representation of the Al-rich ground state diagram of fcc-based GP zones of Al–Mg–Si on a ternary Gibbs' triangle. Filled circles are structures which fall on or near the convex hull and are therefore deemed energetically competitive models for GP zones.

stable GPZ cristallographic structure as Ravi *et al.* [RAV 04] with its direct DFT calculations: Mg_1Si_1 $L1_0$ introduced by Matsuda [MAT 98]. By combining DFT and KMC, Sanberg also investigated nucleation mechanisms of pre-β" and β". Or, the vibrational entropy (TS) term is responsible for their formation, or, vacancies are the ones stabilising the structure preceding the β" phase, which then transforms to the metastable β" phase.

3.1.1.3 Continuous scale methods

At a higher scale, the field methods simplify greatly the physics behind precipitation. The gain in calculation efficiency allows the description of entire precipitation on conceivable ageing times.

First, there is the **phase field** method which originates from a spatio-temporal description of the microstructure with an estimation of the solid solution energy using its concentration in solute. This method is efficient for some phase transformation such as spinodal decomposition but does not properly describe nucleation. Recently, phase-field models have emerged at an atomistic-scale. They are called phase-field crystal models (PFC) [ELD 07]. Fallah *et al.* used the 3D ternary PFC model of Ofory-Opoku *et al.* [OFO 13] to simulate the evolution of clusters in Al-Mg-Si sytem. In this paper, TEM was in good agreement with the model to indicate that the clusters undergo a morphology and orientation evolution before their evolution into non-fcc GPZ as presented in Figure 3.4.

Even if this computational method presents some advantages, it is still rather difficult to perform simultaneous precipitation of different phases.

Several methods used to describe precipitation kinetics are gathered under the name of **mean**

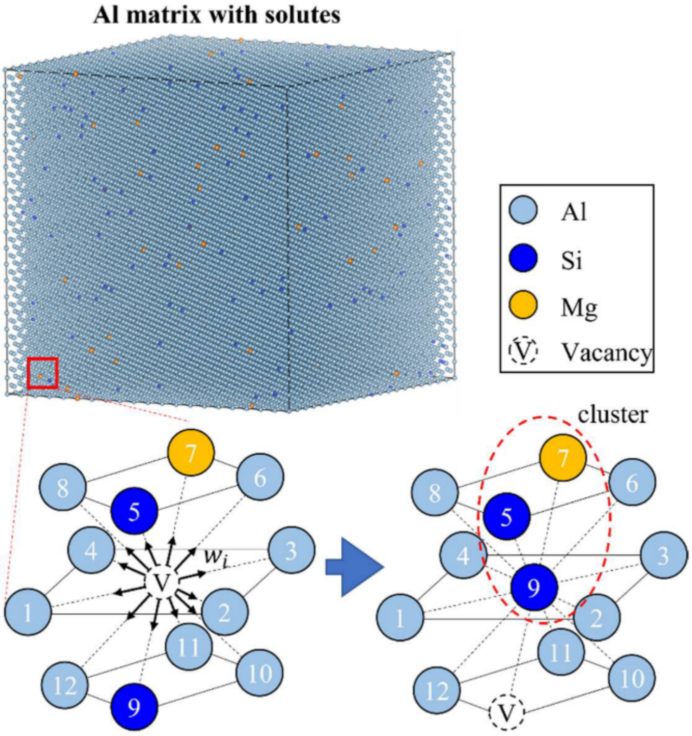

Figure 3.3: Schematic representation of the clustering mechanism in Al–Si–Mg according to the KMC model [LEE 22]

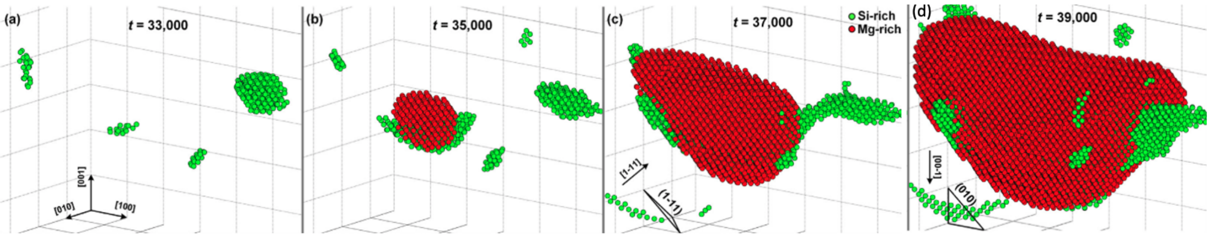

Figure 3.4: Simulated formation of clusters with phase field crystal method [FAL 15]

field approaches. Among them, Classic Nucleation and Growth Theories (CNGTs) are based on evolution equations of radius and number density of the precipitates considering nucleation, growth and coarsening. This approach can even reproduce competition between several phases if their nucleations are independent. It can also simulate non spherical precipitates. These methods without size limits still present some disadvantages though. They display no space representation and they are based on strong hypothesis. For example, there is no crystallographic mismatch between matrix and precipitates and the interface is considered perfect [PER 07]. These approaches can be split in two categories:

- Mean radius approach: the size distribution evolution of the precipitates are only considering mean radius for a certain number of precipitates. This model is using classes management with, among each class, a constant radius and a variable number density of precipitates. The Langer-Schwartz (LS) model is at the base of many of those works [REV 80]. Among them, the classical Lifshitz-Slyozov-Wagner (LSW) treatment allows a better description of coarsening for overageing simulations. Deschamps *et al.* developed this method for Al alloys [DES 98] but bimodal size distribution [HUT 10] and dissolution at constant mean radius [NIC 03, DES 04, DES 10] cannot be correctly reproduce.

- Class models: the precipitates sizes are discretised in numerous classes. Here the number of precipitates in each class is constant and the radius is variable. This class approach was introduced by Kampman and Wagner [KAM 84] and is therefore named Kampman Wagner Numerical (KWN) model. The time step of each class is calculated, or depending on the fluxes between neighbouring classes (Euler implementation), or depending on their size evolution (Lagrange implementation).

In this last category, many works have been performed on Al-Mg-Si alloys. Povoden *et al.* [POV 13] and Du *et al.* [DU 17] developped CALPHAD-coupled Kampmann-Wagner Numerical (KWN) framework in order to properly simulate the full metastability cascade of 6xxx Al alloys from heterogeneous nucleation, including the semi-coherent phases only present for Si excess alloys. Even if the simulation of all the metastable phases through this database is possible, most of the authors are only considering the main hardening ones. Myhr *et al.* [MYH 15] used KWN formalism in order to simulate clusters, β" and β' formations (precipitates were considered spherical). Cinkilic *et al.* [CIN 20] only considered β" in their Al-Mg-Si-Mn precipitation model and presented good experimental correlation for short ageing times. The equations behind KWN models will thus be detailed in the next section.

3.1.2 Precipitation mechanism in KWN models

3.1.2.1 Bases for Classic Nucleation and Growth Theories (CNGTs)

Nucleation originates from two phenomena in opposition. The creation of a more stable crystallographic structure brings the decrease in Gibbs energy ($\Delta G_V < 0$). This variation is proportional to the driving force Δg [J.m^{-3}]. On the other hand, the creation of a matrix-precipitate interface causes an increase in free enthalpy ($\Delta G_S > 0$), unfavourable to the precipitate formation. This difference is proportional to the surface energy between precipitate and matrix γ [J.m^{-2}]. Therefore :

$$\Delta G = \Delta G_S + \Delta G_V = S\gamma + V\Delta g \tag{3.1}$$

For rod type precipitate of a length L and a radius r with an aspect ratio $\xi = L/r$, as in the Figure 3.5, this equation becomes :

$$\Delta G = \frac{\xi}{2}4\pi r^2\gamma + (\frac{3\xi}{4} - \frac{1}{2})\frac{4}{3}\pi r^3\Delta g \tag{3.2}$$

Figure 3.5: Morphology of rod type precipitates [MEY 18b]

Figure 3.6 is representing $\Delta G(r)$ with a fixed ratio ξ.

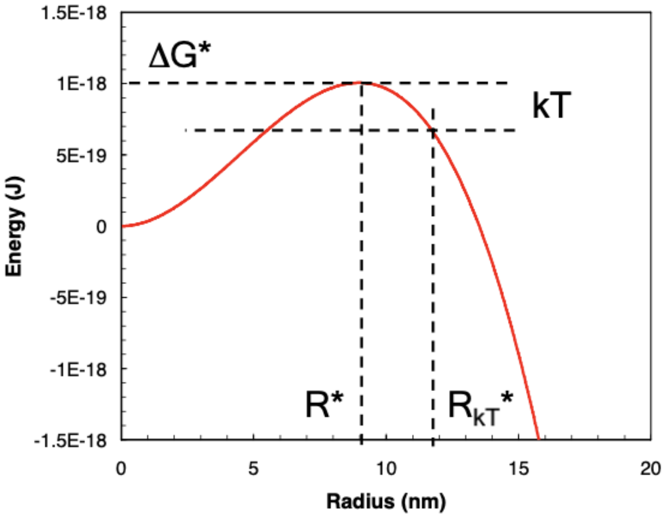

Figure 3.6: Evolution of the free enthalpy with the precipitate radius [PER 07]

The representation of $\Delta G(r)$ clearly shows the competition between the surface (predominant for small radius) and volume (predominant for large radius) effects. There is therefore an energy barrier ΔG^* for a specific size of precipitate separating the unstable from the stable branch of precipitate size and for which G is maximum.

For the rod type precipitate considered:

$$\Delta G^* = \frac{16}{3}\pi\frac{\gamma^3}{\Delta g^2}\frac{2\xi^3}{(3\xi-2)^2} \tag{3.3}$$

$$R^* = -\frac{2\gamma}{\Delta g}\frac{2\xi}{3\xi-2} \tag{3.4}$$

The precipitates with radius smaller than this critical radius R^* are unstable whereas precipitates with larger radius are stable and tend to grow.

In all those equations, the nucleation driving force Δg may be described as:

$$\Delta g = \frac{1}{{V_{at}}^p}\sum_i^N {X_i}^p[\mu_i^{eq} - \mu_i^{ss}] \tag{3.5}$$

with

- ${V_{at}}^p$: precipitate atomic volume
- N: number of chemical elements in the precipitate
- ${X_i}^p$: atomic content of the element i in the precipitate
- μ_i^{eq}: chemical potential of the element i at equilibrium with the interface matrix/precipitate
- μ_i^{ss}: chemical potential of the element i in solid solution

Under the hypothesis of ideal solid solution, the difference in chemical potential lead to the introduction of the supersaturation factor s:

$$\Delta g = -\frac{k_B T}{V_{at}^p} s \tag{3.6}$$

with

- $k_B = 1.38 \times 10^{-23}$ J.K^{-1}: Boltzmann constant
- T: temperature

The surperstaturation is then given by

$$s = \ln \frac{\prod_i^N (X_i^{ss})^{X_i^p}}{\prod_i^N (X_i^{eq})^{X_i^p}} \tag{3.7}$$

with

- ${X_i}^{eq}$: atomic content of the element i in the precipitate at equilibrium with the interface matrix/precipitate
- ${X_i}^{ss}$: atomic content of the element i in solid solution

The supersaturation is representing the excess of solutes in solid solution regarding to the equilibrium content between matrix and precipitate. The driving force rises with the increase of supersaturation. For a precipitate defined as A_xB_y:

$$s = \ln \frac{{X_A}^x {X_B}^y}{({X_A}^{eq})^x ({X_B}^{eq})^y} = \ln \frac{{X_A}^x {X_B}^y}{K^S_{A_xB_y}} \tag{3.8}$$

with $K^S_{A_xB_y}$, the solubility product of the precipitate A_xB_y

If the product of solute contents is lower than the product of the precipitate contents at equilibrium (or to the solubility product), the supersaturation is negative and therefore the driving force positive which inhibits precipitation. On the contrary, if the product of solute contents is superior to solubility product, $s > 0$ and $\Delta g < 0$ which allows precipitation.

The solubility product of a precipitate A_xB_y is described by the following expression:

$$K^S_{A_xB_y} = \exp \frac{-\Delta G_{A_xB_y}}{k_B T} = \exp \left(\frac{S_{A_xB_y}}{k_B} - \frac{\Delta H_{A_xB_y}}{k_B T} \right) \tag{3.9}$$

with $\Delta G_{A_xB_y}$: the Gibbs free energy of formation of the precipitate

$K^S_{A_xB_y}$ is usually expressed as:

$$\log_{10}(K^S_{A_xB_y}) = -\frac{A}{T} + B \tag{3.10}$$

by identification $A = \frac{\Delta H_m^{A_xB_y}}{R \times \ln(10)}$ with $H_m^{A_xB_y}$ the molar formation enthalpy

The surface energy γ is very difficult to measure experimentally. It can be calculated using the nearest neighbours broken bonds approach [KOZ 07]. But, it still often remains as an adjustment parameter even when obtained via quantum mechanics methods such as Density Functional Theories (DFT).

3.1.2.2 Nucleation rate

The nucleation rate represents the number of supercritical precipitates formed by time unit and volume unit. It is expressed thanks to the equation of Kampmann and Wagner [KAM 84]:

$$\frac{dN}{dt}(t,T) = N_0 Z \beta^* \exp\left(-\frac{\Delta G^*}{k_B T}\right) \times f(t,\tau) \tag{3.11}$$

with

- $N_0 = \frac{1}{{V_{at}}^m}$: sites number available for homogeneous precipitation
- Z: Zeldovich factor
- β^* : addition frequency of an atom to the critical nucleus
- τ : incubation time

For rod-type precipitates, Z is defined as following:

$$Z = \frac{{V_{at}}^p}{\pi {R^*}^2 (3\xi - 2)} \sqrt{\frac{2\xi\gamma_p}{k_B T}} \tag{3.12}$$

In the case of cubic lattice, β^* is defined as following:

$$\beta^* = \frac{4\pi {R^*}^2}{a^4} \times \left(\sum \frac{{X_i}^p}{{D_i}^m {X_i}^m}\right)^{-1} \tag{3.13}$$

with

- a: lattice parameter of the matrix
- ${D_i}^m$: diffusion coefficient of the solute i in the matrix
- ${X_i}^m$: atomic fraction of solute i in the matrix
- ${X_i}^p$: atomic content of solute in the precipitate

τ is defined as followed:

$$\tau = \frac{2}{\pi \beta^* Z^2} \tag{3.14}$$

The function $f(t,\tau)$ is the incubation time function. This function has here the expression $1 - \exp(-\frac{t}{\tau})$ [MAU 05].

Finally, the nucleation rate is defined as followed:

$$\frac{dN}{dt}(t,T) = N_0 Z \beta^* \exp\left(-\frac{\Delta G^*}{k_B T}\right) \left(1 - \exp(-\frac{t}{\tau})\right) \tag{3.15}$$

3.1.2.3 Precipitates growth

Precipitates growth is governed by diffusion. For a solute i, the first law of Fick (around a spherical precipitate of radius R) is given by:

$$J(r) = -D\frac{\partial X}{\partial r} = \frac{DR(X_i - X_0)}{r^2} \tag{3.16}$$

with

- X_i solute content at the interface with the matrix
- X_0 solute content very far from the interface or solid solution concentration
- D diffusion coefficient of the solute in the matrix

A mass balance leads to:

$$\frac{dR}{dt} = \frac{D}{R}\left(\frac{X_0 - X_i}{\alpha X_p - X_i}\right) \tag{3.17}$$

with

- X_p : solute content of the precipitate at equilibrium
- $\alpha = \frac{V_{at}^m}{V_{at}^p}$: atomic volume rate matrix-precipitate

In practice, the interface curvature between matrix and precipitate influences the local equilibrium due to the surface energy. It is the Gibbs-Thompson effect. During growth, the solute concentration at the interface depends on the precipitate size. The growth rate is thus redefined as followed:

$$\frac{dR}{dt} = \frac{D}{R}\frac{X_0 - X_i(R)}{\alpha X_p - X_i(R)} \tag{3.18}$$

For a rod-type precipitate A_xB_y the Gibbs-Thomson effect is taken in consideration with a new equation regarding the solubility constant :

$${X_{\mathrm{A}}^i}^x {X_{\mathrm{B}}^i}^y = K_s \exp\left(\frac{r_0}{r}\right) \tag{3.19}$$

with r_0 the capillary radius given by:

$$r_0 = \frac{4\xi\gamma v_{at}^p(x+y)}{(3\xi - 2)k_bT} \tag{3.20}$$

For a rod-type precipitate of length l and radius r, an adjusted equation is also used to predict the growth in length of the precipitates:

$$\frac{dl}{dt} = 1.5\frac{D_A}{2r}\frac{X_A - X_A^i}{\alpha X_A^p - X_A^i} = 1.5\frac{D_B}{2r}\frac{X_B - X_B^i}{\alpha X_B^p - X_B^i} \tag{3.21}$$

Finally, to describe the growth of an A_xB_y precipitate, a non linear system of 3 equations at 3 variables is resolved using the hybrid algorithm of Newton-Raphson/Brent [BRE 13] while respecting the stoechiometry of the precipitates:

$$\begin{cases} \frac{dr}{dt} = \frac{D_A}{r}\frac{X_{\mathrm{A}}^i - X_{\mathrm{A}}^i(r)}{X_{\mathrm{A}}^p - X_{\mathrm{A}}^i(r)} \\ \frac{dr}{dt} = \frac{D_B}{r}\frac{X_{\mathrm{B}}^i - X_{\mathrm{B}}^i(r)}{X_{\mathrm{B}}^p - X_{\mathrm{B}}^i(r)} \\ {X_{\mathrm{A}}^i}^x {X_{\mathrm{B}}^i}^y = K_s \exp(\frac{r_0}{r}) \end{cases} \tag{3.22}$$

3.1.3 Strengthening models

Dislocation is a linear default which creates a discontinuity in the organisation of the crystal structure. Dislocations propagate plastic deformation while moving. The yield strength is the stress at which the material begins to deform plastically. The yield strength is often used to determine the maximum allowable load in a mechanical component without producing permanent deformation. In this section, the general approaches of the strengthening models (which simulate yield strength) are presented. Then, the yield strength expression of models, based on dislocation interactions with obstacles, detailed in the context of rod-type precipitates.

3.1.3.1 General approaches

In order to simulate the evolution of strength within a metal, **phenomenological approaches** were developed. Mathematical functions were optimised in order to fit with the experimental yield strengths observed. The description of complex behaviours were well simulated in 6xxx Al alloys [ABD 09, ABD 10]. These empirical models prevent though the complete comprehension of the physical mechanisms involved in precipitation.

In **physically-based approaches**, the precipitates can be distinguished as sheared and bypassed precipitates (as presented in the literature review of Chapter 2 section 2.1.2.1). The pinning force of the dislocation regarding to the different distortion centres of the lattice (solute atoms, precipitates...) and the number of these objects along the dislocation line make it possible to accurately consider the interaction of dislocations with the microstructure of a given material [FRI 64]. These models describe with more accuracy the evolution of mechanical properties [ENG 19] and can be calculated from microstructural evolution predictive models such as KWN model presented in **section 1.1.3 and 1.2**.

Many studies of precipitation hardening used this second approach [HOY 91, MAT 79, MYH 04, DES 98, BAR 14]. For example, the "process model" of Shercliff *et al.* [SHE 90a] correctly simulated the mechanical properties evolution for 2xxx and 6xxx Al series during isothermal treatment but presented issues for complex thermal treatment [SHE 90b]. Since then, the model was up-graded [HOR 93, DES 98] and a better comprehension of the phenomenon involved during various thermal treatments made it evolved as well [LIU 03, MYH 01, MYH 04, MYH 10, MYH 15, FAZ 08, GAL 08, GHI 18]. Finally, each progress gained in KWN microstructural models improves as well the precision of this yield strength model.

Some variant models simplify the problem and provide yield strength values using empirical proportionality links requiring only radius and volume fraction of precipitates [SIM 12]. One model was developed by Esmaeili *et al.* [ESM 03b] for Al-Mg-Si systems [ESM 05, YAZ 09].

3.1.3.2 Yield strength expression

To estimate the macroscopic yield strength σ_y, an homogenisation of all the obstacles contributions is performed by summing the shear stresses τ generated in the slip plane [ARD 85, QUE 10]. For two contributions:

$$\sigma_y = M\tau_{tot} = M(\tau_1^i + \tau_2^i)^{1/i} \tag{3.23}$$

with M the Taylor factor

The homogenisation form with $i = 1$ is convenient for systems with few strong contributions among many weak contributions [DES 98, QUE 10, BRO 71]. Koppenaal *et al.* [KOP 64] and Kocks *et al.* [KOC 75] used a quadratic form with i = 2 for same magnitude order contributions with different obstacles density [DES 98].

A particularly effective quadratic form obtained good predictions for a very large configuration range [KOC 75]. It is now commonly used by many authors [DES 98, FRI 11, BAR 14]. It gives precipitation hardening alloys yield strength σ_y depending on the different contributions as following:

$$\sigma_y = \sigma_0 + \Delta\sigma_{SS} + \Delta\sigma_{gb} + \sqrt{\Delta\sigma_{sh}^2 + \Delta\sigma_{bp}^2 + \Delta\sigma_d^2} \tag{3.24}$$

with

- σ_0: Pure aluminium yield strength
- $\Delta\sigma_{SS}$: solid solution contribution
- $\Delta\sigma_{gb}$: grain boundaries contribution
- $\Delta\sigma_{sh}$: sheared precipitates contribution
- $\Delta\sigma_{bp}$: by-passed precipitates contribution
- $\Delta\sigma_d$: dislocations contribution

In Chapter 1, the pure Al yield strength and the grain boundaries contribution were considered together using Hall-Petch's law:

$$\sigma_{Al} = \sigma_0 + \frac{k}{\sqrt{d}} \tag{3.25}$$

with

- k the microstructure-dependent constant
- d the mean grain diameter

Still in Chapter 1, the solid solution contribution was experimentally extracted through solid solution mechanical parameters thanks to hardness measurements:

$$\sigma_{SS} = \sum_j k_j x_j^{2/3} \tag{3.26}$$

with

- k_j the solid solution mechanical parameter for solute j
- x_j the solid solution composition for solute j

Regarding the dislocations contribution, the strengthening that they cause is expressed with Taylor relation:

$$\Delta\sigma_d = M\alpha\mu b\sqrt{\rho} \tag{3.27}$$

with

- M the Taylor factor, this value is usually included between 2 and 3 for 7xxx Al alloys [STA 03]

- α constant between 0 and 1 representing the interaction between mobile dislocations and forest of dislocations. Deschamps *et al.* [DES 98] estimated this value at 0.27 in a Al-Zn-Mg alloy.
- $\mu = \frac{E}{2(1+\nu)}$ shearing modulus of pure Al defined for isotropic material with the Young's modulus E and Poisson's ratio ν
- b Burgers vector
- ρ the dislocations density

This contribution is only used for materials with many dislocations such as work-hardened materials.

As introduced in Chapter 2, the precipitates contribution has to consider both shearing and Orowan by-pass mechanisms.

The line tension generated by a dislocation inked between two obstacles is:

$$T = \beta\mu b^2 \tag{3.28}$$

with β a constant which is between 0.25 and 0.5 [DES 98]

For **by-passed precipitates**, the force required to overcome the pining of the dislocation is:

$$F_{bp} = 2T \tag{3.29}$$

The strength is therefore:

$$\sigma_{bp} = \frac{MF_{bp}}{bL} = \frac{M2\beta\mu b^2}{bL} \tag{3.30}$$

with M the Taylor factor and L the mean distance between precipitates

For **sheared precipitates**, Gerold [MAT 79] proposed an expression for the force required to overcome the pining of the dislocation:

$$F_{sh} = k\beta\mu r \tag{3.31}$$

with k the proportionality factor representing the obstacle force opposed by the precipitate to its shearing and r the radius of the precipitate intercepted by the shearing plane

A new distance L_{sh} is introduced by Friedel [FRI 64]. It corresponds to the mean distance between sheared precipitates. It depends on the curve radius of the dislocation which varies with the applied stress:

$$L_{sh} = \sqrt{\frac{2T}{F_{sh}N_a}} \tag{3.32}$$

with N_a the density of precipitates by surface unit

In the same way as previously, the associated strength is:

$$\sigma_{sh} = \frac{MF_{sh}}{bL_{sh}} = \frac{MF_{sh}^{3/2}}{b}\sqrt{\frac{N_a}{2T}} \tag{3.33}$$

In the case of rod type precipitates, these expressions are changed [ESM 03a] in:

$$\Delta\sigma_{bp} = \frac{2M\beta\mu b}{r}\sqrt{\frac{f_v}{2\pi}} \tag{3.34}$$

$$\Delta\sigma_{sh} = 3^{1/8}M\mu k^{3/2}\sqrt{\frac{f_v r}{2\pi\beta b}} \tag{3.35}$$

with f_v *the volume fraction of the precipitates*

These equations can present some variations depending on the slip plane and the configuration of distribution of the precipitates. For rod-type precipitates, only two cases were studied :

- by Esmaeili *et al.* [ESM 03a] : mono-dispersed sheared precipitates in a plane {111}
- by Bardel *et al.* [BAR 14, BAR 15]: poly-dispersed sheared in a plane {111}

For the use of multi-classes precipitation models, the distribution of size can be taken in consideration for strengthening calculation. Deschamps *et al.* [DES 98] hardening contribution approach uses sizes distribution. This approach provided interesting results with small approximations for several studies [MYH 01, MYH 04, GAL 08, BAR 15] in Al rod type precipitates. The number of precipitates which have reached the radius r_i is $N_i = D_i(r)\Delta r$, where D$_i$(r) is the distribution density and Δr is the class size. As presented in Chapter 2, R_c is the transition radius from which the precipitate is either sheared or by-passed. Therefore, in the case of poly-dispersed rod-type precipitates aligned in the direction [100], their contribution to strengthening is given by:

$$\Delta\sigma_{bp} = \sqrt{2}M\beta\mu b\sqrt{\sum_{i>i_c} N_i l_i} \tag{3.36}$$

with i_c *the index of the transition radius*

$$\Delta\sigma_{sh} = 3^{1/8}M(\mu k)^{3/2}\sqrt{\frac{\sum_{i<i_c} N_i l_i}{2\beta b}}\left(\frac{\sum_{i<i_c} N_i r_i}{\sum_{i<i_c} N_i}\right)^{3/2} \tag{3.37}$$

with l_i *the precipitates length in the class i*

These expressions are close to the ones used for 6061 strengthening simulation by Bardel *et al.* [BAR 14]. A correction of the L expression has been taken in consideration though according to Nie *et al.* [NIE 96].

In this literature review, various types of precipitation and strengthening simulation methods were presented. For precipitation in Al-Mg-Si systems, Mhyr *et al.* [MYH 01] model validates the combination of KWN precipitation model with yield strength simulation based on various experimental data. In this study, and in similar studies, only one type of precipitate is used though to represent all the chain of precipitates [MYH 04, SIM 07, BAR 14]. Various thermodynamic databases now take into account the many metastable phases of the β family including those occurring in Si excess alloys. For example, the database provided by Povoden *et al.* [FAL 10, POV 13] has successfully simulated (using MatCalc software) DSC experiments. Using this database and software, Du *et al.* [DU 17] presented an interesting precipitation model adapted for over-ageing. In this context, a coupled precipitation and yield strength model will be developed and carried out on the range of compositions studied in the precedent chapter using numerous precipitates in competition based on the previous work of Meyruey *et al.* [MEY 18b].

3.2 Coupled precipitation/hardening model in a gradient

The main goal is to provide a model which can simulate interesting ageing treatments on various Al-Mg-Si alloys. The parameters will be chosen according to the precipitation study (performed in Chapter 2) on the elaborated graded samples (of Chapter 1).

3.2.1 Presentation of PreciSo software

3.2.1.1 Microstructural evolution simulation

PreciSo software belongs to mean field models and more especially to Classic Nucleation and Growth Theories (CNGT). The class approach used is the one of Kampman Wagner Numerical (KWN) model with a Lagrange implementation.

For each time step t, two equations are solved (Figure 3.7). First, the nucleation rate equation (equation 3.15) provides the number of nuclei formed in a new class. Then, the resolution of the growth rate equations (equation 3.22) changes the radius value of each class present. All these equations are detailed in the previous literature review.

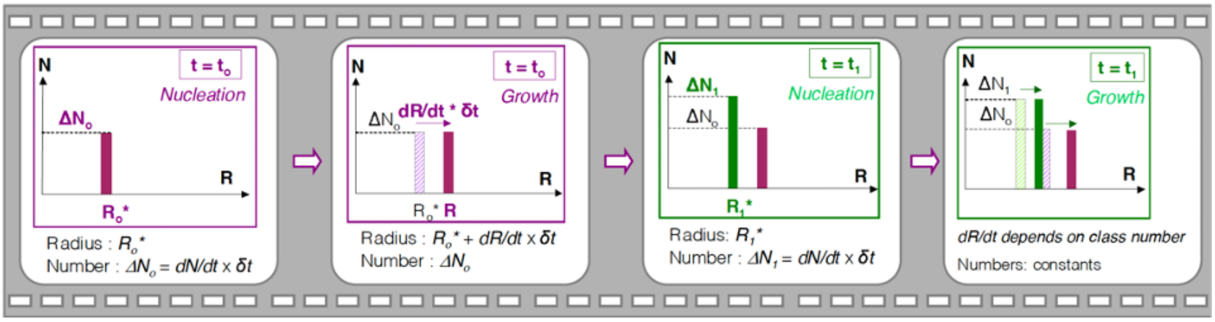

Figure 3.7: Visualisation of the equations resolution of PreciSo for each time step [PER 07]

In PreciSo, a class is created for one time step only if enough precipitates reach the critical radius r* based on the nucleation rate of equation 3.15: $\frac{dN}{dt}t > 10^{-5}N_{tot}$. The number of nuclei can be visualised with:

$$N_i(t + dt) = N_i(t) + \Delta t \frac{dN}{dt} \tag{3.38}$$

After significant nucleation and/or growth of the precipitates, mass balance calculates the evolution of the chemical composition of the matrix during precipitation. The equation used is the following :

$$X_i = \frac{X_i^0 - \alpha f_v X_i^p}{1 - \alpha f_v} \tag{3.39}$$

with

- X_i^0 initial atomic content of the solute i

- X_i^p atomic content of the solute i in the precipitate
- f_v volume fraction of the precipitate formed
- $\alpha = \frac{1}{V_{at}^{SS}} = \frac{1}{a^3}$ coefficient

If no more solute is available in solid solution or if one step consumes too much solute content, the calculation process changes.

During calculation process, two variables are adapted : Δt and the number of classes.

- Δt is multiplied by $\beta = 1.1$, from one time step to another, when: solute content of each solute is remaining (with a coherent value between 0 and 1) and when the variation of the critical radius r* is stable enough (variation inferior to 1%) otherwise Δt is divided by α = 2.
- A target number of classes is set. During calculation, if the real number of classes is too far from that targeted value, intermediary classes are created following a continuous density distribution. Every class is therefore resized according to the same volume fraction.

The Figure 3.8 summarises the functioning steps of PreciSo mentioned previously.

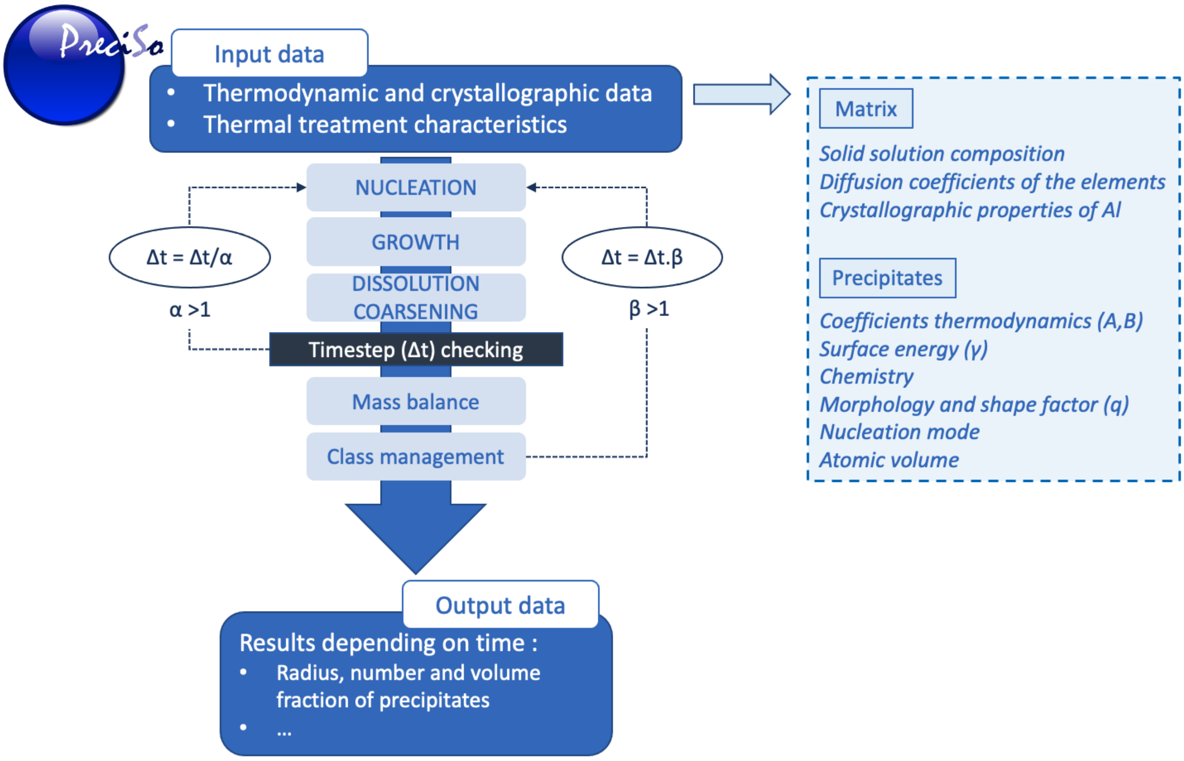

Figure 3.8: General algorithm of PreciSo [MEY 18b]

The simulations showed in the next section used PreciSo software. The following hypothesis are made:

- Homogeneous precipitation
- Rod type precipitates considered as in Figure 3.5. The shape factor $q = l/r$ is considered

constant for each phase.

The detailed input data will be presented and discussed further.

3.2.1.2 Yield strength evolution simulation

The evolution of the precipitates are simulated via the calculation process of PreciSo presented in the **previous section**. Therefore, radius, density, volume fraction and morphology are known for each class of the precipitates distribution during all ageing. Thanks to competition between the different phases, these information are gathered for each considered precipitate of the precipitation sequence.

To calculate the contribution of precipitates to yield strength, PreciSo considers poly-dispersed rod type precipitates. The equations used for the next yield strength simulation are therefore 3.36 for by-passed precipitates and 3.37 for sheared precipitates (presented in the previous **literature review**). For those two equations, two parameters are important. The critical radius r_c and the constant β representing the line tension applied to the dislocation.

The critical radius r_c of each precipitate phase is difficult to measure. It is thus often considered as the T6 mean radius for β". Bardel *et al.* [BAR 14] measured it at 1.8 nm and Wang *et al.* [WAN 03] measured it at 2.5 nm for their respective 6061 and 6111 Al alloys. In the graded samples manufactured during this project, the T6 radius is approximately between (2 ± 1) nm and (3 ± 1) nm for β" according to TEM results (Chapter 2). This parameter can therefore be slightly adjusted for β" around those values. For other precipitates, the adjustment of r_c will be more free.

The mechanical parameter β depends on the form and the nature of dislocations. Different values are presented in the literature for 6xxx Al alloys: 0.25 [BRO 71] 0.28 [GAL 08, SIM 12] 0.36 [MYH 04] 0.37 [MEY 18b] 0.5 [DON 99]. This parameter is then also adjustable. Its value should not be outside [0.25;0.5].

To summarise, this general equation 3.24 (presented in the **previous section**) is used by PreciSo to simulate the total yield strength:

$$\sigma_y = \sigma_0 + \Delta\sigma_{SS} + \Delta\sigma_{gb} + \sqrt{\Delta\sigma_{sh}^2 + \Delta\sigma_{bp}^2 + \Delta\sigma_d^2}$$

with

- $\sigma_d = 0$ because the samples used for mechanical characterisations are non strain hardened
- σ_{bp} is calculated for each possible precipitate using equation 3.36

$$\Delta\sigma_{bp} = \sqrt{2} M \beta \mu b \sqrt{\sum_{i>i_c} N_i l_i}$$

- σ_{sh} is calculated for each possible precipitate using equation 3.37

$$\Delta\sigma_{sh} = 3^{1/8} M (\mu k)^{3/2} \sqrt{\frac{\sum_{i<i_c} N_i l_i}{2\beta b}} \left(\frac{\sum_{i<i_c} N_i r_i}{\sum_{i<i_c} N_i} \right)^{3/2}$$

In this mechanical model: M = 2 [DES 98], E = 71.5 GPa [MAI 10], $\nu = 0.33$ [SHA 00] and $b = 2.86\times10^{-10}$ m [BAR 14] from the Al lattice parameter $a = 4.05\times10^{-10}$ m [RAV 04]. k, the constant representing the precipitate obstacle force opposed to shearing, is also an adjustable parameter specific for each considered precipitate.

In the Chapter 1, the pure Al yield strength and the grain boundaries contribution were considered together using Hall-Petch's law:

$$\sigma_{Al} = \sigma_0 + \frac{k}{\sqrt{d}} \tag{3.40}$$

with

- $\sigma_0 = 10$ MPa the chemistry-dependent constant for pure aluminium [DES 98, COR 16]
- k = 90 MPa·µm$^{1/2}$ the microstructure-dependent constant [COR 16]
- d = 11 µm for Mg-side or 19 µm for Si-side the medium grain diameters from EBSD results

Still in the Chapter 1, the solid solution mechanical parameters, for solid solution contribution (equation 3.26), were experimentally extracted using hardness measurements:

$$\sigma_{SS} = \sum_j k_j x_j^{2/3}$$

with

- $k_{Mg} = 52.9\,\text{MPa·wt\%}^{-2/3}$ from Chapter 1
- $k_{Si} = 12.5\,\text{MPa·wt\%}^{-2/3}$ from Chapter 1

3.2.2 Graded Al-Mg-Si system and considered precipitates

Now that the microstructural and mechanical models have been described, the next section will detail the specificity of the model applied to this study. The system will be defined according to the compositions of the experimental graded samples with the specificity of considering the precipitation of numerous metastable and stable precipitates.

3.2.2.1 Implementation of a matrix with variation of Mg and Si solute contents

Consideration of the gradient

A schematic representation of the 1D modelled system is presented in Figure 3.9.

The length of the numeric sample is corresponding to the length of experimental graded samples ($L_{\text{exp}} = 4.8\,\text{mm}$).

In the model, the sample is cut in N homogeneous slices. This number of nodes is defined according to the precision requested. For proper comparison with experimental data $N = N_{\text{measurements}}$ with:

- $N_{\text{measurements}} = 11$ for sample A (characterised using microhardness) in Chapter 2
- $N_{\text{measurements}} = 9$ for sample B (characterised by DSC, TEM and ATP) in Chapter 2

The surface of exchange between the nodes is fixed with $S = 1\,\text{m}^2$.

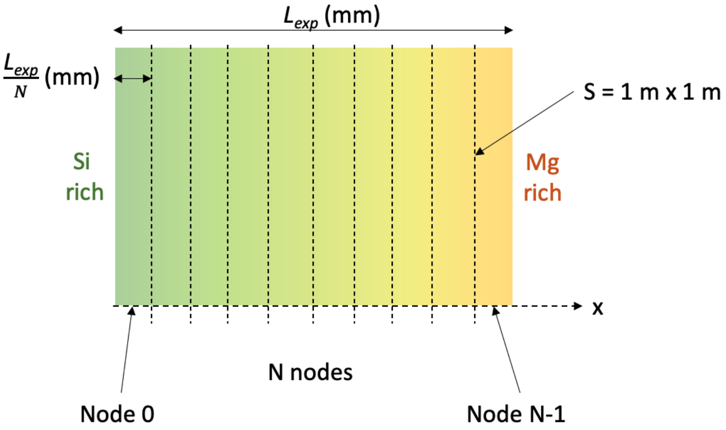

Figure 3.9: Representation of the system considered divided in N nodes

Matrix parameters

As presented in **Introduction**, β precipitates are emerging from the face-centred cubic (FCC) Al matrix, which has a lattice parameter a = 4.05 Å [RAV 04] and an atomic volume of $1.66 \times 10^{-29}\,\mathrm{m}^3$ [VIS 07].

Each initial solid solution (SS) composition along the chosen experimental gradient is then assigned to each node. For each sample, they are described in Chapter 2: Table 2.6 for sample A and 2.7 for sample B. They are also represented on their respective content profile of gradient in Figures 2.15 and 2.20.

The diffusion coefficients of Mg and Si in Al are based on the interdiffusion coefficients found in the literature and presented in Chapter 1:

- $D_0^{Mg} = 6.1 \times 10^{-5}\,\mathrm{m^2{\cdot}s^{-1}}$ and $Q^{Mg} = 127\,000\,\mathrm{J}$ for 2 at.%Mg [MIN 83]
- $D_0^{Si} = 2 \times 10^{-4}\,\mathrm{m^2{\cdot}s^{-1}}$ and $Q^{Si} = 136\,000\,\mathrm{J}$ for $0.6 \leq$ at.%Si < 2 [FUJ 78]

These diffusion coefficients were measured at high temperature (400-650 °C). For lower temperature, such as during the ageing treatment simulated (170 °C), the extrapolation is uncertain as represented in Figure 3.10.

On this figure, the uncertainties (represented in color band) were provided for high temperature as well. The ones at 170 °C are therefore underestimated due to their extrapolation. As they are, the literature diffusion coefficients were delaying β" precipitation. The Si and Mg diffusion coefficients were therefore adapted and multiplied by 15 for the simulations. The sensitivity study on these parameters is detailed further.

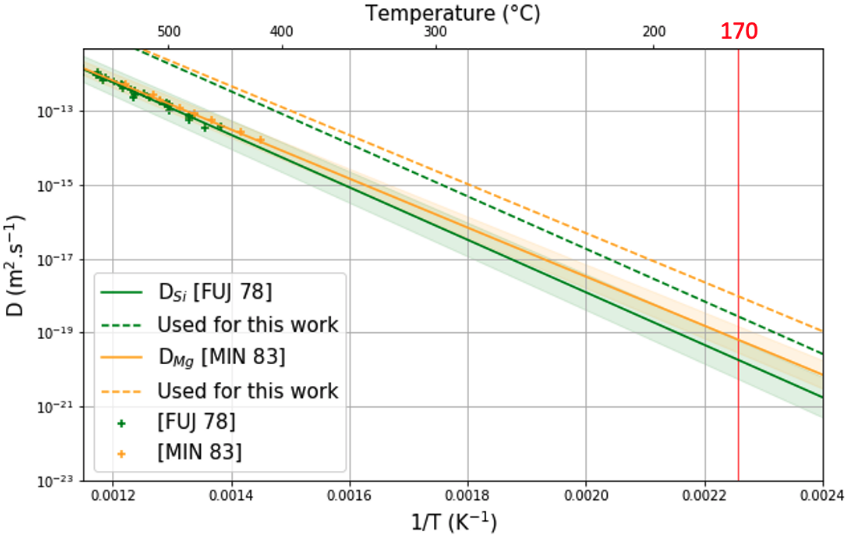

Figure 3.10: Mg and Si interdiffusion coefficients evolution with temperature [FUJ 78, MIN 83]. No experiments were done underneath 400 °C. The extrapolated uncertainties provided by the authors are underestimated for 170 °C.

3.2.2.2 Precipitates parameters

All the observed precipitates by TEM in Chapter 2 : β”, β’, U2, B’ are considered in this simulation. The atomic volume of all these precipitates is considered equal to the one of the FCC Al matrix: $1.66 \times 10^{-29}\,\mathrm{m}^3$ [VIS 07]. In the DSC results of Chapter 2, pure Si precipitation happens at the Si-rich end of the gradient. This phase is therefore introduced in the model and its atomic volume considered is $2.046 \times 10^{-29}\,\mathrm{m}^3$ [ROY 05]. As mentioned in the section before, the nucleation mode of each possible precipitate will be considered homogeneous.

Chemistry of precipitates

The next precipitates data considered are mainly extracted from the TCAL4 database.

In TCAL4 database, the phase description of most of the precipitates does not allowed any change in composition whatever the temperature as they are described as stoichiometric compounds. In Figure 3.11, the chemistry of the precipitates at equilibrium with FCC domain are represented depending on the temperature and for the different nodes of the sample B.

In this figure, only one precipitate, β”, presents a variation of composition. This one depends on both temperature and composition of nodes. For the good use of PreciSo, the chemistry of the precipitates must be integer numbers. All the stoechiometric coefficients are therefore recalculated according to a mathematical algorithm to obtain integer numbers.

First, for each node and for each phase, the composition of the precipitate (x_{Al}, x_{Mg}, x_{Si}) was fixed with the solubility limit composition at T = 170 °C (x_{Al}^{170}, x_{Mg}^{170}, x_{Si}^{170}). Then, each composition is multiplied by an integer k and rounded to be an integer as well: $x_i = round(x_i^{170} \times k)$. The greatest common divisor (GCD) of the three content is calculated: $GCD(x_{\mathrm{Al}}, x_{\mathrm{Mg}}, x_{\mathrm{Si}})$. Each composition is then divided by this GCD: $x_i = x_i/GCD$. Several proportional factor (k between 34 and 100) were tested for each node and phase. Each time, the sum of the integer content,

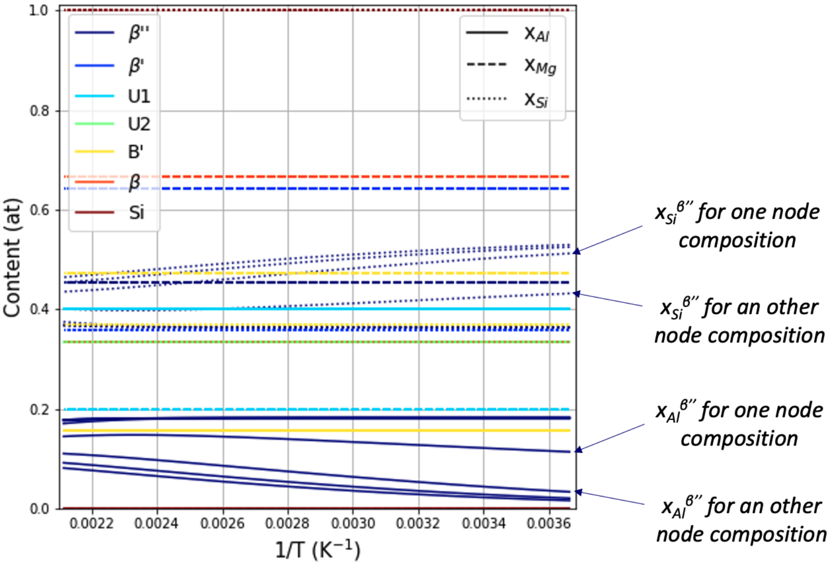

Figure 3.11: Chemistry of the precipitates at equilibrium with FCC domain depending on the inverse temperature and for 9 different node compositions of the sample B

$S = \sum x_i$, and the sum of the standard deviation to the initial content, $D = \sum(x^{170} - x_i/S)^2$, are calculated. The chemistry with the minimum S and D are conserved.

Finally, Table 3.1 is gathering the chemistry of each precipitate (except β”) obtained from this algorithm.

β”	β’	U1	U2	B’	Si
described further	Mg_9Si_5	Al_2MgSi_2	AlMgSi	$Al_3Mg_9Si_7$	Si

Table 3.1: Precipitates composition for hardness and DSC simulated samples

β” compositions obtained from the GCD algorithm are described depending on the node of the numeric sample in Table 3.2.

	Node 0	Node 1	Node 2	Node 3	Node 4	Node 5	6 - 10
A	$Al_2Mg_{14}Si_{15}$	$Al_2Mg_{13}Si_{14}$	$AlMg_6Si_6$	$AlMg_5Si_5$	$Al_3Mg_{11}Si_{10}$	$Al_4Mg_{11}Si_9$	$Al_2Mg_5Si_4$
B	$AlMg_6Si_6$	$AlMg_5Si_5$	$AlMg_4Si_4$	$Al_3Mg_9Si_8$	$Al_2Mg_5Si_4$	$Al_2Mg_5Si_4$	$Al_2Mg_5Si_4$

Table 3.2: β” chemistry for each node along the numeric gradients of samples A and B

Thermodynamic data extracted from solubility limits

To describe properly the stability of a precipitate phase, two aspects are important. The first one is its enthalpy of formation. Between two pure compounds (H=0), the formation of a stable intermediary phase is a gain in energy ($\Delta H < 0$). The enthalpy of formation here has a minimum. In the ternary system Al-Mg-Si, the convex hull caused by the high stability of Mg_2Si is represented in Figure 3.12a.

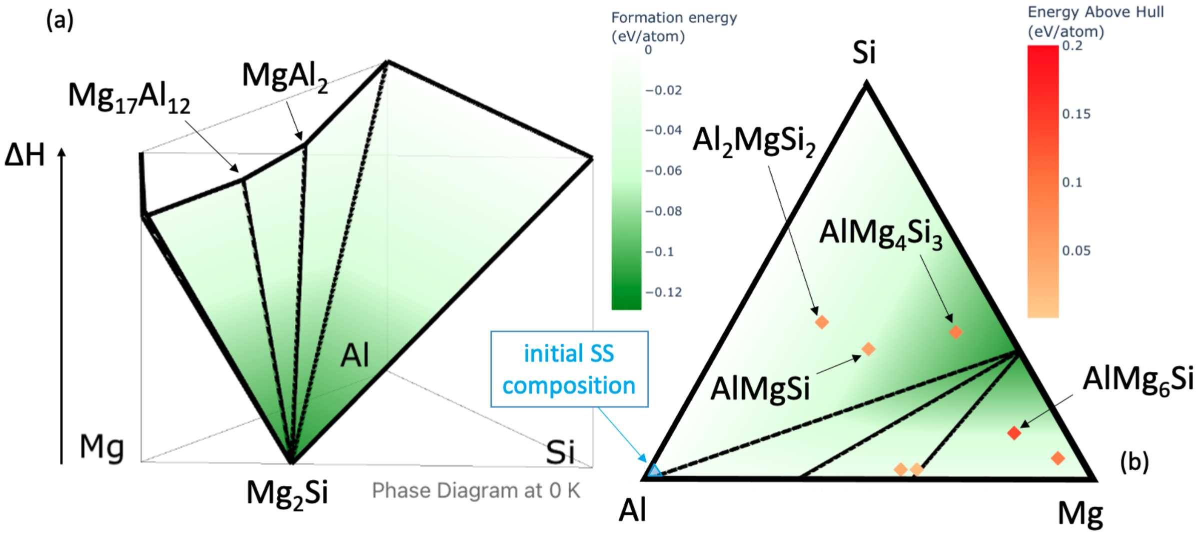

Figure 3.12: Thermodynamic stability at 0 K in Al-Mg-Si systems represented using formation enthalpy a: visualisation of the stable convex hull, b: positions and energy gap between the metastable precipitates and the convex hull [PRO 20]

The metastable phases are above that convex hull as presented in Figure 3.12b. The distance to that convex hull permits to estimate their deviation to stability.

In order to consider their precipitation, a second aspect is influencing. It is their distance with the SS composition compared to the one of the stable intermediary compound (Mg_2Si). Indeed the probability to reach compositions very far from the solid solution composition restrain its precipitation. All these aspects are thus taken in consideration in the calculation of the driving force equation 3.6.

As described in the literature review (equation 3.10), the solubility limit between matrix and precipitate permits to describe this thermodynamic stability thanks to two parameters: A and B. The variation of the solubility products ($\log_{10}(\mathrm{K}_s)$) of each precipitate with temperature (1/T) is presented in Figure 3.13. These solubility products were calculated from TCAL4 database for each node of the sample B.

Because of the differences of chemistry of β” along the gradient, β” has also different variations of solubility limit with temperature.

A and B parameters can be obtained using $\log_{10}(K_s) = A/T + B$. Using these data, the following tables 3.3 and 3.4 are reporting A and B values for the sample B.

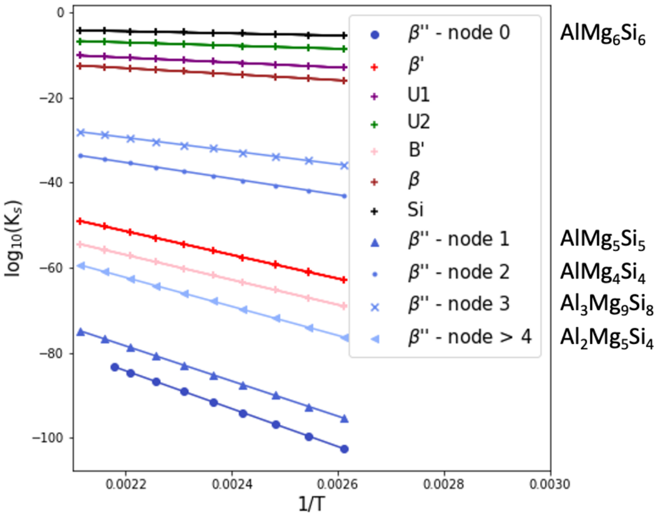

Figure 3.13: Evolution of solubility product with temperature (from TCAL4) for each possible precipitate in the sample B. Thermodynamic parameters A and B are extracted using $\log_{10}(K_s) = A/T + B$

Mg/Si atomic ratio	$A_{\beta''}$ (K^{-1})	$A_{\beta'}$ (K^{-1})	A_{U2} (K^{-1})	$A_{B'}$ (K^{-1})	A_{Si} (K^{-1})
0.1	19005	27828	3691	29308	2499
0.2	15775	27837	3692	29317	2498
0.4	12534	27849	3693	29329	2497
0.8	27732	27865	3698	29351	2495
1.6	14992	27900	3685	29301	2493
2.4	14989	27804	3678	29231	2491
3.2	14976	27761	3674	29193	2490
3.9	14969	27740	3672	29175	2490
4.3	14965	27730	3671	29167	2490

Table 3.3: Thermodynamic parameters A of each precipitate depending on their position in the graded sample B (from TCAL4)

From these thermodynamic parameters A, it is possible to have access to the enthalpy of formation ΔH (equation 3.10) which is useful for DSC simulation. The Table 3.5 is summarising the values of ΔH for the sample B.

The thermodynamic parameters of the sample A are gathered in the Appendix D.

Mg/Si atomic ratio	$B_{\beta''}$	$B_{\beta'}$	B_{U2}	$B_{\mathrm{B'}}$	B_{Si}
0.1	6.5597	9.8288	1.1086	7.5200	1.1178
0.2	5.3314	9.8319	1.1090	7.5235	1.1177
0.4	4.0595	9.8361	1.1097	7.5290	1.1174
0.8	10.5349	9.8445	1.1178	7.5471	1.1169
1.6	6.3788	9.8993	1.1084	7.5226	1.1164
2.4	6.4592	9.8199	1.1065	7.5044	1.1160
3.2	6.4748	9.8112	1.1056	7.4961	1.1158
3.9	6.4791	9.8070	1.1052	7.4923	1.1158
4.3	6.4806	9.8049	1.1050	7.4906	1.1158

Table 3.4: Thermodynamic parameters B of each precipitate depending on their position in the graded sample B (from TCAL4)

Mg/Si	$\Delta H_{\beta''}$ (J.mol^{-1})	$\Delta H_{\beta'}$ (J.mol^{-1})	ΔH_{U2} (J.mol^{-1})	$\Delta H_{\mathrm{B'}}$ (J.mol^{-1})	ΔH_{Si} (J.mol^{-1})
0.1	363826	532738	70655	561072	47837
0.2	301990	532912	70673	561241	47827
0.4	239954	533127	70699	561472	47803
0.8	530900	533446	70790	561881	47761
1.6	287010	534115	70553	560921	47716
2.4	286949	532263	70408	559589	47684
3.2	286699	531457	70330	558861	47669
3.9	286559	531052	70296	558518	47665
4.3	286491	530852	70281	558359	47664

Table 3.5: Molar formation enthalpy in J.mol^{-1} of each precipitate depending on their position in the graded sample B (from TCAL4)

Nature of the interface between matrix and precipitates

As presented in the literature review, the driving force is also in competition with the surface energy γ required for the interface growth between matrix and precipitate. Driving force and surface energy are both taken in consideration in the concept of energy barrier equation 3.3.

The article of Zhang *et al.* [ZHA 10] reminds that the coherent phase β" has an interfacial energy estimated around $0.1\,\mathrm{J{\cdot}m^{-2}}$ whereas semi-coherent precipitates surface energy should be situated between 0.3 and $1\,\mathrm{J{\cdot}m^{-2}}$ [LIU 96, WAN 07].

Du *et al.* [DU 17] simulated precipitation in Al-Mg-Si alloys using KWN model with similar precipitates. As Povoden *et al.* [POV 13], they have calculated the interfacial energies based on the solution enthalpy of the precipitation phase (also named the Broken-bond method developped by Kozeschnik *et al.* [KOZ 07, SON 09]). The interfacial energies γ used in Du's simulation were actually different, see Table 3.6.

Interface	Used by Du	Calculated with Kozeschnik's solution enthalpy
β" and FCC phases	0.084	0.157
β' and FCC phases	0.18	0.198
U1 and FCC phases	0.18	0.112
U2 and FCC phases	0.18	0.121
B' and FCC phases	0.18	0.151

Table 3.6: Surface energies ($\mathrm{J.m^{-2}}$) between FCC matrix and the precipitates [DU 17]

These values are complicated to obtain and very specific to the alloy specificity. They are often adjustable parameters for precipitation modelling as they will be in the present simulation.

The morphology of the precipitates are all considered in rod shape. For pure Si, its shape factor (introduced in a last section) q equals 2 in order to obtain a sphere. The other shape factors q were extracted from TEM. An average was performed on numerous precipitates during a specific ageing state of Chapter 2:

- $q_{\beta''} = (43 \pm 26)$ from B-R1-Si sample (T6 state) and is fixed to 40
- $q_{\beta'} = (40 \pm 25)$ from B-R3-Mg sample (over-aged) and is fixed to 40
- $q_{U2} = (21 \pm 13)$ from B-R3-Si sample (over-aged) and is fixed to 20
- $q_{B'} = (100 \pm 26)$ from B-R3-Si sample (over-aged) and is fixed to 100

These aspect ratios were confronted to the precipitates dimensions of Meyruey *et al.* [MEY 18b].

3.2.3 Choice and adjustments of parameters

Various input parameters have been fixed in the last section but numerous ones are adjustable parameters. In order to provide the best adjusted model, experimental data are confronted to simulations.

3.2.3.1 Adjustment of surface energy for each precipitate

Using TEM results: phase identification and precipitate size

In the last chapter, the sample B was characterised by TEM after ageing at 170 °C. Metastable precipitates were identified and measured for some compositions. These results were obtained for specific compositions sometimes quite different from the composition of the simulated nodes. For TEM and APT samples (B-R), on Mg-side, the mean uncertainty on Mg/Si atomic ratio is 1.3 whereas for Si-side, this uncertainty is set at 0.7 (see Appendix C). The TEM and APT results can thus be confronted to the closest node composition according to these uncertainties.

The surface energy γ of each precipitate is adjusted by starting with precipitation simulations of β” alone. Figure 3.14 is representing the effect of the variation of β” surface energy on its precipitation for a node of composition Mg/Si = 0.8 of the sample B.

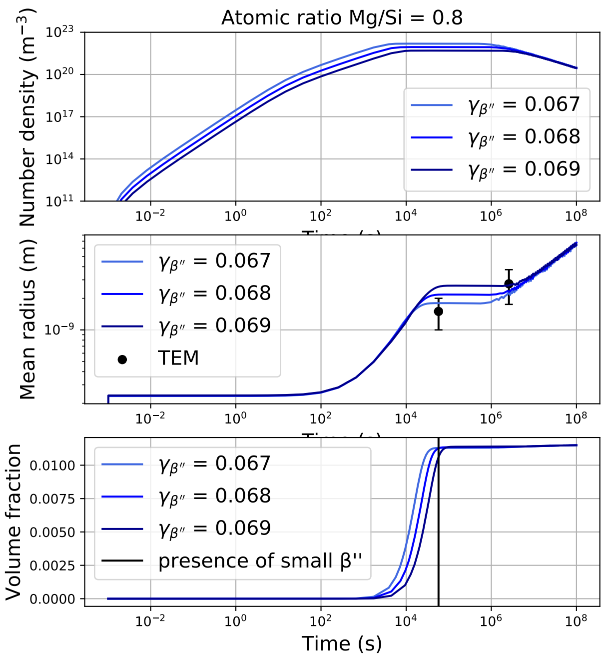

Figure 3.14: Sensitivity study of the energy surface parameter on precipitation of β” (via number density, mean radius and volume fraction) on a node of composition Mg/Si = 0.8 from sample B. Literature diffusion coefficients were here multiplied by 20.

While $\gamma_{\beta''}$ decreases, the density number of β” precipitates rises while the mean radius decreases. For the smallest $\gamma_{\beta''}$, the maximum volume fraction of precipitates is obtained the fastest. Experimental data from TEM are confronted to the different model curves. This figure is an example, the adjustments of $\gamma_{\beta''}$ were actually conducted on several nodes.

Then β' was added to the model and its γ adjusted. The Figure 3.15 is presenting the impact of the variation of $\gamma_{\beta'}$ on both β'' and β' precipitations in a node from the sample B of composition Mg/Si = 1.6.

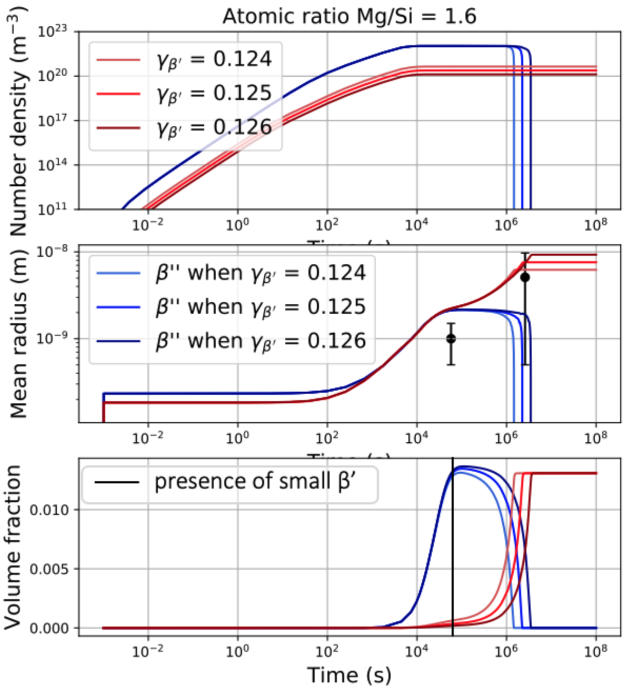

Figure 3.15: Sensitivity study of the surface energy parameter of β' on precipitation (via number density, mean radius and volume fraction) on a node of composition Mg/Si = 1.6 from sample B. Literature diffusion coefficients were here multiplied by 20.

In the same way as previously, the surface energy of β' impacts the precipitation of β'. Here, the precipitation of β' influenced also the precipitation of β". If $\gamma_{\beta'}$ decreases, there will be more small β' precipitates formed earlier and β" precipitates will dissolve earlier. In the same way, TEM results are confronted to the models and the adjustments of $\gamma_{\beta'}$ were also influenced by the other nodes of the sample B.

Finally, U2 and B' are added. The sensitivity study is presented in the Figure 3.16 regarding to the surface energy of B' precipitates. The composition node of the sample B has here a Mg/Si atomic ratio of 0.8.

The influence of one precipitate surface energy on the others are clear. Once again, this composition fit is one between several.

It is also interesting to verify the influence of diffusion coefficients on all these precipitations.

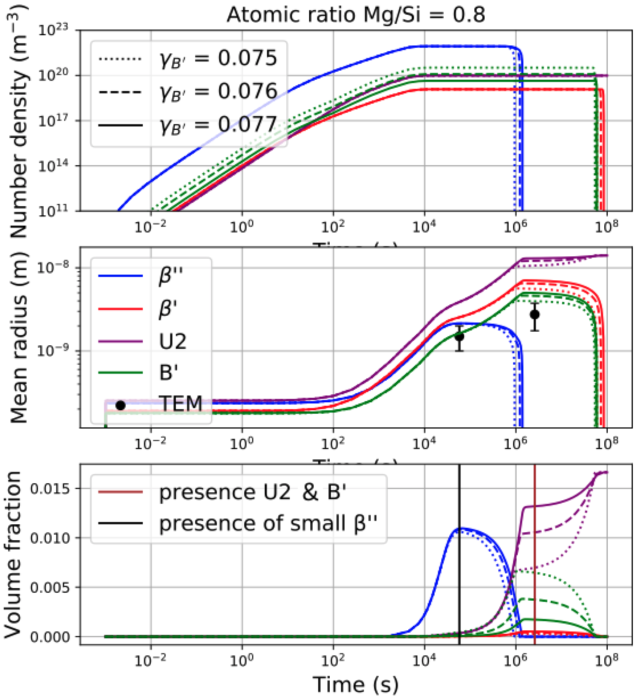

Figure 3.16: Sensitivity study of the surface energy parameter of B’ on precipitation (via number density, mean radius and volume fraction) on a node of composition Mg/Si = 0.8 from sample B. Literature diffusion coefficients were here multiplied by 20.

In the next Figure 3.17 of a node of composition Mg/Si = 4.3 from the sample B, the diffusion coefficients of Mg and Si is multiplied by different factors as evoked in the last section.

Logically, by accelerating diffusion, precipitation is also accelerated. In order to fit mean radius more closely, the diffusion coefficients of Mg and Si will be multiplied by 15 from the extrapolated literature values.

Si was added and adjusted in a second time using DSC simulation (presented in the next section). The final surface energies of the precipitate are finally presented, along with the shape factor q, in the Table 3.7.

Precipitate	β”	β’	U2	B’	Si
γ (J.m^{-2})	0.068	0.125	0.106	0.076	0.311
shape factor q	40	40	20	100	2

Table 3.7: Adjusted precipitate parameters on sample B after experimental TEM confrontation

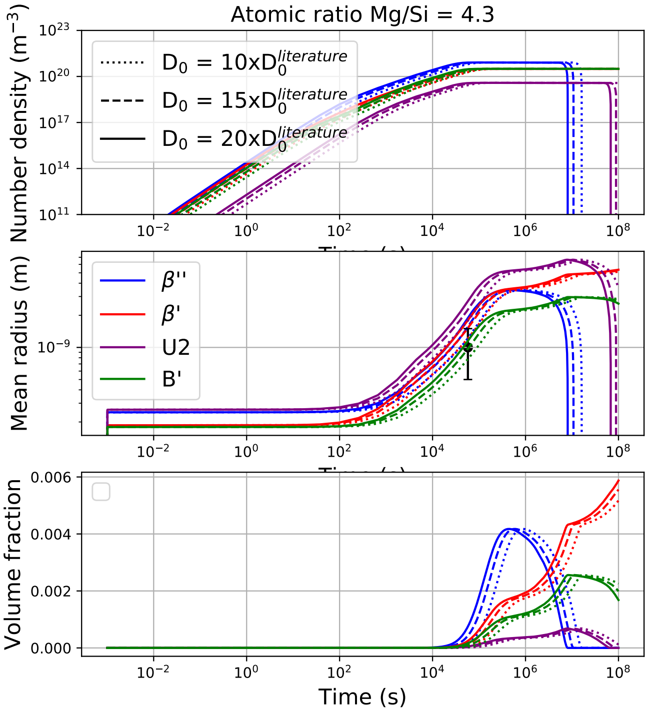

Figure 3.17: sensitivity study of the diffusion coefficients Mg and Si on precipitation (via number density, mean radius and volume fraction) on a node of composition Mg/Si = 4.3 from sample B

Figure 3.18 is representing the evolution of the volume fraction of each precipitate for each node during ageing at 170 °C with all the presented parameters for the sample B. Experimental TEM phase identification used for fitting are also reported.

This figure must be actually visualised with Figure 3.19 which presents the evolution, for each node, of the mean radius and the critical radius of each considered precipitate. This figure is also confronted to the experimental mean radius obtained from TEM measurements.

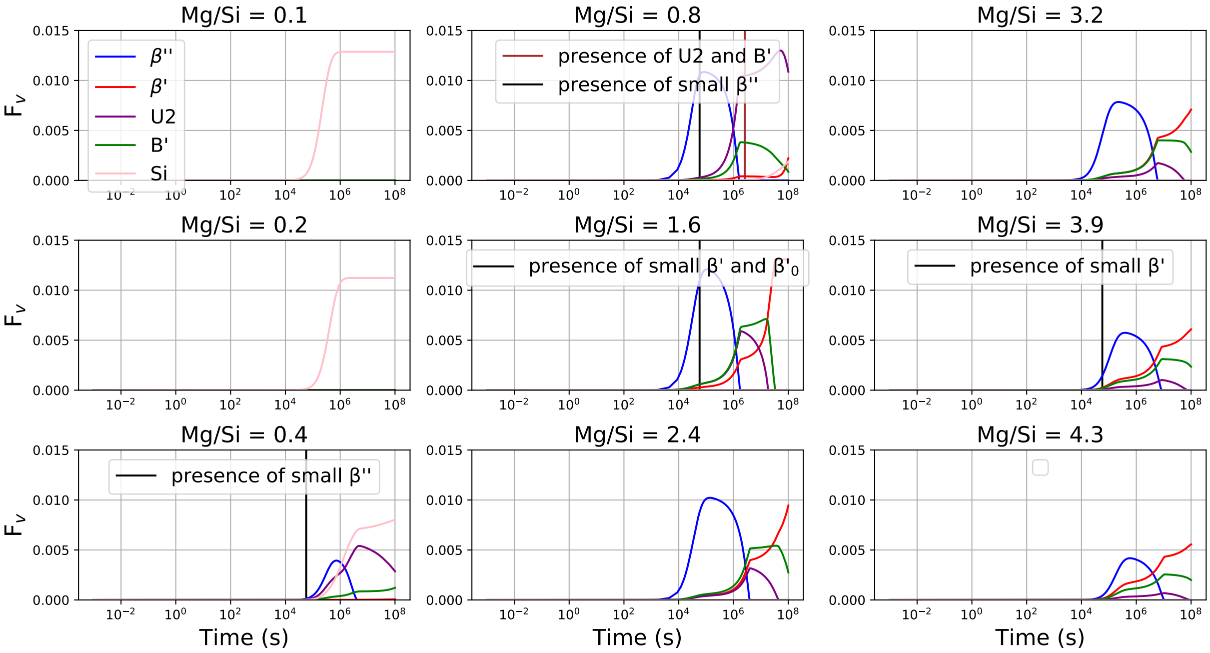

Figure 3.18: Confrontation between experimental TEM results and volume fraction simulation during ageing at 170 °C on sample B for each node

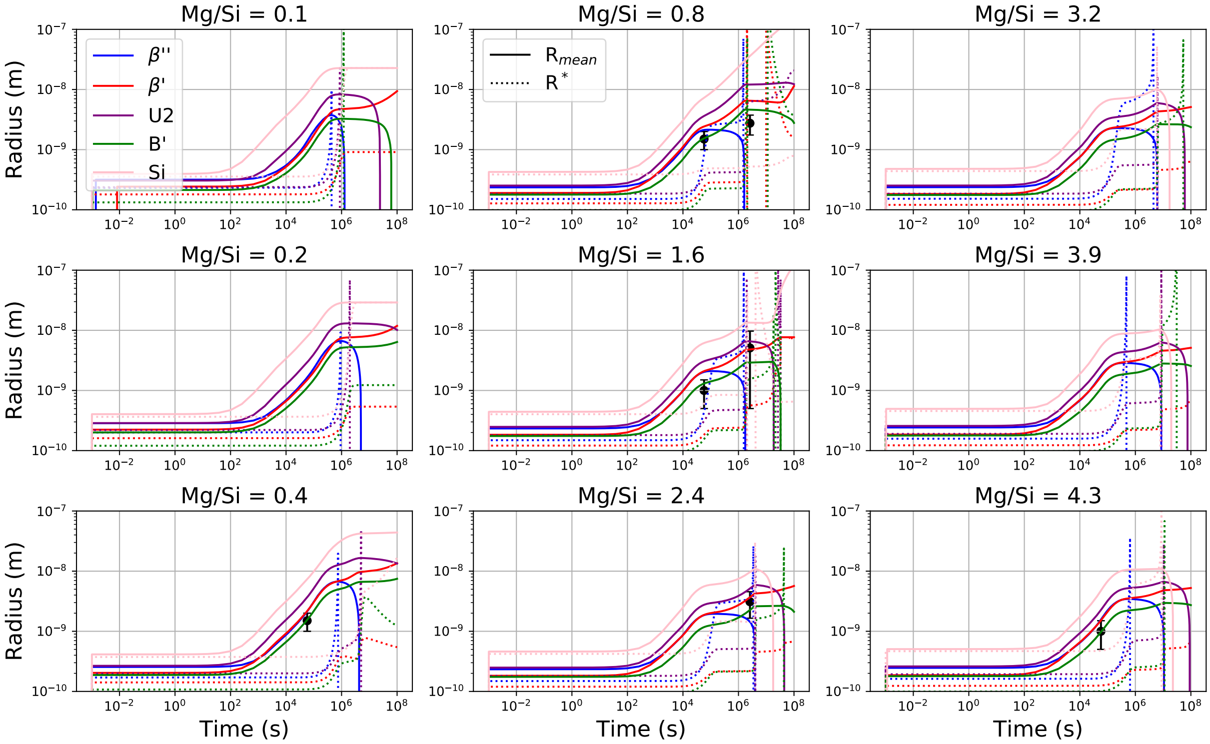

Figure 3.19: Confrontation between experimental TEM results and radius simulation during ageing at 170 °C on sample B for each node

These simulations are in good agreement with the data obtained by TEM. For Mg/Si = 0.4, the β" simulated precipitates have a small volume fraction but their mean radius correspond to the ones measured. For Mg/Si = 1.6 and 3.9 near T6 (16h), the volume fraction of β" is higher than the one of β' whereas experimentally β' was identified and not β". It is important to recall that these TEM identification were complicated, partly due to the small sizes of the precipitates. Indeed many precipitates were not identified and could represent the large population of β".

Confrontation of solid solution evolution with APT results

The evolution of the solid solution predicted by this precipitation model is also compared to the APT measurements. This confrontation is presented in Figure 3.20.

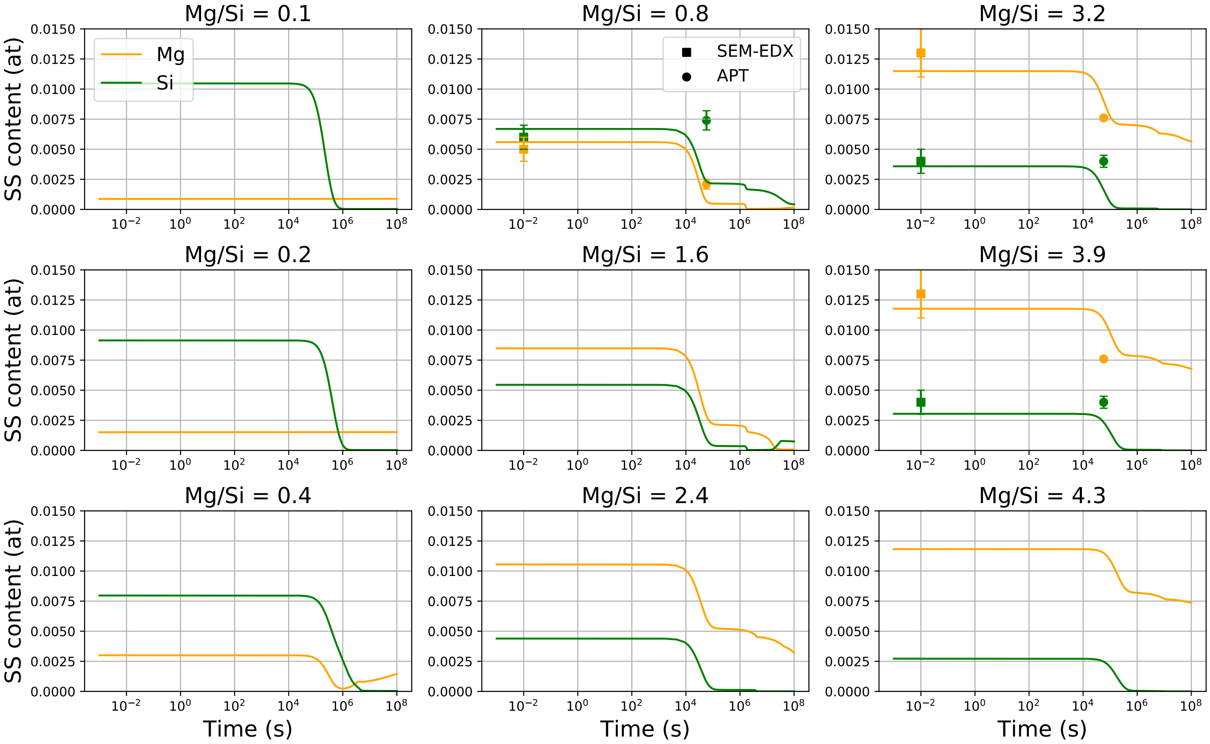

Figure 3.20: Confrontation between solid solution content evolution simulation and experimental APT results during ageing at 170 °C on sample B for each node

These results are satisfying. The experimental diminution of Mg before Si is surprising though. It would have been interesting to have more experimental data, for example, at longer ageing time.

Limits of the thermodynamic parameters for continuous heating DSC simulations
The variation of heat due to the formation of one type of precipitates is described as :

$$\Delta Q = \Delta H_m \times \Delta n_{transformed} \tag{3.41}$$

$$= \Delta H_m \times \frac{\Delta n_t}{\Delta V_t} \times \frac{\Delta V_t}{V_T} \times V_T \tag{3.42}$$

$$= \Delta H_m \times \frac{1}{v_m^p} \times f_v \times \frac{m_T}{\rho_{Al}} \tag{3.43}$$

with ΔH_m *the molar formation enthalpy,* Δn_t *the number of moles transformed and* v_m^p *the molar precipitate volume*

During DSC measurements, several precipitates are involved and all their released heat are summed. The energy is measured per unit of time. It is therefore a power (W = J.s^{-1}). Finally this power is often divided by the total mass m_T in order to be normalised. The previous equation is therefore giving:

$$\frac{1}{m_T}\frac{dQ}{dt} = \frac{1}{\rho_{Al}} \sum \left(\frac{df_v^i}{dt} \frac{\Delta H_m^i N_A}{v_i^p} \right) \tag{3.44}$$

with N_A *the Avogadro constant and* i *the precipitate*

It is therefore possible to simulate DSC experiments from PreciSo volume fractions. In the next Figure 3.21, simulated DSC experiments by PreciSo on the sample B (with the previously presented parameters) are confronted with the true DSC experiments (conducted in the Chapter 2) in the same conditions: from −25 °C to 550 °C with a heating rate of 5 °C/min.

For all the nodes, the two curves are not properly fitting, showing the limits of this model. The main issue is that in non isothermal conditions, precipitates occur at much higher temperature as compared to isothermal treatments, when the driving force is much smaller and thus nucleation mechanisms way different (heterogeneous vs homogeneous). One can not expect the same simple model to apply equally to both conditions.

In addition, for β", the chemistry was chosen for a specific temperature of 170 °C. And finally, at least two important precipitates are not considered in the model because they were not observed: U1 and β.

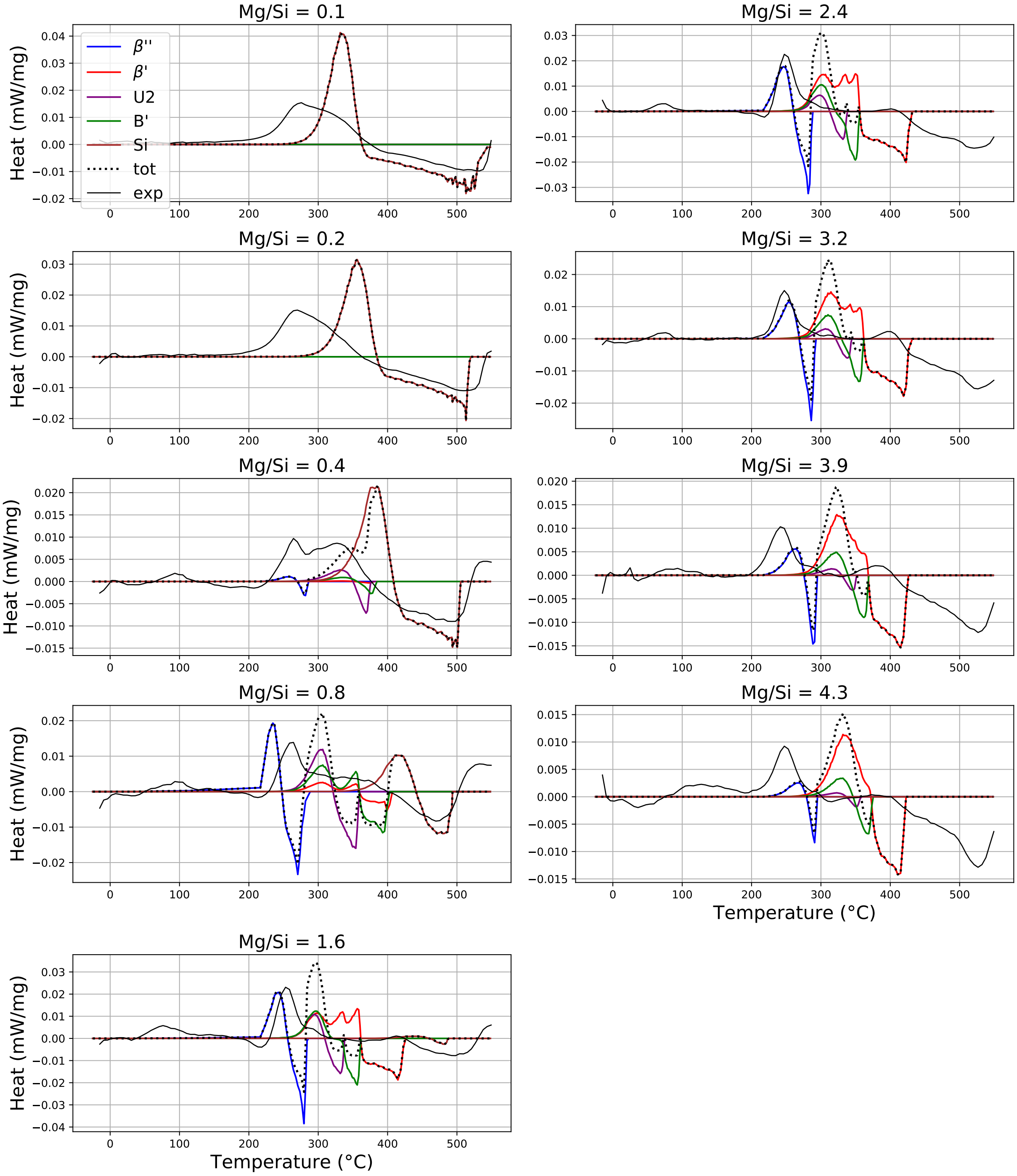

Figure 3.21: Sample B confrontation between experimental DSC results (full line) and simulated heat (dash line) during standard continuous heating for each node

3.2.3.2 Choice of the mechanical parameters

In this section, six parameters have to be adjusted: for each precipitate, the critical radius r_c between sheared and by-passed mechanisms, plus the mechanical parameter β. For these mechanical adjustments the microhardness results performed on the sample A in Chapter 2 are used. These results are converted to yield strength using Myhr conversion (used in Chapter 1): HV $= 0.33\sigma_y + 16$ [MYH 01].

Pure Si is a stable phase. The precipitates interactions with dislocations are thus only considered as by-passed mechanism. By fixing $r_c^{Si} = 1\,\text{nm}$, the fraction of sheared precipitates is null as sought.

As evoked previously, the mechanical parameter β is a constant representing the line tension applied to the dislocation. It depends on the form and the nature of dislocations. For the extreme Si excess node, only pure Si is precipitating and its r_c is fixed. This node was therefore used for the sensitivity study of the mechanical parameter β in Figure 3.22.

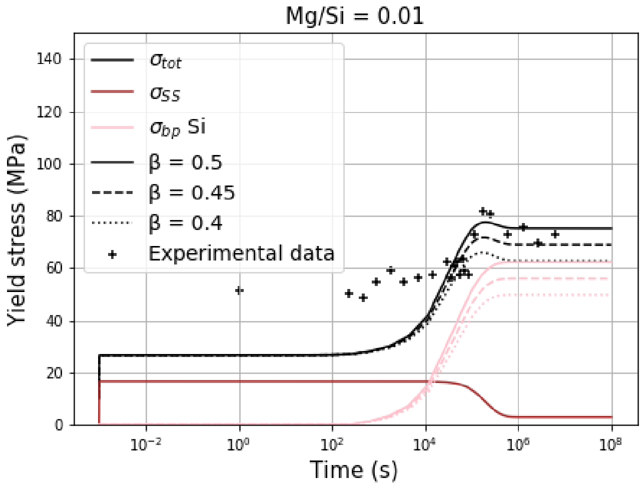

Figure 3.22: Sensitivity study of β on simulated yield strength during ageing at 170 °C for the node of composition Mg/Si = 0.01 of the sample A and confrontation with experimental microhardness results (converted in yield strength following Myhr conversion [MYH 01])

When β increases, the by-passed contribution to yield strength (σ_{bp}) increases, increasing as well the total yield strength (σ_{tot}). β is fixed at 0.5 for the next simulations.

In the Figure 3.23, the influences of $r_c^{\beta''}$ variation on yield strength is presented for the node of composition Mg/Si = 0.6 of the sample A.

The best fit is obtained for $r_c^{\beta''} = 3\,\text{nm}$.

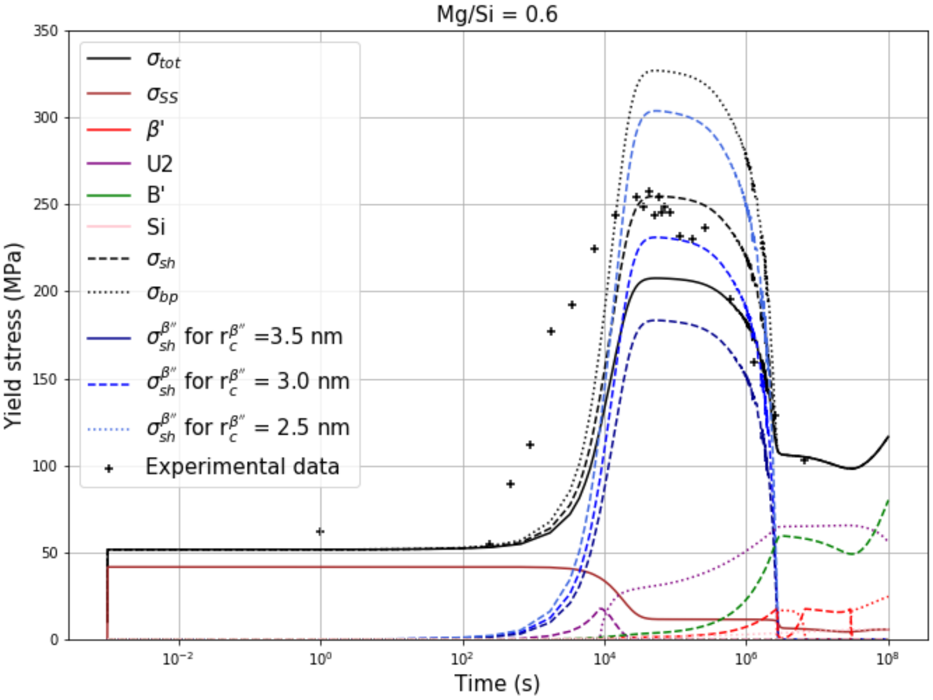

Figure 3.23: Sensitivity study of $r_c^{\beta''}$ yield strength simulation during ageing at 170 °C for the node of composition Mg/Si = 0.6 of the A sample and confrontation between experimental microhardness results (converted in yield strength following Mhyr equation [MYH 01])

With this fitting method, each r_c have been determined. They are all summarised in Table 3.8.

Precipitate	β”	β’	U2	B’	Si
r_c (nm)	3	7	2	7	1
β	0.5				

Table 3.8: Adjusted precipitate parameters on sample A after experimental microhardness confrontation

The simulated and the experimental yield strengths are presented in Figure 3.24 for all the nodes of the sample A.

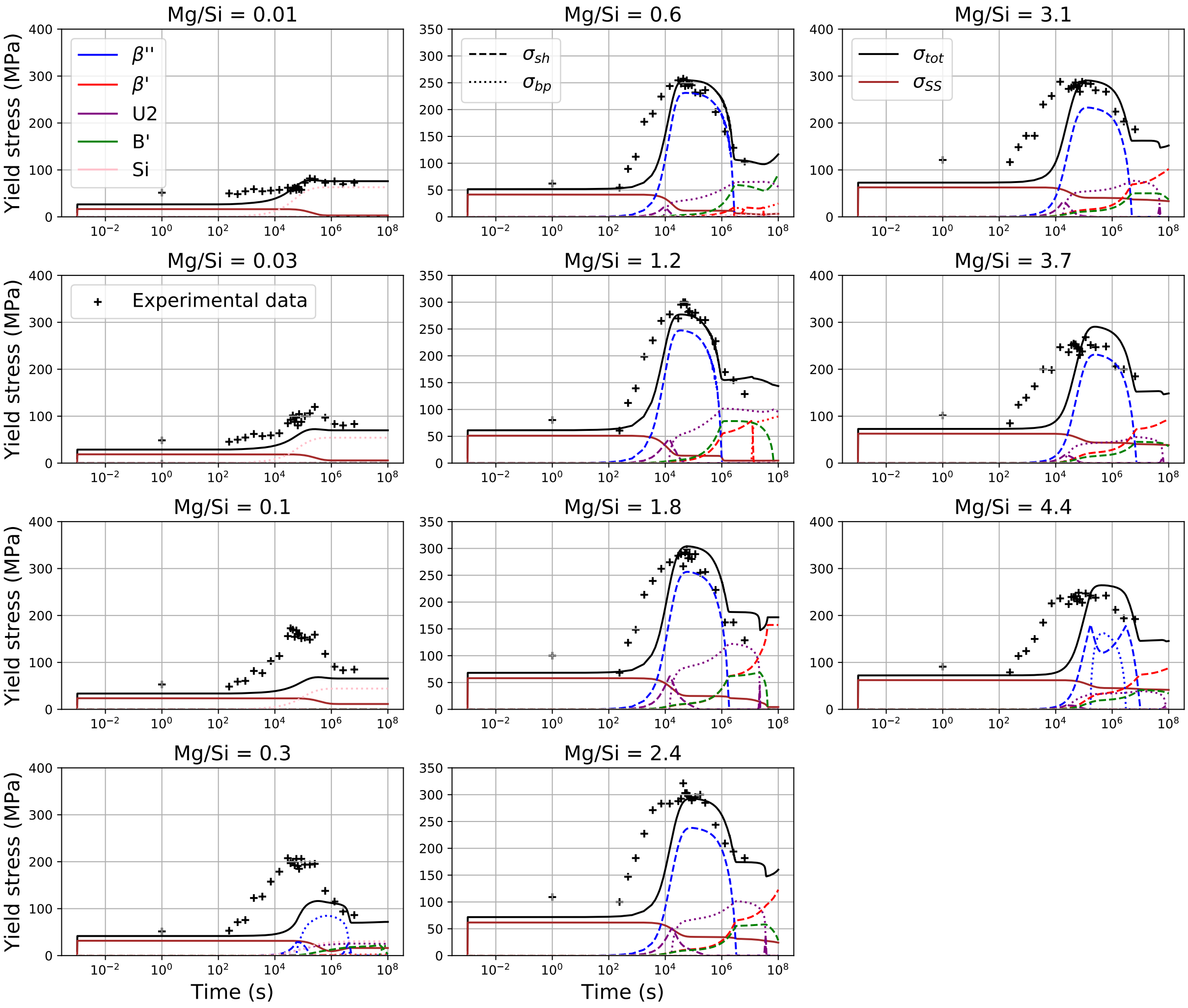

Figure 3.24: Confrontation between yield strength evolution simulation and experimental microhardness results (converted into yield strength) during ageing at 170 °C on sample A for each node

The yield strength model is quite well representative of the experimental results on a large range of compositions. The β" peak is thinner though than for experimental data. There is also a delay of the coherent peak, more and more important with Mg rise, for nodes with Mg/Si $\geq$ 1.8. Finally, the yield strength of nodes with a composition of $0.1 \leq$ Mg/Si ≤ 0.3 is completely under estimated. Some of these inconsistencies could be due to the non consideration of clusters in the model whereas its contribution to hardness is known.

Now that all the parameters have been adjusted, the coupled precipitation/hardening model for graded Al-Mg-Si alloys can be exploited. All the important parameters detailed in this chapter are gathered in Table 3.9.

	Parameters	Value	Sources
		Precipitation simulation	
Ageing conditions	Temperature	T = 170 °C	
	Time	$t = 1 \times 10^{8}$ s	
System	Number of nodes	N = 11 or 9	This work
	Surface	$S = 1\,m^{2}$	This work
Matrix	Lattice parameter	a = 4.05 Å	[RAV 04]
	Atomic volume	$V_{at}^{Al} = 1.66 \times 10^{-29}\,m^{3}$	[VIS 07]
	Solute diffusion coefficients	$D_{0}^{Mg} = 15 \times 6.1 \times 10^{-5}\,m^{2} \cdot s^{-1}$	Adjusted
		$Q^{Mg} = 127\,kJ$	[MIN 83]
		$D_{0}^{Si} = 15 \times 2 \times 10^{-4}\,m^{2} \cdot s^{-1}$	Adjusted
		$Q^{Si} = 136\,kJ$	[FUJ 78]
Precipitates	Chemistry	x_{i}^{p} see Table 3.1 and 3.2	TCAL4
	Atomic volume	$V_{at}^{Si} = 2.046 \times 10^{-29}\,m^{3}$	[ROY 05]
		$V_{at}^{others} = 1.66 \times 10^{-29}\,m^{3}$	[VIS 07]
	Thermodynamic parameters	A see Table 3.3	TCAL4
		B see Table 3.4	TCAL4
	Shape factor	q see Table 3.7	This work
	Surface energy	γ see Table 3.7	Adjusted
		Mechanical simulation	
Matrix	Pure Al yield strength	$\sigma_{0} = 10\,MPa$	[DES 98]
	Microstructure constant	$k = 90\,MPa \cdot \mu m^{1/2}$	[COR 16]
	Grain size	d = 15 µm	This work
	Solid solution mechanical parameter	$k_{Mg} = 52.9\,MPa \cdot wt\%^{-2/3}$	This work
		$k_{Si} = 12.5\,MPa \cdot wt\%^{-2/3}$	This work
Dislocations	Burger vector	$b = 2.86 \times 10^{-10}\,m$	[BAR 14]
	Line tension constant	$\beta = 0.5$	Adjusted
Precipitates	Taylor factor	M = 2	[DES 98]
	Young modulus	E = 71.5 GPa	[MAI 10]
	Poisson coefficients	$\nu = 0.33$	[SHA 00]
	Critical radius	r_{c} see Table 3.8	Adjusted

Table 3.9: Parameters for coupled precipitation/hardening models in graded Al-Mg-Si alloys.

3.3 Model output: link between microstructural and mechanical evolutions

In this section, the coupled precipitation/hardening model on Al-Mg-Si graded alloys, described in the previous part, will be used in order to better understand the link between microstructure and mechanical properties. In the first part, the simulations will remain in the framework of the parameters optimisation: during an ageing at 170 °C. Then, the model will be investigated outside its fitting conditions through Time-Temperature-Transformation diagrams.

3.3.1 Influence of composition on mechanical properties during ageing at 170 °C

3.3.1.1 Final confrontation between microhardness results and yield strength model

From the graded coupled model, a lot of data can be extracted. For each specific ageing time, a microstructure overview (f_v,r_{mean},r^*,N,x^{SS}) is extractable for all the gradient. It is also possible to focus on one composition (one node) and to obtain its kinetics of precipitation. Similarly, a yield strength overview on all the gradient or evolution for one composition is extractable. To have a correct global idea of the influence of composition on hardening kinetics, the data are plotted, in Figure 3.25, as a colormap and is put in parallel to the experimental one presented in Chapter 2.

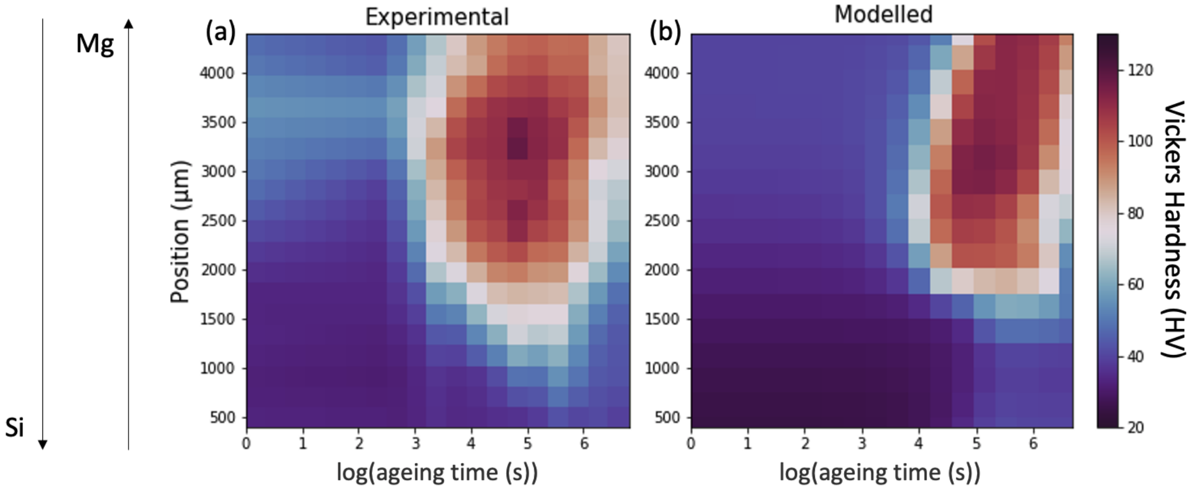

Figure 3.25: Confrontation between experimental hardness and modelled hardness during ageing at 170 °C depending on the position in the gradient A

This model is representing quite well the evolution of yield strength during 170 °C ageing along the gradient A. The modelled domain with high mechanical properties is smaller though. Also, the strong Si excess compositions does not harden at all or sufficiently. And, on all the gradients, the hardening seems delayed (as discussed in the previous chapter). Finally, the variations of hardness are stiffer, especially at the beginning of the precipitation, creating only a plateau instead of a peak. These differences could be mainly explained by one important factor: the non consideration of clusters and GPZ in the model.

On the Figure 3.26, the colormap are plotted depending on Mg/Si instead of the position. It is here important to remind that there is a variation of Mg_2Si SS content between the different ratio (this second variation is also considered in the model).

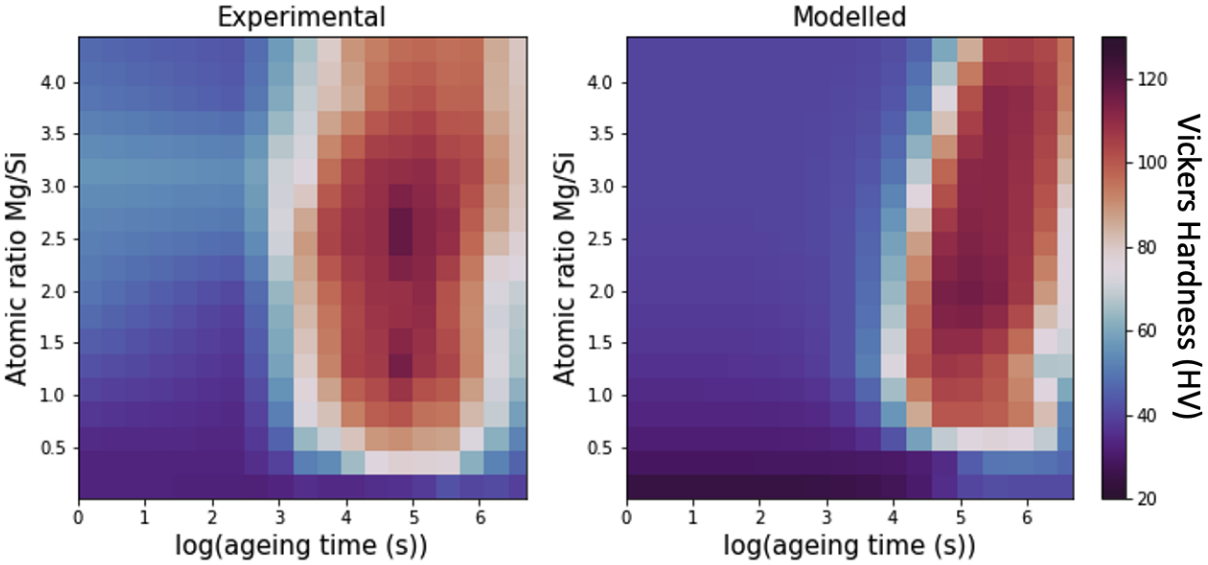

Figure 3.26: Confrontation between experimental hardness and modelled hardness during ageing at 170 °C depending on the atomic ratio Mg/Si within the gradient A

With the model, only one maximum is present for the atomic ratio Mg/Si = 2.0 instead of two local maxima (at Mg/Si = 2.4 and 1.2). This large peak seems to originate from two different contributions though.

3.3.1.2 Phase domains influencing hardening phenomenon

To better understand the contribution of each phase to the mechanical properties, hypothetical precipitation models are used. First, the mechanical results are presented in Figure 3.27a for a model with only β" as possible phase. On this same figure, the volume fraction evolution of each phase are plotted, using three curves, if $f_v^{max} > 0.002$.

In this figure, the high-hardening area is larger than previously, on the long ageing times, than when β', U2 and B' are precipitating (in average 10^8 against 10^7 seconds). The maximum hardness values are following a ridge for Mg/Si between 1 and 2.5 and two maxima are noted for Mg/Si = 1.8 and 1.2. In this gradient A, the maximum SS content in Mg_2Si is indeed obtained for Mg/Si = 1.8. Finally, the chemistry of the precipitate $Al_4Mg_{11}Si_9$ (Table 3.1 sample A node 5) with the nearest ratio to its initial SS node ratio is of 1.2. The model is in agreement with the assumption made in Chapter 2. Excess of Si and Mg_2Si content are the two major contributions influencing the β" hardening and therefore the general hardening of Al-Mg-Si alloys.

In this part, the interpolation for the model was performed with hundreds of points for both Mg/Si and ageing time variables whereas only 10 nodes were actually simulated on the Mg/Si axis. This feature explains the observed horizontal lines for Mg/Si around 1.8 and 3.8. In order

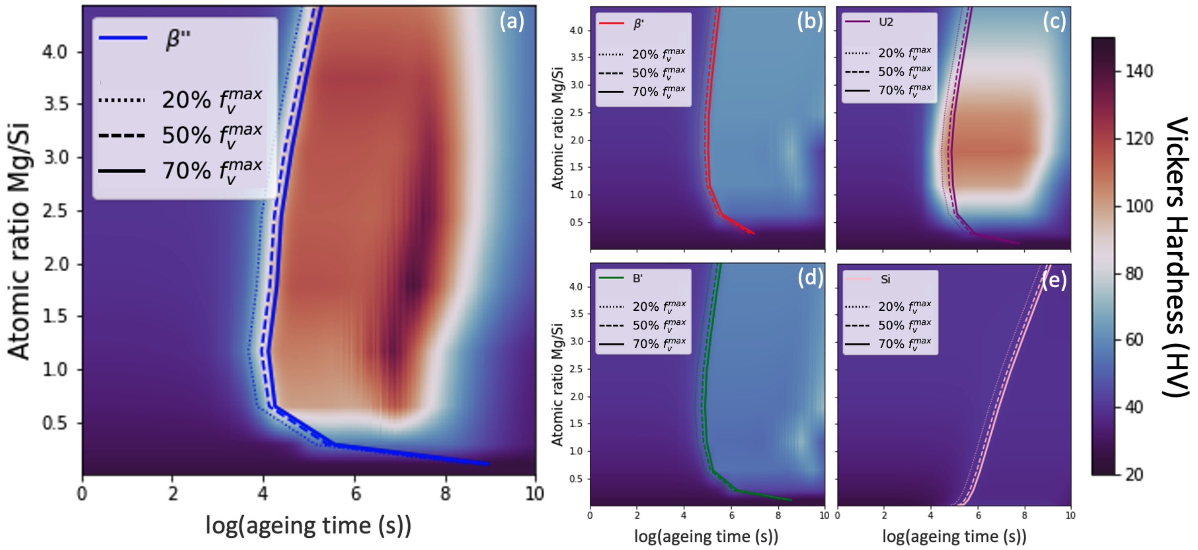

Figure 3.27: Modelled hardness during 170 °C ageing along the A gradient while considering only β" (a), β' (b), U2 (c), B' (d) or Si (e) precipitation

to have a sufficient precise figure provided by the model, a gradient of at least 20 nodes should be simulated.

The same method was used to provide the figures 3.27b, 3.27c, 3.27d and 3.27e with β', U2, B' and Si phases respectively.

β' and B' metastable phases have very low contribution to the modelled yield strength because of their high critical radius ($r_c = 7\,\text{nm}$). Indeed their critical radius have been adjusted in this way probably because their precipitation is overestimated. These excessive precipitations were also visible with the DSC simulation (Figure 3.21). Indeed, no volume fractions were extracted from ASAXS to properly fit the model during the three semi-coherent phases precipitations. Additional TEM experimental data could have been also useful to define mean radius for each phase.

Each maximum of semi-coherent precipitations seems, as expected from their chemistry, situated in the Si excess contents especially for B'. Additional nodes would have been valuable here as well to describe more precisely the U2 domain as instance.

Volume fraction curves of U2 and B' does not represent the variation of f_v^{max} even if they are clearly less important on Mg-side than on Si-side. f_v^{U2} curves are still present on the Mg edge ($f_v^{max,U2} > 0.002$) only because the other phases are not considered.

Figure 3.28 represents the influence of the real phase regions on hardening for short to very long ageing times. Note that for the very long ageing times, two phases are missing β and U1.

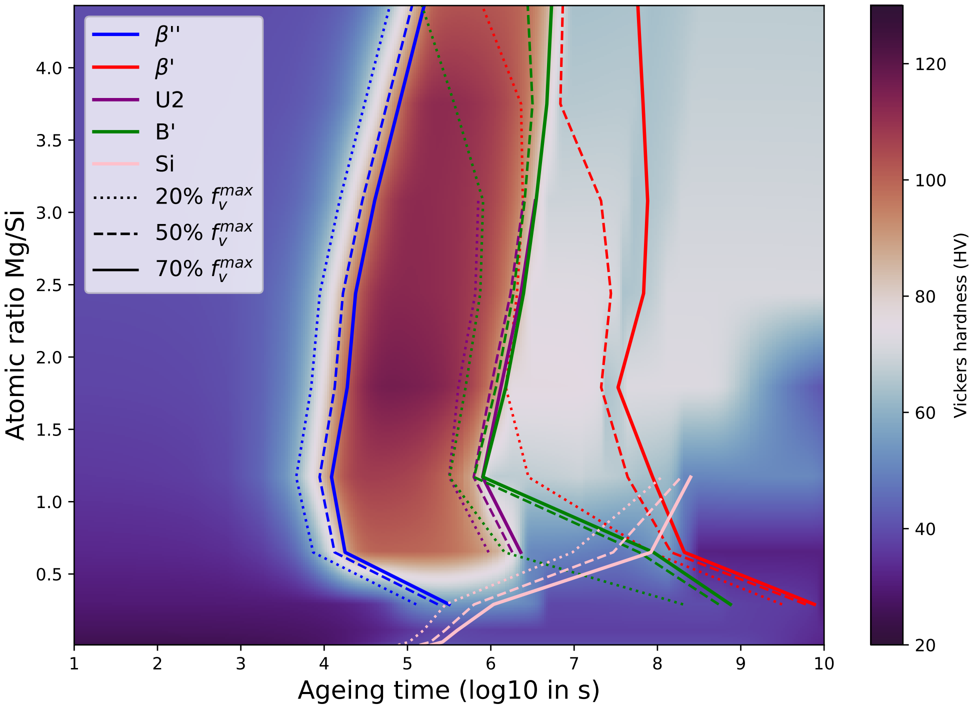

Figure 3.28: Final modelled hardness during 170 °C ageing along the A gradient

With this model, the extreme Si excess compositions (Mg/Si $<$ 0.3) present only precipitation of pure Si. Indeed on the Si-edge of the gradient, no Mg was present whereas on Mg-edge sufficient Si is present to form β metastable phases. Then, for the initial compositions with 0.3 $\leq$ Mg/Si $\leq$ 0.7, β" precipitates before pure Si, which precipitates before the semi-coherent phases B' and β'. With initial compositions with 0.7 $<$ Mg/Si ($<$ 3.0), a supplementary semi-coherent phase is added to the precipitation sequence: U2. Finally, for initial compositions with Mg/Si $>$ 1.2 pure Si does no longer precipitate sufficiently. From this composition until the Mg-edge (Mg/Si = 4.5), β' arrives more and more quickly whereas β" arrives more and more slowly. At the same time, Figure 3.18, there is actually less and less precipitation of U2 and B' even if B' arrives at one point earlier than for compositions with Mg/Si $<$ 3.

Now, the volume fraction evolution of each phase shows that most of the mechanical properties improvement are due to the precipitation of β". β" arrives the earliest for compositions with Mg/Si near 1. The maximum yield strength is obtained for compositions with Mg/Si around 1.8. It is indeed the node for which the initial SS content Mg_2Si is maximum. This composition is not the same as the one measured with hardness characterisations (Chapter 2 or Figure 3.26).

This specificity might be exhibited by taking in consideration clusters. If the model takes in consideration the clusters though, the overall yield strength values will be higher than in the experiment (Figure 3.26). The mechanical parameter β should thus be readjusted.

3.3.2 Influence of composition on mechanical properties during ageing at various temperatures

In this section, after DSC simulation, the model is once again brought out of its fitting conditions (isothermal ageing at 170 °C). Here, the artificial ageings considered remain isothermal, but the tested temperatures are situated between 150 and 350 °C with a temperature step of 5 °C. In this section, three curves will represent, in the same way as on the previous figures, the volume fraction advancement of each phase when $f_v^{max} > 0.002$.

3.3.2.1 Time-temperature-transformation (TTT) diagrams for different compositions

Time-temperature-transformation (TTT) diagrams have been produced for different initial Mg/Si atomic ratio of the gradient A. In Figure 3.29, four compositions are presented: 3.29a for a strong Si excess, 3.29b for a regular Si excess, 3.29c for near pseudo-binary and 3.29d for a Mg excess composition. On two of these TTT diagrams the domains of each precipitate are sketchily outlined.

As discussed previously, for a sufficiently strong Si excess (Mg/Si = 0.8), pure Si is precipitating, mainly between 180 and 280 °C. Here, U2 has its larger domain (between 150 and 240 °C). This domain is shrinking from the top temperatures with the increase in Mg, until almost disappearing for the Mg excess composition (Mg/Si = 3.2).

β” region varies slightly with these different initial compositions. Its domain is mainly contained under 190 °C. As for ageing at 170 °C, β” precipitation starts earlier though for compositions with more Si.

B’ has a largest domain for the composition with Mg/Si = 1.6. B’ still precipitates for Mg excess alloys which should not be the case according to literature. β’ domain is getting bigger and is starting earlier as Mg increases.

These presented domains are an example of what form they could have. Of course, they are certainly not that accurate especially due to the lack of experimental data for semi-coherent phases.

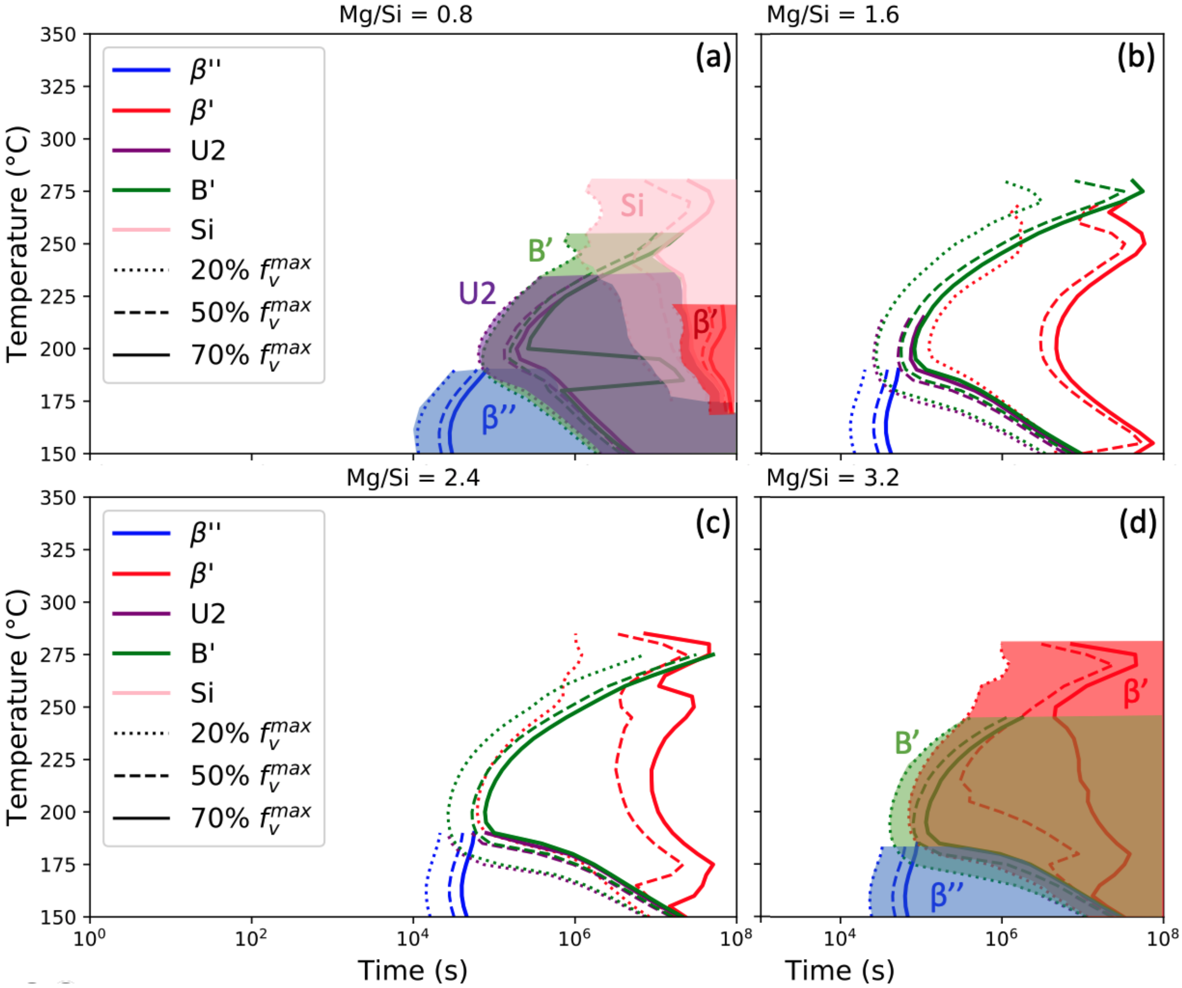

Figure 3.29: TTT diagrams for 4 different initial compositions of B sample of atomic ratio a: Mg/Si = 0.8 (Strong Si excess) b: Mg/Si = 1.6 (Si excess) c: Mg/Si = 2.4 (near pseudo-binary) and d: Mg/Si = 3.2 (Mg excess)

3.3.2.2 Improved TTT diagrams with hardening information for different compositions

Now that the precipitation domains were presented on classical TTT diagrams, simulated yield strength values are added to the TTT diagrams in Figure 3.30.

From, this model, it is clear that first, no improvement of properties is observable above 220 °C for the compositions accessible with the sample B. To be more precise, no major improvements are actually obtained above 200 °C. The best mechanical properties seems to be situated near 175 °C.

It is actually interesting to note that, for all compositions, the hardness peak is not higher but lower for temperature below than 160 °C and that this peak is not delayed. The precipitation of β” at lower temperature is indeed extended in time. The sizes or the volume fraction of the precipitates should be responsible of this hardness reduction.

The best compositions, among the four proposed here, seems to be the one with regular

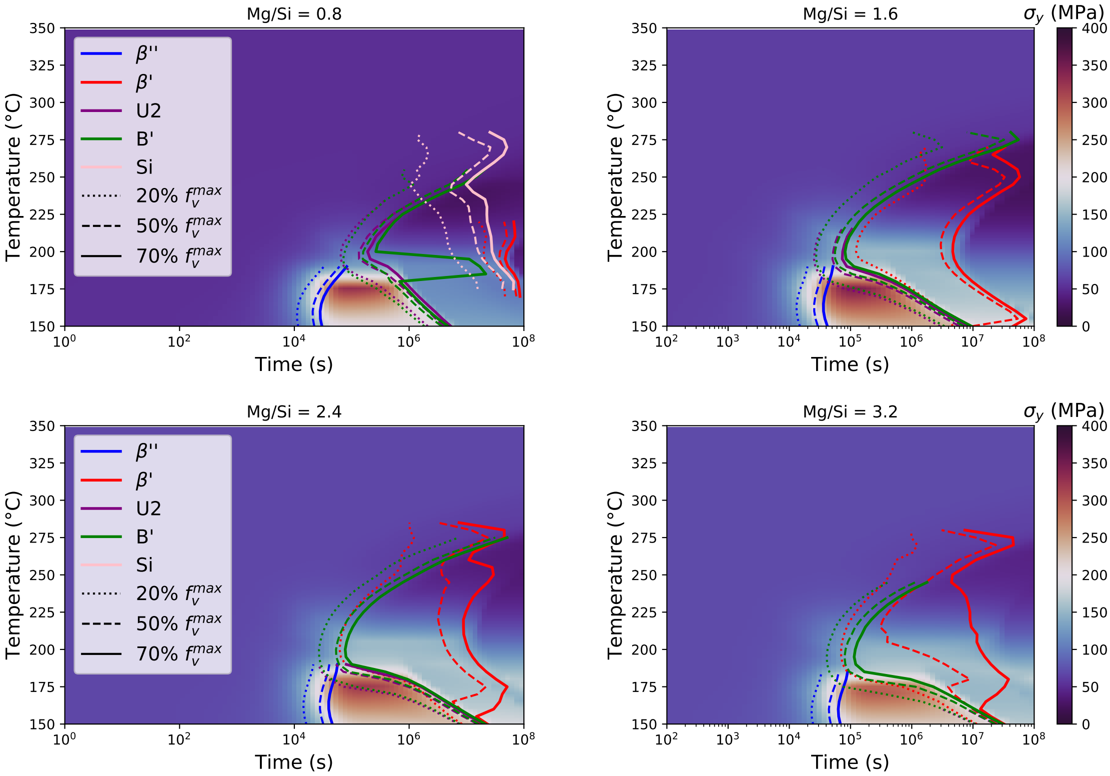

Figure 3.30: TTT diagrams with simulated yield strength for 4 different initial compositions of the sample B with Mg/Si atomic ratio of: 0.8 (Strong Si excess), 1.6 (Si excess), 2.4 (near pseudo-binary) and 3.2 (Mg excess)

excess of Si (Mg/Si = 1.6). It is also with this composition that the hardness peak (T6 state) is obtained the faster.

On these figures, it is also clearly evidenced that the β' and B' critical radius is over-estimated with the drop of mechanical properties when either of these two phases is present alone.

3.4 Summary

In the literature review, many ways of modelling precipitation have been presented. To model further than clustering and GPZ formations in Al-Mg-Si alloys, continuous scale approaches such as mean field framework are widely used. It is possible to simulate the competition of precipitation between the different known metastable phases of β precipitation sequence. But for simplicity and efficiency, many authors only consider either β" [CIN 20] or a representative precipitate for several phases [BAR 14]. To the author's knowledge, only Du's *et al.* [DU 17] model allows the proper precipitation simulation of various Al-Mg-Si alloys (especially for compositions with a regular Si excess) and no hardening simulation were performed in order to evidence the influence of composition in 6xxx.

In this context, a coupled precipitation/hardening model (based on KWN approach and sheared/by-passed mechanims) was developed and adapted to the specific experimental gradients obtained. The numeric samples were thus presenting variations of both Mg/Si atomic ratio and initial SS Mg_2Si content. These numerical samples were actually constituted of approximately 10 nodes of homogeneous compositions. Finally, five possible precipitates were inserted in the model with thermodynamic parameters imported from the TCAL4 database. Eleven parameters had to be adjusted: 5 phases x 2 (γ, r_c) + 1 (β). Careful sensitivity studies were carried out on the adapted samples but the lack of experimental data was significant, in particular for the adjustment of the three semi-coherent phases (β', U2 and B').

Precipitation and hardening kinetics of various ageing treatments can be simulated for this wide range of compositions. As expected, continuous heating treatment are not well suited for this model according to the confrontation with experimental DSC heat curves. Regarding isothermal ageing the results are promising.

First, at 170 °C for the sample A, the model presents only one maximum hardness for the composition Mg/Si = 1.8 after 8 h of isothermal ageing. This difference with the experimental data (2 maxima) can be compensated by the fact that β" precipitation presents two faster local kinetics for the composition of Mg/Si = 1.2 and 2.4. These two values are actually exactly the ones which presented maximum hardness. The difference may come from the non-consideration of clusters/GPZ.

This non-consideration is also impacting the hardness values in general. First, they are underestimated and therefore the value of the mechanical parameter β, that has been adjusted could be lower. Then, the hardening domain is shrunk (for the low ageing times).

Now, outside of its optimisation conditions ($T_{ageing} \neq 170\,°C$), the model is showing that for all compositions, above 200 °C, isothermal ageing is not bringing to a proper hardening because of insufficient β" precipitation. Under 160 °C, the hardening peak is, surprisingly, less important and does not seem particularly delayed.

Conclusion and Perspectives

Recycling Al alloys often leads to uncontrolled composition ranges of alloying elements. Alloy design based on recycling must therefore account for the effect of these composition variations on the alloy properties. To provide many experimental data in the composition space of Al-Mg-Si system, gradients of Mg-Si were manufactured using powder metallurgy. These graded samples were investigated in different ways along the manufacturing route. Then, microstructural high-throughput characterisations, mainly during isothermal ageing at 170 °C, were performed along the gradient. Finally, physics-based precipitation and hardening models simulated the precipitation and competition of five types of precipitates (β", β', U2, B' and Si) in numerical gradients in an attempt to explain what has been observed experimentally.

Main results of this study

Manufacturing graded Al-Mg-Si alloys

A manufacturing route with spark plasma sintering on two blends of powders followed by a 10 days interdiffusion treatment at 550 °C provided the 3 mm Mg-Si target gradient. The gradient in question contains a variation of possible Mg_2Si fractions and a variation of Mg or Si excess with respect to the pseudo-binary alloy (Mg/Si = 2). The gradient can be elongated by rolling to 6 mm. This route could be applied to other metallic systems for combinatorial studies.

Due to the powder metallurgy route, the following microstructural features were observed in the gradients:

- Grain size distributions in the compacts are strongly linked to the initial powders sizes, even after a long solution treatment ;
- Mg-rich powder provides an important network of oxides ;
- Small grain size seems to be responsible for the duality of diffusion (bulk and grain boundaries) of Si element. This effect has been modelled to predict more accurately the extent of the gradient.

In the gradient of composition between Al-1.2.wt.%Si and Al-2.6wt.%Mg, the solid solution strengthening effect was assessed and the Mg and Si strengthening coefficients were determined.

Experimental study of precipitation on the gradients

Precipitation studies have been conducted at different scales of the microstructure and for different purposes. Global investigations with microhardness and DSC experiments permitted to obtain, among others, precipitation kinetics. At the nanoscale, specific precipitation states were observed and characterised (precipitates and solid solution) using ASAXS, TEM and APT.

Provided by microhardness measurements upon interrupted 170 °C ageing treatment, the highest strengthening are obtained for two specific compositions: one for which the content in Mg+Si was maximum (Mg+Si = 1.7 at.%) and the other for which the composition was the closest to Mg_5Si_6 (Mg/Si = 1.2). These features have been confirmed by isothermal DSC and explained, partially, thanks to continuous DSC. The first maximum seems to be obtained because of a fast precipitation kinetic whereas the second one because of high volume fractions of clusters and coherent phases.

By combining results from microhardness, DSC and ASAXS: different precipitation kinetics regimes were identified:

- $Mg/Si \leq 0.3$: extreme Si excess, main precipitation of pure Si, no major improvement in hardness, very slow precipitation, very small diameters of precipitates (approx. 2.6 nm)
- $0.4 \leq Mg/Si \leq 1$: strong Si excess (Si domain), precipitation of pure Si, improvement of hardness, slow precipitation but fast hardening, precipitates of small diameter at the beginning of ageing (approx. 2.8 nm)
- $1 \leq Mg/Si \leq 3$: quasi pseudo-binary compositions (PB domain), may present remains of pure Si precipitation, maximum improvement of hardness, faster hardening, important variation of the diameter of precipitates (average diameter varies from 3.0 nm to 10.0 nm during ageing)
- $Mg/Si > 3$: strong Mg excess (Mg domain), hardness improvement, slow hardening but rapid semi-coherent precipitation, rather large initial average diameter (approx. 3.3 nm)

Then, TEM characterisations on two specific ageing states (T6 and over-aged) and for different compositions domains (Si, PB and Mg) confirmed the observation made with ASAXS: after 1 month, mean diameters of the precipitates have increased more significantly for compositions near Mg/Si = 2. A similar tendency is observed for mean precipitates lengths. The final growing specificity can be summarised for the three observed domains as:

- Si domain: precipitates are rather short initially and expend mostly in length
- PB domain: precipitates become much thicker and expend as well in length
- Mg domain: precipitates thicken and do not seem to expend in length

TEM also showed that at T6 state (16 h under 170 °C), the site in the Mg domain presents a precipitation sequence in advance compared to PB site which was also in advance regarding to Si site. Indeed, β' precipitates were observed for Mg site whereas β_0' precipitates seemed present for PB site and only β" for Si site.

Finally, additional information has been accumulated from a simulation perspective: identification of precipitates for Si site after over-ageing (HR-TEM) and solute contents evolution for 2 gradient compositions (APT).

Simulation of precipitation along the gradients

A coupled precipitation/hardening model adapted to this study has been developed and successfully confronted to the experimental data (for a 170 °C ageing treatment). This model has the particularity to consider five types of precipitates and to provide results simultaneously for a wide range of initial compositions.

Under 170 °C ageing treatment, the model showed that the maximum mechanical properties (yield strength or hardness) are mainly influenced by β" precipitation. Differences in the speed of precipitation are observed depending on the composition:

- under Mg/Si = 0.3: main precipitation of pure Si
- $0.3 \leq$ Mg/Si ≤ 1.2: increase of β" precipitation speed when increasing Mg content
- $1.2 \leq$ Mg/Si ≤ 2.5: slight mean decrease of β" precipitation speed when increasing Mg content
- above Mg/Si = 2.5: decrease of β" and increase of semi-coherent precipitation speed when increasing Mg content

The regimes are similar to those observed experimentally with the various precipitation characterisations.

This model is also capable of providing the precipitation domain of each phase and the hardening peaks for various ageing temperatures (between 150 and 350 °C) and initial SS compositions. For various compositions, the model show a narrow window of temperature, around 175 °C, for which the hardening is maximal.

Conclusion

From an overall perspective, the **main objectives have been reached**. But, it is important to clearly explicit that the samples have complicated the study. Indeed, these materials accumulated various weaknesses:

- the powder metallurgy routes provided **pores** and oxides within the materials: complicating WDS analysis and various sample preparations (TEM, ASAXS, tensile specimens).
- the Mg-Si **gradients** were interesting for the aspects introduced in this document but they were also: complicating sample preparation (DSC, TEM, APT) and conducted to important composition uncertainties.
- the **Al-Mg-Si system** was itself a considerable challenge for ASAXS experiments.

All the encountered issues brought either important uncertainties or a lack of experimental data. The presented model could have been more accurate and complete and so as the interpretations of this study.

Perspectives

Model improvements

The model could bring to much more information and comprehensions with supplementary work. Here is also a list of complements that would upgrade this model:

- Confront the experimental ASAXS mean radius with the model: would permit to verify if the tendencies observed experimentally are well represented by the model. It would be necessary first to have an important reflexion on the composition of the gradients to simulate. A simpler model (without gradients) could be used instead with the parameters determined in this study.
- Add the clusters contribution according to Povoden *et al.* [POV 13] would improve the model and give an overview of the effect of clusters depending on the composition according to that database.

- Obtain a conversion equation from hardness to yield strength (and no longer use the one of Myhr) from tensile tests on graded specimens through Digital Image Correlation (DIC) and implemented it to the model. The samples required for the tensile specimen should be manufactured differently (under HIP, from "clean" powders, etc.) in order to prevent the formation of cracks (from pores diffusion) in these larger samples.

Recommendations for future studies

Before and during the manufacturing process, Al powders should be kept in glove box to reduce the humidification of the oxide layers and prevent for the pores formation.

A more drastic solution would be to avoid powder metallurgy and manufacture the graded materials with diffusion bonding (as presented in **Introduction** [IVA 18, GUM 16]). The interface between the two initial layers would be also more clear and straight.

Hardness measurements were conducted on a manual micro-hardness tester. An automatic machine would have provided additional repeatability values and provided less uncertainty.

Develop ASAXS for Al-Mg-Si

The first ASAXS precipitation characterisations on Al-Mg-Si showed their relevancy even if, these experiments were not performed by a soft X-ray beam-line specialised and well equipped for SAXS. In these conditions, the transmission measurements were incorrect (due to the detector used) and prevented for the normalisation of the results (see Appendix B). Only the mean diameters of the precipitates were extracted, although this technique can be used to acquire a whole range of interesting data on precipitates (composition, volume fraction etc.). With a beam-line well prepared for these experiments, *in-situ* ASAXS on Al-Mg-Si graded samples could be consider. A different experiment configuration could also easily conduct to a higher range of diameters accessible.

High-throughput approach using fixed compositions

To avoid the gradients compositions complexity, a different approach of high-throughput characterisations could be used. Instead of having one sample with various compositions, many bulk samples of various fixed compositions can be printed from the same powders (Laser Metal Deposition for HEA high-throughput investigation, Théo Langlois PhD Mateis).

With these samples, the different techniques: hardness, TEM, APT and DSC could be used on the exact same compositions (ours and additional ones). These results would provide precise thresholds between the composition domains and confirmation of the links established between the characteristics of the observed precipitates and the precipitation kinetics.

Appendix A

Bi-modal diffusion model

A new diffusion model attempts to reproduce the faster diffusion behaviour for Si. The model is based on an interconnected two regimes diffusion with one regular bulk diffusion and one accelerated grain-boundary diffusion.

The length of the gradient is meshed with I nods on a total length of L (view Figure 1.8). The diffusion is considered 1D along x.

For a given time t+Δt, the variation of Si atoms in the bulk in the nod i is:

$$\Delta n = (J_i - J_{i+1})S\Delta t - J_i^{B\to GB} S^{B\to GB}\Delta t \tag{A.1}$$

With the flux:

$$J = -D\frac{\partial C}{\partial x} = -D\frac{\Delta C}{\Delta x} \tag{A.2}$$

So

$$J_i - J_{i+1} = -D\frac{C_i - C_{i-1}}{\Delta x} + D\frac{C_{i+1} - C_i}{\Delta x} = D\frac{C_{i+1} + C_{i-1} - 2C_i}{\Delta x} \tag{A.3}$$

And

$$J_i^{B\to GB} = D\frac{C_i - C_i^{GB}}{\phi^{GB}/2} \tag{A.4}$$

The Si concentration in the bulk is then:

$$C_{i,t+\Delta t} = C_{i,t} + \frac{\Delta n}{S\Delta x} \tag{A.5}$$

In the same way, the variation of Si atoms in grain boundaries (GB) in the nod i at t+Δt is:

$$\Delta n^{GB} = (J_i^{GB} - J_{i+1}^{GB})S^{GB}\Delta t + J_i^{B\to GB} S^{B\to GB}\Delta t \tag{A.6}$$

With

$$J_i^{GB} - J_{i+1}^{GB} = D^{GB}\frac{C_{i+1}^{GB} + C_{i-1}^{GB} - 2C_i^{GB}}{\Delta x} \tag{A.7}$$

And the Si concentration in the grain boundaries is then:

$$C_{i,t+\Delta t}^{GB} = C_{i,t}^{GB} + \frac{\Delta n^{GB}}{V^{GB}} \tag{A.8}$$

The spatial parameters are summarised here:

- $\Delta x = \frac{L}{I}$
- S the exchange surface of a nod slice
- S$_{GB}$ $= \frac{2}{\phi^{GB}} e^{GB} S$ the exchange surface of the grain boundaries of a slice
- S$_{B\to GB}$ $= \frac{3}{\phi^{GB}} \Delta x S$ the exchange surface between the grain boundaries and the bulk in a slice
- V$_{GB}$ $= \frac{3}{\phi^{GB}} e^{GB} \Delta x S$ the volume of the grain boundaries in one slice

The specific parameters to the grain boundaries diffusion are listed here:

- $D^{GB} = \gamma D$ the Si diffusion coefficient in the grain boundaries
- γ the acceleration coefficient

- ϕ^{GB} grains diameter
- e^{GB} the thickness of the grain boundaries
- X_{max}^{GB} the maximum amount of Si possible in the grain boundaries

Finally, the total Si concentration is:

$$C_{i,t}^{tot} = \frac{n_{i,t} + n_{i,t}^{GB}}{\Delta xS} = \frac{C_{i,t}\Delta xS + C_{i,t}^{GB}V^{GB}}{\Delta xS} \tag{A.9}$$

$$C_{i,t}^{tot} = C_{i,t} + C_{i,t}^{GB}\frac{3}{\phi^{GB}}e^{GB} \tag{A.10}$$

Complementary information:
- If $J_i^{GB\to B} < 0$, saturation is taken in consideration :

$$J_i^{GB\to B} = J_i^{GB\to B} * (1 - \frac{C_{i,t}^{GB}}{C_{max}^{GB}}) \tag{A.11}$$

- Convergence criterions $\Delta C_i \leq \frac{C_{i,t}}{2}$:

- $\Delta t \leq \frac{\Delta x^2}{2D}$
- $\Delta t \leq \frac{\phi^{GB}e^{GB}}{4D}$
- $\Delta t \leq \frac{3\Delta x^2}{4D^{GB}}$

Appendix B

Methods for microstructure characterisations

Contents

B.1 Complementary information for content profiles data treatment

EDX and WDS experiments are introduced in the materials and methods section of **Chap 1**. The data treatment procedure on different content profile is detailed here.

The content profiles of samples A and B are presented figures B.1a and B.1b respectively. These data are obtained from WDS measurements.

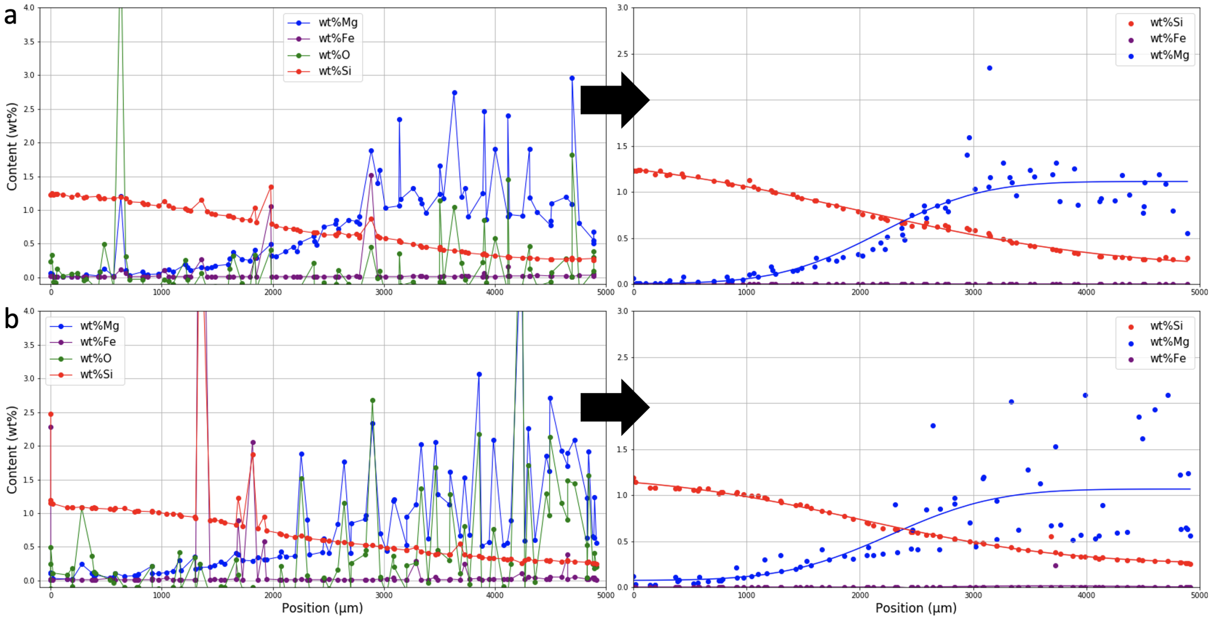

Figure B.1: Treatment data for WDS profile content curves a: sample A used for microhardness analysis, b: sample B used for DSC measurements

For both samples, 3 profile lines were conducted along the gradient at 1 mm distance from each other. The raw data are presented on the left hand side. Then, the final fit is performed on the treated data presented on the right hand side of the arrow on the same figures. The procedure for the data treatment is the following:

- All the points with Fe content ≤ 0.1 : are readjusted. $w_{Fe} = 0$ and w_{Al} is recalculated by difference.
- All the points with $w_{Fe} \geq 0.25\%$ are considered as being influenced by Fe-intermetallics and are discarded
- All the points with $w_O \geq 0.3\%$ and $w_{Mg} - w_O \leq 0.8\ w_{Mg}$ are considered as being influenced by oxides and are discarded (Sample A).
- Readjustment of points composition with remaining O: $w_O = 0$ and w_{Al} is recalculated by difference.

As seen on the raw data (figures B.1a and B.1b) WDS Oxygen measurements are not absolute values. They are just measured in order to spot the oxide points. the values can therefore be quite different from one sample to an other. For sample B, the deletion of oxide points is conducted if $w_O \geq 0.5\%$ and if $w_{Mg} - w_O \leq 0.3\ w_{Mg}$.

For EDX profiles, the data treatment was slightly different:

- All the points with Fe content $\leq 0.25\%$: are readjusted. $w_{Fe} = 0$ and w_{Al} is recalculated by difference.
- Fe-intermetallic points are deleted if $w_{Fe} \geq 1\%$.
- Oxide points are deleted if $w_O \geq 1\%$
- Readjustment of points composition with remaining O: $w_O = 0$ and w_{Al} is recalculated by difference.

B.2 DSC analyses

All the DSC measurements were carried out on a SENSYS evo DSC of Setaram using a 3D captor.

The thin samples were extracted from the B gradient bulk using a wire saw. The 9 slices are assumed to be homogeneous in composition. They are named E1 to E9 with E1 the Si-edge and E9 the Mg-edge of the gradient. Pure Al standard of the same weight as the sample was used for each experiment. The mass of each specimen was around 100 mg.

The **continuous heating analyses** were performed between -25 and 550 °C using an heating rate of 5 °C/min.

Before almost each experiment, one blank experiment was performed with no specimen in both crucibles (standard and sample). In the data treatment the heat curve from the blank experiment was substracted from the specimen heat curves. The base line seemed with these precautions (pure Al standard and removal of the blank) rather correct. In some cases, a small constant was also subtracted to the curve. Some examples are given for 4 samples Figure B.2.

The **isothermal analyses** were performed at 170 °C. Because of technical issues, this is not a common protocol for DSC measurements:

- There is a transitory state because of the overshoot in temperature of the DSC to get to the isotherm temperature. With a rate of 25 °C/min, the transitory state lasts 30 min.
- The time of an experiment is very long and therefore the signal very low. The precipitation sequence is therefore too slow to be visible.

For the isothermal experiments, after 2 days, there is no longer major heat variation. The baseline can thus be adjusted only according to the proper last points of the experiments. The times chosen for the baseline is detailed Table B.1. B1 was extracted on the Si-edge and B9 on the Mg-edge.

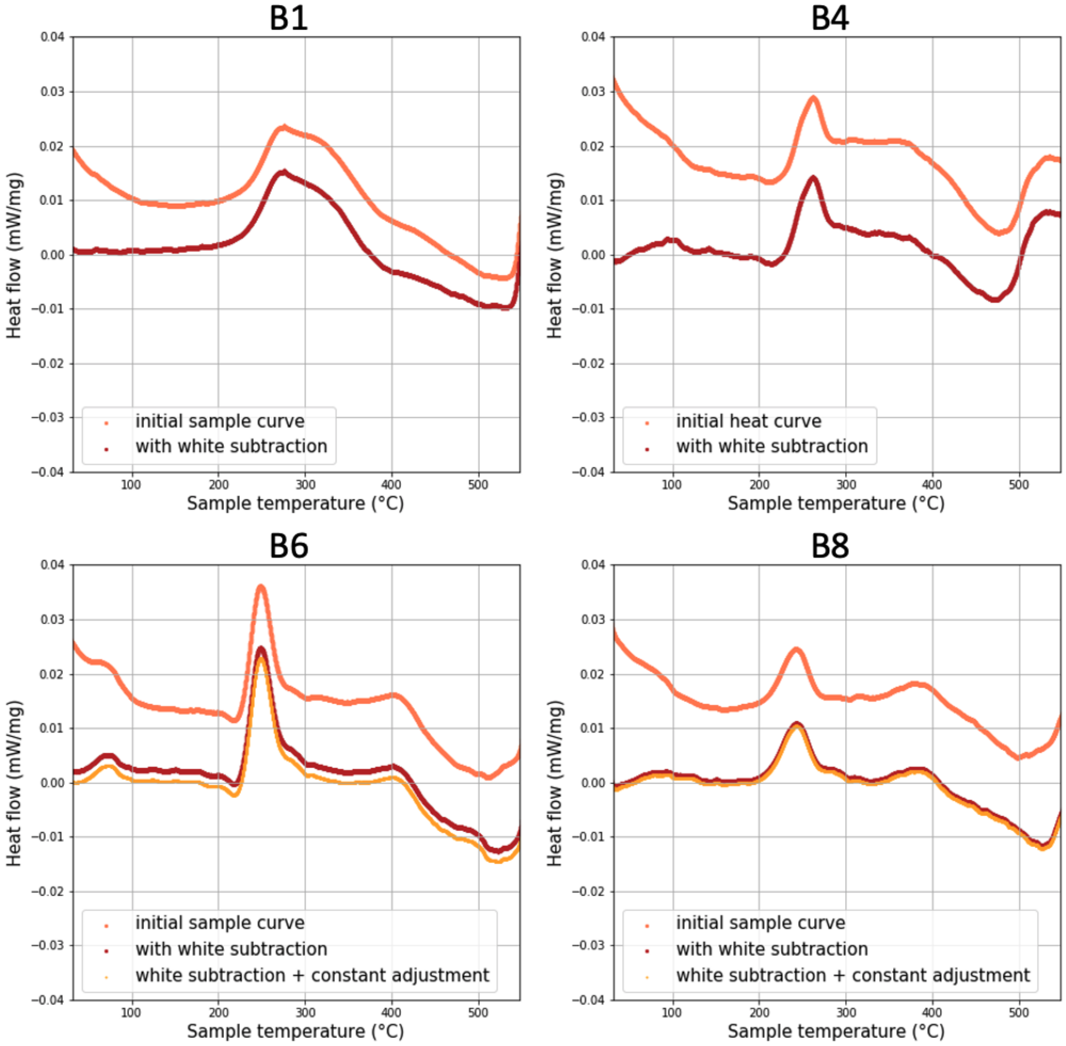

Figure B.2: Initial continuous heating DSC heat curves and baseline adjustment for 4 samples

Specimen	Adjustment time
B1	18 h
B2, B3	2.3 days
B4	2 days
B5 - B9	1.7 days

Table B.1: Times chosen for isothermal DSC experiments to adjust the baseline depending on each specimen

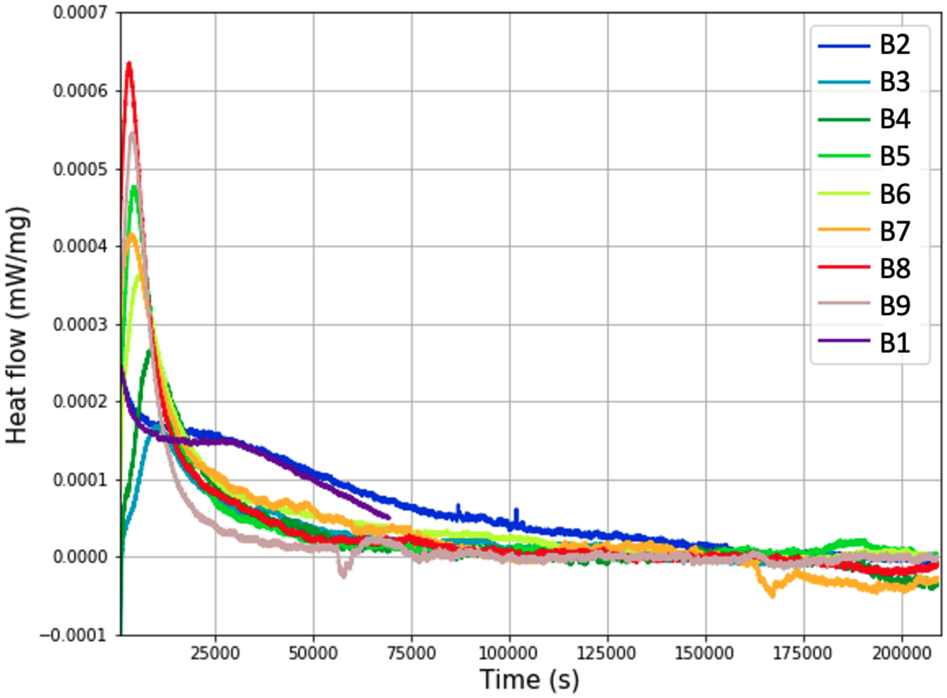

Figure B.3: Baseline adjustment for isothermal DSC experiments

B.3 Scattering characterisations

Small angle X-ray Scattering (SAXS) allows the characterisation of nanometric objects (of few Å to 100 nm). In optimal conditions, various precipitates information are extractable:

- chemical information; such as volume fraction and composition
- morphology information; type and various dimensions

B.3.1 X-ray scattering bases

The X-ray source is passing through the sample, interacts with it and then is collected on a detector, see Figure B.4.

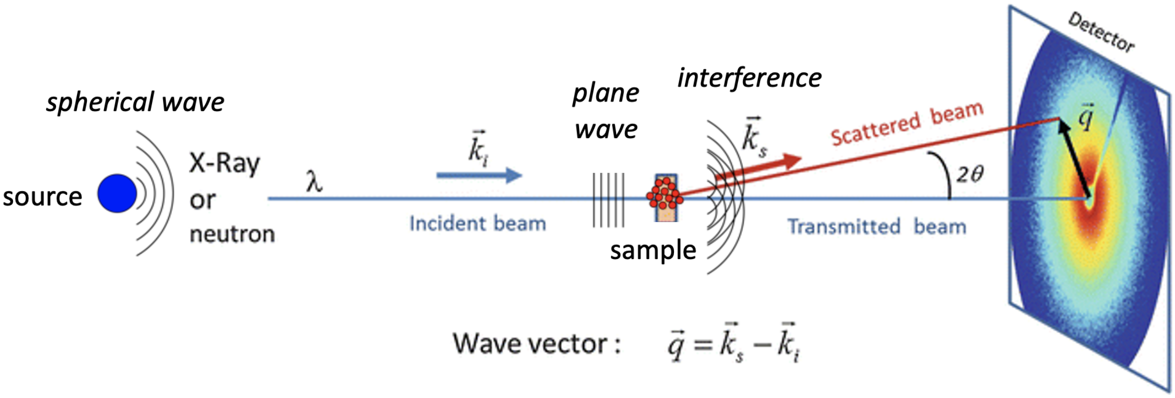

Figure B.4: Principle of Small Angle X-ray Scattering technique

k$_i$ is representing the incident photon from X-ray source and k$_s$ is representing the scattered photon after interaction with the electronic clouds of the atoms of the sample. The difference of electronic density between the heterogeneities and the based material is creating a scattering signal which is at the base of SAXS. The intensity and the contrast is increased with that electronic difference. So if the material is homogeneous, there will be no signal.

The electronic density (ρ) depends on the composition of the element i (C$_i$), its diffusion factor (f_i) and the atomic volume (Ω) :

$$\rho = \sum \frac{C_i \times f_i}{\Omega}$$

In classical conditions, the total diffusion factor is only f = Z with Z the atomic number. By performing several experiments on the same sample with different X-ray energies, it is therefore possible to get information on the precipitates chemistry. Five energies are usually use to describe the parabolic function between the intensity and the energy.

Besides ρ and its chemistry information, the volume fraction (f_v) and the form factor (F) of the precipitates are influencing as well the intensity curve from the scattern patern :

$$I(q) = (\rho_m - \rho_p)^2 \times f_v(1 - f_v) \times V \times F$$

- q is the norm of the diffusion vector q = k_i- k_s, it is principally depending on the position to the detector center D, but also to the wave length of the incident photon λ and to the distance between the sample and the detector L
- ρ_m the electronic density of the matrix
- ρ_p the electronic density of the precipitates
- V the analysed volume

With proper data analyses, volume fraction and morphology are also results of SAXS characterisations.

B.3.2 Specificities of Anomalous SAXS

In Al-Mg-Si alloys though, the atomic number Z of each of these chemical elements are too close. Therefore, in classical conditions (at 8 keV), the different precipitates and the matrix scattern in the same way. There is no contrast. The solution is to make Anomalous SAXS (ASAXS).

ASAXS is performed at an energy of absorption of one of the element (at a K_α edge) in order to enhanced contrast between precipitates and matrix. Indeed, when an atom is totally absorbing a photon, it no longer diffuses it. With an energy (E) near that energy edge, the diffusion factor is no longer equals to Z but to f = Z + f'(E) + if"(E). To avoid fluorescence, it is best to use an energy underneath the K_α edge and not above.

In Al-Mg-Si alloys, the elements are not heavy thus all their K_α are very low energies (around K_α^{Al} = 1.56 keV). These energies are not usual for SAXS and ASAXS measurements. To the author's knowledge, Al-Mg-Si precipitates are therefore never analysed by this technique.

The soft X-ray beamline Sirius of SOLEIL synchrotron works with the proper range of energy even if the settlement is not perfectly adapted for SAXS measuremnts. For this experiment, the five energies used were the following :

- E1 = K_α^{Al} - 6 eV = 1559 eV
- E2 = K_α^{Al} - 12 eV = 1553 eV
- E3 = K_α^{Al} - 25 eV = 1540 eV
- E4 = K_α^{Al} - 50 eV = 1515 eV
- E5 = K_α^{Al} - 100 eV = 1465 eV

with K_α^{Al} = 1565 eV on the beamline Sirius

These low energies used in transmission need to pass through the sample. The sample needs to be very thin: around 25 µm for Al alloys.

In order to compare the samples ASAXS results between each-other, they need to be properly normalise with four values: the sample thickness, the transmission, the intensity of the initial incident beam and the solid angle. Several methods are used to obtained those different values.

In our case, the transmission values measured by the detector were improper, preventing the extraction of the volume fraction and the chemistry of the diffusing precipitates. One morphology information can still be extracted though.

B.3.3 Extraction of diameter

All the data treatment presented in this section was conducted by Frédéric De Geuser (from the laboratory Simap).

The scattern pattern detected describes an intensity depending on a pixel position. After a reduction procedure with an integration along the angle ϕ, the intensity curve I(q) is obtained (Figure B.5).

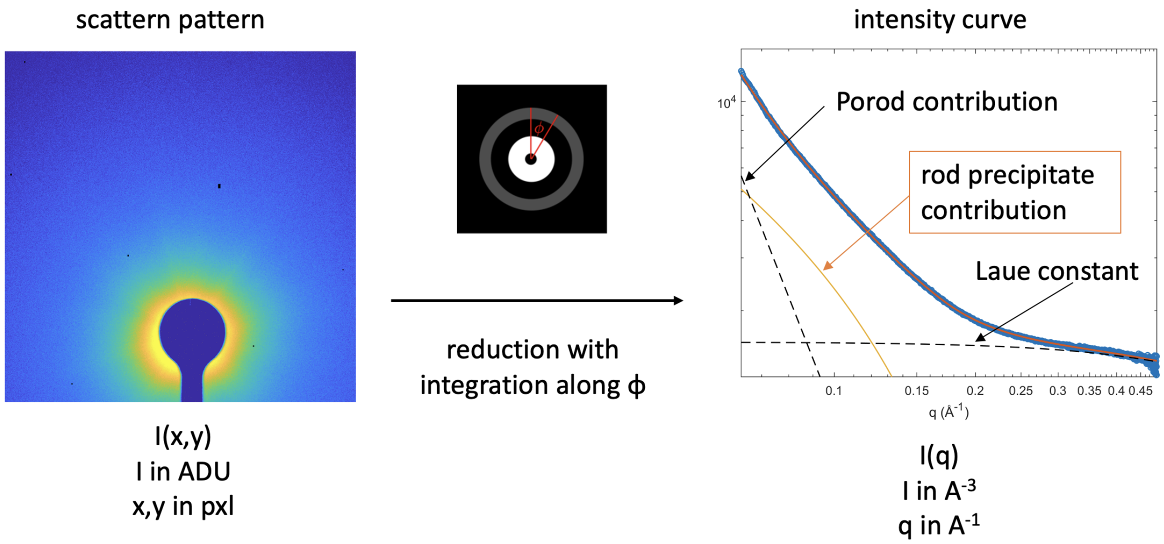

Figure B.5: Extraction, example and interpretation of an intensity curve from the scattern pattern of one site on a graded sample aged at 170 °C during 1 day

The shape of that intensity curve is only influenced by the morphology of the precipitates (type and dimensions).

It is possible to describe precisely that curve by using a complex general form. It is also possible to use a simpler semi-empirical approach to obtain average dimensions. This approach has first been developed by Bocage [BEA 96] and then improved by Hammouda [HAM 10]. For them, small angles scattering intensity curve, obtained from non textured microstructures, can be described with 2 mathematical functions. In the case of non isotrope object such as rod, the Guinier-Porod model becomes the generalised Guinier-Porod model and an intermediary region is added:

- Guinier form: $I(q) = \frac{G_2}{Q^{s_2}} \exp(\frac{-q^2 R_{g2}^2}{3-s_2})$ for q $\leq$ Q_2

- Intermediary region: $I(q) = \frac{G_1}{Q^{s_1}} \exp(\frac{-q^2 R_{g1}^2}{3-s_1})$ for $Q_2 \leq q \leq Q_1$
- Porod form: $I(q) = \frac{D}{q^d}$ for $q \geq Q_1$

With G (Guinier) and D (Porod) scale factors, R_g radius of gyration, d the Porod exponent and s the morphology parameter.

More precisely:

- $G_1 = 6.6 f_v r_{mean}^2$ in the case of long cylinders
- $R_{g1} = \frac{r_{mean}}{\sqrt{2}}$
- $R_{g2} = [\frac{L_{mean}^2}{12} + \frac{r_{mean}^2}{2}]^{1/2}$
- $Q_1 = \frac{1}{R_{g1}}[\frac{(d-s_1)(3-s_1)}{2}]^{1/2}$
- $D = G_1 \exp(\frac{-Q_1^2 Rg1^2}{3-s_1})Q_1^{(d-s_1)}$
- $Q_2 = [(s_1 - s_2)/(\frac{2}{3-s_2}R_{g2}^2 - \frac{2}{3-s_1}R_{g1}^2)]^{1/2}$
- $G_2 = G_1 exp(-Q_2^2(\frac{R_{g1}^2}{3-s_1} - \frac{R_{g2}^2}{3-s_2})Q_2^{(s2-s1)}$

In the case of abrupt interfaces: d = 4. For rod type precipitates, $s_1 = 1$ et $s_2 = 0$. The logarithmic representation of the form factor (F), obtained from this model with fixed R_{g1} and R_{g2}, along q is presented Figure B.6.

Q_1 and Q_2 transitions are here clearly observable. Most of the times, q range (due to the experimental installation) is too narrow to provide information on both Q_1 and Q_2 transitions. In addition, two other contributions are added to this model (see Figure B.5). First, large objects (pores, intermetallics, oxides...) are also scattering in the same way but at lower q (q α 1/R). Their Porod contribution can thus appear for the precipitates low values of q. The second contribution is taken in consideration through the Laue constant. This constant is due to the solid solution scattern, the beam scattern (background noise) and the fluorescence. Here the Laue contribution is principally due to the background noise (not normalised) and to the fluorescence of Mg (energy used slightly above the K_α^{Mg}). Q_2 is thus hard to reach with this method. Q_2 would have given access to the second radius of gyration which leads the large dimension of the precipitate (L_{mean}).

Finally, once the function defined for all the interesting q range. The experimental curves are fitted to f according to 3 parameters: f_v, L_{mean}, R_{mean}. The volume fraction parameter will not be accurate due to the non normalisation of the curves. However, its value will not impact the shape of the curve. L_{mean} value will only impact the Q_2 value which is mainly hidden by the large object Porod contribution (Figure B.5) But this model will provide correctly the small dimension of precipitates related to Q_1 (R_{mean}).

It is important to note the extracted radius is not an arithmetic average radius but weighted by their contribution diffusion. In metallurgy, the size distribution of precipitates are often asymmetric towards the large dimensions. In addition, the large precipitates have more impact on diffusion. The average radius calculated would thus be near the volumic average radius. By comparison, TEM measurements bring more naturally the extracted mean radius to the maximum distribution value which is lower than the volumic average radius. In general, ASAXS extracted radius should better be considered as relative values than absolute values.

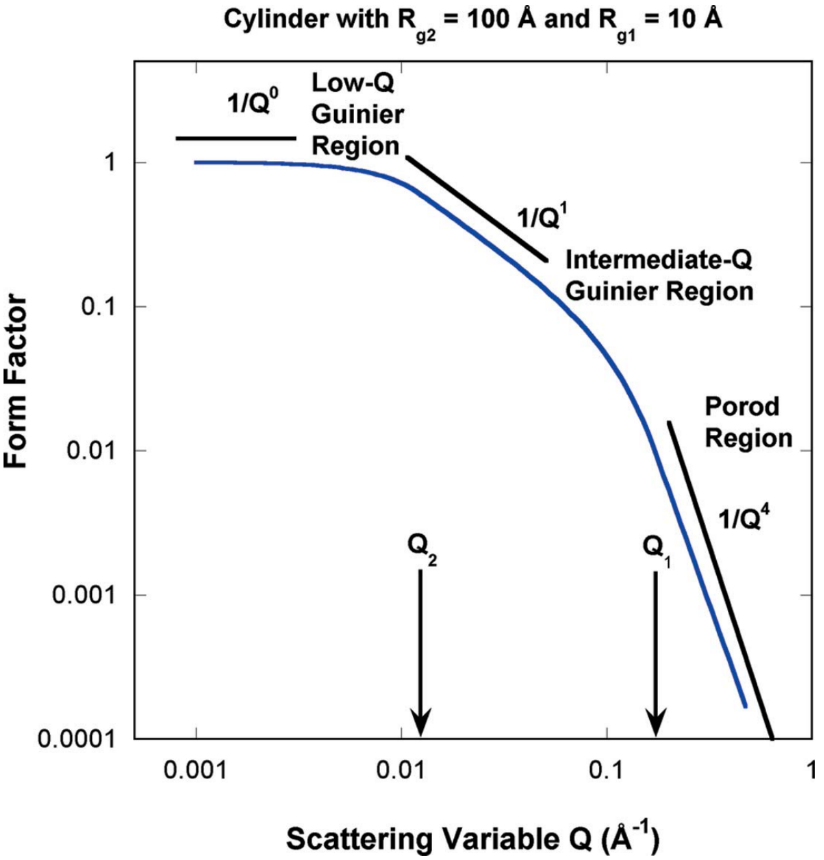

Figure B.6: Form factor for a cylinder plotted using the Guiner-Porod model [HAM 10]

B.3.4 Sample preparation

Homogeneous samples from previous PhD were homogenised:

- 2 h at 540 °C for 6351 alloys
- 2 h at 530 °C for 6061 alloys

The rolled graded samples followed the procedure described in **chap1**. Then, all the samples were aged at their targeted ageing states mostly under 170 °C and some under 250 °C.

They were then mechanically polished as thin as possible until 50-70 µm using 2500P SiC paper for the last step. Finally, they were etch until the 25 µm thickness using this etching solution :

- 10 g $NaNO_2$
- 80 mL distilled H_2O
- 100 mL saturated NaOH

At 25 °C, several minutes were required for each sample etching. The solution was put in movement using a bar magnet.

Unfortunately, the etching was not uniformed on the surface. Small cavities of 10-20 microns were formed. They are certainly at the origin of the high Porod contribution observed in addition to the micrometric particles identify in **chap1** (oxides, Mg_2Si and Fe-intermetallic particles).

B.4 TEM analyses

Conventional mode is used for observations that does not exceed 300 kX, otherwise it is High Resolution (HR) mode.

Three different TEM were used for all the presented TEM analyses. TEM JEOL 2010F at CLYM for high resolution (HR) and some conventional picture (B-R3-Si), TEM JEOL 2100 at ILM for conventional analyses of B-R1-Mg, B-R1-PB and B-R1-Si and an other TEM JEOL 2100 at CTμ for the conventional analyses on B-R3-Mg and B-R3-PB. All the TEM images were obtained at 200 kV.

All the rolled graded samples were polished until a thickness of approximately 100 µm. Then for B-R1 and B-R2 samples, they were punched on the targeted compositions and electropolished. The solution used was a mix of methanol (70%) and nitric acid (30%). The tension used was 20 V at a temperature near $-20\,°C$.

These preparations were complicated. Due to electrical problems with the electropolishing device, the quality of the thin foils prepared using electropolishing was not sufficient for a precise statistical morphology analysis (by conventional) and for a precise identification of the precipitates (by high resolution). Only a few images could be analysed. Therefore, B-R3 samples were extracted from (100)Al orientated grains using FIB technique. However, unfortunately, surface amorphization occurred for two sites: B-R3-Mg and B-R3-PB. This is why, it was difficult to obtain HR-TEM images of the pecipitates.

The statistical analyses of precipitates dimensions were performed on TEM conventional images. The software used was ImageJ. The Figure B.7a represents a raw image. First the images are filtered with a median filter of 2 pxl radius, see Figure B.7b. Then, the precipitates lengths and diameters were measured. For B-R1 and B-R2, they were measured precipitate by precipitate on the few images available (by checking grey values for diameters). For B-R3 sample and its numerous images, an ImageJ routine was developed (Figure B.7b), especially for the diameter measurements. First, the lines with standing precipitates to analyse are chosen (Figure B.7c). Then the line grey values are plotted and the range with a drop of enlightenment is measured (Figure B.7d and e). As presented in Figure B.7e, the measurements can sometimes be ambiguous.

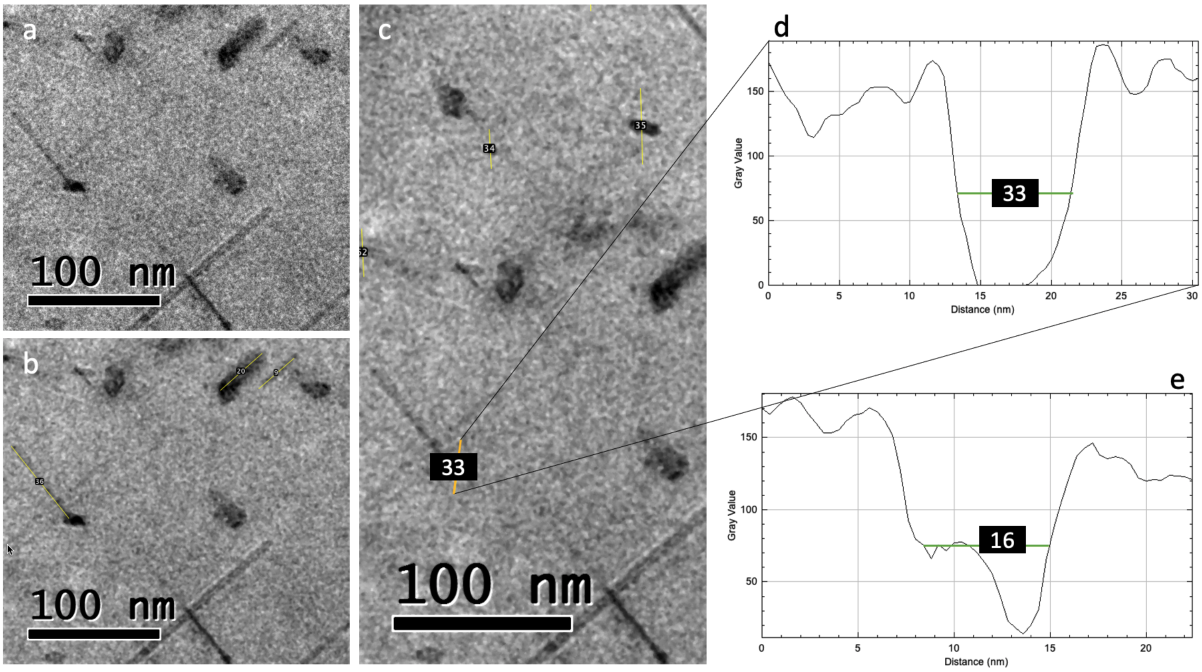

Figure B.7: Example on a B-R3 sample of the data treatment ImageJ routine for precipitates lengths and diameters measurements. a: zoom of a raw image, b: its filtred image with length measurements on laying precipitates, c: filtered image with line disposed on standing precipitates for diameters measurements, d: line 33 grey values and measurement of the precipitate diameter and e: line obtained for an other standing precipitate on the same specimen image

B.5 Atom probe tomography

Atom probe tomography (APT) is a technique which combines evaporation by electric field and time of flight mass spectrometry in order to map in 3D the constitutive atoms of a material. The resolution is therefore quasi-atomic and the volume analysed very small (approximatively $1 \times 10^6\,\mathrm{nm}^3$ containing 10^7 to Ã 10^8 atoms)[GAU 12, KEL 07]. The functioning principle of this technique is detailed in Figure B.8.

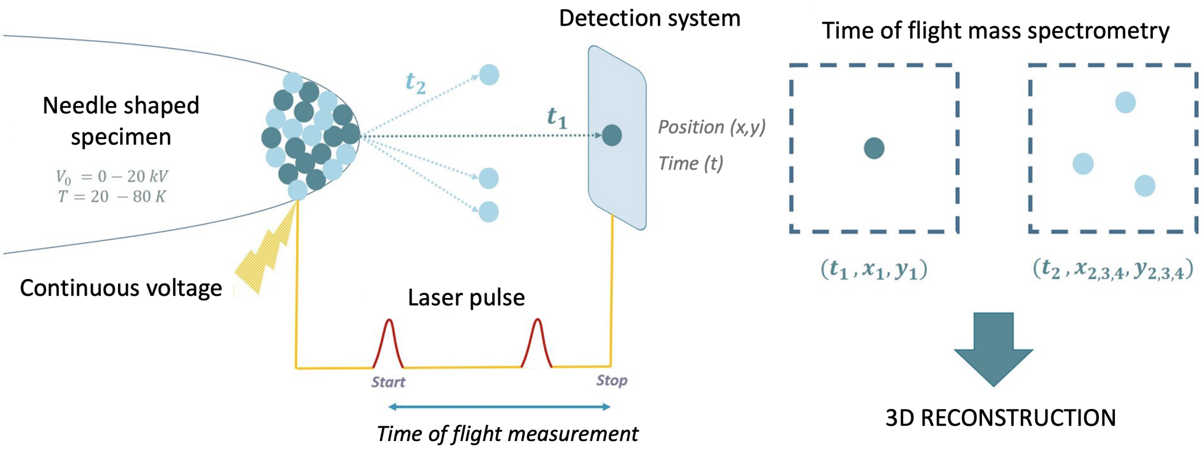

Figure B.8: Functioning principle of Atom Probe Tomography (APT) [MEY 18b]

A continuous electric potential is applied on the specimen shaped as a very thin needle (R = 50 nm on the tip). The voltage is generating on the tip of the needle, an electric field inducing: polarisation of the atoms, then their ionisation and finally their evaporation. In order to enhance and control properly the evaporation, an high voltage pulse (laser or electric) is applied at the surface. Rising the continuous tension, diminishing the temperature of the specimen [BUF 14] or working at very high vacuum amplify this destabilisation of the surface atoms.

For each pulse, the detector, which collects the atoms, is also calculating their time of flight. A light element will go faster than an heavy one. The position on the detector inquire about the initial position of the atom [BLA 99]. The speed of the atom is then calculated. Following the law of energy conservation :

$$v = \sqrt{2\frac{ne\Delta V}{m}} \tag{B.1}$$

with m the atom mass, $n \times e$ its electric charge and ΔV the applied tension
It is thus possible to trace back to the chemistry nature of the atom through its mass and its electric load. This is time of flight mass spectrometry.

Sample preparation

The sample preparation followed the procedure detailed by Lefebvre *et al.* [LEF 16]. Ideally, the needle is shaped from a $0.3 \times 0.3 \times 20\,\mathrm{mm}^3$ stick. Only sticks of $0.2 \times 0.3 \times 15\,\mathrm{mm}^3$ could be extracted from the rolled sample B-R4. These asymmetries interfere during electropolishing and more especially during the APT analyses. Only one sample, B-R4-2, prepared through this protocol was analysed (the volume was very small though). The only truly conform stick, B-R4-1, was directly obtained from Focused Ion Beam Scanning Electron Microscopy (FIB-SEM).

Analysis condition

The APT analyses were performed on a LEAP 5000 XR APT at 40 K under 3×10^{-9} Pa vacuum. The continuous voltage was between 5 and 6.5 kV. The fraction of impulsion was of 20% with a pulse frequency of 250 kHz. 13×10^{6} ions were properly collected for B-R4-1 against 2×10^{6} ions for B-R4-2.

Results treatment

On a specific analysed volume, it is possible to obtain a mass spectrum which correspond to the number of collected ions depending on the chemical information of the ions (through the ratio of mass on electric charge). The mass spectrum of the specimen B-R4-1 is presented Figure B.9 The proportion of each element in the volume is then extractable [LEF16].

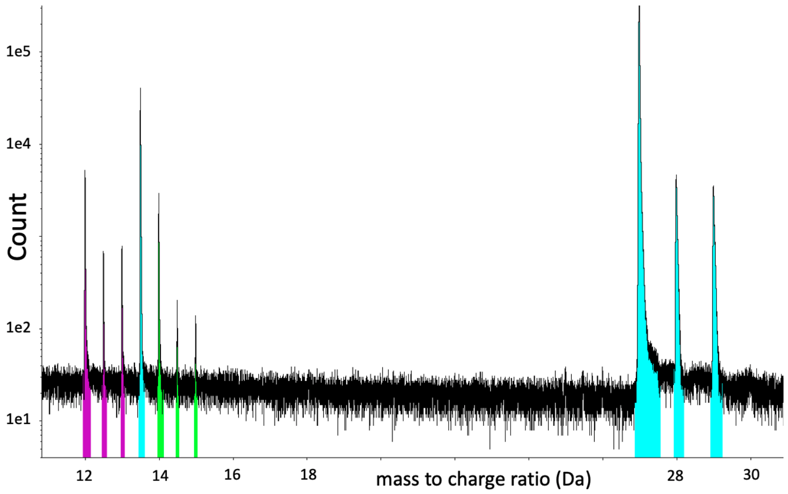

Figure B.9: Mass spectrum for specimen B-R4-1: in violet Mg, in blue Al and in green Si peaks

In order to analyse the solid solution (SS) composition, the volume analysed must be homogeneous. Artefacts, due to the migration of atoms during the experiment, can also be at the origin of non homogeneity. In crystalline materials, the intersection between the peak surface and the atomic plans is creating surface roughness. This roughness is at the origin of electric field inhomogeneity which deviates the trajectory of the ions. On the detector, some zones will have high densities of collected ions whereas others no. An example on the specimen B-R4-2 is given Figure B.10. The observable pattern is typical from the crystalline pole figure. An algorithm can be used to remove those typical crystalline artefact [LEF 16]. An easier solution, when possible, is to select sub-volumes out of the pole figures. This method was used here. The SS compositions of the two specimen B-R4-1 and B-R4-2 are averages of two sub-volume compositions (outside of the pole figure and without precipitates). The uncertainty is calculated via standard deviation on those two sub-compositions.

The evaporation artefact observed for this specimen can probably be explained by the anisop-

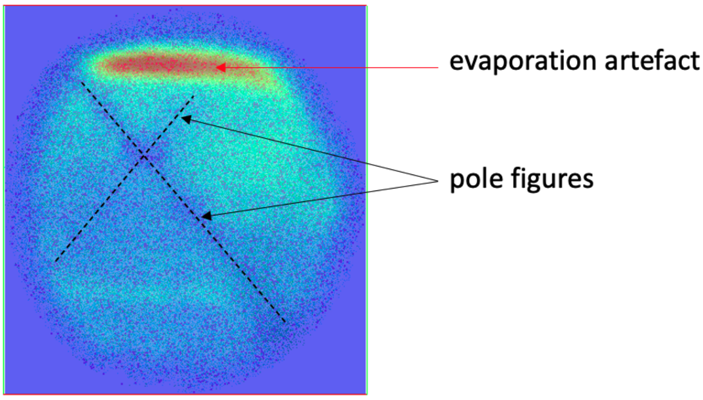

Figure B.10: Pattern on the detector for specimen B-R4-1: evaporation artefact and pole figure lines are visible

tropy morphology of the section of the needle tip (rectangular instead of squared).

For the precipitates characterisation, a method of detection of surface combined with concentration verification is used to assign each atom present in the volume of a phase [HAS 09]. The threshold used in the analysis to define the isosurface was set at 12% of Mg+Si. With this technique some atoms are belonging to the precipitate but are still in the matrix. This is the overlapping zone. To get to the precipitate compositions, a content profile is plotted depending on the distance between the atoms and this interface. This method is named "proxygram" [HAS 09]. An example on an observed precipitate from B-R4-1 specimen is given Figure B.11. Then the protocol of Hasting *et al.* [HAS 09] was applied to differentiate the apparent precipitate/matrix interface from the true interface. Following this protocol, the composition of the precipitate considers all the atoms inside the heart of the precipitate but also the solutes of the overlapping zone [MEY 18b]. The two precipitates observed via APT in specimen B-R4-1 were outside the pole figures.

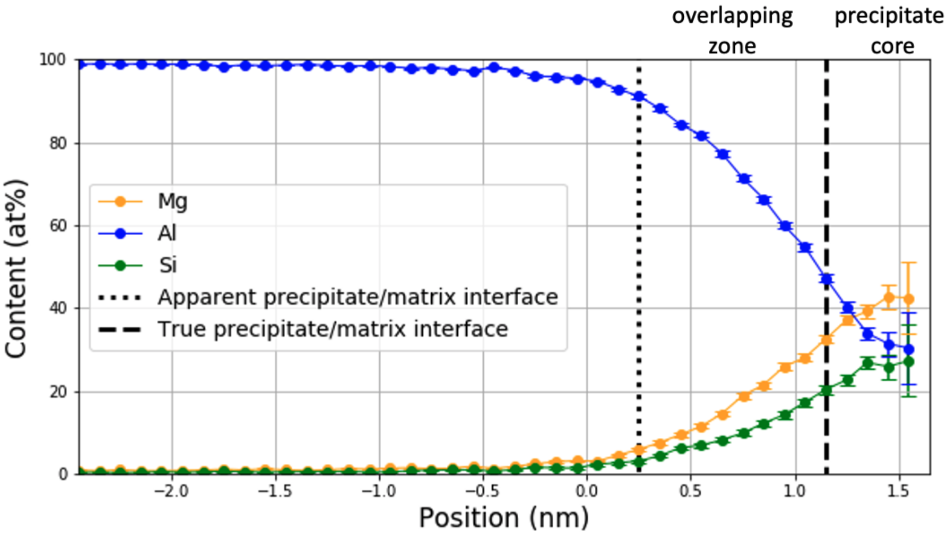

Figure B.11: APT content profile around the isosurface of a precipitate extracted from B-R4 rolled sample. Hasting protocol's was used to fix the different interfaces.

Appendix C

Materials: supplementary EDX content profiles for rolled samples

Contents

C.1 ASAXS samples

All the ASAXS samples presented are coming from the same bulk (C). But the slices extraction, the rolling procedure and the choice of the 6 mm analysed zone are bringing to different content profiles along the gradients. Mg and Si contents were measured on a similar thickness zone to the X-ray beam's one: 250 µm, using 5 lines spaced by 50 µm. The dwell time used for each point was set here at 10 s. On the Figure C.1, they are presented for a sample aged during 1 h at 170 °C.

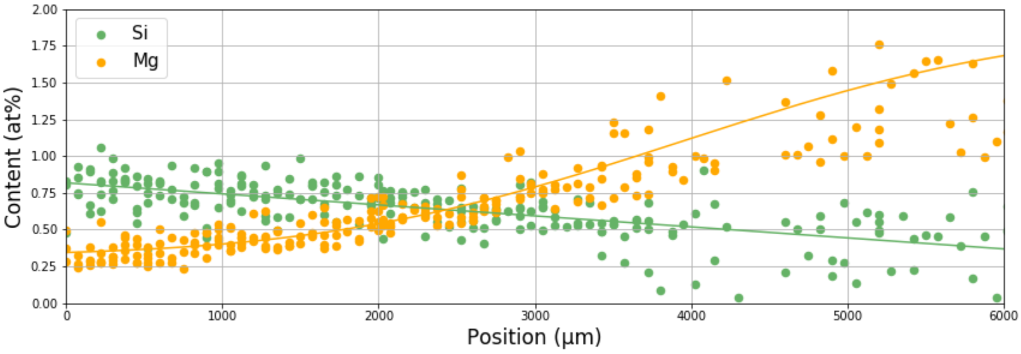

Figure C.1: EDX solid solution composition of a rolled gradient of an Al-1.2.wt%Si Al-2.6wt%Mg diffusion couple after 10 days homogenisation at 550 °C followed by rolling procedure, ASAXS preparation and ageing at 170 °C for 1 h

Due to the ASAXS sample preparation and its etching step, many oxides were present one the Mg-rich side inducing a lot of aberrant values for the solid solution content. This feature is the same on all the other ASAXS samples. Above 0.8 at.% Mg content, less solid solution data were extracted and the standard deviation is way more important then for Si-rich side. The Mg content fit is therefore more imprecise on the Mg-rich part of the gradient.

The next figures of each sample; C.2 for 1 h ageing, C.3 for 8 h ageing, C.4 for 1 day ageing, C.5 for 3 days ageing and C.6 for 8 days ageing, are not representing the standard deviation but they are relevant to properly compare the profiles and their composition information.

By averaging along all the gradients the uncertainties on the content are estimated at :

- $\Delta x_{\mathrm{Mg}} = 0.2$ %
- $\Delta x_{\mathrm{Si}} = 0.05$ %

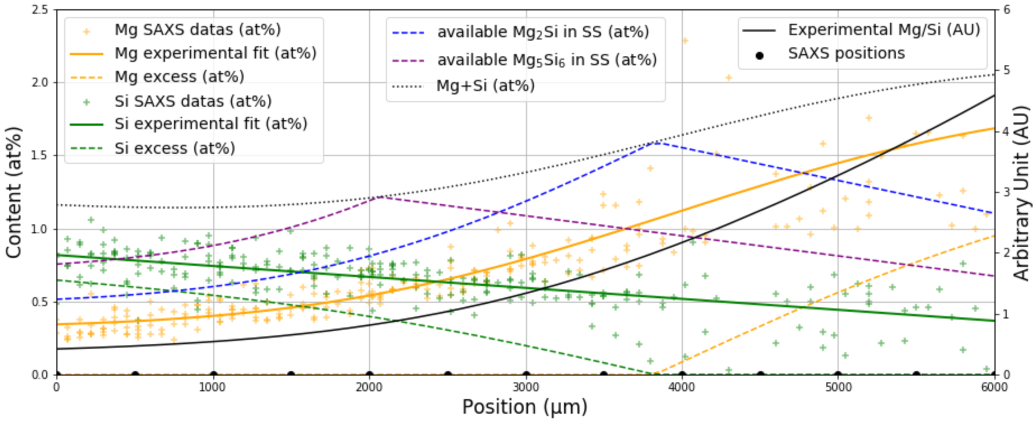

Figure C.2: EDX solid solution composition of a rolled gradient of an Al-1.2.wt%Si Al-2.6wt%Mg diffusion couple after 10 days homogenisation at 550 °C followed by rolling procedure and then aged during 1 h at 170 °C

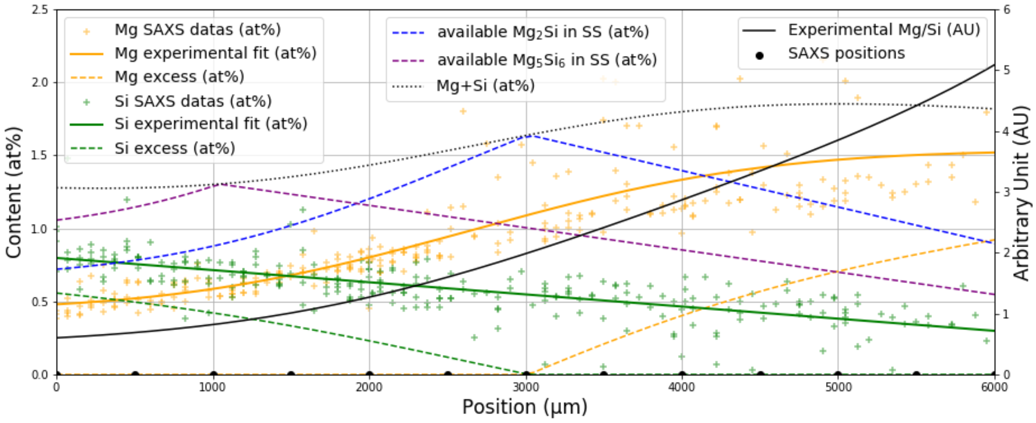

Figure C.3: EDX solid solution composition of a rolled gradient of an Al-1.2.wt%Si Al-2.6wt%Mg diffusion couple after 10 days homogenisation at 550 °C followed by rolling procedure and then aged during 8 h at 170 °C

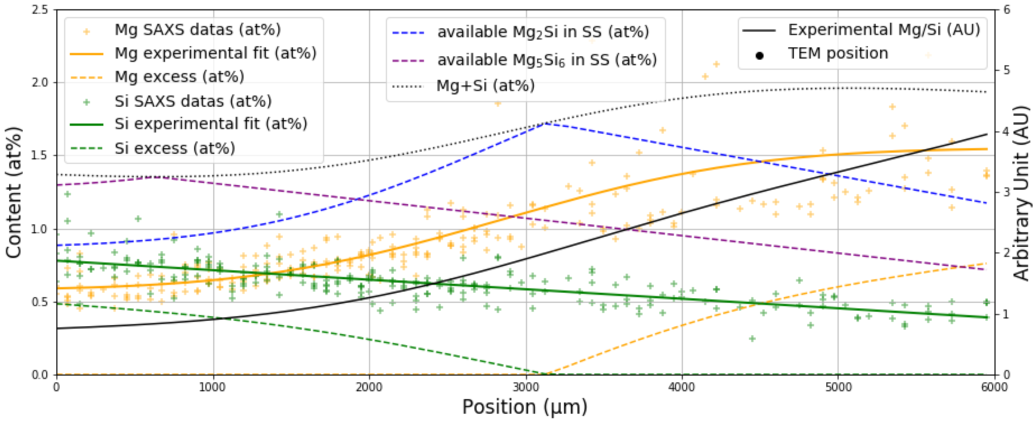

Figure C.4: EDX solid solution composition of a rolled gradient of an Al-1.2.wt%Si Al-2.6wt%Mg diffusion couple after 10 days homogenisation at 550 °C followed by rolling procedure and then aged during 1 day at 170 °C

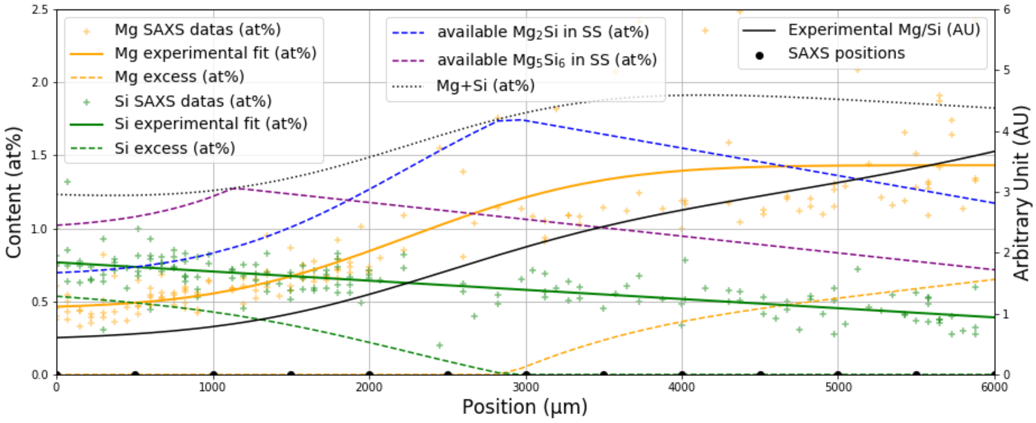

Figure C.5: EDX solid solution composition of a rolled gradient of an Al-1.2.wt%Si Al-2.6wt%Mg diffusion couple after 10 days homogenisation at 550 °C followed by rolling procedure and then aged during 3 days at 170 °C

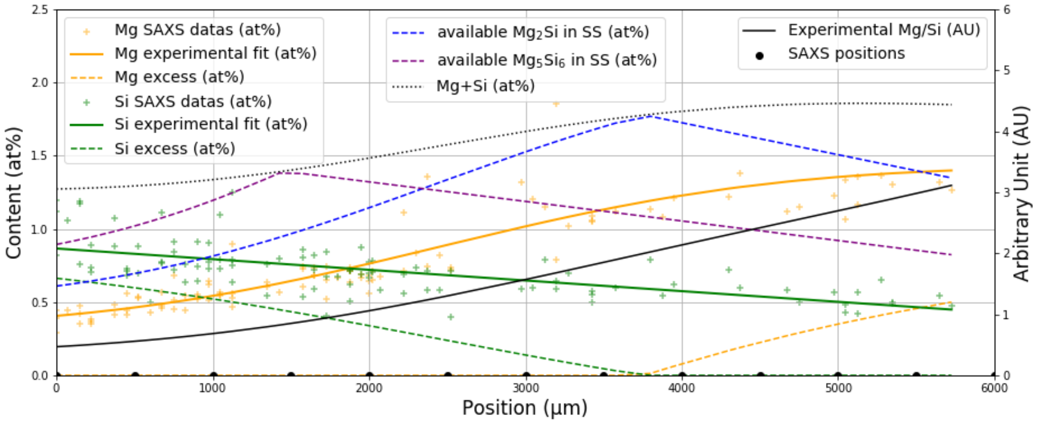

Figure C.6: EDX solid solution composition of a rolled gradient of an Al-1.2.wt%Si Al-2.6wt%Mg diffusion couple after 10 days homogenisation at 550 °C followed by rolling procedure and then aged during 8 days at 170 °C

C.2 TEM and ATP samples

All the rolled samples used for TEM and ATP analyses were extracted from the same bulk (B) which is the same as DSC samples. The real SS composition data of the rolled sample B-R2 was presented in **Chap1**. Mg and Si contents were measured on a thickness zone of 1.6 mm, using 8 lines spaced by 200 µm. The dwell time used for each point was set at 10 s. As for ASAXS samples, Mg-rich part has a wider standard deviation but here it is less important. The Mg fits are more certain.

The next figures; C.7 for B-R1, C.8 for B-R2, C.9 for B-R3 and C.10 for B-R4, give all the important composition information along their gradient on 12 mm.

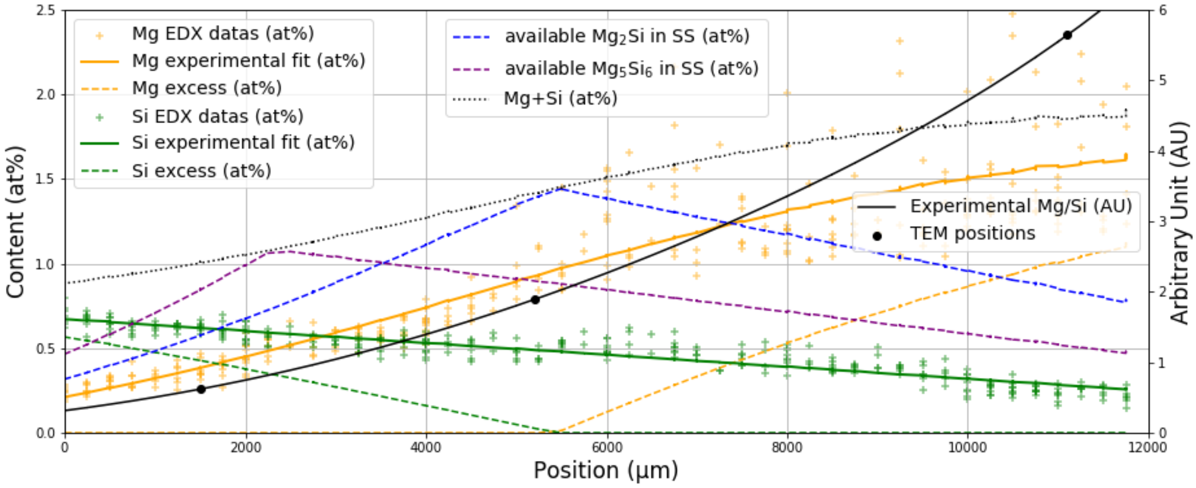

Figure C.7: EDX solid solution composition of B-R1 rolled gradient of an Al-1.2.wt%Si Al-2.6wt%Mg diffusion couple after 10 days homogenisation at 550 °C followed by rolling procedure.

The mean uncertainty of Mg/Si ratio is calculated via:

$$\Delta^{mean}(\mathrm{Mg/Si}) = \frac{x^{mean}_{\mathrm{Mg}}}{x^{mean}_{\mathrm{Si}}} \times \left(\frac{\Delta^{mean} x_{\mathrm{Mg}}}{x^{mean}_{\mathrm{Mg}}} + \frac{\Delta^{mean} x_{\mathrm{Si}}}{x^{mean}_{\mathrm{Si}}} \right) \tag{C.1}$$

With, averages values for the four content profiles:

- On Si-side:
  - $x_{\mathrm{Mg}} = 0.6$ at.%
  - $x_{\mathrm{Si}} = 0.6$ at.%
  - $\Delta^{mean} x_{\mathrm{Mg}} = 0.2$ at.%
  - $\Delta^{mean} x_{\mathrm{Mg}} = 0.2$ at.%

  Mg/Si = 1.0 and $\Delta^{mean}(\mathrm{Mg/Si}) = 0.7$
- On Mg-side:
  - $x_{\mathrm{Mg}} = 1.2$ at.%
  - $x_{\mathrm{Si}} = 0.5$ at.%

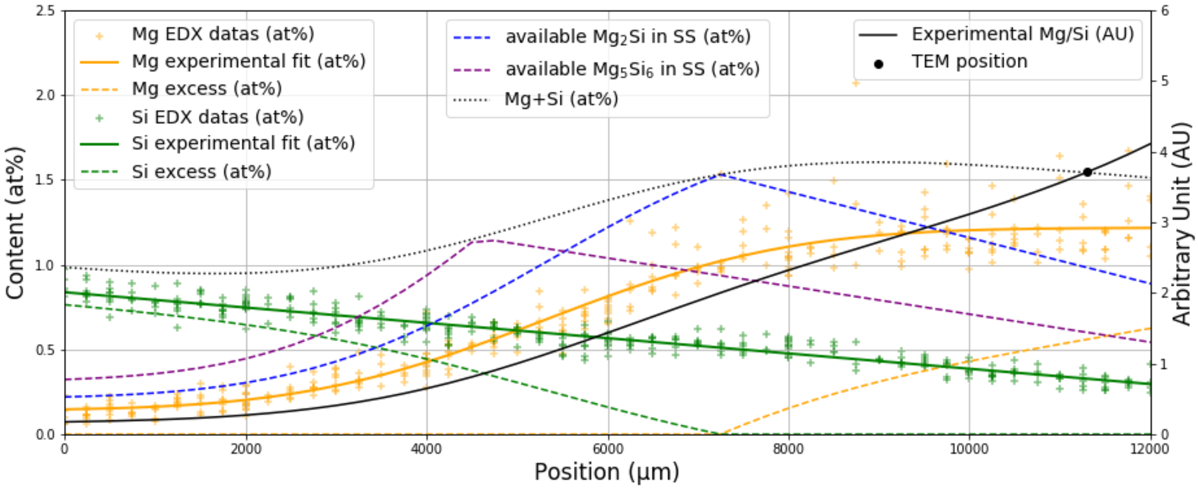

Figure C.8: EDX solid solution composition of B-R2 rolled gradient of an Al-1.2.wt%Si Al-2.6wt%Mg diffusion couple after 10 days homogenisation at 550 °C followed by rolling procedure.

- $\Delta^{mean} x_{\text{Mg}} = 0.4$ at.%
- $\Delta^{mean} x_{\text{Mg}} = 0.1$ at.%

Mg/Si = 3 and $\Delta^{mean}(\text{Mg/Si}) = 1.3$

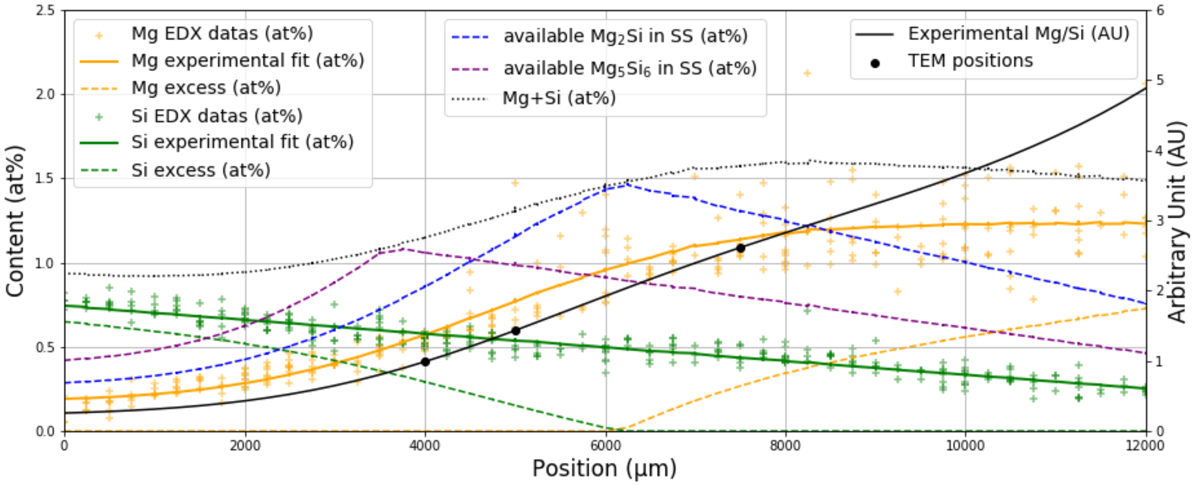

Figure C.9: EDX solid solution composition of B-R3 rolled gradient of an Al-1.2.wt%Si Al-2.6wt%Mg diffusion couple after 10 days homogenisation at 550 °C followed by rolling procedure.

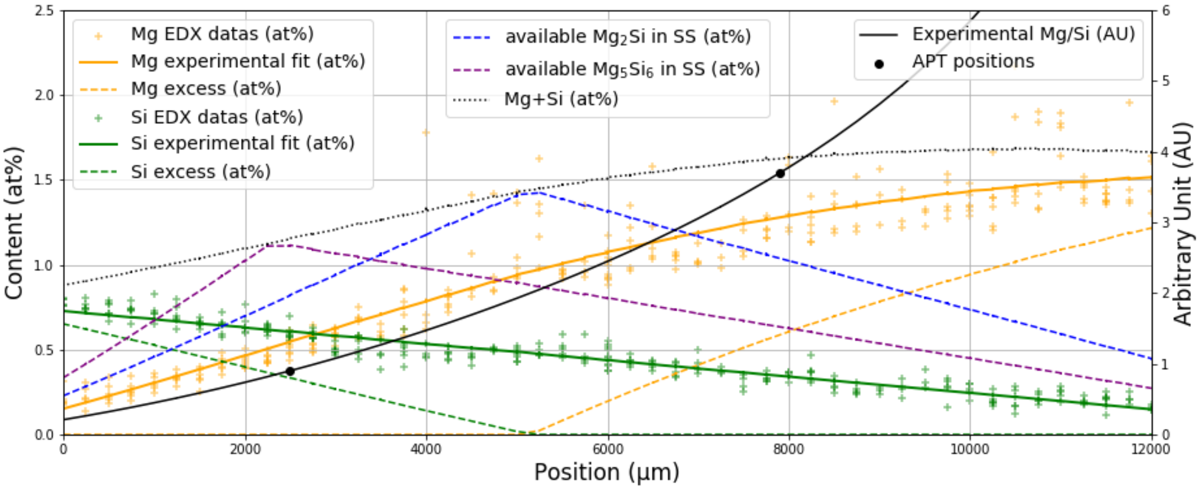

Figure C.10: EDX solid solution composition of B-R4 rolled gradient of an Al-1.2.wt%Si Al-2.6wt%Mg diffusion couple after 10 days homogenisation at 550 °C followed by rolling procedure.

Appendix D

Supplementary simulation parameters

The following tables D.1 and D.2 are reporting A and B thermodynamic parameters (from equation 3.10 of Chapter 3) for the sample A and for each simulated phase.

Mg/Si atomic ratio	$A_{\beta''}$ (K^{-1})	$A_{\beta'}$ (K^{-1})	A_{U2} (K^{-1})	$A_{B'}$ (K^{-1})	A_{Si} (K^{-1})
0	44505.3	27821.4	3690.0	29301.4	2499.5
1	41248.7	27826.1	3690.5	29305.9	2499.3
2	18971.4	27833.1	3691.2	29312.8	2498.7
3	15715.3	27843.3	3692.5	29323.9	2497.4
4	34059.9	27857.3	3694.7	29340.2	2495.4
5	33441.9	27875.0	3690.3	29361.5	2493.1
6	14996.8	27851.9	3681.8	29270.5	2491.2
7	14985.9	27795.4	3676.3	29219.3	2490.1
8	14974.5	27760.1	3673.1	29188.4	2489.6
9	14966.7	27737.5	3671.2	29169.8	2489.4
10	14961.4	27722.1	3670.1	29157.7	2489.4

Table D.1: A thermodynamic parameters of each precipitate depending on their position in the graded sample A (from TCAL4)

Mg/Si atomic ratio	$B_{\beta''}$	$B_{\beta'}$	B_{U2}	$B_{B'}$	B_{Si}
0	13.6802	9.8266	1.1083	7.5175	1.1179
1	12.3588	9.8281	1.1085	7.5191	1.1179
2	6.4890	9.8303	1.1088	7.5217	1.1177
3	5.1935	9.8340	1.1094	7.5263	1.1175
4	12.6533	9.8400	1.1113	7.5360	1.1170
5	14.2388	9.8523	1.1102	7.5752	1.1165
6	6.4285	9.8333	1.1074	7.5137	1.1161
7	6.4661	9.8182	1.1061	7.5018	1.1158
8	6.4767	9.8110	1.1054	7.4951	1.1157
9	6.4807	9.8065	1.1050	7.4912	1.1157
10	6.4825	9.8034	1.1048	7.4888	1.1157

Table D.2: B thermodynamic parameters of each precipitate depending on their position in the graded sample A (from TCAL4)

Appendix E

Example of a Python interface with Preciso as part of the model

4-AlMgSi-graded-10nods-Precipitation

February 3, 2023

1 Precipitation in Al-Mg-Si composition graded alloy with PreciSo

August 2021

1.1 Content

The goal is to make a precipitation simulation along an Al-Mg-Si gradient. Mg and Si are variating along this gradient. In this aproach, 10 nods will represent the gradient. They will then be subjected to a thermal treatment.

1.2 Imports

[1]:
```
import preciso
import numpy as np
from pathlib import Path
import matplotlib.pyplot as plt
import os
from glob import glob
import pandas as pd
from scipy import stats
from scipy import interpolate
from scipy.optimize import least_squares
import math
import matplotlib.pylab as pl
from textwrap import wrap
import plotly.express as px
#from plotly.subplots import make_subplots
import matplotlib.animation as animation
from IPython.display import HTML
from scipy.optimize import curve_fit
from scipy.special import erf
#from mpl_toolkits import mplot3d

#from matplotlib import animation
```

[2]:
```
colors1 = plt.cm.summer(np.linspace(0,0.99,6))
colors2 = plt.cm.autumn(np.linspace(0,0.99,4))

colors=['blue','red','purple','green','pink','brown', 'yellow', 'black',␣
 ↪'orange', 'cyan']
markers = ["o", "^", ".", "x", "v", "<", ">", "d", "s"]
```

1.3 First parameters

Input parameters to perform diffusion between two layers:

- 5 nods represent the layer al-si with wpc_Si and 5 other nods represents the layer al-mg with wpc_Mg
- Diffusion treatment : 10 days = 864 000 s at 550°C
- Diffusion coefficients of Si and, respectively, Mg in Al have been extracted from Fujikawa 1978 and, respectively, Minamino 1983. (Du 2007 is using other coefficients)
- The information about the precipitate are not relevent here (no precipitation will occur at that tempreture)

- M_i = molar mass of the element i
- D0_i = Diffusion coefficient of the element i in Al
- Q_i = activation energy of the element i in Al

[3]:
```
M_Al = 26.982e-3 #kg.mol-1
M_Mg = 24.305e-3
M_Si = 28.086e-3
M_O = 15.999e-3

D0_Si = 2e-4 #m2.s-1
D0_Mg = 6.1e-5
Q_Si = 136000 #J.mol-1
Q_Mg = 127000
```

1.4 Important information along the gradient

[4]:
```
### import gradient compositions

nameSample= 'hardness'
if nameSample == 'dsc' :
    N_nodes = 9
if nameSample == 'hardness' :
    N_nodes = 11

name_file='1-AlMgSi-graded-final-compo-'+nameSample+'.csv'
path_file= Path.home()/'Documents'/'Preciso'/'preciso_git'/name_file
gdt_compo=pd.read_csv(path_file,sep=';')

#print(gdt_compo)
```

```
W_Si=gdt_compo['W_Si']
W_Mg=gdt_compo['W_Mg']

### import gradient thermodynamic parameters

name_file='1-AlMgSi-graded-thermo-param-'+nameSample+'.csv'
path_file= Path.home()/'Documents'/'Preciso'/'preciso_git'/name_file
gdt_thermo=pd.read_csv(path_file,sep=';')

#print(gdt_thermo)

### import gradient precipitates chemistry

name_file='1-AlMgSi-graded-precipitates-chemistry-'+nameSample+'.csv'
path_file= Path.home()/'Documents'/'Preciso'/'preciso_git'/name_file
gdt_precipitates=pd.read_csv(path_file,sep=';')

#print(gdt_precipitates)

### import atomic volume of each phase (not calculated finally)

V_at_betapp = 1.66e-29
V_at_betap = 1.66e-29
V_at_beta = 1.66e-29
V_at_u1 = 1.66e-29
V_at_u2 = 1.66e-29
V_at_Bp = 1.66e-29
V_at_si = 2.046e-29 # source internet materialsproject.org
#V_at_almg = 1.66e-29

### import of hardness results

name_file='1-AlMgSi-graded-hardness-kine.csv'
path_file= Path.home()/'Documents'/'Preciso'/'preciso_git'/name_file
gdt_hardness=pd.read_csv(path_file,sep=';',header=0)

#print(gdt_hardness)
```

1.5 Age-hardening conditions

[5]:
```
t_prec = 1e8 #s = 40 mois
#print(t_prec)
T_prec = 170 + 273 #K

initialTime=1e-3
finalTime=t_prec
```

```
timeInter=np.logspace(np.log10(initialTime+1),np.log10(finalTime-1),100)
```

1.6 Input datas

[6]:
```
input_template_property_table = ""
input_template_property_table_i = ""
input_template_node = ""
input_template_node_i = ""
input_template_connectivity = ""
input_template_connectivity_i = ""

for i in range (N_nodes) :

    input_template_property_table_i = """
nodeProperty """+str(i)+""" """+str(i)+""" element Si """+str(W_Si[i]*100)+"""␣
 ↪{{M_Si}} {{D0_Si}} {{Q_Si}}
nodeProperty """+str(i)+""" """+str(i)+""" element Mg """+str(W_Mg[i]*100)+"""␣
 ↪{{M_Mg}} {{D0_Mg}} {{Q_Mg}}
nodeProperty """+str(i)+""" """+str(i)+""" precipitate betapp {{VBetapp}} 0.068␣
 ↪"""+str(gdt_thermo["A_betapp"][i])+" "+str(gdt_thermo["B_betapp"][i])+" rod␣
 ↪40 homogeneous "+ gdt_precipitates["betapp"][i]+"""
nodeProperty """+str(i)+""" """+str(i)+""" precipitate betap {{VBetap}} 0.125␣
 ↪"""+str(gdt_thermo["A_betap"][i])+" "+str(gdt_thermo["B_betap"][i])+""" rod␣
 ↪40 homogeneous """+ gdt_precipitates["betap"][i]+"""
nodeProperty """+str(i)+""" """+str(i)+""" precipitate u2 {{VU2}} 0.106␣
 ↪"""+str(gdt_thermo["A_u2"][i])+" "+str(gdt_thermo["B_u2"][i])+""" rod 20␣
 ↪homogeneous """+ gdt_precipitates["u2"][i]+"""
nodeProperty """+str(i)+""" """+str(i)+""" precipitate Bp {{VBp}} 0.076␣
 ↪"""+str(gdt_thermo["A_Bp"][i])+" "+str(gdt_thermo["B_Bp"][i])+""" rod 100␣
 ↪homogeneous """+ gdt_precipitates["Bp"][i]+"""
nodeProperty """+str(i)+""" """+str(i)+""" precipitate si {{VSi}} 0.311␣
 ↪"""+str(gdt_thermo["A_si"][i])+" "+str(gdt_thermo["B_si"][i])+""" rod 2␣
 ↪homogeneous """+gdt_precipitates["si"][i]+"""
"""
    input_template_node_i = """node """+str(i)+""" """+str(i*4.8e-3/
 ↪N_nodes)+""" """+""" 0 0 4e-4
"""

    input_template_property_table += input_template_property_table_i
    input_template_node += input_template_node_i

for i in range (N_nodes-1) :

    input_template_connectivity_i = """ connect """+str(i)+""" """+str(i+1)+"""␣
 ↪1
"""
```

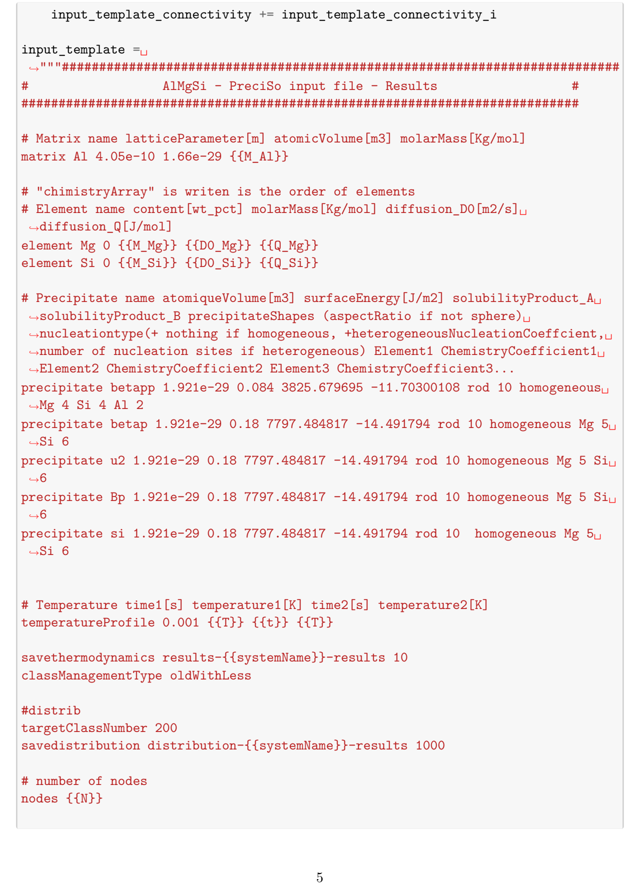

```
    input_template_connectivity += input_template_connectivity_i

input_template =␣
 ↪"""##########################################################################
#                   AlMgSi - PreciSo input file - Results                   #
##########################################################################

# Matrix name latticeParameter[m] atomicVolume[m3] molarMass[Kg/mol]
matrix Al 4.05e-10 1.66e-29 {{M_Al}}

# "chimistryArray" is writen is the order of elements
# Element name content[wt_pct] molarMass[Kg/mol] diffusion_D0[m2/s]␣
 ↪diffusion_Q[J/mol]
element Mg 0 {{M_Mg}} {{D0_Mg}} {{Q_Mg}}
element Si 0 {{M_Si}} {{D0_Si}} {{Q_Si}}

# Precipitate name atomiqueVolume[m3] surfaceEnergy[J/m2] solubilityProduct_A␣
 ↪solubilityProduct_B precipitateShapes (aspectRatio if not sphere)␣
 ↪nucleationtype(+ nothing if homogeneous, +heterogeneousNucleationCoeffcient,␣
 ↪number of nucleation sites if heterogeneous) Element1 ChemistryCoefficient1␣
 ↪Element2 ChemistryCoefficient2 Element3 ChemistryCoefficient3...
precipitate betapp 1.921e-29 0.084 3825.679695 -11.70300108 rod 10 homogeneous␣
 ↪Mg 4 Si 4 Al 2
precipitate betap 1.921e-29 0.18 7797.484817 -14.491794 rod 10 homogeneous Mg 5␣
 ↪Si 6
precipitate u2 1.921e-29 0.18 7797.484817 -14.491794 rod 10 homogeneous Mg 5 Si␣
 ↪6
precipitate Bp 1.921e-29 0.18 7797.484817 -14.491794 rod 10 homogeneous Mg 5 Si␣
 ↪6
precipitate si 1.921e-29 0.18 7797.484817 -14.491794 rod 10  homogeneous Mg 5␣
 ↪Si 6


# Temperature time1[s] temperature1[K] time2[s] temperature2[K]
temperatureProfile 0.001 {{T}} {{t}} {{T}}

savethermodynamics results-{{systemName}}-results 10
classManagementType oldWithLess

#distrib
targetClassNumber 200
savedistribution distribution-{{systemName}}-results 1000

# number of nodes
nodes {{N}}
```

```
# Specific information on node #i (node_index x_node y_node z_node node_volume)
"""+str(input_template_node) +"""

# Connectivity table (node#i node#j surface_bet_#i_and_#j)
"""+str(input_template_connectivity) +"""

# Property table (node#i node#i Element name content[wt_pct] molarMass[Kg/mol]␣
 ↪diffusion_D0[m2/s] diffusion_Q[J/mol] Precipitate ... )
"""+str(input_template_property_table) +"""

minDissolutionLimit 1e-10
maxDissolutionLimit 2e-10
criterion solContent
#criterion rstar
#maxCriterionIncrease 0.01

#mechanicModel 1=rod
mechanicModel 1

#SSconstant element unit StrengthConst
SSconstant Si MPa_Wpct 12.5
SSconstant Mg MPa_Wpct 52.9

#precipitateConstants Name critialRad arrangement youngModulus poissCoef hard1␣
 ↪hard2 hard3 k_sh
precipitateConstants betapp 3e-009 triangularPath 71.5e9 0.33 0 0 0 0
precipitateConstants betap 7e-009 triangularPath 71.5e9 0.33 0 0 0 0
precipitateConstants u2 2e-009 triangularPath 71.5e9 0.33 0 0 0 0
precipitateConstants Bp 7e-009 triangularPath 71.5e9 0.33 0 0 0 0
precipitateConstants si 1e-009 triangularPath 71.5e9 0.33 0 0 0 0

#dislocations initialDensity strength betaff
dislocations 0 0.5 0.5

#cristalloConstants sigma_0 M a0 lattice
cristalloConstant 10000000 2.0 4.05e-010 cfc

grainSize 15e-6 0 0 0
young 273 71.5e9
poisson 273 0.33

"""

#print(input_template)
```

Note : Any keyword can be replaced by a tag like `{{temperature}}` to allow templating features. For more details, see notebook N+1.

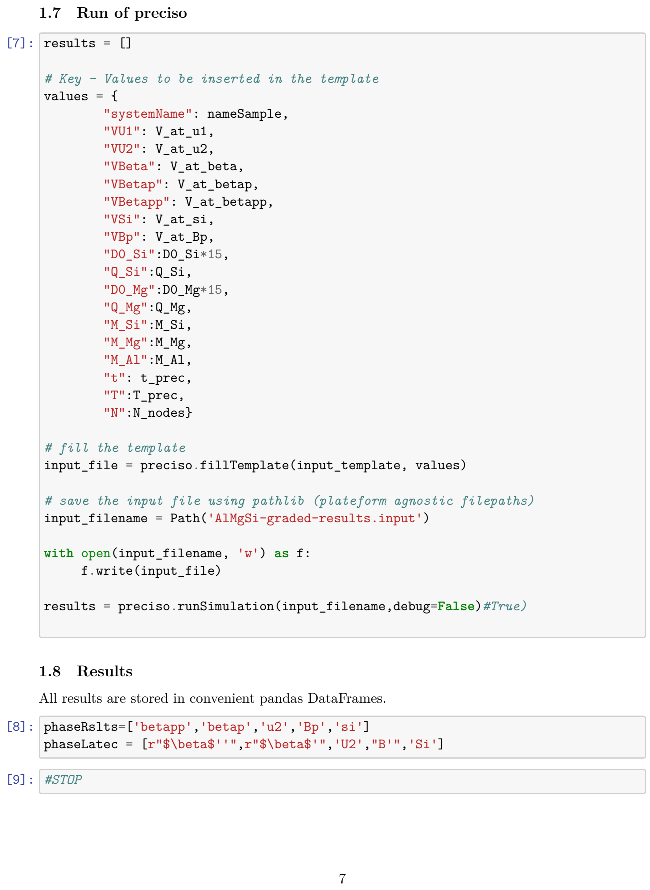

1.7 Run of preciso

```
[7]: results = []

     # Key - Values to be inserted in the template
     values = {
             "systemName": nameSample,
             "VU1": V_at_u1,
             "VU2": V_at_u2,
             "VBeta": V_at_beta,
             "VBetap": V_at_betap,
             "VBetapp": V_at_betapp,
             "VSi": V_at_si,
             "VBp": V_at_Bp,
             "D0_Si":D0_Si*15,
             "Q_Si":Q_Si,
             "D0_Mg":D0_Mg*15,
             "Q_Mg":Q_Mg,
             "M_Si":M_Si,
             "M_Mg":M_Mg,
             "M_Al":M_Al,
             "t": t_prec,
             "T":T_prec,
             "N":N_nodes}

     # fill the template
     input_file = preciso.fillTemplate(input_template, values)

     # save the input file using pathlib (plateform agnostic filepaths)
     input_filename = Path('AlMgSi-graded-results.input')

     with open(input_filename, 'w') as f:
          f.write(input_file)

     results = preciso.runSimulation(input_filename,debug=False)#True)
```

1.8 Results

All results are stored in convenient pandas DataFrames.

```
[8]: phaseRslts=['betapp','betap','u2','Bp','si']
     phaseLatec = [r"$\beta$''",r"$\beta$'",'U2',"B'",'Si']
```

```
[9]: #STOP
```

1.8.1 Overview along the gradient for one particular time in hour

```
[10]: t_choice_h_preci = 16 #choice time in hour for the age hardening treatment
```

```
[11]: ## table of interesting data

      t_choice = t_choice_h_preci * 3600
      #print(t_choice)

      results_int_t_choice = []

      node_real=0

      for node in results.precipitation.values():

          results_node_int_t_choice = []
          columns = []

          for column in node.columns :

              results_int_time = interpolate.
       ↪interp1d(node['t[s]'],node[column],kind='linear')
              #print('node :'+str(node_real)+'column :
       ↪'+str(column),results_int_time(t_choice))

              results_node_int_t_choice.append(results_int_time(t_choice))

              columns.append(column)

          node_real=node_real+1

          results_int_t_choice.append(results_node_int_t_choice)

      df_results_t_choice = pd.DataFrame(results_int_t_choice,index=[i for i in␣
       ↪range(N_nodes)], columns=columns)

      #print(df_results_t_choice)
      #print(df_results_t_choice['N_betapp'][0])
```

```
[12]: ## figure settings

      fig1,ax = plt.subplots(nrows=3, ncols=1,figsize=(7,4*3))

      for i in range(3):
          ax[i].grid(True)

      k = 0
```

```
for j in phaseRslts :

    N = [df_results_t_choice['N_'+str(j)][elem] for elem in range(N_nodes)]
    ax[0].semilogy(N, color=colors[k], label=str(j))

    rmean = [df_results_t_choice['rmean_'+str(j)+'[m]'][elem] for elem in␣
↪range(N_nodes)]
    ax[1].semilogy(rmean, color=colors[k], label=str(j))

    fv= [df_results_t_choice['fv_'+str(j)][elem] for elem in range(N_nodes)]
    ax[2].plot(fv, color=colors[k], label=str(j))

    k+=1

ax[0].set_ylabel('Final number density (#/m$^3$)')
ax[0].set_label('Node')
ax[0].set_title("\n".join(wrap('Precipitation in the gradient after␣
↪'+str(t_choice_h_preci)+' hours at 170°C',60)))
ax[0].legend(loc='best')

ax[1].set_ylabel('Final mean radius(m)')
ax[1].set_xlabel('Node')
ax[1].legend(loc='best')

ax[2].set_ylabel('Final volume fraction')
ax[2].set_xlabel('Node')
ax[2].legend(loc='best')
```

```
[12]: <matplotlib.legend.Legend at 0x7fac7f502ad0>
```

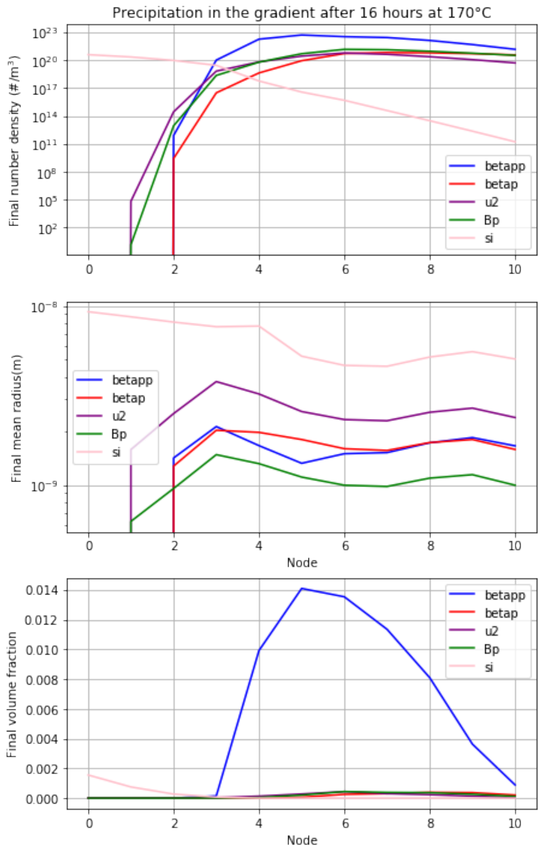

1.8.2 Overview along the gradient for one particular time in day

```
[13]: t_choice_d_preci = 60 #choice time in days for the age hardening treament
```

```
[14]: #conversion of that time in seconds and addition of the first 10days treatment

t_choice = t_choice_d_preci * 3600 * 24
#print(t_choice)

results_int_t_choice = []

node_real=0

for node in results.precipitation.values():

    results_node_int_t_choice = []
    columns = []

    for column in node.columns :

        results_int_time = interpolate.
↪interp1d(node['t[s]'],node[column],kind='linear')
        #print('node :'+str(node_real)+'column :
↪'+str(column),results_int_time(t_choice))

        results_node_int_t_choice.append(results_int_time(t_choice))

        columns.append(column)

    node_real=node_real+1

    results_int_t_choice.append(results_node_int_t_choice)

df_results_t_choice = pd.DataFrame(results_int_t_choice,index=[i for i in␣
↪range(N_nodes)], columns=columns)

#print(df_results_t_choice)
#print(df_results_t_choice['N_betapp'][0])
```

```
[15]: fig1,ax = plt.subplots(nrows=3, ncols=1,figsize=(7,4*3))

for i in range(3):
```

```
    ax[i].grid(True)

k = 0

for j in phaseRslts :

    N = [df_results_t_choice['N_'+str(j)][elem] for elem in range(N_nodes)]
    ax[0].semilogy(N, color=colors[k], label=str(j))

    rmean = [df_results_t_choice['rmean_'+str(j)+'[m]'][elem] for elem in␣
↪range(N_nodes)]
    ax[1].semilogy(rmean, color=colors[k], label=str(j))

    fv= [df_results_t_choice['fv_'+str(j)][elem] for elem in range(N_nodes)]
    ax[2].plot(fv, color=colors[k], label=str(j))

    k+=1

ax[0].set_ylabel('Number density (#/m$^3$)')
ax[0].set_label('Node')
ax[0].set_title("\n".join(wrap('Precipitation in the gradient after␣
↪'+str(t_choice_d_preci)+' days at 170°C',60)))
ax[0].legend(loc='best')

ax[1].set_ylabel('Mean radius(m)')
ax[1].set_xlabel('Node')
ax[1].legend(loc='best')

ax[2].set_ylabel('Volume fraction')
ax[2].set_xlabel('Node')
ax[2].legend(loc='best')
```

```
[15]: <matplotlib.legend.Legend at 0x7fac7f469fd0>
```

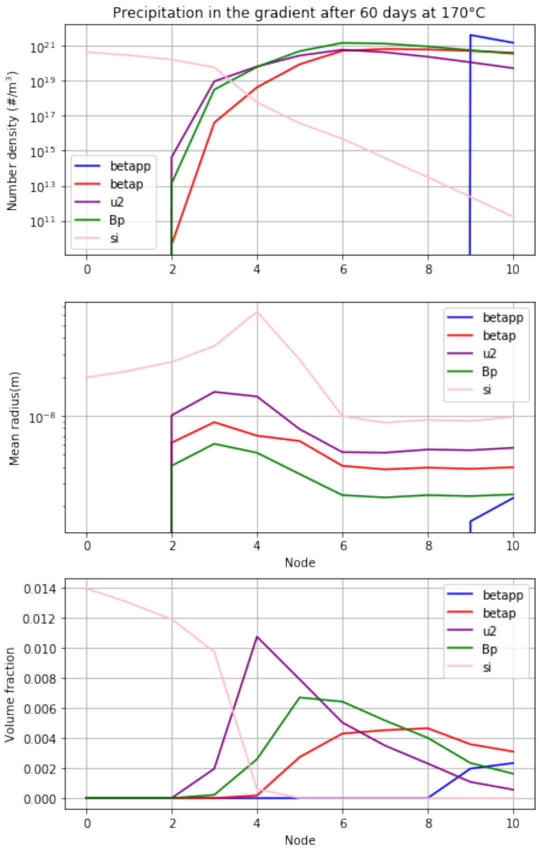

1.8.3 Overview along the gradient for all time steps

[16]:
```
### consrtruction of plotly animations

## first column of the dataframe : node

l = [i for i in range(0,N_nodes)]
l1 = []

for j in range(N_nodes) :
    for k in range (len(results.precipitation[0]['t[s]'])) :
        l1.append(str(l[j]))

df_results_interpolate_final = pd.DataFrame(l1,columns=['node'])
#print(df_results_interpolate_final )

#print(df_results_interpolate_final.index)

# useless interpolation but working to build the dataframe

df_results_interpolate = pd.DataFrame()

t_new = np.linspace(results.precipitation[0]['t[s]'].loc[0],results.
 ↪precipitation[0]['t[s]'].iloc[-1],len(results.precipitation[0]['t[s]']))

for node in results.precipitation.values():

    df_results_int = pd.DataFrame()

    for column in node.columns :
        results_int_time = interpolate.
 ↪interp1d(node['t[s]'],node[column],kind='linear')
        #plt.plot(t_new, results_int_time(t_new),linestyle = ':', linewidth = 0.
 ↪25, color =  'black')
        results_int=pd.Series(results_int_time(t_new),name=column)
        #print(results_int)
        df_results_int = pd.concat([df_results_int,results_int],axis=1,␣
 ↪sort=False)

    #index=ratio,columns=str_x1
    #print(df_results_int)

    df_results_interpolate = pd.
 ↪concat([df_results_interpolate,df_results_int],axis=0,sort=False)
```

```
    #print(df_results_interpolate)



df_results_interpolate.reset_index(drop=True, inplace=True)

df_results_interpolate_final = pd.
 ↪concat([df_results_interpolate_final,df_results_interpolate],axis=1,sort=False)

#print(df_results_interpolate_final)
```

[17]:
```
## animation of the evolution of the density numbers with time along the␣
 ↪gradient

px.line(df_results_interpolate_final,x="node",y=["N_"+str(i) for i in␣
 ↪phaseRslts],animation_frame="t[s]",
       range_x=[0,N_nodes],range_y=[1e3,2e22],log_y=True,markers=True,
       title='Evolution of the density numbers with time along the gradient')
```

[18]:
```
## animation of the evolution of the mean radius with time along the gradient
px.line(df_results_interpolate_final, x="node", y=["rmean_"+str(i)+"[m]" for i␣
 ↪in phaseRslts],
       animation_frame="t[s]",range_x=[0,N_nodes],␣
 ↪range_y=[1e-9,2e-7],log_y=True,markers=True,
       title='Evolution of mean radius with time along the gradient')
```

[19]:
```
## animation of the evolution of the volume fraction with time along the␣
 ↪gradient
px.line(df_results_interpolate_final, x="node", y=["fv_"+str(i) for i in␣
 ↪phaseRslts],animation_frame="t[s]",
       range_x=[0,N_nodes],title='evolution of volume fractions with time␣
 ↪along the gradient',
       range_y=[0,0.015],markers=True)
```

1.8.4 Kinetics for one node / composition

kinetics for one node

[20]:
```
nod_kine=8
```

[21]:
```
results_nod_kine=[]
results_nod_kine=results.precipitation[nod_kine] # df : dataframes

#print(results_nod_kine)
#print(results_nod_kine.shape)
```

```
fig1,ax = plt.subplots(nrows=3, ncols=1,figsize=(7,7))

for i in range(3):
    ax[i].grid(True)

k = 0

for j in phaseRslts :

    N = results_nod_kine['N_'+str(j)]
    ax[0].loglog(results_nod_kine["t[s]"],N, color=colors[k], label=str(j))

    rmean = results_nod_kine["rmean_"+str(j)+"[m]"]
    ax[1].loglog(rmean, color=colors[k], label="Rmean "+str(j))

    rstar = results_nod_kine["r*_"+str(j)+"[m]"]
    ax[1].loglog(rstar, color=colors[k], label="R* "+str(j),ls=':')

    fv= results_nod_kine["fv_"+str(j)]
    ax[2].semilogx(fv, color=colors[k], label=str(j))

    k+=1

ax[0].set_ylabel('Number density (#/m$^3$)')
ax[0].set_label('Time (s)')
ax[0].set_title("\n".join(wrap('Precipitation in the gradient on nod␣
 ↪'+str(nod_kine)+' during ageing at 170°C',60)))
ax[0].legend(loc='best')

ax[1].set_ylabel('Radius(m)')
ax[1].set_xlabel('Time (s)')
ax[1].legend(loc='best')

ax[2].set_ylabel('Volume fraction')
ax[2].set_xlabel('Time (s)')
ax[2].legend(loc='best')
#ax[2].set_xlim([0.001,1e8])
```

[21]:
```
<matplotlib.legend.Legend at 0x7fac8212ac90>
```

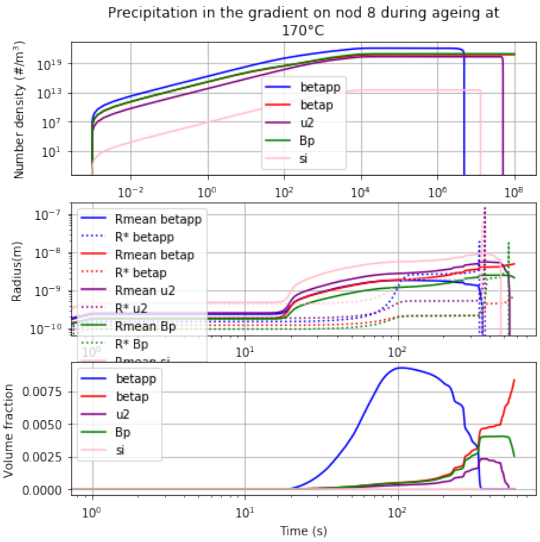

1.9 Mechanics

1.9.1 mechanics for one time along the gradient

[22]:

```
t_choice_h_preci = 16 #time age hardening treatment in hours
```

[23]:

```
fig=plt.figure(figsize=(14,7))

#conversion of that time in second and addition of the first 10days treatment

t_choice = t_choice_h_preci * 3600
#print(t_choice)
```

```
meca_results_int_t_choice = []

node_real=0

for node in results.mechanics.values():

    results_node_int_t_choice = []
    columns = []

    for column in node.columns :

        results_int_time = interpolate.
 ↪interp1d(node['t[s]'],node[column],kind='linear')
        #print('node :'+str(node_real)+'column :
 ↪'+str(column),results_int_time(t_choice))

        results_node_int_t_choice.append(results_int_time(t_choice))

        columns.append(column)

    node_real=node_real+1

    meca_results_int_t_choice.append(results_node_int_t_choice)

df_meca_results_t_choice = pd.DataFrame(meca_results_int_t_choice,index=[i for␣
 ↪i in range(N_nodes)], columns=columns)

#print(df_results_t_choice)
#print(df_results_t_choice['N_betapp'][0])


## attribution données pour chaque phase :

#print (table_meca_raw_final)

sigma_SS_final = [df_meca_results_t_choice['SigmaSS[MPa]'][elem] for elem in␣
 ↪range(N_nodes)]
plt.plot(sigma_SS_final, color='brown', label="sigma Solid Solution [MPa]")

sigma_tot_final = [df_meca_results_t_choice['sigmaFlowMicro[MPa]'][elem] for␣
 ↪elem in range(N_nodes)]
plt.plot(sigma_tot_final, color='black', label="sigma tot [MPa]")

k= 0

for j in phaseRslts :
```

```
    sigma_bp_final= [df_meca_results_t_choice['sigma'+str(j)+'_bp[MPa]'][elem]␣
 ↪for elem in range(N_nodes)]
    plt.plot(sigma_bp_final, color=colors[k], label="by-passed "+str(j),ls=':')

    sigma_sh_final= [df_meca_results_t_choice['sigma'+str(j)+'_sh[MPa]'][elem]␣
 ↪for elem in range(N_nodes)]
    plt.plot(sigma_sh_final, color=colors[k], label="sheared "+str(j),ls='--')

    k+=1


#plt.ylim((0,20))
plt.ylabel('Yield stress (MPa)',fontsize=15)
plt.xlabel('Node',fontsize=15)
plt.title('Yield stress along the gradient after '+str(t_choice_h_preci)+' h at␣
 ↪170°C',fontsize=15)
plt.legend(loc='best',fontsize=13)

plt.savefig('YieldStressAlongGradient.pdf', dpi=96)
```

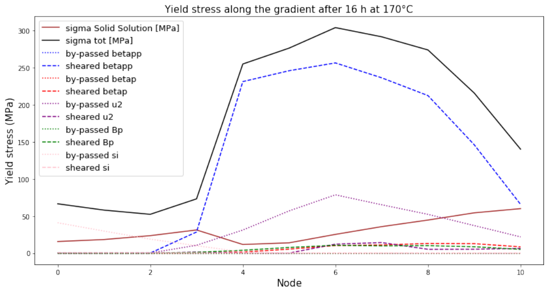

[24]:

```
#STOP
```

1.9.2 Animation of the evolution of the yield stress with time along the gradient

[25]:

```
### creation of tables for plotly animations and for colormap

#-------------plotly animations table (YS)

## first colum of the dataframe : node

l = [i for i in range(0,N_nodes)]
l1 = []

for j in range(N_nodes) :
    for k in range (len(results.mechanics[0]['t[s]'])) :
        l1.append(str(l[j]))


df_results_meca_final = pd.DataFrame(l1,columns=['node'])

# useless interpolation but working to build the dataframe

df_results_meca = pd.DataFrame()

t_new = np.linspace(results.mechanics[0]['t[s]'][0],results.
 ↪mechanics[0]['t[s]'].iloc[-1],len(results.mechanics[0]['t[s]']))

for node in results.mechanics.values():

    df_results = pd.DataFrame()

    for column in node.columns :
        results_meca_time = interpolate.
 ↪interp1d(node['t[s]'],node[column],kind='linear')
        #plt.plot(t_new, results_int_time(t_new),linestyle = ':', linewidth = 0.
 ↪25, color =  'black')
        results_meca=pd.Series(results_meca_time(t_new),name=column)
        #print(results_int)
        df_results = pd.concat([df_results,results_meca],axis=1, sort=False)


    df_results_meca = pd.concat([df_results_meca,df_results],axis=0,sort=False)
    #print(df_results_meca)

df_results_meca.reset_index(drop=True, inplace=True)

df_results_meca_final = pd.
 ↪concat([df_results_meca_final,df_results_meca],axis=1,sort=False)
```

```
#print(df_results_meca_final)

#---------------------- ColorMap table (hardness)

df_results_colormap = pd.DataFrame(results.mechanics[0]['t[s]'])
df_results_colormapHV = pd.DataFrame(results.mechanics[0]['t[s]'])
df_results_colormapHVad = pd.DataFrame(results.mechanics[0]['t[s]'])

for n in l:
    df_results_colormap_i = results.mechanics[n]['sigmaFlowMicro[MPa]']
    df_results_colormap = pd.
 ↪concat([df_results_colormap,df_results_colormap_i], axis=1, sort=False)

    df_results_colormapHV_i = 0.33*results.
 ↪mechanics[n]['sigmaFlowMicro[MPa]']+16 #conversion YS to hardness Mhyr
    df_results_colormapHV = pd.
 ↪concat([df_results_colormapHV,df_results_colormapHV_i], axis=1, sort=False)

    df_results_colormapHVad_i = 0.32*results.
 ↪mechanics[n]['sigmaFlowMicro[MPa]']+20 #conversion YS to hardness Ju
    df_results_colormapHVad = pd.
 ↪concat([df_results_colormapHVad,df_results_colormapHVad_i], axis=1,␣
 ↪sort=False)



df_results_colormap = df_results_colormap.T
df_results_colormapHV = df_results_colormapHV.T
df_results_colormapHVad = df_results_colormapHVad.T

l2=['t[s]']
for i in range(0,N_nodes):
    l2.append(str(i))
l2 = pd.Series(l2)

df_results_colormap = df_results_colormap.set_index(l2)
df_results_colormap = df_results_colormap.T
df_results_colormap = df_results_colormap.set_index(['t[s]'])
#print(df_results_colormap)

df_results_colormapHV = df_results_colormapHV.set_index(l2)
df_results_colormapHV = df_results_colormapHV.T
df_results_colormapHV = df_results_colormapHV.set_index(['t[s]'])

df_results_colormapHVad = df_results_colormapHVad.set_index(l2)
df_results_colormapHVad = df_results_colormapHVad.T
df_results_colormapHVad = df_results_colormapHVad.set_index(['t[s]'])
```

[26]:
```
## animation of the evolution of the yield stress with time along the gradient

px.line(df_results_meca_final, x="node",␣
 ↪y=['sigmabetapp[MPa]','sigmabetap[MPa]','sigmau2[MPa]','sigmaBp[MPa]',"SigmaSS[MPa]",
        "sigmaFlowMicro[MPa]"], animation_frame="t[s]",range_x=[0,N_nodes],␣
 ↪range_y=[0,400],markers=True,
        title='Evolution of the yield stress with time along the gradient')
```

[27]:
```
## confrontation colors map durete experimentale et yield stress modelisé

gdt_hardness_notime = gdt_hardness.drop(['# duree'],axis=1)


## donnees durete

x = np.log10(gdt_hardness['# duree'])
y = np.linspace(400,4400,11)
#X, Y = np.meshgrid(x, y)
#print(X,Y)
Z = gdt_hardness_notime.T
#print(Z)

x2 = np.linspace(x.min(), x.max(), 20) #100)
y2 = np.linspace(y.min(), y.max(), 20) #100)
f = interpolate.interp2d(x, y, Z, kind='linear')
Z2 = f(x2, y2)
X2, Y2 = np.meshgrid(x2, y2)

## donnees modele yield stress

x3 = np.log10(df_results_colormap.index.get_level_values('t[s]'))
y3 = np.linspace(0,4800,N_nodes)
#X3, Y3 = np.meshgrid(x3, y3)
#print(X,Y)
Z3 = df_results_colormap.T
#print(Z)

x4 = np.linspace(x3.min(), x3.max(), 30) #150)
y4 = np.linspace(y3.min(), y3.max(), 20) #100)
f = interpolate.interp2d(x3, y3, Z3, kind='linear')
Z4 = f(x4, y4)
X4, Y4 = np.meshgrid(x4, y4)

## figure

fig, ax = plt.subplots(nrows=1, ncols=2,figsize=(13,5))
```

```
f1 = ax[0].pcolormesh(X2, Y2, Z2,cmap='twilight_shifted',vmin=20, vmax=130)
plt.colorbar(f1,label='Vickers hardness (HV)',ax=ax[0])

f2 = ax[1].pcolormesh(X4, Y4, Z4,cmap='twilight_shifted',vmin=0, vmax=350)
plt.colorbar(f2,label='Yield stress (MPa)',ax=ax[1])


#plt.legend(fontsize=15)

ax[0].set_ylabel('Position ( m)',fontsize=15)
#ax[1].set_ylabel('Position ( m)',fontsize=15)
ax[0].set_xlabel('Ageing time (log10 in s)',fontsize=15)
ax[1].set_xlabel('Ageing time (log10 in s)',fontsize=15)

ax[0].set_title('Experimental hardness',fontsize=15)
ax[1].set_title('Modelled yield stress',fontsize=15)


ax[1].set_xlim([0,np.log10(5e6)])#1e10)])
ax[1].set_ylim([400,4400])

#plt.savefig('4-'+nameSample+'-YS-ColorMap.png')
```

[27]:
```
(400, 4400)
```

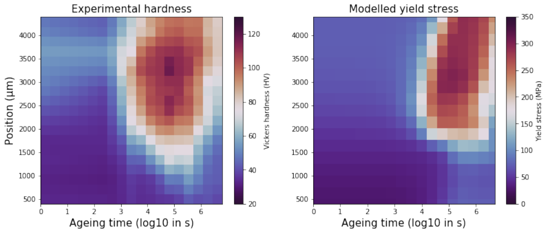

[28]:
```
## confrontation expe hardness and modelled hardness (after conversion from YS)

gdt_hardness_notime = gdt_hardness.drop(['# duree'],axis=1)


## expe hardness data
```

```
x = np.log10(gdt_hardness['# duree'])
y = np.linspace(400,4400,11)
#X, Y = np.meshgrid(x, y)
#print(X,Y)
Z = gdt_hardness_notime.T
#print(Z)

x2 = np.linspace(x.min(), x.max(), 100) #100)
y2 = np.linspace(y.min(), y.max(), 100) #100)
f = interpolate.interp2d(x, y, Z, kind='linear')
Z2 = f(x2, y2)
X2, Y2 = np.meshgrid(x2, y2)

## modelled hardness data (converted from YS by mhyr expression)

x3 = np.log10(df_results_colormapHV.index.get_level_values('t[s]'))
print(len(x3))
y3 = np.linspace(0,4800,N_nodes)
#X3, Y3 = np.meshgrid(x3, y3)
#print(X,Y)
Z3 = df_results_colormapHV.T
#print(Z)

x4 = np.linspace(x3.min(), x3.max(), 500) #500)
y4 = np.linspace(y3.min(), y3.max(), 400) #400)
f = interpolate.interp2d(x3, y3, Z3, kind='linear')
Z4 = f(x4, y4)
X4, Y4 = np.meshgrid(x4, y4)

## modelled hardness data (converted from YS by my expression)

x5 = np.log10(df_results_colormapHVad.index.get_level_values('t[s]'))
y5 = np.linspace(0,4800,N_nodes)
Z5 = df_results_colormapHVad.T

x6 = np.linspace(x5.min(), x5.max(), 500) #500)
y6 = np.linspace(y5.min(), y5.max(), 400) #400)
f = interpolate.interp2d(x5, y5, Z5, kind='linear')
Z6 = f(x6, y6)
X6, Y6 = np.meshgrid(x6, y6)

## figure

fig, ax = plt.subplots(nrows=1, ncols=2,figsize=(13,5))

f1 = ax[0].pcolormesh(X2, Y2, Z2,cmap='twilight_shifted',vmin=20, vmax=130)
```

```
plt.colorbar(f1,label='Vickers hardness (HV)',ax=ax[0])

f2 = ax[1].pcolormesh(X4, Y4, Z4,cmap='twilight_shifted',vmin=20, vmax=130)
plt.colorbar(f2,label='Vickers hardness (HV)',ax=ax[1])

#f3 = ax[2].pcolormesh(X6, Y6, Z6,cmap='twilight_shifted',vmin=20, vmax=130)
#plt.colorbar(f3,label='Vickers hardness (HV)',ax=ax[2])


#plt.legend(fontsize=15)

ax[0].set_ylabel('Position ( m)',fontsize=15)
#ax[1].set_ylabel('Position ( m)',fontsize=15)
ax[0].set_xlabel('Ageing time (log10 in s)',fontsize=15)
ax[1].set_xlabel('Ageing time (log10 in s)',fontsize=15)
#ax[2].set_xlabel('Ageing time (log10 in s)',fontsize=15)

ax[0].set_title('Experimental',fontsize=15)
ax[1].set_title('Modelled (Mhyr conversion)',fontsize=15)
#ax[2].set_title('Modelled (Adpated conversion)',fontsize=15)


ax[1].set_xlim([0,np.log10(5e6)])
ax[1].set_ylim([400,4400])
#ax[2].set_xlim([0,np.log10(5e6)])
#ax[2].set_ylim([400,4400])

plt.savefig('4-'+nameSample+'-confrontation-ColorMap.png')
```

```
582
```

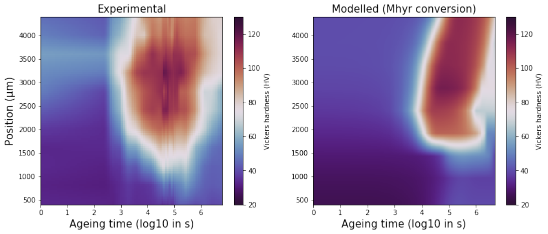

```
[29]: ## ColorMap depending on the Mg/Si atomic ratio + with phase domain visible␣
      ↪using fv curves
```

```
[30]: # new data depending on ratio

      df_colormapHV = pd.DataFrame(results.mechanics[0]['t[s]'])

      for n in l:
          df_colormapHV_i = 0.33*results.mechanics[n]['sigmaFlowMicro[MPa]']+16␣
       ↪#conversion YS to hardness Mhyr
          #df_colormapHV_i = 0.32*results.mechanics[n]['sigmaFlowMicro[MPa]']+20␣
       ↪#conversion YS to hardness Ju
          df_colormapHV = pd.concat([df_colormapHV,df_colormapHV_i], axis=1,␣
       ↪sort=False)

      df_colormapHV = df_colormapHV.T

      l3=['t[s]']
      for i in range(0,N_nodes):
          l3.append(round(gdt_compo['X_Mg'][i]/gdt_compo['X_Si'][i],2))
      l3 = pd.Series(l3)
      ratio=l3[1:]

      df_colormapHV = df_colormapHV.set_index(l3)
      df_colormapHV = df_colormapHV.T
      df_colormapHV = df_colormapHV.set_index(['t[s]'])
      #print(df_results_colormap)
```

```
[31]: # calculation of volume fraction of each phase

      t_m=np.zeros((len(phaseRslts),len(ratio)))
      t_50=np.zeros((len(phaseRslts),len(ratio)))
      t_p=np.zeros((len(phaseRslts),len(ratio)))
      fv_max_max = 0.02
      #gdt=[]
      sigma=[]

      #print(t_m)
      #print(len(phaseRslts))
      #print(l)

      for i in l:
          #print(i)
          #print(T[i])
          data= results.precipitation[i]
          #print(data)
          data_mech=results.mechanics[i]
```

```
    for j in range(len(phaseRslts)):
        #print(j)
        #print(phaseRslts[j])
        fv=[]
        t=[]
        fv=data["fv_"+phaseRslts[j]].tolist()
        #print(fv)
        t=data['t[s]'].tolist()
        fv_max=max(fv)
        #print(fv_max)
        if fv_max >= 0.1*fv_max_max:
            max_index = fv.index(fv_max)
            #print(max_index)
            fv=fv[0:max_index+1]
            t=t[0:max_index+1]
            #print(fv,t)
            f = interpolate.interp1d(fv,t)
            #t_m.append([])
            #t_50.append([])
            #t_p.append([])
            #print(f(fv_max*0.7))
            t_m[j,i]= f(0.2*fv_max)
            t_50[j,i]= f(0.5*fv_max)
            t_p[j,i]=f(0.7*fv_max)
            #print(t_m[j],t_50[j],t_p[j])
        else:
            t_m[j,i] = np.NaN
            t_50[j,i]= np.NaN
            t_p[j,i] = np.NaN


    #gdt.append(ratio[i])

    g=interpolate.interp1d(data['t[s]'],data_mech["sigmaFlowMicro[MPa]"])
    #print(data_mech)
    #print(data['t[s]'])
    #print(timeInter)
    sigma.append(g(timeInter))

#print(T)
#print(t_m)

ratioInter=np.arange(0,4.5,.5)

f=interpolate.interp2d(timeInter,ratio,sigma)
sigmaInter=f(timeInter,ratioInter)
```

```
[32]: ## expe hardness data

      y = l3[1:]
      Z = gdt_hardness_notime.T

      y2 = np.linspace(y.min(), y.max(), 100) #100)
      f = interpolate.interp2d(x, y, Z, kind='linear')
      Z2 = f(x2, y2)
      X2, Y2 = np.meshgrid(x2, y2)

      ## modelled mhyr data

      y3 = l3[1:]
      Z3 = df_colormapHV.T

      y4 = np.linspace(y3.min(), y3.max(), 400) #400)
      f = interpolate.interp2d(x3, y3, Z3, kind='linear')
      Z4 = f(x4, y4)
      X4, Y4 = np.meshgrid(x4, y4)

      ## figure

      fig, ax = plt.subplots(nrows=1, ncols=2,figsize=(13,5))

      #colormap

      f1 = ax[0].pcolormesh(X2, Y2, Z2,cmap='twilight_shifted',vmin=20, vmax=130)
      plt.colorbar(f2,label='Vickers hardness (HV)',ax=ax[0])

      f2 = ax[1].pcolormesh(X4, Y4, Z4,cmap='twilight_shifted',vmin=20, vmax=130)
      plt.colorbar(f2,label='Vickers hardness (HV)',ax=ax[1])

      #fv

      #for j in range(len(phaseRslts)):
          #print(t_m[j])
       #   ax.plot(np.log10(t_m[j]), ratio, color=colors[j], linewidth=1.5,␣
       ↪linestyle=':')
        #  ax.plot(np.log10(t_50[j]),ratio, color=colors[j],linewidth=1.5,ls='--')
         # ax.plot(np.log10(t_p[j]), ratio, color=colors[j],␣
       ↪linewidth=2,label=phaseLatec[j])

      #legend
      #ax.plot(-1,1, color='black',ls=':',label='20% $f^{max}_v$')
      #ax.plot(-1,1, color='black',ls='--',label='50% $f^{max}_v$')
      #ax.plot(-1,1, color='black',label='70% $f^{max}_v$')
```

```
ax[0].set_ylabel('Atomic ratio Mg/Si',fontsize=15)
ax[0].set_xlabel('log(ageing time (s))',fontsize=15)
ax[0].set_xlim([0,np.log10(5e6)]) #1e10)])
ax[1].set_ylabel('Atomic ratio Mg/Si',fontsize=15)
ax[1].set_xlabel('log(ageing time (s))',fontsize=15)
ax[1].set_xlim([0,np.log10(5e6)])
#ax.set_ylim([400,4400])

ax[0].set_title('Experimental',fontsize=15)
ax[1].set_title('Modelled',fontsize=15)

#ax[0].legend(loc='upper left',fontsize=13)

plt.savefig('4-'+nameSample+'-confrontation-ColorMap-fv.png')
```

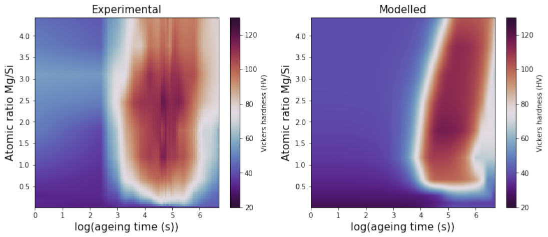

[33]:

```
## expe hardness data

y = l3[1:]
Z = gdt_hardness_notime.T

y2 = np.linspace(y.min(), y.max(), 100)
f = interpolate.interp2d(x, y, Z, kind='linear')
Z2 = f(x2, y2)
X2, Y2 = np.meshgrid(x2, y2)

## modelled mhyr data

y3 = l3[1:]
Z3 = df_colormapHV.T
```

```
y4 = np.linspace(y3.min(), y3.max(), 400)
f = interpolate.interp2d(x3, y3, Z3, kind='linear')
Z4 = f(x4, y4)
X4, Y4 = np.meshgrid(x4, y4)

## figure

fig, ax = plt.subplots(nrows=1, ncols=1,figsize=(10,7))

#colormap

#f1 = ax[0].pcolormesh(X2, Y2, Z2,cmap='twilight_shifted',vmin=20, vmax=130)
#plt.colorbar(f1,label='Vickers hardness (HV)',ax=ax[0])

f2 = ax.pcolormesh(X4, Y4, Z4,cmap='twilight_shifted',vmin=20, vmax=130)
plt.colorbar(f2,label='Vickers hardness (HV)')#,ax=ax[0])

#fv

for j in range(len(phaseRslts)):
    #print(t_m[j])
    ax.plot(np.log10(t_m[j]), ratio, color=colors[j], linewidth=1.5,␣
 ↪linestyle=':')
    ax.plot(np.log10(t_50[j]),ratio, color=colors[j],linewidth=1.5,ls='--')
    ax.plot(np.log10(t_p[j]), ratio, color=colors[j],␣
 ↪linewidth=2,label=phaseLatec[j])

#legend
ax.plot(-1,1, color='black',ls=':',label='25% $f^{max}_v$')
ax.plot(-1,1, color='black',ls='--',label='50% $f^{max}_v$')
ax.plot(-1,1, color='black',label='75% $f^{max}_v$')

ax.set_ylabel('Atomic ratio Mg/Si',fontsize=15)
ax.set_xlabel('log(ageing time (s))',fontsize=15)
ax.set_xlim([1,np.log10(1e10)])#5e6)])
#ax[1].set_ylabel('Atomic ratio Mg/Si',fontsize=15)
#ax[1].set_xlabel('Ageing time (log10 in s)',fontsize=15)
#ax[1].set_xlim([0,np.log10(1e10)])#5e6)])
#ax.set_ylim([400,4400])

#ax[0].set_title('Experimental',fontsize=15)
#ax[1].set_title('Modelled (Mhyr conversion)',fontsize=15)

ax.legend(loc='upper left',fontsize=13)

plt.savefig('4-'+nameSample+'-confrontation-ColorMap-fv.pdf')
```

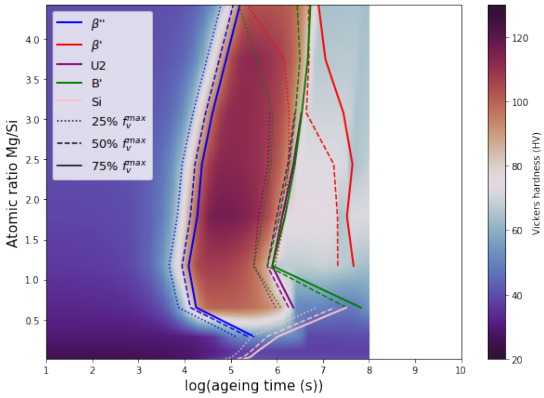

References

[ABD 08] Abdala M. R., Garcia de Blas J. C., Barbosa C., Acselrad O.
Thermoelectrical power analysis of precipitation in 6013 aluminum alloy. *Materials Characterization*, vol. 59, n° 3, 2008, p. 271–277.

[ABD 09] Zain-ul Abdein M., Nelias D., Jullien J. F., Deloison D.
Prediction of laser beam welding-induced distortions and residual stresses by numerical simulation for aeronautic application. *Journal of Materials Processing Technology*, vol. 209, n° 6, 2009, p. 2907–2917.

[ABD 10] Zain-ul abdein M., Nélias D., Jullien J. F., Wagan A. I.
Thermo-mechanical characterisation of AA 6056-T4 and estimation of its material properties using Genetic Algorithm. *Materials and Design*, vol. 31, n° 9, 2010, p. 4302–4311, Elsevier Ltd.

[AFI 08] Afify N., Gaber A., Mostafa M. S., Abbady G.
Influence of Si concentration on the precipitation in Al-1 at.% Mg alloy. *Journal of Alloys and Compounds*, vol. 462, n° 1-2, 2008, p. 80–87.

[AND 98] Andersen S. J., Zandbergen H. W., Jansen J., Træholt C., Tundal U., Reiso O.
The crystal structure of the β" phase in Al-Mg-Si Alloys. *Acta Materialia*, vol. 46, n° 9, 1998, p. 3283–3298.

[ARD 85] Ardell A. J.
Precipitation hardening. *Metallurgical Transactions A*, vol. 16, n° 12, 1985, p. 2131–2165.

[ARU 15] Aruga Y., Kozuka M., Takaki Y., Sato T.
Formation and reversion of clusters during natural aging and subsequent artificial aging in an Al-Mg-Si alloy. *Materials Science and Engineering A*, vol. 631, 2015, p. 86–96, Elsevier.

[BAR 50] Barnes R. S.
Diffusion of copper along the grain boundaries of nickel. *Nature*, vol. 166, n° 4233, 1950, p. 1032–1033.

[BAR 08] Bardel D.
Role de la microstructure d'un alliage a durcissement structural sur son comportement et sa tenue mecanique sous sollicitations cycliques apres un transitoire thermique. Thèse de doctorat, INSA Lyon, 2008.

[BAR 14] Bardel D., Perez M., Nelias D., Deschamps A., Hutchinson C. R., Maisonnette D., Chaise T., Garnier J., Bourlier F.
Coupled precipitation and yield strength modelling for non-isothermal treatments of a 6061 aluminium alloy. *Acta Materialia*, vol. 62, n° 1, 2014, p. 129–140, Acta Materialia Inc.

[BAR 15] Bardel D., Perez M., Nelias D., Dancette S., Chaudet P., Massardier V.
Cyclic behaviour of a 6061 aluminium alloy: Coupling precipitation and elastoplastic modelling. *Acta Materialia*, vol. 83, 2015, p. 256–268, Acta Materialia Inc.

[BAS 06] Bastier A.
Modélisation du soudage d'alliages d'aluminium par friction et malaxage. Thèse de doctorat, Ecole polytechnique, 2006.

[BEA 96] Beaucage G.
Small-angle scattering from polymeric mass fractals of arbitrary mass-fractal dimension. *Journal of Applied Crystallography*, vol. 29, n° 2, 1996, p. 134–146, International Union of Crystallography.

[BLA 99] Blavette D., Danoix F., Cadel E., Géandieret G., Menand A.
Apports de la tomographie atomique dans l'observation et l'analyse des interfaces. *Journal De Physique. IV : JP*, vol. 9, n° 4, 1999.

[BOR 16] Borkar T., Gwalani B., Choudhuri D., Mikler C. V., Yannetta C. J., Chen X., Ramanujan R. V., Styles M. J., Gibson M. A., Banerjee R.
A combinatorial assessment of AlxCrCuFeNi2 (0 < x < 1.5) complex concentrated alloys: Microstructure, microhardness, and magnetic properties. *Acta Materialia*, vol. 116, 2016, p. 63–76, Elsevier Ltd.

[BRE 13] Brent R. P.
Algorithms for minimization without derivatives. Courier Corporation, 2013.

[BRO 71] Brown L., Ham R.
Strengthening methods in crystals. *Applied Science, London*, vol. 9, 1971.

[BUF 14] Buffiere J., Maire E.
Imagerie 3D en mécanique des matériaux. *Hermès, La Revue-Cognition, communication, politique*, , 2014.

[CAO 15] Cao S., Zhao J. C.
Application of dual-anneal diffusion multiples to the effective study of phase diagrams and phase transformations in the Fe-Cr-Ni system. *Acta Materialia*, vol. 88, 2015, p. 196–206, Acta Materialia Inc.

[CAY 00] Cayron C., Buffat P. A.
Transmission electron microscopy study of the β' phase (Al-Mg-Si alloys) and QC phase (Al-Cu-Mg-Si alloys): ordering mechanism and crystallographic structure. *Acta Materialia*, vol. 48, n° 10, 2000, p. 2639–2653.

[CHA 15] Chang C. S. T., De Geuser F., Banhart J.
In situ characterization of β" precipitation in an Al-Mg-Si alloy by anisotropic small-angle neutron scattering on a single crystal. *Journal of Applied Crystallography*, vol. 48, 2015, p. 455–463, International Union of Crystallography.

[CHE 20] Chen H., Lu J., Kong Y., Li K., Yang T., Meingast A., Yang M., Lu Q., Du Y.
Atomic scale investigation of the crystal structure and interfaces of the B' precipitate in Al-Mg-Si alloys. *Acta Materialia*, vol. 185, 2020, p. 193–203, Elsevier Ltd.

[CHU 15] Chua A. S., Brochu M., Bishop D. P.
Spark plasma sintering of prealloyed aluminium powders. *Powder Metallurgy*, vol. 58, n° 1, 2015, p. 51–60.

[CIN 20] Cinkilic E., Yan X., Luo A. A.
Modeling precipitation hardening and yield strength in cast Al-Si-Mg-Mn alloys. *Metals*, vol. 10, n° 10, 2020, p. 1–14.

[CLO 04] Clouet E., Nastar M., Sigli C.
Nucleation of Al3Zr and Al3Sc in aluminum alloys: From kinetic Monte Carlo simulations to classical theory. *Physical Review B - Condensed Matter and Materials Physics*, vol. 69, n° 6, 2004, p. 1–14.

[COR 16] Cordero Z. C., Knight B. E., Schuh C. A.
Six Decades of the Hall–Petch Effect – a Survey of Grain-Size Strengthening Studies on Pure Metals. *International Materials Reviews*, vol. 61, n° 8, 2016, p. 495–512.

[DAH 07] Dahmus J. B., Gutowski T. G.
What gets recycled: An information theory based model for product recycling. *Environmental Science and Technology*, vol. 41, n° 21, 2007, p. 7543–7550.

[DAS 10] Das S., Green J., Kaufman J., Emadi D., Mahfoud M.
Aluminium Recyling - An integrated industrywide approach. *JOM*, vol. 62, n° 2, 2010, p. 3–6.

[DAV 95] Davis S. J., Miodownik A. P., Watts J. F.
Degassing and surface analysis of gas atomized aluminium alloy powders. *Journal of Materials Science*, vol. 30, n° 15, 1995, p. 3811–3819.

[DEG 15] De Geuser F., Styles M. J., Hutchinson C. R., Deschamps A.
High-throughput in-situ characterization and modeling of precipitation kinetics in compositionally graded alloys. *Acta Materialia*, vol. 101, 2015, p. 1–9, Acta Materialia Inc.

[DES 98] Deschamps A., Brechet Y.
Influence of predeformation and ageing of an Al-Zn-Mg Alloy-II. Modeling of precipitation kinetics and yield stress. *Acta Materialia*, vol. 47, n° 1, 1998, p. 293–305.

[DES 04] Deschamps A., Nicolas M., Perrard F., Perez M.
Caractérisation quantitative et modélisation des cinétiques de précipitation: Vers la précipitation anisotherme et les phénomènes couplés. *Revue de Metallurgie. Cahiers D'Informations Techniques*, vol. 101, n° 5, 2004, p. 361–379.

[DES 10] Deschamps A., Perez M.
Mesoscopic modelling of precipitation: A tool for extracting physical parameters of phase transformations in metallic alloys. *Comptes Rendus Physique*, vol. 11, n° 3-4, 2010, p. 236–244, Elsevier Masson SAS.

[DES 21] Deschamps A., Hutchinson C. R.
Precipitation kinetics in metallic alloys: Experiments and modeling. *Acta Materialia*, vol. 220, 2021, Page 117338, Elsevier Ltd.

[DEV 92] Develay R.
Propriétés de l'aluminium et des alliages d'aluminium corroyés. *Rapport technique, Techniques de l'Ingénieur M*, vol. 440, 1992, Page 1992.

[DOA 02] Doan L. C., Nakai K., Matsuura Y., Kobayashi S., Ohmori Y.
Effects of excess Mg and Si on the isothermal ageing behaviours in the Al-Mg2Si alloys. *Materials Transactions*, vol. 43, n° 6, 2002, p. 1371–1380.

[DON 98] Donnadieu P., Carsughi F., Redjaïmia A., Diot C., Lapasset G.
Nanoscale Hardening Precipitation in AlMgSi Alloys: A Transmission Electron Microscopy

and Small-Angle Neutron Scattering Study. *Journal of Applied Crystallography*, vol. 31, n° 2, 1998, p. 212–222.

[DON 99] Donnadieu P., Roux-Michollet M., Chastagnier V.
A quantitative study by transmission electron microscopy of nanoscale precipitates in Al-Mg-Si alloys. *Philosophical Magazine A: Physics of Condensed Matter, Structure, Defects and Mechanical Properties*, vol. 79, n° 6, 1999, p. 1347–1366.

[DU 17] Du Q., Tang K., Marioara C. D., Andersen S. J., Holmedal B., Holmestad R.
Modeling over-ageing in Al-Mg-Si alloys by a multi-phase CALPHAD-coupled Kampmann-Wagner Numerical model. *Acta Materialia*, vol. 122, 2017, p. 178–186, Elsevier Ltd.

[DUT 91] Dutta I., Allen M.
A calorimetric study of precipitation in commercial aluminium alloy 6061. *Journal of Materials Science*, vol. 10, n° letters, 1991, p. 323–326.

[EDW 94] Edwards G. A., Stiller K., Dunlop G.
APFIM investigation of fine-scale precipitation in Aluminium Alloy 6061. *Applied Surface Science*, vol. 77, 1994, p. 219–225.

[EDW 98] Edwards G. A., Stiller K., Dunlop G. L., Couper M. J.
The precipitation sequence in Al-Mg-Si alloys. *Acta Materialia*, vol. 46, n° 11, 1998, p. 3893–3904.

[ELD 07] Elder K. R., Provatas N., Berry J., Stefanovic P., Grant M.
Phase-field crystal modeling and classical density functional theory of freezing. *Physical Review B - Condensed Matter and Materials Physics*, vol. 75, n° 6, 2007, p. 1–14.

[ENG 19] Engler O., Marioara C. D., Aruga Y., Kozuka M., Myhr O. R.
Effect of natural ageing or pre-ageing on the evolution of precipitate structure and strength during age hardening of Al–Mg–Si alloy AA 6016. *Materials Science and Engineering A*, vol. 759, n° February, 2019, p. 520–529, Elsevier B.V.

[ESM 03a] Esmaeili S., Lloyd D. J., Poole W. J.
A yield strength model for the Al-Mg-Si-Cu alloy AA6111. *Acta Materialia*, vol. 51, n° 8, 2003, p. 2243–2257.

[ESM 03b] Esmaeili S., Lloyd D. J., Poole W. J.
Modeling of precipitation hardening for the naturally aged Al-Mg-Si-Cu alloy AA6111. *Acta Materialia*, vol. 51, n° 12, 2003, p. 3467–3481.

[ESM 05] Esmaeili S., Lloyd D. J.
Modeling of precipitation hardening in pre-aged AlMgSi(Cu) alloys. *Acta Materialia*, vol. 53, n° 20, 2005, p. 5257–5271.

[FAL 10] Falahati A., Povoden-Karadeniz E., Lang P., Warczok P., Kozeschnik E.
Thermo-kinetic computer simulation of differential scanning calorimetry curves of AlMgSi alloys. *International Journal of Materials Research*, vol. 101, n° 9, 2010, p. 1089–1096.

[FAL 15] Fallah V., Korinek A., Ofori-Opoku N., Raeisinia B., Gallerneault M., Provatas N., Esmaeili S.
Atomic-scale pathway of early-stage precipitation in Al-Mg-Si alloys. *Acta Materialia*, vol. 82, 2015, p. 457–467, Acta Materialia Inc.

[FAL 16] Fallah V., Langelier B., Ofori-Opoku N., Raeisinia B., Provatas N., Esmaeili S.

Cluster evolution mechanisms during aging in Al-Mg-Si alloys. *Acta Materialia*, vol. 103, 2016, p. 290–300, Elsevier Ltd.

[FAZ 08] Fazeli F., Poole W. J., Sinclair C. W.
Modeling the effect of Al3Sc precipitates on the yield stress and work hardening of an Al-Mg-Sc alloy. *Acta Materialia*, vol. 56, n° 9, 2008, p. 1909–1918.

[FRI 64] Friedel J.
Dislocations pergamon. *New York*, vol. 274, 1964.

[FRI 11] Fribourg G., Bréchet Y., Deschamps A., Simar A.
Microstructure-based modelling of isotropic and kinematic strain hardening in a precipitation-hardened aluminium alloy. *Acta Materialia*, vol. 59, n° 9, 2011, p. 3621–3635.

[FRØ 03a] Frøseth A. G., Andersen S. J., Marioara C. D., Derlet P. M., Hoier R.
Solving the Structure of the Phases in the Al-Mg-Si Alloy System with the Help of Ab Initio Modelling. *Materials Research Society Symposium - Proceedings*, vol. 755, 2003, p. 19–24.

[FRØ 03b] Frøseth A. G., Høier R., Derlet P. M., Andersen S. J., Marioara C. D.
Bonding in MgSi and Al-Mg-Si compounds relevant to Al-Mg-Si alloys. *Physical Review B - Condensed Matter and Materials Physics*, vol. 67, n° 22, 2003, p. 1–11.

[FUJ 78] ichiro Fujikawa S., ichi Hirano K., Fukushima Y.
Diffusion of silicon in aluminum. *Metallurgical Transactions A*, vol. 9, n° 12, 1978, p. 1811–1815.

[FUK 06] Fukui K., Takeda M., Endo T.
Influence of excess Si on the morphology and thermal stability of metastable precipitates formed in an Al-Mg-Si alloy. *Nippon Kinzoku Gakkaishi/Journal of the Japan Institute of Metals*, vol. 70, n° 8, 2006, p. 715–719.

[GAB 07] Gaber A., Ali A. M., Matsuda K., Kawabata T., Yamazaki T., Ikeno S.
Study of the developed precipitates in Al-0.63Mg-0.37Si-0.5Cu (wt.%) alloy by using DSC and TEM techniques. *Journal of Alloys and Compounds*, vol. 432, n° 1-2, 2007, p. 149–155.

[GAL 08] Gallais C., Denquin A., Bréchet Y., Lapasset G.
Precipitation microstructures in an AA6056 aluminium alloy after friction stir welding: Characterisation and modelling. *Materials Science and Engineering A*, vol. 496, n° 1-2, 2008, p. 77–89.

[GHI 18] Ghiaasiaan R., Shankar S.
Structure-property models in Al-Zn-Mg-Cu alloys: A critical experimental assessment of shape castings. *Materials Science and Engineering A*, vol. 733, n° April, 2018, p. 235–245, Elsevier B.V.

[GHO 03] Ghosh M., Chatterjee S.
Diffusion bonded transition joints of titanium to stainless steel with improved properties. *Materials Science and Engineering A*, vol. 358, n° 1-2, 2003, p. 152–158.

[GRA 11] Graedel T. E., Allwood J., Birat J. P., Buchert M., Hagelüken C., Reck B. K., Sibley S. F., Sonnemann G.
What do we know about metal recycling rates? *Journal of Industrial Ecology*, vol. 15, n° 3, 2011, p. 355–366.

[GRE 13] Green M. L., Takeuchi I., Hattrick-Simpers J. R.
Applications of high throughput (combinatorial) methodologies to electronic, magnetic, optical, and energy-related materials. *Journal of Applied Physics*, vol. 113, n° 23, 2013.

[GUI 59] Guinier A.
Heterogeneities in Solid Solutions. *Solid State Physics - Advances in Research and Applications*, vol. 9, n° C, 1959, p. 293–398.

[GUM 16] Gumbmann E., De Geuser F., Deschamps A., Lefebvre W., Robaut F., Sigli C.
A combinatorial approach for studying the effect of Mg concentration on precipitation in an Al-Cu-Li alloy. *Scripta Materialia*, vol. 110, 2016, p. 44–47, Acta Materialia Inc.

[GUP 01] Gupta A., Lloyd D., Court A.
Precipitation hardening in Al–Mg–Si alloys with and without excess Si A.K. *Materials Science and Engineering*, vol. A316, 2001, p. 11–17.

[GUT 13] Gutowski T. G., Sahni S., Allwood J. M., Ashby M. F., Worrell E.
The energy required to produce materials: Constraints on energy-intensity improvements, parameters of demand. *Philosophical Transactions of the Royal Society A: Mathematical, Physical and Engineering Sciences*, vol. 371, n° 1986, 2013.

[HAM 10] Hammouda B.
A new Guinier-Porod model. *Journal of Applied Crystallography*, vol. 43, n° 4, 2010, p. 716–719, International Union of Crystallography.

[HAN 17] Han Y., Shao D., Chen B. A., Peng Z., Zhu Z. X., Zhang Q., Chen X., Liu G., Li X. M.
Effect of Mg/Si ratio on the microstructure and hardness–conductivity relationship of ultrafine-grained Al–Mg–Si alloys. *Journal of Materials Science*, vol. 52, n° 8, 2017, p. 4445–4459.

[HAS 09] Hasting H. S., Frøseth A. G., Andersen S. J., Vissers R., Walmsley J. C., Marioara C. D., Danoix F., Lefebvre W., Holmestad R.
Composition of β" precipitates in Al-Mg-Si alloys by atom probe tomography and first principles calculations. *Journal of Applied Physics*, vol. 106, n° 12, 2009.

[HOR 93] Hornbogen E., Starke E. A.
Overview no. 102 Theory assisted design of high strength low alloy aluminum. *Acta Metallurgica Et Materialia*, vol. 41, n° 1, 1993, p. 1–16.

[HOY 91] Hoyt J. J.
On the coarsening of precipitates located on grain boundaries and dislocations. *Acta Metallurgica Et Materialia*, vol. 39, n° 9, 1991, p. 2091–2098.

[HUT 10] Hutchinson C. R.
Modeling the kinetics of precipitation in aluminium alloys. Woodhead Publishing Limited, 2010.

[IVA 18] Ivanov R., Deschamps A., De Geuser F.
High throughput evaluation of the effect of Mg concentration on natural ageing of Al-Cu-Li-(Mg) alloys. *Scripta Materialia*, vol. 150, 2018, p. 156–159, Elsevier Ltd.

[JAC 72] Jacobs M. H.
The Structure of the Metastable Precipitates Formed During Ageing of an Al-Mg-Si Alloy. *Journal de Physique Théorique et Appliquée*, vol. 26, n° 1, 1972, p. 1–13.

[JÉG 21] Jégourel Y.
Entre deux mondes : un marché international de l'aluminium en pleine mutation. *Policy Brief*, vol. 44, n° 21, 2021, p. 1–9.

[JUL 21] Julienne D.
Geopolitics of Metals: Between Strategies of Power and Influence. *Mineral Resources Economy 1: Context and Issues*, , 2021, Page 53, John Wiley & Sons.

[KAM 84] Kampmann R., Wagner R.
Decomposition of Alloys: the Early Stages: Proc. *2nd Acta-Scripta Metallurgica Conf., ed. by P. Haasen, V. Gerold, R. Wagner and MF Ashby, Pergamon Press, Oxford, UK*, vol. 91, 1984.

[KOC 75] Kocks U., Argon A., Ashby M.
Models for macroscopic slip. *Prog. Mater. Sci*, vol. 19, 1975, p. 171–229.

[KOJ 20] Koju R. K., Mishin Y.
Atomistic study of grain-boundary segregation and grain-boundary diffusion in Al-Mg alloys. *Acta Materialia*, vol. 201, 2020, p. 596–603, Elsevier Ltd.

[KOP 64] Koppenaal T. J., Kuhlmann-Wilsdorf D.
The effect of prestressing on the strength of neutron-irradiated copper single crystals. *Applied Physics Letters*, vol. 4, n° 3, 1964, p. 59–61.

[KOZ 07] Kozeschnik E., Holzer I., Sonderegger B.
On the potential for improving equilibrium thermodynamic databases with kinetic simulations. *Journal of Phase Equilibria and Diffusion*, vol. 28, n° 1, 2007, p. 64–71.

[LAD 15] Lad R.
Impact of Bauxite Mining on Soil: A Case Study of Bauxite Mines at Udgiri, Dist-Kolhapur, Maharashtra State, India. *Int. Res. J. Environment Sci. International Science Congress Association*, vol. 4, n° 2, 2015, p. 77–83.

[LE 13] Le G. M., Godfrey A., Hansen N.
Structure and strength of aluminum with sub-micrometer/micrometer grain size prepared by spark plasma sintering. *Materials and Design*, vol. 49, 2013, p. 360–367.

[LEE 22] Lee S., Kang H., Jeon J., Bae D.
Influence of the Composition and Vacancy Concentration on Cluster Decomposition Behavior in Al–Si–Mg Alloy: A Kinetic Monte Carlo Study. *Materials*, vol. 15, n° 19, 2022.

[LEF 16] Lefebvre W., Vurpillot F., Sauvage X.
Atom probe tomography: put theory into practice. Academic Press, 2016.

[LIU 96] Liu Z. K.
Theoretic calculation of ferrite growth in supersaturated austenite in Fe-C alloy. *Acta Materialia*, vol. 44, n° 9, 1996, p. 3855–3867.

[LIU 03] Liu G., Zhang G., Ding X., Sun J., Chen K.
Modeling the strengthening response to aging process of heat-treatable aluminum alloys containing plate/disc- or rod/needle-shaped precipitates. *Materials Science and Engineering: A*, vol. 344, n° 1-2, 2003, p. 113–124.

[LYN 82] Lynch J. P., Brown L. M., Jacobs M. H.
Microanalysis of age-hardening precipitates in aluminium alloys. *Acta Metallurgica*, vol. 30, n° 7, 1982, p. 1389–1395.

[MAI 10] Maisonnette D.
Influences mécaniques et métallurgiques de procédés haute température sur un alliage d'aluminium 6061-T6. Thèse de doctorat, INSA Lyon, 2010.

[MAR 97] Maruyama N., Uemori R., Hashimoto N., Saga M., Kikuchi M.
Effect of silicon addition on the composition and structure of fine-scale precipitates in Al-Mg-Si alloys. *Scripta Materialia*, vol. 36, n° 1, 1997, p. 89–93.

[MAR 01] Marioara C. D., Andersen S. J., Jansen J., Zandbergen H. W.
Atomic model for GP-zones in a 6082 Al-Mg-Si system. *Acta Materialia*, vol. 49, n° 2, 2001, p. 321–328.

[MAR 05] Marioara C. D., Andersen S. J., Zandbergen H. W., Holmestad R.
The influence of alloy composition on precipitates of the Al-Mg-Si system. *Metallurgical and Materials Transactions A: Physical Metallurgy and Materials Science*, vol. 36, n° 13, 2005, p. 691–702.

[MAR 06] Marioara C. D., Nordmark H., Andersen S. J., Holmestad R.
Post-β'' phases and their influence on microstructure and hardness in 6xxx Al-Mg-Si alloys. *Journal of Materials Science*, vol. 41, n° 2, 2006, p. 471–478.

[MAS 00] Massardier V., Epicier T., Merle P.
Correlation between the microstructural evolution of A 6061 aluminium alloy and the evolution of its thermoelectric power. *Acta Materialia*, vol. 48, n° 11, 2000, p. 2911–2924.

[MAT 79] Matthews J., Nabarro F.
Dislocations in solids. *North-Holland, Amsterdam*, vol. 2, 1979, Page 461.

[MAT 93a] Matsuda K., Ikeno S., Tada S.
Crystal Structure of Rod-shaped Precipitates in Al-1.0 mass%Mg2Si Alloy. *Journal of Japan Institute of Light Metals*, vol. 57, n° 10, 1993, p. 1107–1113.

[MAT 93b] Matsuda K., Tada S., Ikeno S.
The morphology of precipitates in an Al-1 wt% Mg2Si alloy. *Journal of Electron Microscopy*, vol. 42, n° 1, 1993, p. 1–6.

[MAT 96] Matsuda K., Ikeno S., Sato T., Kamio A.
Classification of metastable phases in Al-Mg2Si alloys by HRTEM. *Materials Science Forum*, vol. 217-222, n° PART 2, 1996, p. 707–712.

[MAT 98] Matsuda K., Gamada H., Fujii K., Uetani Y., Sato T., Kamio A., Ikeno S.
High-resolution electron microscopy on the structure of guinier-preston zones in an Al-1.6 mass Pet Mg2Si alloy. *Metallurgical and Materials Transactions A: Physical Metallurgy and Materials Science*, vol. 29, n° 4, 1998, p. 1161–1167.

[MAT 99] Matsuda K., Naoi T., Fujii K., Uetani Y., Sato T., Kamio A., Ikeno S.
Crystal structure of the β" phase in an Al-1.0mass%Mg2Si-0.4mass%Si alloy. *Materials Science and Engineering A*, vol. 262, n° 1-2, 1999, p. 232–237.

[MAT 00] Matsuda K., Sakaguchi Y., Miyata Y., Uetani Y., Sato T., Kamio A., Ikeno S.
Precipitation sequence of various kinds of metastable phases in Al-1.0mass% Mg2Si-0.4mass% Si alloy. *Journal of Materials Science*, vol. 35, 2000, p. 179–189, Springer US.

[MAT 05] Matsuda K., Ikeno S., Matsui H., Sato T., Terayama K., Uetani Y.
Comparison of precipitates between excess Si-type and balanced-type Al-Mg-Si alloys during continuous heating. *Metallurgical and Materials Transactions A: Physical Metallurgy and Materials Science*, vol. 36, n° 8, 2005, p. 2007–2012.

[MAT 06] Matsuda K., Ishida Y., Mullerova I., Frank L., Ikeno S.
Cube-phase in excess Mg-type Al-Mg-Si alloy studied by EFTEM. *Journal of Materials Science*, vol. 41, n° 9, 2006, p. 2605–2610.

[MAU 05] Maugis P., Soisson F., Lae L.
Kinetics of precipitation: Comparison between Monte Carlo simulations, cluster dynamics and the classical laws. *Defect and Diffusion Forum*, vol. 237-240, n° PART 2, 2005, p. 671–676.

[MEY 18a] Meyruey G., Massardier V., Lefebvre W., Perez M.
Over-ageing of an Al-Mg-Si alloy with silicon excess. *Materials Science and Engineering A*, vol. 730, n° April, 2018, p. 92–105, Elsevier B.V.

[MEY 18b] Meyruey G.
Caractérisation et modélisation du vieillissement thermique d'un composite à base d'alliage d'Aluminium. Thèse de doctorat, INSA Lyon, 2018.

[MIN 83] Minamino Y., Yamane T., Shimomura A., Shimada M., Koizumi M., Ogawa N., Takahashi J., Kimura H.
Effect of high pressure on interdiffusion in an Al-Mg alloy. *Journal of Materials Science*, vol. 18, n° 9, 1983, p. 2679–2687.

[MIR 17] Miracle D., Majumdar B., Wertz K., Gorsse S.
New strategies and tests to accelerate discovery and development of multi-principal element structural alloys. *Scripta Materialia*, vol. 127, 2017, p. 195–200, Elsevier B.V.

[MIS 99] Mishin Y., Herzig C.
Grain boundary diffusion: Recent progress and future research. *Materials Science and Engineering A*, vol. 260, n° 1-2, 1999, p. 55–71.

[MIY 12] Miyazaki T.
Development of "macroscopic Composition Gradient Method" and its application to the phase transformation. *Progress in Materials Science*, vol. 57, n° 6, 2012, p. 1010–1060.

[MON 76] Mondolfo L.
luminium alloys : structure and properties. 1976.

[MOR 14] Morozova N. V., Ovsyannikov S. V., Korobeinikov I. V., Karkin A. E., Takarabe K. I., Mori Y., Nakamura S., Shchennikov V. V.
Significant enhancement of thermoelectric properties and metallization of Al-doped Mg2Si under pressure. *Journal of Applied Physics*, vol. 115, n° 21, 2014.

[MUR 84] Murray J. L., McAlister A. J.
The Al-Si (Aluminum-Silicon) system. *Bulletin of Alloy Phase Diagrams*, vol. 5, n° 1, 1984, p. 74–84.

[MUR 98a] MURAYAMA M., HONO K.
Atom probe characterization of pre-precipitate clusters and precipitates in Al-Mg-Si(-Cu) alloys. *Proc. Inter. Conf. Aluminum Alloys*, vol. 6, 1998.

[MUR 98b] Murayama M., Hono K., Saga M., Kikuchi M.
Atom probe studies on the early stages of precipitation in Al-Mg-Si alloys. *Materials Science and Engineering A*, vol. 250, n° 1, 1998, p. 127–132.

[MUR 99] Murayama M., Hono K.
Pre-precipitate clusters and precipitation processes in Al-Mg-Si alloys. *Acta Materialia*, vol. 47, n° 5, 1999, p. 1537–1548.

[MYH 01] Myhr O. R., Grong O., Andersen S. J.
Modelling of the age hardening behaviour of Al-Mg-Si alloys. *Acta Materialia*, vol. 49, n° 1, 2001, p. 65–75.

[MYH 04] Myhr O. R., Grong, Fjær H. G., Marioara C. D.
Modelling of the microstructure and strength evolution in al-mg-si alloys during multistage thermal processing. *Acta Materialia*, vol. 52, n° 17, 2004, p. 4997–5008.

[MYH 10] Myhr O. R., Grong ø., Pedersen K. O.
A combined precipitation, yield strength, and work hardening model for Al-Mg-Si alloys. *Metallurgical and Materials Transactions A: Physical Metallurgy and Materials Science*, vol. 41, n° 9, 2010, p. 2276–2289.

[MYH 15] Myhr O. R., Grong Ø., Schäfer C.
An Extended Age-Hardening Model for Al-Mg-Si Alloys Incorporating the Room-Temperature Storage and Cold Deformation Process Stages. *Metallurgical and Materials Transactions A: Physical Metallurgy and Materials Science*, vol. 46, n° 12, 2015, p. 6018–6039.

[NIC 03] Nicolas M., Deschamps A.
Characterisation and modelling of precipitate evolution in an Al-Zn-Mg alloy during non-isothermal heat treatments. *Acta Materialia*, vol. 51, n° 20, 2003, p. 6077–6094.

[NIE 96] Nie J. F., Muddle B. C., Polmear I. J.
The effect of precipitate shape and orientation on dispersion strengthening in high strength aluminium alloys. *Materials Science Forum*, vol. 217-222, n° PART 2, 1996, p. 1257–1262.

[NIN 13] Ning Y., Yao Z., Guo H., Fu M. W.
Structural-gradient-materials produced by gradient temperature heat treatment for dual-property turbine disc. *Journal of Alloys and Compounds*, vol. 557, 2013, p. 27–33.

[NIN 14] Ninive P. H., Strandlie A., Gulbrandsen-Dahl S., Lefebvre W., Marioara C. D., Andersen S. J., Friis J., Holmestad R., Løvvik O. M.
Detailed atomistic insight into the β" phase in Al-Mg-Si alloys. *Acta Materialia*, vol. 69, 2014, p. 126–134, Acta Materialia Inc.

[NUN 16] Nunez P., Jones S.
Cradle to gate: life cycle impact of primary aluminium production. *International Journal of Life Cycle Assessment*, vol. 21, n° 11, 2016, p. 1594–1604, The International Journal of Life Cycle Assessment.

[OFO 13] Ofori-Opoku N., Fallah V., Greenwood M., Esmaeili S., Provatas N.
Multicomponent phase-field crystal model for structural transformations in metal alloys. *Physical Review B - Condensed Matter and Materials Physics*, vol. 87, n° 13, 2013, p. 1–15.

[OHM 02] Ohmori Y., Doan L. C., Nakai K.
Ageing processes in Al-Mg-Si alloys during continuous heating. *Materials Transactions*, vol. 43, n° 2, 2002, p. 246–255.

[OST 15] Osten J., Milkereit B., Schick C., Kessler O.
Dissolution and precipitation behaviour during continuous heating of Al-Mg-Si alloys in a wide range of heating rates. *Materials*, vol. 8, n° 5, 2015, p. 2830–2848.

[PAR 16] Paraskevas D., Kellens K., Van De Voorde A., Dewulf W., Duflou J. R.
Environmental Impact Analysis of Primary Aluminium Production at Country Level. *Procedia CIRP*, vol. 40, 2016, p. 209–213, Elsevier B.V.

[PER 07] Perez M.
Approche multi-échelle de la précipitation. rapport, 2007.

[POL 95] Polmear
Light Alloys : metallurgy of the light metals. 1995.

[POR 09] Porter D. A., Easterling K. E., Sherif M. Y.
Phase transformations in metals and alloys, third edition. 2009.

[POR 22] Portis-Guerin M.
. La filiere aluminium francaise fragilisee par les consequences de la guerre en Ukraine, 3 2022.

[POT 11] Potyrailo R., Rajan K., Stoewe K., Takeuchi I., Chisholm B., Lam H.
Combinatorial and high-throughput screening of materials libraries: Review of state of the art. *ACS Combinatorial Science*, vol. 13, n° 6, 2011, p. 579–633.

[POU 84] Pouchou J., Pichoir F.
Un nouveau modèle de calcul pour la microanalyse par spectrometrie de Rayons X partiel: Application à l'analyse d'Echantillons homogènes. *La recherche aérospatiale*, vol. 5, 1984, p. 167–191.

[POV 13] Povoden-Karadeniz E., Lang P., Warczok P., Falahati A., Jun W., Kozeschnik E.
CALPHAD modeling of metastable phases in the Al-Mg-Si system. *Calphad: Computer Coupling of Phase Diagrams and Thermochemistry*, vol. 43, 2013, p. 94–104, Elsevier.

[PRO 20] Project T. M.
Materials Data on MgAlSi by Materials Project. , 2020.

[QUE 10] Queyreau S., Monnet G., Devincre B.
Orowan strengthening and forest hardening superposition examined by dislocation dynamics simulations. *Acta Materialia*, vol. 58, n° 17, 2010, p. 5586–5595, Acta Materialia Inc.

[RAA 22] Raabe D., Ponge D., Uggowitzer P. J., Roscher M., Paolantonio M., Liu C., Antrekowitsch H., Kozeschnik E., Seidmann D., Gault B., De Geuser F., Deschamps A., Hutchinson C., Liu C., Li Z., Prangnell P., Robson J., Shanthraj P., Vakili S., Sinclair C., Bourgeois L., Pogatscher S.
Making sustainable aluminum by recycling scrap: The science of "dirty" alloys. *Progress in Materials Science*, vol. 128, n° April, 2022.

[RAV 04] Ravi C., Wolverton C.
First-principles study of crystal structure and stability of Al-Mg-Si-(Cu) precipitates. *Acta Materialia*, vol. 52, n° 14, 2004, p. 4213–4227.

[REV 80] Revie P.
Kinetics of nucleation in near-critical fluids. *Journal of Aerosol Science*, vol. 11, n° 1, 1980, Page 112.

[ROY 05] Roy P. B., Roy S. B.
Applicability of isothermal three-parameter equations of state of solids - A reappraisal. *Journal of Physics Condensed Matter*, vol. 17, n° 39, 2005, p. 6193–6216.

[SAG 96] Sagalowicz L., Lapasset G., Hug G.
Transmission electron microscopy study of a precipitate which forms in the Al-Mg-Si system. *Philosophical Magazine Letters*, vol. 74, n° 2, 1996, p. 57–66.

[SAN 07] Sandberg N., Slabanja M., Holmestad R.
Ab initio simulations of clustering and precipitation in Al-Mg-Si alloys. *Computational Materials Science*, vol. 40, n° 3, 2007, p. 309–318.

[SCH 13] Schlesinger M.
Aluminium recycling: second edition. 2013.

[SHA 00] Sharma S. C.
Effect of albite particles on the coefficient of thermal expansion behavior of the Al6061 alloy composites. *Metallurgical and Materials Transactions A: Physical Metallurgy and Materials Science*, vol. 31, n° 3, 2000, p. 773–780.

[SHE 90a] Shercliff H. R., Ashby M. F.
A process model for age hardening of aluminium alloys-I. The model. *Acta Metallurgica Et Materialia*, vol. 38, n° 10, 1990, p. 1789–1802.

[SHE 90b] Shercliff H. R., Ashby M. F.
A process model for age hardening of aluminium alloys-II. Applications of the model. *Acta Metallurgica Et Materialia*, vol. 38, n° 10, 1990, p. 1803–1812.

[SHI 01] Shirzadi A. A., Assadi H., Wallach E. R.
Interface evolution and bond strength when diffusion bonding materials with stable oxide films. *Surface and Interface Analysis*, vol. 31, n° 7, 2001, p. 609–618.

[SIM 07] Simar A., Bréchet Y., de Meester B., Denquin A., Pardoen T.
Sequential modeling of local precipitation, strength and strain hardening in friction stir welds of an aluminum alloy 6005A-T6. *Acta Materialia*, vol. 55, n° 18, 2007, p. 6133–6143.

[SIM 12] Simar A., Bréchet Y., De Meester B., Denquin A., Gallais C., Pardoen T.
Integrated modeling of friction stir welding of 6xxx series Al alloys: Process, microstructure and properties. *Progress in Materials Science*, vol. 57, n° 1, 2012, p. 95–183, Elsevier Ltd.

[SJÖ 11] Sjölander E., Seifeddine S., Svensson I. L.
Modelling yield strength of heat treated Al-Si-Mg casting alloys. *International Journal of Cast Metals Research*, vol. 24, n° 6, 2011, p. 338–346.

[SON 09] Sonderegger B., Kozeschnik E.
Generalized nearest-neighbor broken-bond analysis of randomly oriented coherent interfaces in multicomponent Fcc and Bcc structures. *Metallurgical and Materials Transactions A: Physical Metallurgy and Materials Science*, vol. 40, n° 3, 2009, p. 499–510.

[SON 11] Son S. K., Matsumura S., Fukui K., Takeda M.
The compositions of metastable phase precipitates observed at peak hardness condition in an Al-Mg-Si alloy. *Journal of Alloys and Compounds*, vol. 509, n° 2, 2011, p. 241–245, Elsevier B.V.

[SPE 03] Specht E. D., Rar A., Pharr G. M., George E. P., Zschack P., Hong H., Ilavsky J.
Rapid structural and chemical characterization of ternary phase diagrams using synchrotron radiation. *Journal of Materials Research*, vol. 18, n° 10, 2003, p. 2522–2527.

[SPR 12] Springer H., Raabe D.
Rapid alloy prototyping: Compositional and thermo-mechanical high throughput bulk combinatorial design of structural materials based on the example of 30Mn-1.2C-xAl triplex steels. *Acta Materialia*, vol. 60, n° 12, 2012, p. 4950–4959, Acta Materialia Inc.

[STA 03] Starink M. J., Wang S. C.
A model for the yield strength of overaged Al-Zn-Mg-Cu alloys. *Acta Materialia*, vol. 51, n° 17, 2003, p. 5131–5150.

[SVE 15] Sverdrup H. U., Ragnarsdottir K. V., Koca D.
Aluminium for the future: Modelling the global production, market supply, demand, price and long term development of the global reserves. *Resources, Conservation and Recycling*, vol. 103, 2015, p. 139–154, Elsevier B.V.

[SWE 14] Sweet G. A., Brochu M., Hexemer R. L., Donaldson I. W., Bishop D. P.
Microstructure and mechanical properties of air atomized aluminum powder consolidated via spark plasma sintering. *Materials Science and Engineering A*, vol. 608, 2014, p. 273–282, Elsevier.

[TAK 96] Takeda M., Ohkubo F., Shirai T., Fukui K.
Precipitation behaviour of Al-Mg-Si ternary alloys. *Materials Science Forum*, vol. 217-222, n° PART 2, 1996, p. 815–820.

[TEI 11] Teichmann K., Marioara C. D., Andersen S. J., Pedersen K. O., Gulbrandsen-Dahl S., Kolar M., Holmestad R., Marthinsen K.
HRTEM study of the effect of deformation on the early precipitation behaviour in an AA6060 Al-Mg-Si alloy. *Philosophical Magazine*, vol. 91, n° 28, 2011, p. 3744–3754.

[THO 61] Thomas G.
The Aging Characteristics of Aluminum Alloys Electron Transmission Studies of Al-Mg-Si Alloys. , 1961.

[TSA 05] Tsao C. S., Jeng U. S., Chen C. Y., Kuo T. Y.
Small-angle X-ray scattering study of nanostructure evolution of β" precipitates in Al-Mg-Si alloy. *Scripta Materialia*, vol. 53, n° 11, 2005, p. 1241–1245.

[TUR 13] Turconi R., Boldrin A., Astrup T.
Life cycle assessment (LCA) of electricity generation technologies: Overview, comparability and limitations. *Renewable and Sustainable Energy Reviews*, vol. 28, 2013, p. 555–565, Elsevier.

[VIL 21] Villaret F., Boulnat X., Aubry P., Yano Y., Ohtsuka S., Fabrègue D., de Carlan Y.
Laser Beam Direct Energy Deposition of graded austenitic-to-martensitic steel junctions compared to dissimilar Electron Beam welding. *Materials Science and Engineering A*, vol. 824, n° March, 2021.

[VIS 07] Vissers R., van Huis M. A., Jansen J., Zandbergen H. W., Marioara C. D., Andersen S. J.
The crystal structure of the β' phase in Al-Mg-Si alloys. *Acta Materialia*, vol. 55, n° 11, 2007, p. 3815–3823.

[WAN 03] Wang X., Poole W. J., Esmaeili S., Lloyd D. J., Embury J. D.
Precipitation strengthening of the aluminum alloy AA6111. *Metallurgical and Materials Transactions A: Physical Metallurgy and Materials Science*, vol. 34, n° 12, 2003, p. 2913–2924.

[WAN 07] Wang Y., Liu Z. K., Chen L. Q., Wolverton C.
First-principles calculations of β"-Mg5Si6/α-Al interfaces. *Acta Materialia*, vol. 55, n° 17, 2007, p. 5934–5947.

[WEI 13] Wei C., Zheng X., Cahill D. G., Zhao J. C.
Invited Article: Micron resolution spatially resolved measurement of heat capacity using dual-frequency time-domain thermoreflectance. *Review of Scientific Instruments*, vol. 84, n° 7, 2013.

[WEI 18] Wei C., Zhao J. C.
Gradient temperature heat treatment for efficient study of phase precipitation in a high-temperature Fe-Cr-Mo ferritic steel. *Materialia*, vol. 3, 2018, p. 31–40, Elsevier Ltd.

[WES 79] Westengen H., Ryum N.
Precipitation Reactions in an Aluminium 1 wt.% Mg,Si Alloy. *International Journal of Materials Research*, vol. 70, n° 8, 1979, p. 528–535.

[XU 16] Xu X., Yang Z., Ye Y., Wang G., He X.
Effects of various Mg/Si ratios on microstructure and performance property of Al-Mg-Si alloy cables. *Materials Characterization*, vol. 119, 2016, p. 114–119, Elsevier Inc.

[YAM 06] Yamasaki M., Kawamura Y.
Changes in the surface characteristics of gas-atomized pure aluminum powder during vacuum degassing. *Materials Transactions*, vol. 47, n° 8, 2006, p. 1902–1905.

[YAM 11] Yamada M., Ueda A., Matsumoto K., Ohzuku T.
Silicon-Based Negative Electrode for High-Capacity Lithium-Ion Batteries: “SiO”-Carbon Composite. *Journal of The Electrochemical Society*, vol. 158, n° 4, 2011, Page A417.

[YAN 20] Yang C., Masquellier N., Gandiolle C., Sauvage X.
Multifunctional properties of composition graded Al wires. *Scripta Materialia*, vol. 189, 2020, p. 21–24, Elsevier Ltd.

[YAZ 09] Yazdanmehr M., Bahrami A., Anijdan S. H.
A precipitation-hardening model for non-isothermal ageing of Al-Mg-Si alloys. *Computational Materials Science*, vol. 45, n° 2, 2009, p. 385–387, Elsevier B.V.

[ZAD 07] Zadra M., Casari F., Girardini L., Molinari A.
Spark plasma sintering of pure aluminium powder: Mechanical properties and fracture analysis. *Powder Metallurgy*, vol. 50, n° 1, 2007, p. 40–45.

[ZAN 97] Zandbergen H. W., Andersen S. J., Jansen J.
Structure determination of Mg5Si6:particles in Al by dynamic electron diffraction studies. *Science*, vol. 277, n° 5330, 1997, p. 1221–1225.

[ZHA 04] Zhao J. C.
Reliability of the diffusion-multiple approach for phase diagram mapping. *Journal of Materials Science*, vol. 39, n° 12, 2004, p. 3913–3925.

[ZHA 10] Zhang H., Wang Y., Shang S. L., Ravi C., Wolverton C., Chen L. Q., Liu Z. K.
Solvus boundaries of (meta)stable phases in the Al-Mg-Si system: First-principles phonon calculations and thermodynamic modeling. *Calphad: Computer Coupling of Phase Diagrams and Thermochemistry*, vol. 34, n° 1, 2010, p. 20–25, Elsevier Ltd.

[ZHA 12] Zhao J. C., Zheng X., Cahill D. G.
Thermal conductivity mapping of the Ni-Al system and the beta-NiAl phase in the Ni-Al-Cr system. *Scripta Materialia*, vol. 66, n° 11, 2012, p. 935–938, Acta Materialia Inc.

[ZHE 08] Zheng X., Cahill D. G., Weaver R., Zhao J. C.
Micron-scale measurements of the coefficient of thermal expansion by time-domain probe beam deflection. *Journal of Applied Physics*, vol. 104, n° 7, 2008.

[ZHE 17] Zheng Y., Luo B., Bai Z., Wang J., Yin Y.
Study of the precipitation hardening behaviour and intergranular corrosion of Al-Mg-Si alloys with differing Si contents. *Metals*, vol. 7, n° 10, 2017.

FOLIO ADMINISTRATIF

THESE DE L'UNIVERSITE DE LYON OPEREE AU SEIN DE L'INSA LYON

NOM : TAURINES DATE de SOUTENANCE : le 27 Mars 2023

Prénoms : Justine

TITRE : Composition-dependent precipitation in Mg/Si graded 6xxx aluminium alloys: from powder metallurgy to hardening kinetics simulation

NATURE : Doctorat Numéro d'ordre : 2023ISAL0023

École doctorale : ED 34 Matériaux de Lyon

Spécialité : Matériaux

RÉSUMÉ :

Recycling Al alloys often leads to uncontrolled ranges of alloying elements compositions. Alloy design based on recycling must therefore account for these composition variations on the alloy properties. High-throughput approaches, such as graded material studies are well adapted to tackle this problem. 6XXX series is a good case study since the contributions of Mg and Si on the metastability cascades are not perfectly understood.

In this PhD, graded materials, with a variation in both Mg and Si contents, are manufactured by powder metallurgy. Mg-rich powder is first poured on Si-rich powder. Then these two powder beds are consolidated by Spark Plasma Sintering and then subjected to a solutionizing treatment during which Mg and Si gradients form and widen. Microstructure and hardness are first characterised along the gradient. Then, an ageing treatment at 170°C is performed to get a whole range of precipitation sequences. The effect of composition on precipitation kinetics (precipitation pathways, precipitation state, hardness) are characterised using TEM, DSC and SAXS. A mean field framework based on classical nucleation and growth theories coupled with a hardening model has been developed and successfully compared to the experiments.

MOTS-CLÉS : powder metallurgy, graded materials, precipitation, Al-Mg-Si, mean field simulation

Laboratoire (s) de recherche : MATEIS – UMR CNRS 5510, LMI – UMR CNRS 5615

Directeur de thèse :
Xavier BOULNAT (Maitre de conférences), INSA Lyon
Michel PEREZ (Professeur), INSA Lyon
Olivier DEZELLUS (Maitre de conférences), UCBL
Alexis DESCHAMPS (Professeur), INP Grenoble

Composition du jury :	Myriam DUMONT	(Professeure), ENSAM	Rapporteure
	Aude SIMAR	(Professeure), UCLouvain	Rapporteure
	Williams LEFEBVRE	(Professeur), Université de Rouen	Examinateur
	Véronique MASSARDIER	(Maitre de conférences), INSA Lyon	Examinatrice
	Fanny MAS	(Docteure), Constellium	Invitée